Wind Turbine Rotors with Active Vibration Control

Svendsen, Martin Nymann

Publication date:
2011

Document Version
Publisher's PDF, also known as Version of record

Wind Turbine Rotors with Active Vibration Control

PhD Thesis

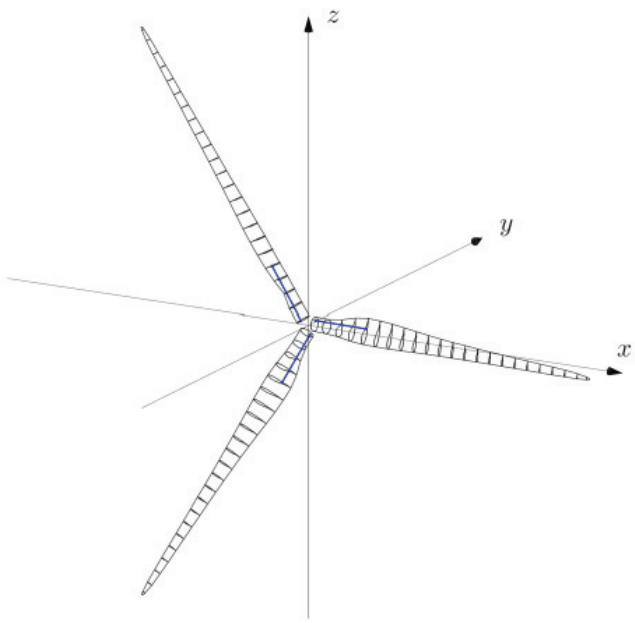

Martin Nymann Svendsen
DCAMM Special Report No. S122
Januar 2011

DTU Mechanical Engineering
Department of Mechanical Engineering

Wind Turbine Rotors with Active Vibration Control

Martin Nymann Svendsen

TECHNICAL UNIVERSITY OF DENMARK
DEPARTMENT OF MECHANICAL ENGINEERING
SECTION OF COASTAL, MARITIME AND STRUCTURAL ENGINEERING
MARCH 2011

Published in Denmark by
Technical University of Denmark

Section of Coastal, Maritime and Structural Engineering
Department of Mechanical Engineering
Technical University of Denmark
Nils Koppels Alle, Building 403, DK-2800 Kgs. Lyngby, Denmark
Phone +45 4525 1360, Telefax +45 4588 4325
E-mail: info.skk@mek.dtu.dk
WWW: http://www.mek.dtu.dk/

Publication Reference Data
Svendsen, M. N.
Wind Turbine Rotors with Active Vibration Control
PhD Thesis
Technical University of Denmark, Section of Coastal, Maritime and Structural Engineering.
March, 2011
ISBN 978-87-90416-42-3
Keywords: Active vibration control, resonant control, finite beam element, rotating beams, rotor dynamics, whirling modes, wind turbine control, gyroscopic systems, aeroelastic modeling

Abstract

This thesis presents a framework for structural modeling, analysis and active vibration damping of rotating wind turbine blades and rotors. A structural rotor model is developed in terms of finite beam elements in a rotating frame of reference. The element comprises a representation of general, varying cross-section properties and assumes small cross-section displacements and rotations, by which the associated elastic stiffness and inertial terms are linear. The formulation consistently describes all inertial terms, including centrifugal softening and gyroscopic forces. Aerodynamic lift forces are assumed to be proportional to the relative inflow angle, which also gives a linear form with equivalent stiffness and damping terms. Geometric stiffness effects including the important stiffening from tensile axial stresses in equilibrium with centrifugal forces are included via an initial stress formulation. The element provides an accurate representation of the eigenfrequencies and whirling modes of the gyroscopic system, and identifies lightly damped edge-wise modes. By adoption of a method for active, collocated resonant vibration of multi-degree-of-freedom systems it is demonstrated that the basic modes of a wind turbine blade can be effectively addressed by an in-blade 'active strut' actuator mechanism. The importance of accounting for background mode flexibility is demonstrated. Also, it is shown that it is generally possible to address multiple beam modes with multiple controllers, given that these are geometrically well separated. For active vibration control in three-bladed wind turbine rotors the present work presents a resonance-based method for groups of one collective and two whirling modes. The controller is based on the existing resonant format and introduces a dual system targeting the collective mode and the combined whirling modes respectively, via a shared set of collocated sensor/actuator pairs. The collective mode controller is decoupled from the whirling mode controller by an exact linear filter, which is identified from the fundamental dynamics of the gyroscopic system. As in the method for non-rotating systems, an explicit procedure for optimal calibration of the controller gains is established. The control system is applied to an 86 m wind turbine rotor by means of active strut actuator mechanisms. The prescribed additional damping ratios are reproduced almost identically in the targeted modes and the observed spill-over to other modes is very limited and generally stabilizing. It is shown that physical controller positioning for reduced background noise is important to the calibration. By simulation of the rotor response to both simple initial conditions and a stochastic wind load it is demonstrated that the amplitudes of the targeted modes are effectively reduced, while leaving the remaining modes virtually unaffected.

Resumé

I denne afhandling præsenteres en metoderamme for modellering, analyse og aktiv vibrationsdæmpning af roterende vindmølleblade og rotorer. En strukturel model udvikles i form af rumlige bjælkelementer i en roterende referenceramme. Elementet indeholder en repræsentation af generelle, varierende tværsnitsegenskaber og antager små tværsnitsflytninger og rotationer, hvorved de tilhørende elastiske led og inertialled bliver lineære. Formuleringen beskriver på konsistent vis alle inertialled, inklusiv negativ centrifugalstivhed og gyroskopiske kræfter. Aerodynamisk lift antages at være proportionalt til den relative indfaldsvinkel, hvilket også giver en lineær form med ækvivalente stivheds- og dæmpningsled. Geometriske stivhedseffekter, herunder det vigtige stivhedsbidrag fra trækspændinger i ligevægt med centrifugalbelastningen, er inkluderede via en initialspændingsformulering. Elementet giver en præcis representation af egenfrekvenser og hvirvlende svingningsformer i det gyroskopiske system, og lavt aerodynamisk dæmpede kantvise svingningsformer identificeres. Ved indførelse af en metode for aktiv, kollokeret, resonansbaseret vibrationskontrol af fler-frihedsgradssystemer demonstreres det, at de grundlæggende svingningsformer af et isoleret vindmølleblad effektivt kan dæmpes via en aktiv trækstangsmekanisme. Vigtigheden af at inkludere effekten af modal baggrundsfleksibilitet demonstreres. Det vises endvidere at det er muligt at addressere flere svingningsformer med flere separate kontrolsystemer, når formerne er geometrisk vel adskilt. Til aktiv vibrationskontrol i trebladede vindmøllerotorer præsenteres en resonansbaseret metode, målrettet grupper bestående af en kollektiv og to hvivlende svingningsformer. Kontrolsystemet er baseret på det kendte format og introducerer et dobbelt format som adresserer henholdsvis den kollektive og de hvirvlende svingningsformer, via et delt sæt af kollokerede sensor/aktuator par. Kontroldelen til den kollektive svingningsform er afkoblet fra kontroldelen til de hvirvlende svingningsformer via et eksakt lineært filter der er identificeret på baggrund af det gyroskopiske systems grundlæggende dynamik. Som i metoden for ikke-roterende systemer etableres en eksplicit kalibreringsprocedure. Kontrolsystemet anvendes på en 86 m vindmøllerotor via aktive trykstænger. De foreskrevne supplerende dæmpningsforhold reproduceres næsten identisk i de adresserede svingningsformer og den observerede interaktion med andre svingningsformer er meget begrænset og generelt stabiliserende. Det vises at fysisk positionering af kontrolsystemet for reduceret baggrundsflexibilitet er vigtigt for kalibreringen. Ved simulering af rotorens respons til både simple begyndelsesbetingelser og et stokastisk vindfelt demonstreres det, at amplituderne af de adresserede svingningsformer effektivt reduceres, mens de øvrige svingninger nærmest ikke påvirkes.

Preface

This thesis is submitted in partial fulfilment of the Ph.D. degree from the Technical University of Denmark. The work has primarily been performed at the Department of Mechanical Engineering at the Technical University of Denmark, in the period January 2008 to January 2011. The study has been performed under the supervision of Professor Dr. Techn. Steen Krenk as main supervisor and Associate Professor Jan Høgsberg as co-supervisor. I owe my deepest gratitude to Steen Krenk and Jan Høgsberg for their excellent guidance and support throughout the entire project.

The project is part of the Danish Industrial PhD programme and part of the work has been carried out at Vestas Wind Systems A/S under the supervision of Rasmus Svendsen and Per Brath. I would like to express my gratitude to both for their support and inspiring enthusiasm. The financing from the Danish Agency for Science, Technology and Innovation and Vestas Wind Systems A/S is also gratefully acknowledged.

Finally, I would like to express my most sincere thanks to those close to me for their patience and support. And, in particular, Maria, for being always encouraging and understanding.

Martin Nymann Svendsen

Copenhagen, January 2011

Publications

Appended papers

[P1] M.N. Svendsen, S. Krenk, J. Høgsberg,
Resonant vibration control of rotating beams,
Journal of Sound and Vibration, (2010), (doi:10.1016/j.jsv.2010.11.008).

[P2] M.N. Svendsen, S. Krenk, J. Høgsberg,
Resonant vibration control of wind turbine blades,
TORQUE 2010: The Science of Making Torque from Wind, 543–553,
June 28–30, Creete, Greece, 2010.

[P3] S. Krenk, M.N. Svendsen, J. Høgsberg,
Resonant vibration control of three-bladed wind turbine rotors,
(2011), *Paper submitted*.

Other Contributions

M.N. Svendsen, S. Krenk, J. Høgsberg,
Resonant vibration control of beams under stationary rotation,
Proceedings of the Twenty Second Nordic Seminar on Computational Mechanics, 75–78,
October 22–23, Aalborg, Denmark, 2009.

Contents

Chapter 1

Introduction

The cost of energy produced by a modern, three-bladed wind turbine is related to the lifetime of the machine. It is therefore of practical interest to consider methods for reducing fatigue loads, as these increase with expected component lifetime. Fatigue loading is present in large, modern wind turbines for a number of reasons. One is stochastic and periodic aerodynamic loading, Bossanyi [1], and another is continuous activity in the so-called 'edge-wise' vibration modes which are typically subject to weak aerodynamic damping, see e.g. Riziotis et al. [2] or Hansen et al. [3].

Figure 1.1: A modern wind turbine, the Vestas V112-3.0MW.

Stochastic aerodynamic loading is associated with the turbulent structure of the wind field. As rotor sizes increase, the turbulence in the swept area becomes less correlated, and this leads to larger lift variations on the individual blades. With size, also the periodic aerodynamic load variations due to wind shear become more pronounced. A common feature of these sources of fatigue loading is the stochastic or periodic variations in aerodynamic lift experienced by the individual blades. One of the early advances in reducing lift-based fatigue loads on pitch-regulated wind turbines was the use of individual pitch control [1], using the existing blade pitch system which was originally implemented for power output control. More recent advances operate within the concept of 'smart rotors', of which an overview is given by Barlas and van Kuik [4]. In this concept, the turbine blades are equipped with local, aerodynamic control surfaces. The most common example is probably the trailing edge flap concept, see e.g. Andersen et al. [5]. The blade response associated with wind speed variations is almost quasi-static and dominated by deformations out of the rotor plane, as the aerodynamic lift has a large component in this direction. The aerodynamic control surface concept produces control forces in the same direction, and has good controllability of the blade deformation states in question.

The edge-wise vibration modes are characterized by blade bending about the strong blade axis and are therefore dominated by displacements within the plane of rotation. The controllability of aerodynamic control surfaces towards these blade deformation states is therefore relatively low. Thus, reduction of fatigue loads associated with continuous activity in the lightly damped edge-wise vibration modes requires a somewhat different approach. This

work presents an active vibration control method for introducing damping to the first group of edge-wise vibration modes of three-bladed wind turbine rotors, Krenk et al. [6]. The group consists of three modes, namely the collective mode where all blades vibrate in phase and thereby activate the torsional flexibility of the main rotor shaft, and the backward and forward whirling modes which activate the transverse flexibility of the rotor shaft. The actuator system is based on assumed in-blade mechanisms, capable of imposing local bending moments. An example is shown in Fig. 1.2 where an active strut, see e.g. Preumont et al. [7], is positioned near the blade root with attachment points at the two shown cross-sections. By contraction or elongation the strut imposes a bending moment about the local blade $\tilde{y}$-axis. This gives good controllability of the edge-wise modes.

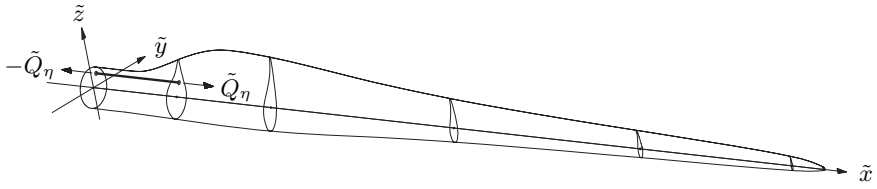

FIGURE 1.2: An active strut applied to a wind turbine blade.

As opposed to the somewhat quasi-static nature of the out-of-plane blade deformation problem, the targeted modal edge-wise response is purely dynamic. For this reason the present active control system is based on resonant interaction with the flexible structure. An early example of a passive, resonant vibration control system is the tuned mass damper, Ormondroyd & Den Hartog [8] which was originally designed for application to a single-degree-freedom-system. One of the pioneering works addressing modal vibrations in flexible, continuous structures was performed by Meirovitch [9] in terms of the 'independent modal space control' formulation. A formulation for active damping of one or more selected modes with zero spill-over was given, provided that a distributed sensor/actuator system is available. A more practical form of the modal control concept was given by Balas [10] in terms of a feedback controller with a finite number of discrete sensors and actuators. This work also introduced the use of modal state observers and gain calibration according to the theory of optimal linear quadratic control. Furthermore the concepts of modal observability and controllability were introduced, along with the concepts of observation and control spill-over and associated closed-loop instability issues.

The amount of relevant literature concerning resonant vibration control for three-bladed rotors appears limited. Also, the application of active resonant control to rotating systems in general seems limited. Recent investigations on vibration control of isolated, rotating beams have primarily focused on the use of novel smart materials, implementing well established control algorithms, such as direct velocity feedback, Choi et al. [11] or optimal linear quadratic control based on either estimated modal states, Khulief [12] or physical system states, see e.g. Shete et al. [13] or Chandiramani [14]. The present control method is based on the active, collocated resonant controller format given by Krenk & Høgsberg [15, 16]. Here an explicit calibration scheme was given for the controller filters, including a correction for the quasi-static flexibility of higher modes of multi-degree-of-freedom structure. The method was adopted for application to an isolated wind turbine blade in Svendsen et al. [17, 18] and the explicit calibration scheme provided almost optimal tuning and performance of the control system.

The rotor control method is based on a dual controller system targeting the collective mode and the whirling modes, respectively. The controllers interact with the rotor via a shared set of collocated sensor/actuator pairs. The whirling mode controller introduces a

multi-component format which is necessary to control the out-of-phase motion of the three blades associated with whirling. For calibration, the coupled system of multi-degree-of-freedom structural equations and multi-component controller equations are collapsed into scalar modal equations analogous to those of the basic resonant system of [15, 16], and the optimal filter parameters are identified by comparison. As input, the explicit calibration procedure takes the desired additional damping ratios, eigenfrequencies and complex-valued mode shapes of the targeted modes. Also, the physical connectivity of the collocated sensor/actuator configuration is used. As such, the calibration of the control system is based entirely on the properties of the targeted modes. The controller operates with a discrete acceleration feedback measured directly from the physical rotor deformation states. Thus, the operating controller makes no use of model reduction techniques or (modal) state observers. A concise proof of closed-loop stability and robustness has not been established, but the aforementioned features renders its existence probable.

As an example, the control system is applied to an 86 m wind turbine rotor using symmetrically positioned active struts as shown in Fig. 1.3. It is demonstrated by modal analysis of the closed-loop system that the calibration procedure provides the intended additional damping to the desired modes, with insignificant spill-over. Time integration of the rotor response to a simulated turbulent wind field, Krenk et al. [6], furthermore demonstrates that the control system effectively reduces the targeted modal vibration amplitudes in a stochastic environment.

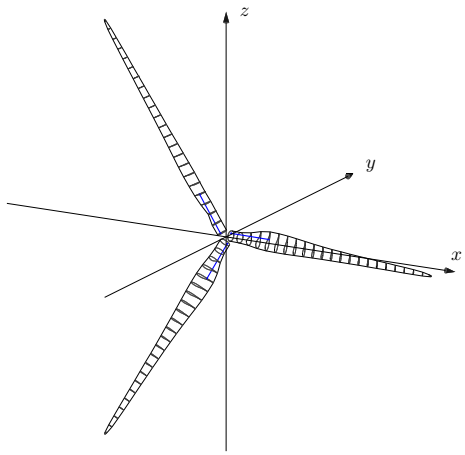

FIGURE 1.3: Three-bladed wind turbine rotor with actuator struts.

The wind turbine rotor is modeled using finite beam elements in a rotating frame of reference, Svendsen et al. [17, 18]. The element comprises a representation of general, varying cross-section properties including e.g. the positions of the elastic, shear and mass centers. The formulation assumes small cross-section displacements and rotations, by which the associated elastic stiffness and inertial terms are linear. Aerodynamic lift and drag forces are assumed to be proportional to the relative inflow angle, which also gives a linear form with equivalent stiffness and damping terms for small relative angle changes. Geometric stiffness effects are included via an initial stress formulation based on the undeformed structural geometry. This gives a linear stiffness contribution in terms of initial cross-section forces and moments. In the present application no initial stresses are present, and the formulation is intended to approximate the effects from current stresses due to aerodynamic and inertial loads. These are treated as initial stresses and the associated geometric stiffness effects are computed based on the undeformed structural geometry. The use of current stresses

introduces a non-linearity in the model, as the balance between structural deformation and equivalent stiffness due to internal stresses must be established by iteration. For stationary angular velocity of the rotor and no turbulence the structural equations of motion have constant terms and modal analysis can be performed following e.g. Géradin & Rixen [19]. For frequency response analysis of the gyroscopic system a formulation which captures both the symmetric contribution due to non-rotating effects and the skew-symmetric gyroscopic effects is used, Krenk et al. [6].

The text is organized as follows. In Chapter 2 the assumed beam kinematics is presented and the gyroscopic, aeroelastic equations of motion with geometric stiffness effects are derived for the finite beam element in a rotating frame of reference. The element matrices and load vectors appear in integral form and the used method for evaluation by Gaussian quadrature is presented. Finally, a framework for modal analysis and frequency response analysis of the gyroscopic system is given. Elements of the rotor model assembly and simulation procedures are initially given in Chapter 3. The fundamental dynamic features of three-bladed rotors are subsequently illustrated by a few numerical examples, and the dynamics of whirling are discussed in detail. Chapter 4 is initiated by a presentation of the basic format of a resonant controller. This is followed by an overview of the adopted formulation for multi-degree-of-freedom structures, and an example of application to a 42 m wind turbine blade is given, using the active strut actuator mechanism. The first flap-wise mode and the first edge-wise mode are addressed and the issue of optimal controller positioning is addressed. Subsequently, an overview of the control system format for flexible, three-bladed rotors is given. The numerical example with application to an 86 m rotor then follows. The example includes a discussion of the implications of physical sensor/actuator positioning and a simple time simulation example is given to present the fundamental function of the controller. In Chapter 5 the primary developments of the presented work are summarized.

Chapter 2

Rotating Finite Beam Element

The wind turbine rotor consists of three flexible blades connected in a common flexible support point, and can in this sense be seen as a system of rotating beam-like structures. The present resonant vibration control formulation for flexible three-bladed rotors is defined in terms of a finite element representation of the targeted structure, and in this chapter a consistent three-dimensional finite element formulation for beams in a rotating frame of reference is developed. Geometric stiffness effects including the important stiffening from tensile axial stresses in equilibrium with centrifugal forces are included via an initial stress formulation and the inertial terms capture the gyroscopic forces which are essential in the representation of whirling modes. A simple aerodynamic formulation is included to allow a realistic loading of the system and to distinguish weakly aerodynamically damped edge-wise vibration modes from strongly damped flap-wise vibration modes. Both the local structural properties of the blades and the global dynamic properties of the rotor captured by use of this element will later prove to be of great importance to the calibration of the resonant controller.

The equations of motion for the conservative rotating system are established from Lagrange's equations, expressed in a nodal format compatible with the finite element formulation, Kawamoto et al. [20]. The chapter initially defines the local, rotating frame of reference for the beam element. The kinematic representation of the flexible, rotating beam is then given and the kinetic energy is established. Stiffness effects arise from potential energy formulations. The elastic effects are expressed via a formulation of the complementary potential energy adopted from Krenk [21], and the geometric stiffness effects are established by transformation of a formulation for the potential energy associated with initial stresses given by Krenk [22]. The finite element formulation for the non-conservative, state-proportional aerodynamic forces is then obtained via a linearization of the relative inflow angle, Fung [23], Larsen et al. [24] and Hansen [25]. The aeroelastic contributions to the equations of motion are established via the principle of virtual work, after which all conservative and non-conservative terms are combined to obtain the full, coupled equations of motion for the rotating beam element. The equations are written in standard configuration-space format with a constant mass matrix, an operation state-dependent equivalent damping matrix, a non-linear operation state-dependent equivalent stiffness matrix and an operation state-dependent forcing term. A state-space format for modal analysis is given, according to e.g. Géradin and Rixen [19], followed by a formulation for frequency response analysis of the gyroscopic system, [6].

2.1 Inertial Effects

In order to obtain a consistent representation of the inertial properties of a body, a suitable kinematic representation must be established. In the following a convenient description of beam kinematics is presented, Svendsen et al. [17]. The format is employed in a derivation of the kinetic energy, from where the characteristic inertial terms are extracted. The derivation follows Kawamoto et al. [20], where a formulation for isoparametric elements is established. In the present case nodal rotations are a fundamental part of the kinematic description, necessitating extension of the formulation in [20] to Hermitian shape functions.

2.1.1 Beam Kinematics

In Fig. 2.1 the flexible beam is shown in the inertial frame of reference $\{X, Y, Z\}$ and the rotating frame of reference $\{x, y, z\}$. The beam is initially straight and has the local x-axis as longitudinal reference axis. The coordinates of a point in the undeformed beam are represented in the rotating frame by the position vector $\mathbf{x} = [\, x, y, z \,]^T$.

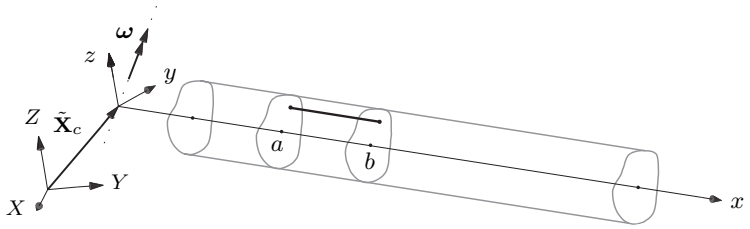

FIGURE 2.1: Inertial and rotating frames for a beam with an active strut.

The displacement of the point $\mathbf{x}$ due to beam deformation is denoted $\Delta\mathbf{x} = [\, \Delta x, \Delta y, \Delta z \,]^T$, and the total position of a point in the deformed state is

$$\mathbf{x}_t = \mathbf{x} + \Delta\mathbf{x} \tag{2.1}$$

Cross-sections of the deformed beam are defined as planar thin slices of the beam, orthogonal to the reference axis x. Cross-sections are assumed to remain planar under beam deformation. The displacement field $\Delta\mathbf{x}$ of a cross-section intersecting the reference axis at the point $[\, x, 0, 0 \,]^T$ is represented via the linearized interpolation (2.2) over the undeformed cross-section,

$$\Delta\mathbf{x} = \mathbf{N}_A(y,z) \begin{bmatrix} \mathbf{q}(x) \\ \mathbf{r}(x) \end{bmatrix}, \quad \mathbf{N}_A(y,z) = \begin{bmatrix} 1 & 0 & 0 & 0 & z & -y \\ 0 & 1 & 0 & -z & 0 & 0 \\ 0 & 0 & 1 & y & 0 & 0 \end{bmatrix} \tag{2.2}$$

where $\mathbf{q} = [\, q_x, q_y, q_z \,]^T$ are displacements and $\mathbf{r} = [\, r_x, r_y, r_z \,]^T$ are rotations with respect to the reference axes in the local frame, as indicated in Fig. 2.2a. The linearized format of the area interpolation matrix $\mathbf{N}_A$ assumes small cross-section rotations $\mathbf{r}$.

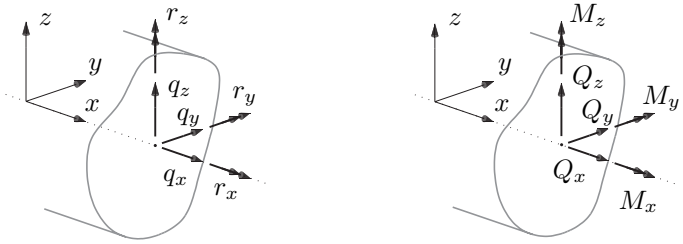

FIGURE 2.2: (a) Displacements $\mathbf{q}$ and rotations $\mathbf{r}$. (b) Forces $\mathbf{Q}$ and moments $\mathbf{M}$.

In order to obtain a discrete finite element formulation, cross-section displacements and rotations along the element reference axis are interpolated by nodal displacements and rotations $\mathbf{u}^T = [\, \mathbf{q}_a^T, \mathbf{r}_a^T, \mathbf{q}_b^T, \mathbf{r}_b^T \,]$ and the longitudinal interpolation functions $\mathbf{N}_x(x)$,

$$\begin{bmatrix} \mathbf{q}(x) \\ \mathbf{r}(x) \end{bmatrix} = \mathbf{N}_x(x)\mathbf{u} \tag{2.3}$$

The subscripts a and b indicate the two element nodes and the shape functions $\mathbf{N}_x(x)$ used in the present case are given in Appendix A.1. Axial cross-section displacements q_x and torsional rotations r_x are interpolated linearly while transverse displacements $\{q_y,\, q_z\}$ and rotations $\{r_y,\, r_x\}$ are interpolated with cubic shape functions. The deformed position field $\mathbf{x}_t$ may then be written as

$$\mathbf{x}_t = \mathbf{x} + \mathbf{N}_A(y,z)\mathbf{N}_x(x)\mathbf{u} \tag{2.4}$$

whereby the interpolation of the deformation field $\Delta\mathbf{x}$ is separated into a local cross-section area interpolation $\mathbf{N}_A(y,z)$ and a length-wise interpolation $\mathbf{N}_x(x)$.

2.1.2 Kinetic Energy

The kinetic energy associated with rigid-body motion and motion due to deformation of the beam is given by the volume integral

$$T = \tfrac{1}{2}\int_V \mathbf{v}_t^T\mathbf{v}_t\ \varrho\, dV \tag{2.5}$$

where $\mathbf{v}_t$ is the absolute velocity of a point in the local frame of reference and $\varrho = \varrho(x,y,z)$ is mass density.

The center of the local frame of reference is located in $\mathbf{X}_c$. The orientation of the local frame of reference is determined by the rotation matrix $\mathbf{R}$, corresponding to a finite rotation by the angle φ about an arbitrary axis $\mathbf{n} = [\,n_x,\, n_y,\, n_z\,]^T$, as discussed by Argyris [26]. The rotation parameters φ and $\mathbf{n}$ can be combined in the pseudo-vector $\boldsymbol{\varphi} = \varphi\,\mathbf{n}$ which will be used in the following to denote angular velocity $\boldsymbol{\omega} = \dot{\boldsymbol{\varphi}}$ and angular acceleration $\boldsymbol{\alpha} = \dot{\boldsymbol{\omega}}$ of the local reference frame. The rotation matrix $\mathbf{R}$ can be written as

$$\mathbf{R} = \cos\varphi\,\mathbf{I} + \sin\varphi\,\hat{\mathbf{n}} + (1-\cos\varphi)\,\mathbf{n}\,\mathbf{n}^T \tag{2.6}$$

see e.g. Argyris [26], Géradin & Cardona [27] or Krenk [28]. The rotation matrix is non-linear, indicating the fundamental difference between infinitesimal (small) and finite rotations. Small rotations are commuting, i.e. a particle translated by two sequential rotations can follow two approximately piece-wise linear paths and reach approximately the same point regardless of the mutual order of the two rotations. This property allows e.g. the simple interpolation (2.2) where the assumption of small rotations allows these to be represented in vector format. A particle translated by two large sequential rotations will follow two different paths on the surface of a sphere, depending on the mutual order of the rotations. The two paths will lead the particle to two distinctly different positions. In (2.6) $\mathbf{I}$ is the identity matrix and $\hat{\mathbf{n}}$ has the skew-symmetric form

$$\hat{\mathbf{n}} = \begin{bmatrix} 0 & -n_z & n_y \\ n_z & 0 & -n_x \\ -n_y & n_x & 0 \end{bmatrix} \tag{2.7}$$

In the present case the axis of rotation is assumed to intersect the center of the rotating reference frame. The deformed position with respect to the inertial frame $\mathbf{X}_t$ can then be written as

$$\mathbf{X}_t = \mathbf{X}_c + \mathbf{R}\mathbf{x}_t \tag{2.8}$$

The absolute velocity $\dot{\mathbf{X}}_t$ is found by differentiation of $\mathbf{X}_t$ with respect to time,

$$\dot{\mathbf{X}}_t = \dot{\mathbf{X}}_c + \mathbf{R}\dot{\mathbf{x}}_t + \dot{\mathbf{R}}\mathbf{x}_t \tag{2.9}$$

where $\dot{\mathbf{X}}_c$ is the velocity of the rotating reference frame. The absolute velocity in the local frame of reference $\mathbf{v}_t$ is found by pre-multiplication with $\mathbf{R}^T$,

$$\mathbf{v}_t = \mathbf{R}^T\dot{\mathbf{X}}_t = \mathbf{v}_c + \dot{\mathbf{x}}_t + \hat{\boldsymbol{\omega}}\mathbf{x}_t \tag{2.10}$$

The first term represents the velocity of the rotating frame with respect to the local orientation and the second term represents the local velocity due to deformation. The last contribution represents the rotational velocity of the local frame of reference, where the skew-symmetric matrix $\hat{\boldsymbol{\omega}}$, denoting the vector product $\boldsymbol{\omega}\times$, is defined as

$$\hat{\boldsymbol{\omega}} = \boldsymbol{\omega}\times = \mathbf{R}^T\dot{\mathbf{R}} = \begin{bmatrix} 0 & -\omega_z & \omega_y \\ \omega_z & 0 & -\omega_x \\ -\omega_y & \omega_x & 0 \end{bmatrix} \tag{2.11}$$

Thus, $\hat{\boldsymbol{\omega}}\,\mathbf{x}_t = \boldsymbol{\omega}\times\mathbf{x}_t$, where $\boldsymbol{\omega} = \dot{\boldsymbol{\varphi}}$ is the angular velocity of the local frame of reference.

2.1.3 Inertial Matrices

When inserting (2.4) into (2.10) the interpolated velocity field $\mathbf{v}_t$ appears as

$$\mathbf{v}_t = \mathbf{v}_c + \mathbf{N}_A\mathbf{N}_x\dot{\mathbf{u}} + \hat{\boldsymbol{\omega}}\mathbf{x} + \hat{\boldsymbol{\omega}}\mathbf{N}_A\mathbf{N}_x\mathbf{u} \tag{2.12}$$

where arguments of the interpolation arrays have been omitted for brevity. Substitution of (2.12) into (2.5) leads to the following expression for the kinetic energy,

$$\begin{aligned} T = {} & \tfrac{1}{2}\dot{\mathbf{u}}^T\mathbf{M}\dot{\mathbf{u}} + \mathbf{v}_c^T\mathbf{M}_0\dot{\mathbf{u}} + \dot{\mathbf{u}}^T\mathbf{G}\mathbf{u} + \mathbf{v}_c^T\mathbf{G}_0\mathbf{u} + \tfrac{1}{2}\mathbf{u}^T\mathbf{C}\mathbf{u} \\ & + \mathbf{u}^T\mathbf{f}_C + \dot{\mathbf{u}}^T\mathbf{f}_G^* + \tfrac{1}{2}m\mathbf{v}_c^T\mathbf{v}_c + \tfrac{1}{2}\int_V \mathbf{x}^T\hat{\boldsymbol{\omega}}^T\hat{\boldsymbol{\omega}}\mathbf{x}\varrho dV + \tfrac{1}{2}\int_V \mathbf{v}_c^T\hat{\boldsymbol{\omega}}\mathbf{x}\varrho dV \end{aligned} \tag{2.13}$$

This expression consists of a set of well-defined contributions to the kinetic energy in the form of characteristic inertial terms. The last three terms of (2.13) represent the kinetic energy associated with a uniform translational velocity and angular velocity of the undeformed structure. Here m is the mass of the beam element, while the last two terms represent rotational and gyroscopic inertia, respectively. These constant terms do not produce contributions to the equations of motion in the local frame of reference. The term $\mathbf{f}_G^*$ enters the equations of motion as the angular acceleration term $\mathbf{f}_G = \dot{\mathbf{f}}_G^*$, as shown in the following. $\mathbf{M}$ is the classic symmetric mass matrix associated with motion due to deformation of the body,

$$\mathbf{M} = \int_L \mathbf{N}_x^T\Big(\int_A \mathbf{N}_A^T\mathbf{N}_A\varrho dA\Big)\mathbf{N}_x dx \tag{2.14}$$

The volume integral is separated into a local area integral and an integral over the element length. The area integral can be written explicitly as

$$\int_A \mathbf{N}_A^T\mathbf{N}_A\varrho dA = \begin{bmatrix} A^\varrho & 0 & 0 & 0 & S_z^\varrho & -S_y^\varrho \\ & A^\varrho & 0 & -S_z^\varrho & 0 & 0 \\ & & A^\varrho & S_y^\varrho & 0 & 0 \\ & & & I^\varrho & 0 & 0 \\ & \text{Sym.} & & & I_{zz}^\varrho & -I_{zy}^\varrho \\ & & & & & I_{yy}^\varrho \end{bmatrix} \tag{2.15}$$

where the weighted area A_ϱ, section moments $\{S_y^\varrho,\, S_z^\varrho\}$ and moments of inertia $\{I_{yy}^\varrho,\, I_{zz}^\varrho,\, I_{yz}^\varrho\}$ are defined by

$$\mathbf{J}_\varrho = \begin{bmatrix} A^\varrho & S_y^\varrho & S_z^\varrho \\ & I_{yy}^\varrho & I_{yz}^\varrho \\ & & I_{zz}^\varrho \end{bmatrix} = \int_A \begin{bmatrix} 1 & y & z \\ & yy & yz \\ & & zz \end{bmatrix} \varrho\, dA \tag{2.16}$$

the weighted area A_ϱ is the cross-section mass density and the static moments $\{S_y^\varrho,\, S_z^\varrho\}$ represent the distance between the cross-section mass center and the element reference axis. When the mass center does not coincide with the reference axis, axial displacement q_x

couples with bending rotations $\{r_y,\, r_z\}$ and transverse displacements $\{q_y,\, q_z\}$ couple with torsion r_x. The torsional coupling is particularly important to the stability of certain aerodynamic vibration modes, as explained in more detail in Sec. 2.4. The moments of inertia $\{I^{\varrho}_{yy},\, I^{\varrho}_{zz}\}$ represent the rotational cross-section inertia about the transverse element axes $\{y,\, z\}$ and I^{ϱ}_{yz} is a coupling term that arises when the transverse element axes do not coincide with the axes of mass symmetry. Pure torsional inertia I_{ϱ} is evaluated as $I_{\varrho} = I^{\varrho}_{yy} + I^{\varrho}_{zz}$.

The remaining inertial vectors and matrices introduced in (2.13) are defined in the following. Inertial forces due to uniform body accelerations $\mathbf{a}_c = \ddot{\mathbf{x}}_c$ enter via the matrix

$$\mathbf{M}_0 = \int_L \mathbf{N}_x^T \Big(\int_A \mathbf{N}_A \varrho dA \Big) \mathbf{N}_x dx \tag{2.17}$$

where the area integral can be written explicitly in terms of the mass density A^{ϱ} and the first order moments $\{S^{\varrho}_y,\, S^{\varrho}_z\}$. The skew-symmetric gyroscopic coupling matrix is given as

$$\mathbf{G} = \int_L \mathbf{N}_x^T \Big(\int_A \mathbf{N}_A^T \hat{\boldsymbol{\omega}} \mathbf{N}_A \varrho dA \Big) \mathbf{N}_x dx \tag{2.18}$$

which is composed of products between the angular velocity components of $\boldsymbol{\omega} = [\,\omega_x,\, \omega_y,\, \omega_z\,]^T$ and the parameters (2.16). The skew-symmetry of the gyroscopic matrix implies that the forces are non-working, i.e. the term merely represents an internal redistribution of energy. It can be shown that a conservative linear system cannot be made unstable by gyroscopic forces, see e.g. Ziegler [29]. The gyroscopic forces play a critical role in the dynamics of three-bladed rotors, as these are the driving forces of the whirling modes. In Sec. 3.4 the dynamics of whirling in three-bladed rotors are explained in detail. The term $\mathbf{v}_c^T \mathbf{G}_0 \mathbf{u}$ represents the kinetic energy associated with gyroscopic forces due to a uniform velocity of the rotating frame, and $\mathbf{G}_0$ is simply given as

$$\mathbf{G}_0 = \hat{\boldsymbol{\omega}} \mathbf{M}_0 \tag{2.19}$$

As shown in Section 2.4.1 the forces associated with $\mathbf{G}_0$ are not present in the equations of motion in the local frame. The centrifugal stiffness enters through the centrifugal matrix

$$\mathbf{C} = \int_L \mathbf{N}_x^T \Big(\int_A \mathbf{N}_A^T \hat{\boldsymbol{\omega}}^T \hat{\boldsymbol{\omega}} \mathbf{N}_A \varrho dA \Big) \mathbf{N}_x dx \tag{2.20}$$

which is symmetric, but not necessarily positive definite. Displacements within the plane of rotation may lead to increased centrifugal forces which are oriented away from the undeformed position of the structure, hence reducing the effective structural stiffness. Consequently, the presence of centrifugal stiffness can destabilize a system and the effect is also known as centrifugal softening. The centrifugal forces are defined as

$$\mathbf{f}_C = \int_L \mathbf{N}_x^T \Big(\int_A \mathbf{N}_A^T \hat{\boldsymbol{\omega}}^T \hat{\boldsymbol{\omega}} \mathbf{x} \varrho dA \Big) dx \tag{2.21}$$

where several products within the area integral contain the factor x, representing the distance from the cross-section reference point to the intersection between the rotation axis and the beam reference axis. In Section 2.4.1 the equations of motion are derived from Lagrange's equations, where the forces due to angular acceleration $\boldsymbol{\alpha} = \dot{\boldsymbol{\omega}}$ enter via the time derivative of $\mathbf{f}^*_G$. These forces can therefore be computed by the integral

$$\mathbf{f}_G = \int_L \mathbf{N}_x^T \Big(\int_A \mathbf{N}_A^T \hat{\boldsymbol{\alpha}} \mathbf{x} \varrho dA \Big) dx \tag{2.22}$$

The gyroscopic and centrifugal matrices are time dependent, as the angular velocity $\boldsymbol{\omega}$ may vary in time. In time simulations, these matrices as well as the centrifugal and angular acceleration force vectors must be updated accordingly. This may be done by explicit

evaluation of area integrals based on the constant cross-section parameters (2.16) and prescribed or predicted angular velocities and accelerations, followed by numerical evaluation of length-wise integrals (2.18)-(2.22). The area integrals in (2.18)-(2.22) are given explicitly in Appendix A.2 and in Section 2.4.4 a procedure is given for numerical computation of the length-wise integrals by Gaussian quadrature.

2.2 Stiffness Effects

The elastic and geometric stiffness contributions to the equations of motion are established from the variation of the structural potential energy U. The potential energy is here evaluated as the sum $U = U_e + U_g$ of the potential strain energy U_e and the potential energy U_g associated with deformation of a body with initial stresses $\boldsymbol{\sigma}^0 = \{\sigma^0_{xx}, \sigma^0_{xy}, \sigma^0_{xz}\}$. The variation of the potential energy can be written as

$$\frac{\partial U}{\partial \mathbf{u}^T} = \mathbf{g}(\mathbf{u}) \tag{2.23}$$

which is fundamentally a nonlinear function of the system states $\mathbf{u}$. Assuming small deformations and linear elastic material properties, the variation of the potential strain energy can be written as a linear function in $\mathbf{u}$, with the elastic stiffness matrix $\mathbf{K}_e$ as proportionality factor. As discussed by Washizu [30], the variation of the potential strain energy associated with internal stresses can be linearized by considering the internal stress field as a constant initial stress field $\boldsymbol{\sigma}^0$ which resides in the undeformed structure and is independent of changes in $\mathbf{u}$. Application of these linearizations of the elastic and geometric stiffness gives the following linearized form of the variation of the potential energy,

$$\mathbf{g}(\mathbf{u}) \simeq \big(\mathbf{K}_e + \mathbf{K}_g(\boldsymbol{\sigma}^0)\big)\mathbf{u} \tag{2.24}$$

where $\mathbf{K}_g(\boldsymbol{\sigma}^0)$ is the geometric stiffness matrix based on an initial state of stress $\boldsymbol{\sigma}^0$. The static field of the present beam formulation consists of cross-section forces $\mathbf{Q} = [\, Q_x,\, Q_y,\, Q_z \,]^T$ and moments $\mathbf{M} = [\, M_x,\, M_y,\, M_z \,]^T$, as illustrated in Fig. 2.2b. The axial force Q_x and the transverse shear forces Q_y and Q_z are defined by the area integrals

$$Q_x = \int_A \sigma_{xx}\, dA, \quad Q_y = \int_A \sigma_{xy}\, dA, \quad Q_z = \int_A \sigma_{xz}\, dA \tag{2.25}$$

and the torsional moment M_x and the two bending moments M_y and M_z are defined as

$$M_x = \int_A (\sigma_{xz} y - \sigma_{xy} z)\, dA, \quad M_y = \int_A \sigma_{xx} z\, dA, \quad M_z = -\int_A \sigma_{xx} y\, dA \tag{2.26}$$

The sign convention is chosen such that positive axial stresses σ_{xx} are associated with tension in the material and shear stresses $\{\sigma_{xz}, \sigma_{xy}\}$ are positive in the corresponding directions of transverse shear strains.

2.2.1 Elastic Stiffness

The elastic stiffness matrix is established from the complementary potential energy following Krenk [21]. The flexibility of a two-node beam element with six degrees of freedom per node can be obtained from six independent deformation modes, corresponding to a set of end loads in static equilibrium. Since the static fields are independent of the beam configuration, the flexibility method allows an exact lengthwise integration of the potential strain energy in beams with general and varying cross-section properties. This differentiates the method from classical stiffness methods based on approximate interpolation of kinematic fields.

The ability to represent general, varying elastic cross-section properties is particularly relevant in the case of wind turbine blades. These are generally inhomogeneous, orthotropic composite structures of non-trivial geometry, optimized for stiffness, strength, weight and aerodynamic performance. An example is shown in Fig. 2.3 where the aerodynamic profile and inhomogeneous composition of a typical cross-section is seen. As it will be illustrated in the next chapter, a typical turbine blade furthermore has significant variation of cross-section properties in the longitudinal direction. This underlines the importance of consistently accounting for varying cross-section properties within the element, as permitted by the adopted elastic formulation.

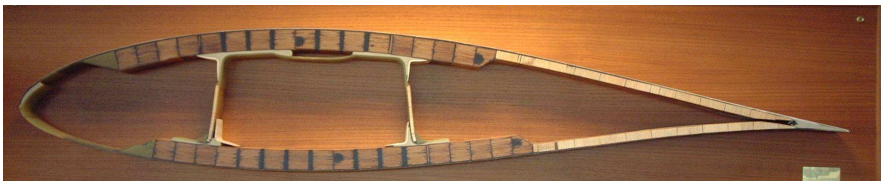

FIGURE 2.3: An example of a wind turbine blade cross-section.

The deformations associated with the static field defined in (2.25) and (2.26) are described in terms of generalized strains $\boldsymbol{\gamma} = \mathbf{q}'$ and curvatures $\boldsymbol{\kappa} = \mathbf{r}'$, where the superscript $'$ denotes lengthwise differentiation d/dx. The component γ_x is the axial strain, while γ_y and γ_z are the shear strains. The rate of twist is denoted κ_x, while κ_y, κ_z are the curvatures associated with bending. The assumption of planar cross-sections corresponds to assuming homogeneous St. Venant torsion, with identical cross-sectional warping along the beam. For thin-walled beams this assumption is often reasonable for beams with closed cross-sections, Vlasov [31]. As illustrated in Fig. 2.3, this applies to wind a turbine blade.

In the case of linear material properties, the cross-section forces and moments are energetically conjugate to the generalized strains and curvatures via the non-singular cross-section stiffness matrix $\mathbf{D}_c$,

$$\begin{bmatrix} \mathbf{Q} \\ \mathbf{M} \end{bmatrix} = \mathbf{D}_c \begin{bmatrix} \boldsymbol{\gamma} \\ \boldsymbol{\kappa} \end{bmatrix} \tag{2.27}$$

In the case where the beam is composed of isotropic cross-section materials and both the shear center A and the elastic center C coincide with the element reference axis, $\mathbf{D}_c$ takes the following symmetric, block-diagonal form

$$\mathbf{D}_c = \begin{bmatrix} A^E & 0 & 0 & 0 & 0 & 0 \\ & A^G_{yy} & A^G_{yz} & 0 & 0 & 0 \\ & & A^G_{zz} & 0 & 0 & 0 \\ & & & K^G & 0 & 0 \\ & \text{Sym.} & & & I^E_{zz} & I^E_{yz} \\ & & & & & I^E_{yy} \end{bmatrix} \tag{2.28}$$

The elastic center C is defined as the point in the cross-section where an applied axial force will not introduce bending. This corresponds to vanishing components at positions $(1,5)$ and $(1,6)$ and their symmetric counterparts in $\mathbf{D}_c$. The shear center A is defined as the point in the cross-section through which a transverse force does not introduce torsion. This corresponds to vanishing components at positions $(2,4)$ and $(3,4)$ and their symmetric counterparts. Assuming that the elastic center C coincides with the element reference axis,

the axial stiffness parameters of $\mathbf{D}_c$ are given explicitly as

$$\mathbf{J}_E = \begin{bmatrix} A^E & 0 & 0 \\ & I^E_{yy} & I^E_{yz} \\ & & I^E_{zz} \end{bmatrix} = \int_A \begin{bmatrix} 1 & y & z \\ & yy & yz \\ & & zz \end{bmatrix} E\, dA \tag{2.29}$$

where $E(y, z)$ is the elastic modulus of the material. The parameter A^E is the axial stiffness and the second order moments $\{I^E_{zz},\, I^E_{yy}\}$ are the cross-section bending stiffnesses resisting the beam curvatures $\{\kappa_y,\, \kappa_z\}$ about the y- and z-axes respectively. The principal elastic axes of a cross-section are defined as the two orthogonal axes in the cross-section plane, about which bending uncouples. The off-diagonal coupling term I^E_{yz} appears when the elastic principal axes are not parallel to the element reference axes. While the axial parameters weighted by E are given explicitly by area integrals similar to their inertial equivalents, the shear stiffness parameters $\{A^G_{yy},\, A^G_{zz}, A^G_{yz}\}$ and the torsional stiffness K^G typically require the shear stress distribution. The principal shear axes of a cross-section are defined as the two orthogonal axes in the cross-section plane, about which shear deformations uncouple and the off-diagonal component A^G_{yz} appears when the shear principal axes are not parallel to the element reference axes.

The kinematic behavior of a cross-section is defined by the positions of the shear and elastic centers and the orientations of the principal shear and elastic axes. These characteristic properties allow a good intuitive understanding of both static and dynamic beam behavior and for design purposes it can therefore be useful to define cross-section properties with respect to these. In Appendix B.2 it is shown how $\mathbf{D}_c$ can be established on the basis of these characteristic properties such as to account consistently for the resulting coupling effects. In the general case of anisotropic non-homogeneous material properties the matrix $\mathbf{D}_c$ may be determined by numerical methods, see e.g. Hodges et al. [32].

The potential strain energy of a beam element is given by integration of the cross-section energy density,

$$U_e = \tfrac{1}{2} \int_L \left[\, \boldsymbol{\gamma}^T,\ \boldsymbol{\kappa}^T \,\right] \mathbf{D}_c \begin{bmatrix} \boldsymbol{\gamma} \\ \boldsymbol{\kappa} \end{bmatrix} dx = \tfrac{1}{2} \int_L \left[\, \mathbf{Q}^T,\ \mathbf{M}^T \,\right] \mathbf{C}_c \begin{bmatrix} \mathbf{Q}^T \\ \mathbf{M}^T \end{bmatrix} dx \tag{2.30}$$

The first integral utilizes a description of the kinematic field and the associated cross-section stiffness, while the second integral brings the static field and the associated cross-section flexibility into play, introducing the flexibility matrix $\mathbf{C}_c = \mathbf{D}_c^{-1}$. In a beam without external loads the internal normal force, the shear forces and the torsional moment are constant, while bending moments vary linearly. Thus, the desired distribution of the internal forces along the beam element can be parameterized in terms of the element mid point values $\mathbf{Q}_m$ and $\mathbf{M}_m$. Substitution of the parametric representation of $\mathbf{Q}$ and $\mathbf{M}$ in terms of $\mathbf{Q}_m$ and $\mathbf{M}_m$ into (2.30) yields

$$U_e = \tfrac{1}{2} \left[\, \mathbf{Q}_m^T,\ \mathbf{M}_m^T \,\right] \mathbf{H} \begin{bmatrix} \mathbf{Q}_m \\ \mathbf{M}_m \end{bmatrix} \tag{2.31}$$

where the element flexibility matrix $\mathbf{H}$ represents the integral of the elastic energy density associated with cross-section flexibility and the desired distribution of the static fields. By inversion of the element flexibility matrix and appropriate transformation from the constant mid point internal forces and moments into nodal displacements and rotations $\mathbf{u}$, the potential energy can be written as

$$U_e = \tfrac{1}{2} \mathbf{u}^T \mathbf{K}_e \mathbf{u} \tag{2.32}$$

defining the elastic element stiffness matrix $\mathbf{K}_e$. This matrix is symmetric and positive definite and is given explicitly in [21].

2.2.2 Geometric Stiffness

A theory for linearized stability analysis based on initial stresses was formulated by Vlasov [31], who used direct vector arguments to obtain the equilibrium conditions in differential equation format. This form does not immediately lead to a symmetric matrix formulation of the finite element equations, and it appears to be more convenient to combine the continuum format of the linearized initial stress problem, Washizu [30], with the displacement field used in the beam theory, Krenk [22]. In this formulation the additional contribution to the energy functional from the initial stress is obtained on the basis of a general three-dimensional state of stress with initial normal stress σ^0_{xx} and initial shear stresses $\sigma^0_{xy}, \sigma^0_{xz}$, corresponding to the basic assumptions of beam theory. The corresponding potential energy has the form

$$\begin{aligned} U_g = \int_V \Big(& \tfrac{1}{2}\sigma^0_{xx}\Big[\frac{\partial(\Delta z)}{\partial x}\frac{\partial(\Delta z)}{\partial x} + \frac{\partial(\Delta y)}{\partial x}\frac{\partial(\Delta y)}{\partial x} \Big] \\ & + \sigma^0_{xy}\frac{\partial(\Delta z)}{\partial x}\frac{\partial(\Delta z)}{\partial y} + \sigma^0_{xz}\frac{\partial(\Delta y)}{\partial x}\frac{\partial(\Delta y)}{\partial z} \Big)\, dV \end{aligned} \tag{2.33}$$

The effect of the initial stress on the equilibrium conditions is represented via the change of orientation of the initial state of stress, expressed via the lengthwise derivatives of the transverse displacements,

$$\frac{\partial(\Delta y)}{\partial x} = q'_y - r'_x z, \quad \frac{\partial(\Delta z)}{\partial x} = q'_z + r'_x y \tag{2.34}$$

where the kinematic relations are here taken from the linearized interpolation (2.2). Hereby the initial stresses, that were in equilibrium in the undeformed state, produce additional terms in the equilibrium equations. The corresponding quadratic energy functional is

$$\begin{aligned} U_g = \int_L \Big(& \int_A \tfrac{1}{2}\Big[(q'_y - r'_x z)^2 + (q'_z + r'_x y)^2 \Big]\sigma^0_{xx}\, dA \\ & - r_x \int_A \tfrac{1}{2}\Big[(q'_y - r'_x z)\,\sigma^0_{xz} - (q'_z + r'_x y)\,\sigma^0_{xy} \Big]\, dA \Big)\, dx \end{aligned} \tag{2.35}$$

By evaluation of the area integrals, the potential energy can be written in terms of initial cross-section forces $\mathbf{Q}^0$ and moments $\mathbf{M}^0$. In this integration the definition of the shear center A with coordinate vector $\mathbf{a} = [\, a_x,\, a_y,\, a_z \,]^T$ is used in its stress equilibrium definition,

$$\int_A \sigma_{xy}(y - a_y)\, dA = 0, \quad \int_A \sigma_{xz}(z - a_z)\, dA = 0 \tag{2.36}$$

This allows the eliminations $\int_A \sigma^0_{xy} y dA = a_y \int_A \sigma^0_{xy} dA$ and $\int_A \sigma^0_{xz} z dA = a_z \int_A \sigma^0_{xz} dA$, by which the potential energy can be written in terms of initial cross-section forces and moments and the shear center coordinates $\mathbf{a}$,

$$\begin{aligned} U_g = \int_L \Big(& \tfrac{1}{2}q'_y q'_y Q^0_x + \tfrac{1}{2}q'_z q'_z Q^0_x - r'_x q'_y M^0_y - r'_x q'_z M^0_z \\ & + \frac{1}{2} r'_x r'_x S^0 - r_x q'_y Q^0_z + r_x q'_z Q^0_y + r'_x r_x (a_y Q^0_y + a_z Q^0_z) \Big)\, dx \end{aligned} \tag{2.37}$$

The expression (2.37) furthermore includes the stress integral S^0, as defined in (2.38). The parameter is seen to directly influence the equivalent torsional stiffness and is primarily important in torsional stability problems for beam-columns with low torsional stiffness. Open thin-walled cross-sections have a relatively low torsional stiffness, whereas closed cross-sections such as wind turbine blades have a relatively high torsional stiffness. Thus, the

positive torsional stiffening effect of S^0 for a wind turbine under tensile loads due to centrifugal forces will typically be small compared to the elastic torsional stiffness K^G of the blade.

$$S^0 = \int_A (y^2 + z^2)\sigma_{xx}^0 \, dA \tag{2.38}$$

The parameter S^0 must generally be evaluated numerically, as an explicit evaluation of the integral becomes difficult in cases of both combined bending and axial deformation as well as inhomogeneous material compositions. In the simple case of a homogeneous material composition and an axial load through the elastic center, the axial stresses have the constant value $\sigma_{xx}^0 = Q_x/A_s$ where A_s is the area of the cross-section. The stress integral is in this case given explicitly as $S^0 = Q_x(I_{yy}^E + I_{zz}^E)/(A_s E)$.

The original formulation by Krenk [22] of the potential energy associated with initial stresses also includes the effect of an externally applied distributed load which is not included here. The contribution to the potential energy from initial stresses (2.37) can hereby be expressed in the following quadratic matrix format [17],

$$U_g = \tfrac{1}{2}\int_L \left[\, \mathbf{q}^T,\ \mathbf{r}^T,\ \mathbf{q}'^T,\ \mathbf{r}'^T \,\right] \mathbf{S} \begin{bmatrix} \mathbf{q} \\ \mathbf{r} \\ \mathbf{q}' \\ \mathbf{r}' \end{bmatrix} dx \tag{2.39}$$

where the symmetric initial stress matrix $\mathbf{S}$ is given as

$$\mathbf{S} = \begin{bmatrix}
0 & 0 & 0 & 0 & 0 & 0 & 0 & 0 & 0 & 0 & 0 & 0 \\
 & 0 & 0 & 0 & 0 & 0 & 0 & 0 & 0 & 0 & 0 & 0 \\
 & & 0 & 0 & 0 & 0 & 0 & 0 & 0 & 0 & 0 & 0 \\
 & & & 0 & 0 & 0 & 0 & -Q_z^0 & Q_y^0 & a_z Q_z^0 + a_y Q_y^0 & 0 & 0 \\
 & & & & 0 & 0 & 0 & 0 & 0 & 0 & 0 & 0 \\
 & & & & & 0 & 0 & 0 & 0 & 0 & 0 & 0 \\
 & & & & & & 0 & 0 & 0 & 0 & 0 & 0 \\
 & & & & & & & Q_x^0 & 0 & -M_y^0 & 0 & 0 \\
 & & & & & & & & Q_x^0 & -M_z^0 & 0 & 0 \\
 & & & \text{Sym.} & & & & & & S^0 & 0 & 0 \\
 & & & & & & & & & & 0 & 0 \\
 & & & & & & & & & & & 0
\end{bmatrix} \tag{2.40}$$

The cross-section displacements $\mathbf{q}$ and rotations $\mathbf{r}$, and the corresponding derivatives $\mathbf{q}'$ and $\mathbf{r}'$ are interpolated as defined in (2.3), i.e. in terms of shape functions $\mathbf{N}_x$ and nodal degrees of freedom $\mathbf{u}$,

$$\begin{bmatrix} \mathbf{q} \\ \mathbf{r} \\ \mathbf{q}' \\ \mathbf{r}' \end{bmatrix} = \begin{bmatrix} \mathbf{N}_x \\ \mathbf{N}_x' \end{bmatrix} \mathbf{u} \tag{2.41}$$

where the derivative of the shape function matrix $\mathbf{N}_x'$ is given in Appendix A.1. The differentiation leads to a constant mean representation of the axial strain q_x' and the twist rate r_x' and quadratic interpolation of curvatures $\{q_y', q_z'\}$. By substituting the interpolation (2.41) into the expression (2.39) the following compact form of the potential energy is obtained,

$$U_g = \tfrac{1}{2}\mathbf{u}^T \mathbf{K}_g \mathbf{u} \tag{2.42}$$

where the geometric element stiffness matrix $\mathbf{K}_g$ is defined as

$$\mathbf{K}_g = \int_L \left[\mathbf{N}_x^T,\ \mathbf{N}_x'^T \right] \mathbf{S} \begin{bmatrix} \mathbf{N}_x \\ \mathbf{N}_x' \end{bmatrix} dx \tag{2.43}$$

The geometric stiffness matrix is symmetric, but not necessarily positive definite, as e.g. compressive axial stresses introduce negative restoring forces when rotated outwards under beam bending. This effect is represented by the axial section force Q_x^0 appearing in the diagonal of the initial stress matrix $\mathbf{S}$. The off-diagonal moments M_y^0 and M_z^0 in $\mathbf{S}$ introduce a similar effect where opposing beam sides are softened and stiffened by axial stresses, respectively. Initial shear forces couple transverse displacements and torsion and directly influence torsional stiffness in the case of a shear center offset from the element reference axis.

2.3 Aerodynamic Effects

In this section the formulation for the state-proportional aerodynamic forces is presented, [18]. A constant aerodynamic forcing term $\mathbf{f}_a$ arises corresponding to the undeformed structural geometry, while a stiffness term $-\mathbf{K}_a\mathbf{u}$ and a damping term $-\mathbf{D}_a\dot{\mathbf{u}}$ arise from deformation-induced changes in inflow angle.

2.3.1 Angle of Attack

Figure 2.4 illustrates a typical operational position of a wind turbine profile. The wind speed at the cross-section is defined as $\mathbf{U} = [\,U_x,\, U_y,\, U_z\,]^T$. The profile is shown with a positive chord twist angle β and the profile chord is indicated by the dotted line. The relative flow speed U is defined as $U = (U_y^2 + U_z^2)^{1/2}$ and represents the relative flow speed 'seen' by the profile due to its velocity relative to the atmospheric wind velocity.

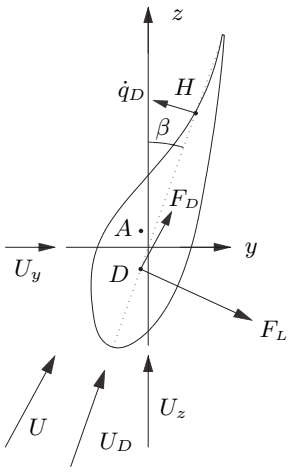

FIGURE 2.4: Airfoil and flow velocities.

Aerodynamic lift is assumed to be proportional to the inflow angle α, defined as

$$\alpha = \alpha_f + \alpha_K + \alpha_D \tag{2.44}$$

where α_f is the inflow angle component in the undeformed position of the aerodynamic profile, α_K is the inflow angle component due to twist of the profile and α_D is the relative inflow angle component due to the transverse velocity of the profile. The subscripts are chosen with

direct reference to the associated force vector $\mathbf{f}_a$, stiffness matrix $\mathbf{K}_a$ and damping matrix $\mathbf{D}_a$.

The mean wind flow angle α_U is the angle between the relative wind flow U and the cross-section reference axis z. The angle is given by the relation

$$\tan \alpha_U = \frac{U_y}{U_z} \tag{2.45}$$

where U_y is the atmospheric wind speed in the y-direction and U_z is the profile velocity due to the angular blade velocity. The mean inflow angle α_f may then be written as

$$\alpha_f = \alpha_U - \beta + \alpha_0 \tag{2.46}$$

where α_0 represents a constant lift contribution due to profile camber and β is the chord twist angle. This defines the inflow angle α_f for stationary operation which produces the static lift force on the cross-section. It is seen that the contribution α_U to the inflow angle increases with the atmospheric flow velocity U_y while it decreases with angular velocity $\boldsymbol{\omega}$ and in particular with the distance $\|\mathbf{x}\|$ to the axis of rotation. If a constant inflow angle is wanted throughout the blade, this can be achieved by decreasing the chord twist angle β for increasing radial position x.

The inflow angle component due to cross-section torsion α_K is simply written as

$$\alpha_K = r_x \tag{2.47}$$

where r_x is the torsional degree of freedom. This part of the aerodynamic inflow angle is proportional to the state deformation and therefore results in an aerodynamic stiffness term.

The last term of (2.44), α_D, is based on the relative inflow angle generated by the characteristic profile velocity $\dot{q}_D$, perpendicular to the chord as shown in Fig. 2.4. For airfoils with torsional oscillations, $\dot{q}_D$ is measured at the rear aerodynamic center H, located on the chord one quarter of the chord length from the trailing edge, [23]. This leads to the following expression for $\dot{q}_D$,

$$\dot{q}_D = \dot{q}_z \sin\beta - \dot{q}_y \cos\beta + \dot{r}_x h \tag{2.48}$$

where h is the chordwise distance between the shear center A and the rear aerodynamic center H with coordinates $\mathbf{h} = [\, h_x,\, h_y,\, h_z \,]^T$. This distance is given as

$$h = |\mathbf{h}| - \frac{\mathbf{h}^T \mathbf{a}}{|\mathbf{h}|} \tag{2.49}$$

In (2.48) the characteristic velocity $\dot{q}_D$ is written as a linear combination of structural velocity states. By linearization of the associated relative inflow angle, the corresponding lift force component will appear as a damping term in the element equations of motions. The relative inflow angle component α_D can be determined from the relation

$$\tan \alpha_D = \frac{\dot{q}_D}{U_D} \tag{2.50}$$

where U_D is the flow speed parallel to the chord, i.e. the projection of the relative flow speed U on to the chordwise direction. This flow speed is given as

$$U_D = U \cos(\alpha_U - \beta) \tag{2.51}$$

It is seen from (2.50) and (2.51) that the formulation becomes singular for $\alpha_U - \beta = \pm\pi/2$, corresponding to the chord twist angle being perpendicular to the relative inflow direction.

In the operation regime, the wind turbine blades are oriented such that $\alpha_U - \beta < \pi/2$ at all times. For small angles, i.e. $\dot{q}_D \ll U_D$, the following approximation can be made,

$$\alpha_D \simeq \frac{1}{U_D}\left(\dot{q}_z \sin\beta - \dot{q}_y \cos\beta + \dot{r}_x h\right) \tag{2.52}$$

Substitution of (2.46), (2.47) and (2.52) into (2.44) gives the following expression for the inflow angle α,

$$\alpha = \alpha_U + \beta + \alpha_0 + r_x + \frac{1}{U_D}\left(\dot{q}_z \sin\beta - \dot{q}_y \cos\beta + \dot{r}_x h\right) \tag{2.53}$$

The first three terms give rise to a constant lift and the fourth term represents a lift component proportional to profile torsion, hereby representing a stiffness contribution. The last term of the aerodynamic inflow angle is proportional to the velocity states, hence representing aerodynamic damping.

2.3.2 Aerodynamic Forces

The aerodynamic pressure distribution is assumed to correspond to a resulting lift force F_L, perpendicular to the flow angle α_U, and a resulting drag force F_D, parallel to the flow angle α_U. The two forces are assumed to act through the aerodynamic center D with coordinates $\mathbf{d} = [\, d_x,\, d_y,\, d_z \,]^T$. For a thin flat plate the aerodynamic center is located one quarter of the plate width from the leading edge. The aerodynamic forces F_L and F_D are organized in the vector $\mathbf{F}_U$ and given as

$$\mathbf{F}_U = \begin{bmatrix} F_L \\ F_D \end{bmatrix} = \tfrac{1}{2}\varrho_a C U^2\, \alpha \begin{bmatrix} C'_L \\ C'_D \end{bmatrix} \tag{2.54}$$

where ϱ_a is the air mass density, C is the chord length, and C'_L, C'_D are lift and drag curve inclinations. By insertion of (2.53) into (2.54) the following expression for $\mathbf{F}_U$ can be written,

$$\mathbf{F}_U = \mathbf{F}_a + \mathbf{A}_K \begin{bmatrix} \mathbf{q} \\ \mathbf{r} \end{bmatrix} + \mathbf{A}_D \begin{bmatrix} \dot{\mathbf{q}} \\ \dot{\mathbf{r}} \end{bmatrix} \tag{2.55}$$

The first term represents the stationary lift and drag in the aerodynamic center,

$$\mathbf{F}_a = \tfrac{1}{2}\varrho_a C U^2 (\alpha_U + \beta + \alpha_0) \begin{bmatrix} C'_L \\ C'_D \end{bmatrix} \tag{2.56}$$

where the last two terms represent the state-proportional lift and drag forces, written in terms of the standard organization $[\, \mathbf{q}^T,\, \mathbf{r}^T \,]^T$ of cross-section displacements and rotations. The matrix $\mathbf{A}_K$ is given as

$$\mathbf{A}_K = \tfrac{1}{2}\varrho_a C U^2 \begin{bmatrix} 0 & 0 & 0 & C'_L & 0 & 0 \\ 0 & 0 & 0 & C'_D & 0 & 0 \end{bmatrix} \tag{2.57}$$

and the matrix $\mathbf{A}_D$ is given as

$$\mathbf{A}_D = \tfrac{1}{2}\varrho_a C \frac{U^2}{U_D} \begin{bmatrix} 0 & -C'_L\cos(\beta) & C'_L\sin(\beta) & C'_L h & 0 & 0 \\ 0 & -C'_D\cos(\beta) & C'_D\sin(\beta) & C'_D h & 0 & 0 \end{bmatrix} \tag{2.58}$$

In order obtain a formulation compatible with the beam element format, the lift and drag forces $\mathbf{F}_U$ acting in the aerodynamic center D must be transformed into equivalent aerodynamic forces $\mathbf{Q}$ and moments $\mathbf{M}$ acting at the element reference axis. The relation is written as

$$\begin{bmatrix} \mathbf{Q} \\ \mathbf{M} \end{bmatrix} = \mathbf{T}_a \mathbf{R}_a \mathbf{F}_U \tag{2.59}$$

Here $\mathbf{R}_a$ is a transformation matrix for rotation of $\mathbf{F}_U$ into equivalent forces in D aligned with the element coordinate system,

$$\mathbf{R}_a = \begin{bmatrix} 0 & 0 \\ \cos\alpha_U & \sin\alpha_U \\ -\sin\alpha_U & \cos\alpha_U \end{bmatrix} \tag{2.60}$$

and $\mathbf{T}_a$ is a transformation matrix that establishes the equivalent forces and moments at the reference axis,

$$\mathbf{T}_a = \begin{bmatrix} 1 & 0 & 0 \\ 0 & 1 & 0 \\ 0 & 0 & 1 \\ 0 & -d_z & d_y \\ d_z & 0 & 0 \\ -d_y & 0 & 0 \end{bmatrix} \tag{2.61}$$

Equation (2.59) establishes the equivalent non-conservative aerodynamic forces and moments acting at the element reference axis. Corresponding nodal forces and moments compatible with the existing element formulation can then be established by the principle of virtual work, by which the aerodynamic force vector and the aerodynamic stiffness and damping matrices are defined. This is shown in Sec. 2.4.2.

2.4 Equations of Motion

In this section the full, aeroelastic equations of motion for the rotating beam element are derived. The conservative terms arising from the kinetic energy and the quadratic energy potentials are derived by insertion into a suitable form of Lagrange's equations, and the non-conservative aerodynamic terms are established via the principle of virtual work. The coupled system is then defined in terms of a mass matrix, an equivalent damping matrix accounting for aerodynamic forces and non-working gyroscopic coupling forces and an equivalent stiffness matrix accounting for elastic, geometric, centrifugal and damping stiffness effects. Finally the Gaussian quadrature rule used for numerical integration of element matrices is presented.

2.4.1 Conservative Terms via Lagrange's Equations

As the kinetic energy (2.13) and the potential energy contributions (2.32) and (2.42) have been established, the equations of motion for the conservative system in the local frame of reference can be derived from Lagrange's equations. These are given in terms of the nodal variables $\mathbf{u}$ [20],

$$\frac{d}{dt}\Big(\frac{\partial T}{\partial \dot{\mathbf{u}}^T}\Big) - \frac{\partial T}{\partial \mathbf{u}^T} + \frac{\partial U}{\partial \mathbf{u}^T} = \mathbf{f}_e \tag{2.62}$$

where $\mathbf{f}_e$ is an external force vector. The variation of the kinetic energy with respect to the system velocity states $\dot{\mathbf{u}}^T$ is found directly by differentiation,

$$\frac{\partial T}{\partial \dot{\mathbf{u}}^T} = \mathbf{M}\dot{\mathbf{u}} + \mathbf{M}_0^T\mathbf{v}_c + \mathbf{f}_G^* + \mathbf{G}\mathbf{u} \tag{2.63}$$

where the second term in has been transposed prior to the differentiation. In connection with finding the time derivative of (2.63) the time derivative of the velocity of the moving frame with respect to the local frame orientation $\mathbf{v}_c$ is needed. For a rotating frame, i.e $\dot{\mathbf{R}} \neq 0$, the time derivative $\dot{\mathbf{v}}_c$ is not simply equal to the uniform acceleration of the local frame $\mathbf{a}_c$, i.e. $\dot{\mathbf{v}}_c \neq \mathbf{a}_c$, as $\mathbf{a}_c$ does not account for the angular velocity of the local coordinate

system. This can be seen by taking the time derivative of $\mathbf{v}_c$ expressed in terms of the global reference frame $\dot{\mathbf{X}}_c$,

$$\dot{\mathbf{v}}_c = \frac{d}{dt}\Big(\mathbf{R}^T\dot{\mathbf{X}}_c\Big) = \mathbf{R}^T\ddot{\mathbf{X}}_c + \dot{\mathbf{R}}^T\dot{\mathbf{X}}_c \tag{2.64}$$

The first term accounts for the uniform acceleration of the local frame and the second term accounts for the change of the orientation of the local frame due to its angular velocity. Substituting the relation $\dot{\mathbf{X}}_c = \mathbf{R}\mathbf{v}_c$ gives the following expression,

$$\dot{\mathbf{v}}_c = \mathbf{a}_c - \hat{\boldsymbol{\omega}}\mathbf{v}_c \tag{2.65}$$

where $\dot{\mathbf{v}}_c$ is now written completely with reference to the local frame. The time derivative of (2.63) can then be written as

$$\frac{d}{dt}\Big(\frac{\partial T}{\partial \dot{\mathbf{u}}^T}\Big) = \mathbf{M}\ddot{\mathbf{u}} + \mathbf{M}_0^T(\mathbf{a}_c - \hat{\boldsymbol{\omega}}\mathbf{v}_c) + \mathbf{f}_G + \mathbf{G}\dot{\mathbf{u}} + \dot{\mathbf{G}}\mathbf{u} \tag{2.66}$$

where the definition $d(\mathbf{f}_G^*)/dt = \mathbf{f}_G$ is used. The variation of the kinetic energy with respect to the system states $\mathbf{u}^T$ becomes

$$\frac{\partial T}{\partial \mathbf{u}^T} = \mathbf{C}\mathbf{u} + \mathbf{f}_C + \mathbf{G}^T\dot{\mathbf{u}} + \mathbf{G}_0^T\mathbf{v}_c \tag{2.67}$$

where the gyroscopic terms are transposed prior to the differentiation. The sum of the two first terms of Lagrange's equations (2.62) is now evaluated. It is used that the skew-symmetric matrices change sign upon transposition, e.g. $\hat{\boldsymbol{\omega}}^T = -\hat{\boldsymbol{\omega}}$ and $\mathbf{G}^T = -\mathbf{G}$. Furthermore the relation $\mathbf{G}_0^T = -\mathbf{M}_0^T\boldsymbol{\omega}$ is used, and the resulting expression is

$$\frac{d}{dt}\Big(\frac{\partial T}{\partial \dot{\mathbf{u}}^T}\Big) - \frac{\partial T}{\partial \mathbf{u}^T} = \mathbf{M}\ddot{\mathbf{u}} + \mathbf{M}_0^T\mathbf{a}_c + 2\mathbf{G}\dot{\mathbf{u}} + \big(\dot{\mathbf{G}} - \mathbf{C}\big)\mathbf{u} - \mathbf{f}_C + \mathbf{f}_G \tag{2.68}$$

which defines all inertial terms in the beam element equations of motion.

In the present application no initial stresses are present in the undeformed structure. For large rotational velocities perpendicular to the beam axis, centrifugal forces may produce axial stresses of significant magnitude relative to the geometric stiffness effects. The corresponding structural deformations are however relatively small, and in the present application the associated geometric stiffness effects are therefore approximated via the initial stress formulation. The initial stresses $\boldsymbol{\sigma}^0$ are hereby approximated by the current stresses $\boldsymbol{\sigma}$ based on an equilibrium state at current time. Hereby, the variation of the potential energy can be written as

$$\frac{\partial U}{\partial \mathbf{u}^T} \simeq \big(\mathbf{K}_e + \mathbf{K}_g(\boldsymbol{\sigma})\big)\mathbf{u} \tag{2.69}$$

In a time integration procedure the geometric stiffness at a given time step can be established with good accuracy by a few iterations. An example of the solution convergence for a typical wind turbine blade is shown in shown in Sec. 3.3.

2.4.2 Non-Conservative Aerodynamic Terms via Virtual Work

Aerodynamic nodal forces and moments are obtained by the virtual work δV expressed in terms of the conjugate virtual displacements $\delta\mathbf{q}$ and rotations $\delta\mathbf{r}$,

$$\delta V = \int_L \big[\,\delta\mathbf{q}^T,\ \delta\mathbf{r}^T\,\big]^T \begin{bmatrix}\mathbf{Q}\\ \mathbf{M}\end{bmatrix} dx \tag{2.70}$$

Inserting the shape function interpolation (2.3) gives

$$\delta V = \delta\mathbf{u}^T \int_L \mathbf{N}_x^T \begin{bmatrix}\mathbf{Q}\\ \mathbf{M}\end{bmatrix} dx \tag{2.71}$$

The aerodynamic forces $[\,\mathbf{Q}^T,\,\mathbf{M}^T\,]^T$ are defined in (2.59) and by insertion the aerodynamic virtual work can be written as

$$\delta V = \delta\mathbf{u}^T\left(\,\mathbf{f}_a + \mathbf{K}_a\mathbf{u} + \mathbf{D}_a\dot{\mathbf{u}}\,\right) \tag{2.72}$$

The three terms arise according to the partition shown in (2.55) where the aerodynamic lift and drag is seen to have a constant term, a torsion proportional term and a term dependent on the transverse displacement velocities and the torsional velocity. The aerodynamic load vector $\mathbf{f}_a$ is given as

$$\mathbf{f}_a = \int_L \mathbf{N}_x^T\mathbf{T}_a\mathbf{R}_a\mathbf{F}_a\,dx \tag{2.73}$$

and the aerodynamic stiffness matrix $\mathbf{K}_a$ takes the form

$$\mathbf{K}_a = \int_L \mathbf{N}_x^T\mathbf{T}_a\mathbf{R}_a\mathbf{A}_K\mathbf{N}_x\,dx \tag{2.74}$$

The aerodynamic stiffness matrix is not symmetric and not necessarily positive definite. Thus, aerodynamic stiffness effects may reduce or increase structural eigenfrequencies. If a negative aerodynamic stiffness contribution becomes large enough to cancel the combined stiffness of the system, i.e. the equivalent stiffness matrix becomes negative definite, this will lead to monotonously growing displacements if the system is disturbed. This static instability is also known as divergence, a dangerous phenomenon to e.g. aircraft wings operating at high wind speeds. The third term in (2.72) includes the aerodynamic damping matrix, given as

$$\mathbf{D}_a = \int_L \mathbf{N}_x^T\mathbf{T}_a\mathbf{R}_a\mathbf{A}_D\mathbf{N}_x\,dx \tag{2.75}$$

Also the aerodynamic damping matrix is neither symmetric nor necessarily positive definite. This implies that the damping forces are not necessarily purely dissipative, i.e. negatively damped modes may arise which will grow monotonously in amplitude if excited. This is the flutter phenomenon which is similarly known from e.g. aircraft wings.

As briefly mentioned in Sec. 2.1, torsional couplings play an important role to the stability of certain aerodynamic modes. The mutual positions of the mass center G, the shear center A and the aerodynamic center D in combination with any elastic couplings due to material anisotropy determine the relative phases between cross-section torsion r_x and displacements $\{q_y,\,q_z\}$ throughout the blade. If e.g. a vibration mode is dominated by out-of-plane displacements q_y, which couple positively to torsion, the effective stiffness of this mode will be reduced. With increasing inflow speeds the modal frequency will decrease until the divergence limit in which the modal frequency vanishes. The flutter stability of a given vibration mode depends on the sign of the work performed by the aerodynamic forces during a single oscillation. For real-valued modes the work will integrate to zero, whereas the complex-valued modes of a damped system represent the phase differences between degrees of freedom that allow aerodynamic forces to accumulate or dissipate energy. Again, this energy balance is determined by the interplay between the inertial, elastic, geometric and aerodynamic couplings of the system.

2.4.3 Aeroelastic Equations of Motion

At this point all matrices and force vectors of the rotating beam element have been defined, and so the fully coupled aeroelastic equations of motion for the element can be defined. The beam element is assumed to be purely rotating, i.e. $\mathbf{a}_c = \mathbf{0}$. Lagrange's equations for the conservative system is written in terms of the inertial terms (2.68) and the stiffness terms (2.69), and by stating that the virtual work in (2.72) must vanish for any admissible virtual

displacement, the non-conservative aerodynamic terms can be added to the equations. These can then be written in the classical format,

$$\mathbf{M}\ddot{\mathbf{u}} + \mathbf{D}\dot{\mathbf{u}} + \mathbf{K}\mathbf{u} = \mathbf{f} \tag{2.76}$$

where the equivalent force vector $\mathbf{f}$ is given as the sum of the centrifugal forces $\mathbf{f}_C$, the angular acceleration forces $\mathbf{f}_G$, the aerodynamic forces $\mathbf{f}_a$ and other external forces $\mathbf{f}_e$,

$$\mathbf{f} = \mathbf{f}_C - \mathbf{f}_G + \mathbf{f}_a + \mathbf{f}_e \tag{2.77}$$

The equivalent damping matrix $\mathbf{D}$ is the sum of two times the skew-symmetric gyroscopic coupling matrix $\mathbf{G}$ and the aerodynamic damping matrix $\mathbf{D}_a$,

$$\mathbf{D} = 2\mathbf{G} - \mathbf{D}_a \tag{2.78}$$

and the equivalent stiffness matrix $\mathbf{K}$ becomes the sum of the elastic stiffness matrix $\mathbf{K}_e$, the geometric stiffness matrix $\mathbf{K}_g$, the gyroscopic angular acceleration matrix $\dot{\mathbf{G}}$, the centrifugal stiffness matrix $\mathbf{C}$ and the aerodynamic stiffness matrix $\mathbf{K}_a$,

$$\mathbf{K} = \mathbf{K}_e + \mathbf{K}_g + \dot{\mathbf{G}} - \mathbf{C} - \mathbf{K}_a \tag{2.79}$$

Nodal section forces and moments $[\,\mathbf{Q}_a^T,\, \mathbf{M}_a^T,\, \mathbf{Q}_b^T,\, \mathbf{M}_b^T\,]^T$ can be determined from the dynamic equilibrium of the element,

$$[\,-\mathbf{Q}_a^T,\, -\mathbf{M}_a^T,\, \mathbf{Q}_b^T,\, \mathbf{M}_b^T\,]^T = \mathbf{M}\ddot{\mathbf{u}} + \mathbf{D}\dot{\mathbf{u}} + \mathbf{K}\mathbf{u} - (\mathbf{f}_a + \mathbf{f}_C - \mathbf{f}_G) \tag{2.80}$$

where any external forces distributed over the element length are included in the parenthesis. This expression for nodal section forces and moments is essential for not only the evaluation of geometric stiffness, but also for the later evaluation of controller performance.

2.4.4 Beam Element Integration

The beam element matrices are all given in terms of an integration over the element length. Beam cross-section properties, section forces and moments or aerodynamic terms may vary freely within the element and will typically be available at discrete data points along the element axis. If the cross-section properties are interpolated linearly between the data points, the longitudinal integrand becomes a piecewise polynomial function which can be integrated exactly by Gaussian quadrature rules. The Lobatto variant of Gaussian quadrature is particularly convenient in this case, as it includes the end point integrand values in the considered interval, see e.g. Hughes [33]. The present application of the Lobatto quadrature is described in this section.

In the following the element integrand is denoted $\mathbf{f}(x)$. One example is e.g. the integrand of the aerodynamic damping matrix, $\mathbf{f}(x) = \mathbf{N}_x(x)^T\mathbf{T}_a(x)\mathbf{R}_a(x)\mathbf{A}_D(x)\mathbf{N}_x(x)$, as shown in (2.75) without the axial argument x. If $\mathbf{f}(x)$ is defined in terms of $N-1$ piecewise functions $\mathbf{f}_n(x)$, corresponding to a data set with N data points, the integral of $\mathbf{f}(x)$ over the interval $0 \le x \le L$ can be written as

$$\int_0^L \mathbf{f}(x)\,dx = \sum_{n=1}^{N-1} \Big[\int_{x_n}^{x_{n+1}} \mathbf{f}_n(x)\,dx \Big] \tag{2.81}$$

A coordinate transformation is introduced to obtain a longitudinal coordinate $-1 \le s \le 1$,

$$x = \tfrac{1}{2}L_n(1+s), \quad L_n = x_{n+1} - x_n \tag{2.82}$$

where L_n is the length of the n'th interval between to data points. The integral of the n'th interval can then be written as

$$\int_{x_n}^{x_{n+1}} \mathbf{f}_n(x)\, dx = \tfrac{1}{2} L_n \int_{-1}^{1} \mathbf{f}_n(s)\, ds \tag{2.83}$$

If $\mathbf{f}_n(s)$ is a polynomial it can be integrated exactly by the sum

$$\tfrac{1}{2} L_n \int_{-1}^{1} \mathbf{f}_n(s)\, ds = \tfrac{1}{2} L_n \sum_{m=1}^{M} \mathbf{f}_n(s_m^n)\, w_m^n \tag{2.84}$$

where s_m^n are the coordinates of the integration points in the n'th interval and w_m^n are the associated weights according to the chosen quadrature rule. The number of integration points M allows exact integration of polynomials of degree $2M-1$ or less.

The integrands of the inertial matrices $\mathbf{M}$, $\mathbf{C}$ and $\mathbf{G}$ are a product of the explicit shape functions of maximal order 3 squared and linearly interpolated cross-section inertial properties, i.e. the integrands become piecewise polynomials of degree 7 or less. Also the geometric stiffness matrix $\mathbf{K}_g$ has an integrand with piecewise polynomials of a maximal order of 8, as the stress matrix $\mathbf{S}$ contains the product of shear center coordinates $\{a_y,\, a_z\}$ and shear forces $\{Q_y^0,\, Q_z^0\}$ which are interpolated linearly. The integrand of the elastic stiffness matrix $\mathbf{K}_e$ has the maximal polynomial degree of 3 as moments vary linearly in the static decomposition and cross-section flexibility is interpolated linearly. The integrand of the aerodynamic damping matrix is not defined as a pure polynomial as it contains the rational factor $(U_D(x))^{-1}$. In the present case the term is non-singular and monotonously growing in the considered range, and so the Gaussian integration of the polynomial multiplied by this factor is considered a reasonable approximation. The degree of the polynomial part of the integrand is 12, as $\mathbf{T}_a(x)$, $\mathbf{R}_a(x)$, $C(x)$ and the matrix components of $\mathbf{A}_D$ are interpolated linearly while $U(x)^2$ is a polynomial of degree 2 due to linear interpolation of $U(x)$.

The necessary number of integration points in each interval in order to exactly integrate a polynomial function of degree 12 is $M = 7$, as $2 \cdot 7 - 1 = 13$. In the present case a 7-point quadrature rule is implemented accordingly. Integration point coordinates and weights for the 7-point Lobatto quadrature rule are given in Table 2.1.

TABLE 2.1: 7-point Lobatto quadrature rule.

$\pm s_m$	w_m
1.00000000	0.04761904
0.83022390	0.27682604
0.46884879	0.43174538
0.00000000	0.48761904

A summary of the procedure for beam element integration is given in Table 2.2. As an initial step the beam element reference coordinate system $\{x,\, y,\, z\}$ is chosen. Cross-section data, as given in N data points and current section forces and moments, given in the element nodes are then imported. Also, the element operating conditions in terms of angular velocity $\boldsymbol{\omega}$ and acceleration $\boldsymbol{\alpha}$ as well as the local wind speed $\mathbf{U}$ at data points are imported. For each of the $N-1$ intervals between data points, the length L_n is determined. The M integration points s_m^n are distributed and the corresponding element axis positions x_m^n are determined. In these positions cross-section properties, current section forces and moments and local wind speeds are linearly interpolated and shape functions are explicitly evaluated. The element

integrands are then computed in the integration points by which the element matrices are integrated according to (2.81) and (2.84). The mass matrix $\mathbf{M}$ and the elastic stiffness matrix $\mathbf{K}_e$ are independent of operating conditions and are therefore conveniently handled together in a computational environment. The geometric stiffness matrix depends on the current internal stress field $\boldsymbol{\sigma}$ and is therefore computed individually. The apparent inertial terms $\mathbf{G}$, $\dot{\mathbf{G}}$, $\mathbf{C}$, $\mathbf{f}_C$ and $\mathbf{f}_G$ depend on the angular velocity $\boldsymbol{\omega}$ and the angular acceleration $\boldsymbol{\alpha}$ and are therefore conveniently integrated collectively. The aerodynamic terms $\mathbf{D}_a$, $\mathbf{K}_a$ and $\mathbf{f}_a$ are computed collectively, as these depend both on the angular velocity $\boldsymbol{\omega}$ of the element and the wind field $\mathbf{U}$. When all element matrices and load vectors are integrated, these are combined according to (2.77)-(2.79) to obtain the classical format (2.76).

TABLE 2.2: Beam element integration.

1)	Define element reference coordinate system:
	$\{x,\, y,\, z\}$
2)	Import cross-section data and nodal section forces and moments:
	$\mathbf{J}_\varrho,\ \mathbf{J}_E,\ \{\mathbf{Q}_a, \mathbf{M}_a, \mathbf{Q}_b, \mathbf{M}_b\},\ \mathbf{a},\ \mathbf{h},\ C,\ \beta$
3)	Import operating conditions and wind speeds:
	$\boldsymbol{\omega},\ \boldsymbol{\alpha},\ \mathbf{U}$
4)	Compute integration interval lengths and integration point coordinates:
	$L_n,\ x_m^n$
5)	Evaluate shape functions and cross-section data in integration points:
	$\mathbf{N}_m^n,\ \mathbf{N}_m'^n,\ \mathbf{J}_{\varrho,m}^n,\ \mathbf{J}_{E,m}^n,\ \{\mathbf{Q}_m^n, \mathbf{M}_m^n\},\ \mathbf{a}_m^n,\ \mathbf{h}_m^n,\ C_m^n,\ \beta_m^n,\ \mathbf{U}_m^n$
6)	Integrate constant element matrices:
	$\mathbf{M},\ \mathbf{K}_e$
7)	Integrate geometric stiffness matrix:
	$\mathbf{K}_g$
8)	Integrate apparent inertial matrices and force vectors:
	$\mathbf{G},\ \dot{\mathbf{G}},\ \mathbf{C},\ \mathbf{f}_C,\ \mathbf{f}_G$
9)	Integrate aerodynamic matrices and force vector:
	$\mathbf{D}_a,\ \mathbf{K}_a,\ \mathbf{f}_a$
10)	Combine element matrices and force vectors:
	$\mathbf{D} = 2\mathbf{G} - \mathbf{D}_a, \quad \mathbf{K} = \mathbf{K}_e + \mathbf{K}_g + \dot{\mathbf{G}} - \mathbf{C} - \mathbf{K}_a, \quad \mathbf{f} = \mathbf{f}_C - \mathbf{f}_G + \mathbf{f}_a$
11)	Equations of motion in classical format:
	$\mathbf{M}\ddot{\mathbf{u}} + \mathbf{D}\dot{\mathbf{u}} + \mathbf{K}\mathbf{u} = \mathbf{f}$

2.5 Modal Analysis for Stationary Rotation

For stationary rotation with $\boldsymbol{\alpha} = \mathbf{0}$ and a non-turbulent wind field the system matrices of (2.76) are constant. If the effect of the constant centrifugal force is furthermore included only in terms of initial stresses corresponding to local equilibrium, the homogeneous part of (2.76) describes a linear system with natural eigenfrequencies and associated eigenvectors. In this section the adopted framework for modal analysis of the rotating system is presented.

2.5.1 State-Space Formulation

A method for modal analysis of the conservative part of (2.76), i.e. without the aerodynamic terms is discussed in e.g. Géradin & Rixen [19]. The eigenvalue problem associated with the homogeneous part of (2.76) in the original configuration-space is quadratic due to the presence of the equivalent damping term $\mathbf{D} = 2\mathbf{G} - \mathbf{D}_a$. This implies that the eigenvectors of the standard eigenvalue problem formulation $(\mathbf{K} + \lambda\mathbf{M})\mathbf{u} = \mathbf{0}$ do not allow a modal decoupling of the gyroscopic system. Such uncoupling is however possible when the equations of motion (2.76) are written in the following state-space format,

$$\begin{bmatrix} \mathbf{M} & \mathbf{0} \\ \mathbf{0} & \mathbf{K} \end{bmatrix} \begin{bmatrix} \ddot{\mathbf{u}} \\ \dot{\mathbf{u}} \end{bmatrix} + \begin{bmatrix} \mathbf{D} & \mathbf{K} \\ -\mathbf{K} & \mathbf{0} \end{bmatrix} \begin{bmatrix} \dot{\mathbf{u}} \\ \mathbf{u} \end{bmatrix} = \begin{bmatrix} \mathbf{f} \\ \mathbf{0} \end{bmatrix} \tag{2.85}$$

which is a system of first order differential equations of twice the size of the original system. This format was introduced by Meirovitch [34] in his original solution of the associated eigenvalue problem for conservative gyroscopic systems. By defining the state vector $\mathbf{z}^T = [\,\dot{\mathbf{u}}^T,\, \mathbf{u}^T\,]$ the problem can be written in the following compact form,

$$\mathbf{A}\dot{\mathbf{z}} + \mathbf{B}\mathbf{z} = \mathbf{F} \tag{2.86}$$

To formulate the eigenvalue problem associated with (2.86) it is now assumed that the solution to the homogeneous part of (2.86) is of exponential form,

$$\mathbf{z} = \mathbf{z}_j e^{\lambda_j t} \tag{2.87}$$

where $\mathbf{z}$ is a constant vector and λ is the inverse of a time constant. Inserting the solution (2.87) into (2.86) the following generalized eigenvalue problem is obtained,

$$\big(\mathbf{B} + \lambda_j \mathbf{A}\big)\mathbf{z}_j = \mathbf{0} \tag{2.88}$$

where λ_j is the eigenvalue and $\mathbf{z}_j$ the associated eigenvector. In the original solution of the eigenvalue problem for gyroscopic systems, Meirovitch [34] divided the problem into the solution of two real-valued problems on standard form, for which the eigenvalues and associated eigenvectors were also real-valued. In the present case the eigenvalue problem (2.88) is solved directly using standard numerical techniques and the resulting complex-valued mode shapes are interpreted directly as shown in the following section.

2.5.2 Eigensolution Analysis

The state-space eigenvectors $\mathbf{z}_j$ include the classical eigenvectors $\mathbf{u}_j$, as they appear in the form

$$\mathbf{z}_j^T = [\,\lambda_j \mathbf{u}_j^T,\, \mathbf{u}_j^T\,] \tag{2.89}$$

Thus, the physical modal vibration shape $\mathbf{u}_j$ of a given mode is available from the state-space format and is simply extracted as the upper or lower half of the eigenvector $\mathbf{z}_j$. According to e.g. [19] the eigenvalues λ_j of the conservative part of the state-space eigenvalue problem (2.88), i.e. for $\mathbf{K}_a = \mathbf{0}$ and $\mathbf{D}_a = \mathbf{0}$, can be written in the form

$$\lambda_j = -\frac{\bar{\mathbf{z}}_j^T \mathbf{B}\mathbf{z}_j}{\bar{\mathbf{z}}_j^T \mathbf{A}\mathbf{z}_j} = -\frac{2i\,\mathbf{x}_j^T \mathbf{B}\mathbf{y}_j}{\mathbf{x}_j^T \mathbf{A}\mathbf{x}_j + \mathbf{y}_j^T \mathbf{A}\mathbf{y}_j} \tag{2.90}$$

where the third term is obtained by writing the state-space eigenvector in terms of its real and imaginary parts, $\mathbf{z}_j = \mathbf{x}_j + i\mathbf{y}_j$. In the case of conservative gyroscopic systems, i.e. for $\boldsymbol{\alpha} = \mathbf{0}$ and $\mathbf{K}_a = \mathbf{0}$ the equivalent stiffness matrix $\mathbf{K}$ is symmetric and positive definite. Consequently, $\mathbf{A}$ is positive definite and symmetric. Furthermore, with $\mathbf{D}_a = \mathbf{0}$, $\mathbf{B}$ is skew-symmetric. As shown in e.g. [34, 19] this leads to purely imaginary eigenvalues appearing

in conjugate pairs $\{\lambda_j, \tilde{\lambda}_j\}$ with associated complex-valued eigenvectors $\{\mathbf{z}_j, \tilde{\mathbf{z}}_j\}$. These properties are particularly important to the problem of vibration control of whirling modes, as these are fundamentally undamped, mutual conjugates which can therefore be addressed simultaneously. This is further discussed in Chapters 3 and 4.

In the non-conservative case where aerodynamic stiffness and damping is included, both eigenvalues and associated eigenvectors are complex-valued and appear in conjugate pairs. The eigenvalues are then conveniently interpreted in the form

$$\lambda_j = \omega_j^0 \left(-\zeta_j + i\sqrt{1-\zeta_j^2} \right) \tag{2.91}$$

where ω_j^0 are the eigenfrequencies of the undamped system, ζ_j are the modal damping ratios and $i = \sqrt{-1}$ is the complex identity, see e.g. [19]. The eigenfrequencies ω_j and the damping ratios ζ_j of the undamped system are given explicitly as

$$\omega_j = \omega_j^0 \sqrt{1-\zeta_j^2} = \mathrm{Re}(\lambda_j), \quad \zeta_j = \frac{-\mathrm{Re}(\lambda_j)}{\sqrt{\mathrm{Re}(\lambda_j)^2 + \mathrm{Im}(\lambda_j)^2}} \tag{2.92}$$

where $\mathrm{Re}(\lambda_j)$ and $\mathrm{Im}(\lambda_j)$ are the real and imaginary values of λ_j, respectively. The state-space formulation of the eigenvalue problem (2.88) associated with the explicit evaluation of complex-valued modal eigenfrequencies ω_j and damping ratios ζ_j in (2.92) provides the basis for modal analysis of the present non-conservative gyroscopic system. Also, when a linear vibration control system is applied to the flexible structure, this framework allows for computation of the modal properties of the closed-loop system consisting of structure and controller.

2.5.3 Frequency Response Analysis

In the analysis of the resonant response of a particular vibration mode in a flexible structure subject to active vibration control, it can be necessary to capture the response of higher background modes as well, see e.g. Preumont [35]. The structural admittance matrix for non-rotating multi-degree-of-freedom structures can be written as the following series of modal responses

$$\left(\mathbf{K} - \omega^2\mathbf{M}\right)^{-1} = \sum_{j=1}^{N} \frac{\omega_j^2}{\omega_j^2 - \omega^2} \mathbf{u}_j \mathbf{u}_j^T \tag{2.93}$$

In Krenk & Høgsberg [15, 16] the resonant response of the mode n which is targeted by the resonant controller is of interest, and the structural admittance matrix is approximated by

$$\left(\mathbf{K} - \omega^2\mathbf{M}\right)^{-1} \simeq \frac{\omega_n^2}{\omega_n^2 - \omega^2} \mathbf{u}_n \mathbf{u}_n^T + \left(\mathbf{K}^{-1} - \mathbf{u}_n \mathbf{u}_n^T \right) \tag{2.94}$$

The approximate expression includes the resonant response of the resonant mode in the first term. The second term represents the quasi-static response of all other modes in the structure. In the applications in [15, 16] the targeted mode is generally the lowest mode of the structure, and so if the other modes in the structure are not too close in frequency to the targeted mode it is reasonable to approximate their response by the quasi-static expression. The normalization of mode shapes in [15, 16] is performed with respect to the mass matrix, whereas in the expressions above the normalization is performed with respect to the structural stiffness as described in [6].

According to Krenk et al. [6], frequency response analysis of undamped gyroscopic systems can be based on the expanded format (2.86), in order for both the symmetric contribution

due to non-rotating effects and the skew-symmetric gyroscopic effects to be represented. This leads to the following form of the structural admittance matrix,

$$\big(\mathbf{K}+i\omega 2\mathbf{G}-\omega^2\mathbf{M}\big)^{-1} = \sum_{j=1}^{N}\Big[\frac{\omega_j^2}{\omega_j^2-\omega^2}\tfrac{1}{2}\big(\mathbf{u}_j\bar{\mathbf{u}}_j^T+\bar{\mathbf{u}}_j\mathbf{u}_j^T\big)+\frac{\omega\omega_j}{\omega_j^2-\omega^2}\tfrac{1}{2}\big(\mathbf{u}_j\bar{\mathbf{u}}_j^T-\bar{\mathbf{u}}_j\mathbf{u}_j^T\big)\Big] \quad (2.95)$$

which is seen to be a $2N$ form of (2.93). The first term is real and symmetric and represents the non-gyroscopic part of the response, while the second term is complex and skew-symmetric and represents the gyroscopic part of the response for rotating structures represented in the rotating frame. To reach (2.95) the normalization

$$\bar{\mathbf{z}}_k^T\bar{\mathbf{A}}\,\mathbf{z}_j^T \;=\; 2\delta_{kj}, \quad \bar{\mathbf{z}}_k^T\bar{\mathbf{B}}\,\mathbf{z}_j^T \;=\; -2\lambda_j\,\delta_{kj} \quad (2.96)$$

is employed. The resonant response of mode n including a quasi-static approximation for the higher modes is written in the form,

$$(\mathbf{K}+2i\omega\mathbf{G}-\omega^2\mathbf{M})^{-1} \simeq \frac{\omega_n^2}{\omega_n^2-\omega^2}\,\mathbf{u}_n\bar{\mathbf{u}}_n^T+\Big(\mathbf{K}^{-1}-\tfrac{1}{2}\big(\mathbf{u}_n\bar{\mathbf{u}}_n^T+\bar{\mathbf{u}}_n\mathbf{u}_n^T\big)\Big) \quad (2.97)$$

which is analogous to (2.94). It is seen that (2.94) is reproduced when the angular velocity becomes zero and the eigenvectors become real-valued. The responses of the lower modes, $1 \le j < n$ have been omitted in (2.97). This approximation is reasonable when these modes have low participation $\bar{\mathbf{u}}_j^T\mathbf{f}$ under the assumed harmonic loading of the system $\mathbf{f}$. In [17] the expression (2.94) was used successfully despite the fact that the blade was rotating. The application was successful due to the fact that the MatLab programming environment automatically produces a Hermitian transpose of the complex-valued modes shapes, and that the skew-symmetric contribution from gyroscopic forces is relatively small in the present application.

Chapter 3

Rotor Systems in Finite Elements

The purpose of the present chapter is to present and illustrate the fundamental dynamic properties of three-bladed rotors, both in general analytic form and in the particular case of wind turbine rotors with blades of complex structural configuration and state-proportional aerodynamics. As will be shown in Chapter 4, an analytic insight into and a good numerical reproduction of the three-bladed aeroelastic rotor system dynamics is essential for optimal signal filtering and gain calibration of the resonant vibration control system. The present chapter includes a series of numerical examples to illustrate selected properties of both isolated rotating blades and of full three-bladed rotors with realistic linearized properties of the structure, the aerodynamics and the operating conditions.

The finite element rotor model is assembled using a limited number of elements per blade and the present chapter initially gives a simple procedure for coupling of the element equations. Local blade equations of motion are transformed into a common rotor coordinate system following the theory of consecutive finite rotations, see e.g. [27, 28]. Time integration of the rotor equations of motion is performed directly in the configuration-space format by the classical Newmark procedure [36]. Rotor simulations are based on prescribed operating conditions including e.g. angular rotor velocity and blade pitch angles. In each time step operation-dependent inertial and aerodynamic terms are updated explicitly and the nonlinear geometric stiffness effects are subsequently established iteratively. An example of an isolated rotating prismatic blade is given to introduce the direct complex mode shape analysis and to demonstrate how the model captures various geometric stiffness and inertial effects in a transient analysis of a slightly modified reference blade, Maqueda et al. [37]. An aeroelastic analysis of an isolated realistic 42 m wind turbine blade under stationary operating conditions is performed and it is demonstrated that the finite element formulation [21, 17, 18] effectively models the blade with a limited number of elements. It is furthermore demonstrated that the aerodynamic formulation produces a separation of strongly damped flap-wise modes and weakly damped edge-wise modes. The modal dynamics of bladed rotors with whirling effects is presented according to Krenk et al. [6] and the dynamics of whirling are discussed in detail. An example based on an 86 m wind turbine rotor is given which illustrates the presence of the theoretical vibration phenomena in a realistic setting. The general description of three-bladed rotor dynamics and the numerical reproduction of these for the realistic aeroelastic 86 m wind turbine rotor forms the basis for the development and validation of the resonant vibration control strategy presented in Chapter 4.

3.1 Rotor Assembly and Simulation

The full rotor is described in a rotating frame of reference $\{x,\, y, z\}$, in which the equations of motion are defined. The rotor coordinate system rotates about the y-axis, by which the angular velocity of the rotor is $\boldsymbol{\omega} = [\,0,\, \omega_y,\, 0\,]^T$. The blades are discretized and assembled identically, according to a default local coordinate system $\{\tilde{x},\, \tilde{y},\, \tilde{z}\}$ in which the cross-section properties are described. The local blade coordinate system is initially coinciding with the rotor coordinate system, i.e. before the blade element matrices are rotated into position in the rotor coordinate system. Prior to the assembly of the full rotor model, the system

matrices of each blade are transformed into the rotor coordinate system according to the blade pitch angle β_k, coning angle γ_k and azimuth angle θ_k where the index k represents the blade number, i.e. $k = 1, 2, 3$. The pitch rotation axis $\mathbf{n}_\beta$, the coning rotation axis $\mathbf{n}_\gamma$ and the azimuth rotation axis $\mathbf{n}_\theta$ are defined as

$$\mathbf{n}_\beta = [\,1,\,0,\,0\,]^T, \quad \mathbf{n}_\gamma = [\,0,\,0,\,1\,]^T, \quad \mathbf{n}_\theta = [\,0,\,1,\,0\,]^T \tag{3.1}$$

The pitch axis $\mathbf{n}_\beta$ initially coincides with the element reference axis, corresponding to actual blade pitch used in wind turbines for aerodynamic performance. In the present analysis the blades are assumed to have constant, identical pitch angles $\beta_k = \beta_p$. The coning rotation axis is seen to rotate the local blade coordinate system out of the rotor plane $\{x,\, z\}$. It i common for wind turbines to operate with a small, constant coning of each blade, i.e. $\gamma_k = \gamma_c$. This is to ensure tower clearance in the case of large out-of-plane blade deformations. The azimuth rotation axis positions the blades symmetrically with respect to the rotor axis y, e.g. with $\{\theta_1,\, \theta_2,\, \theta_3\,\} = \{0,\, \frac{2}{3}\pi,\, \frac{4}{3}\pi\,\}$.

3.1.1 Finite Element Rotor Model Assembly

The blades are assembled in the default local coordinate system, after which the equations of motion for each blade are transformed according to the actual position and orientation of the blade in the rotor coordinate system. The rotor model is assembled by merging the three blade root nodes in a common node, which defines the hub of the rotor. The rotor is connected to the rotating frame by a flexible support of the hub, which is simply established via a beam element which is coupled in one end to the rotor hub node and rigidly fixed in the other end to the rotating coordinate system.

The relation between a coordinate vector designating a point in the local blade coordinate system $\tilde{\mathbf{x}}_k$ and the corresponding vector in the rotor coordinate system $\mathbf{x}$ is defined as

$$\mathbf{x} = \mathbf{R}_k \tilde{\mathbf{x}}_k \tag{3.2}$$

where $\mathbf{R}_k$ is the rotation matrix corresponding to the combined sequence of pitch rotation $\boldsymbol{\beta}_k$, coning rotation $\boldsymbol{\gamma}_k$ and azimuthal rotation $\boldsymbol{\theta}_k$ in the mentioned order. As described in Sec. 2.1 finite rotations are non-commuting, meaning that the sequence must chosen correctly to obtain the desired combined rotation. The rotation matrix $\mathbf{R}_k$ is given as

$$\mathbf{R}_k = \mathbf{R}^k_\theta \, \mathbf{R}^k_\gamma \, \mathbf{R}^k_\beta \tag{3.3}$$

where the rotation matrices $\mathbf{R}^k_\beta$, $\mathbf{R}^k_\gamma$ and $\mathbf{R}^k_\theta$ correspond to pure pitch, coning and azimuthal rotation respectively. The matrices are evaluated according to (2.6) and the sequential order in (3.3) is defined as the reverse order of the combined rotation sequence, according to the theory of consecutive finite rotations [27, 28].

Prior to the integration of inertial and aerodynamic blade element matrices, the local angular velocity $\tilde{\boldsymbol{\omega}}_k$ and angular acceleration $\tilde{\boldsymbol{\alpha}}_k$ is determined according to the position of the element in the rotor coordinate system, i.e. relative to the rotor angular velocity $\boldsymbol{\omega}$ and angular acceleration $\boldsymbol{\alpha}$. The local blade angular velocities and accelerations are found by pre-multiplication with $\mathbf{R}^T_k$, e.g.

$$\tilde{\boldsymbol{\omega}}_k = \mathbf{R}^T_k \boldsymbol{\omega} \tag{3.4}$$

The aerodynamic element matrices and force vectors require the relative wind velocity $\tilde{\mathbf{U}}_k$ in the local element coordinate system, for all data points defined along the element axis. This is obtained by the same inverse rotation of wind speeds defined in the rotor coordinate system $\mathbf{U}$,

$$\tilde{\mathbf{U}}_k = \mathbf{R}^T_k \mathbf{U} \tag{3.5}$$

for blade k. The wind velocity vector $\mathbf{U}$ at the position $\mathbf{x}$ in the rotor coordinate system is evaluated as

$$\mathbf{U} = \begin{bmatrix} U_x(\mathbf{x}) \\ U_y(\mathbf{x}) \\ U_z(\mathbf{x}) \end{bmatrix} - \boldsymbol{\omega} \times \mathbf{x} \tag{3.6}$$

where the first term is obtained from a simulated or measured wind field and the second term represents the velocity of the undeformed structure.

When the blade elements are assembled in the local blade coordinate system the associated degrees of freedom are denoted $\tilde{\mathbf{u}}_k$, the size of which depends on the number of nodes in the discretization of the blades. The corresponding blade degrees of freedom in the rotor coordinate system $\mathbf{u}_k$ relate to the local blade degrees of freedom by the transformation

$$\mathbf{u}_k = \underline{\mathbf{R}}_k \tilde{\mathbf{u}}_k, \quad \underline{\mathbf{R}}_k = \begin{bmatrix} \mathbf{R}_k & & \\ & \ddots & \\ & & \mathbf{R}_k \end{bmatrix} \tag{3.7}$$

where the blade transformation matrix $\underline{\mathbf{R}}_k$ consists of $\mathbf{R}_k$ as block-diagonal terms, corresponding in number to the number of nodes in blade k. The local blade matrices $\tilde{\mathbf{M}}_k$, $\tilde{\mathbf{D}}_k$, $\tilde{\mathbf{K}}_k$ and force vectors $\tilde{\mathbf{f}}_k$ are similarly transformed into the corresponding matrices and force vectors in the rotor coordinate system $\mathbf{M}_k$, $\mathbf{D}_k$, $\mathbf{K}_k$ and $\mathbf{f}_k$ by the transformations

$$\mathbf{M}_j = \underline{\mathbf{R}}_k \tilde{\mathbf{M}}_k \underline{\mathbf{R}}_k^T, \quad \mathbf{D}_k = \underline{\mathbf{R}}_k \tilde{\mathbf{D}}_k \underline{\mathbf{R}}_k^T, \quad \mathbf{K}_k = \underline{\mathbf{R}}_k \tilde{\mathbf{K}}_k \underline{\mathbf{R}}_k^T, \quad \mathbf{f}_k = \underline{\mathbf{R}}_k \tilde{\mathbf{f}}_k \tag{3.8}$$

In order to obtain the equations of motion for the fully coupled rotor, the blade matrices $\mathbf{M}_k$, $\mathbf{D}_k$, $\mathbf{K}_k$ and vectors $\mathbf{f}_k$ are assembled in a single matrix form, where the root nodes of each blade are coupled in a common node, representing the hub of the rotor. A single beam element is used to provide a flexible shaft-like support of the rotor, through which the blades exchange root forces and moments. The element is perpendicular to the $\{x, z\}$ rotor plane and is defined with cross-section properties corresponding to a solid, cylindrical shaft with homogeneous material properties. One node is merged into the rotor hub node and the degrees of freedom of the other node are assumed to be fixed to the origin of the rotor coordinate system. This is the constraint that fixes the rotor to the rotating coordinate system and makes the structural system non-singular. The fixed degrees of freedom of the shaft element are conveniently eliminated from the equations of motion of the rotor. Correspondingly, the rotor model in the developed finite beam element formulation only has nodes in the blades and the flexible rotor hub. The resulting equations of motion for the rotor can then be written in the standard configuration-space format corresponding to (2.76),

$$\mathbf{M}\ddot{\mathbf{u}} + \mathbf{D}\dot{\mathbf{u}} + \mathbf{K}\mathbf{u} = \mathbf{f} \tag{3.9}$$

where $\mathbf{M}$ is the rotor mass matrix, $\mathbf{D}$ is the equivalent rotor damping matrix, $\mathbf{K}$ is the equivalent rotor stiffness matrix and $\mathbf{f}$ is the rotor load vector, including both aerodynamic and inertial terms. The rotor assembly procedure is summarized in Table 3.1.

3.1.2 Integration of Rotor Equations of Motion

The rotor equations of motion (3.9) are simulated via the classical Newmark integration algorithm [36]. The algorithm establishes the system states $\{\mathbf{u}_{m+1}, \dot{\mathbf{u}}_{m+1}\}$ in time step $m+1$ based on known states $\{\mathbf{u}_m, \dot{\mathbf{u}}_m\}$ in time step m and known load vectors in the previous and current time steps $\{\mathbf{f}_m, \mathbf{f}_{m+1}\}$. The algorithm is based on an approximate expression of the displacement and velocity increments in terms of weighted values of the

TABLE 3.1: Rotor assembly.

1)	Define local blade reference axis:
	$\{\tilde{x}, \tilde{y}, \tilde{z}\}$
2)	Global operating conditions:
	$\boldsymbol{\theta}$, $\boldsymbol{\omega}$, $\boldsymbol{\alpha}$, $\mathbf{U}$
3)	Rotation matrices:
	$\mathbf{R}_k$, $\underline{\mathbf{R}}_k$
4)	Compute local operating conditions:
	$\tilde{\boldsymbol{\omega}}_k = \mathbf{R}_k^T \boldsymbol{\omega}, \quad \tilde{\boldsymbol{\alpha}}_k = \mathbf{R}_k^T \boldsymbol{\alpha}, \quad \tilde{\mathbf{U}}_k = \mathbf{R}_k^T \mathbf{U}_k$
5)	Integrate local beam element matrices and load vectors:
	$\tilde{\mathbf{M}}$, $\tilde{\mathbf{D}}$, $\tilde{\mathbf{K}}$, $\tilde{\mathbf{f}}$
6)	Assemble blade matrices and load vectors in local reference axes:
	$\tilde{\mathbf{M}}_k$, $\tilde{\mathbf{D}}_k$, $\tilde{\mathbf{K}}_k$, $\tilde{\mathbf{f}}_k$
7)	Rotate blade matrices and load vectors:
	$\mathbf{M}_k = \underline{\mathbf{R}}_k \tilde{\mathbf{M}}_k \underline{\mathbf{R}}_k^T, \quad \mathbf{D}_k = \underline{\mathbf{R}}_k \tilde{\mathbf{D}}_k \underline{\mathbf{R}}_k^T, \quad \mathbf{K}_k = \underline{\mathbf{R}}_k \tilde{\mathbf{K}}_k \underline{\mathbf{R}}_k^T, \quad \mathbf{f}_k = \underline{\mathbf{R}}_k \tilde{\mathbf{f}}_k$
8)	Assemble global blade matrices and load vectors to obtain rotor model:
	$\mathbf{M}$, $\mathbf{D}$, $\mathbf{K}$, $\mathbf{f}$
9)	Equations of motion in classical format:
	$\mathbf{M}\ddot{\mathbf{u}} + \mathbf{D}\dot{\mathbf{u}} + \mathbf{K}\mathbf{u} = \mathbf{f}$

accelerations in the previous and current acceleration states $\{\ddot{\mathbf{u}}_m, \ddot{\mathbf{u}}_{m+1}\}$, see e.g. [19, 28]. The displacement and velocity increments can be written as

$$\begin{aligned} \dot{\mathbf{u}}_{m+1} &= \dot{\mathbf{u}}_m + \int_{t_m}^{t_{m+1}} \ddot{\mathbf{u}}(\tau)\, d\tau \\ \mathbf{u}_{m+1} &= \mathbf{u}_m + h\dot{\mathbf{u}}_m + \int_{t_m}^{t_{m+1}} (t_{m+1} - \tau)\ddot{\mathbf{u}}(\tau)\, d\tau \end{aligned} \tag{3.10}$$

where h is the time interval length, $h = t_{m+1} - t_m$. The integrals are then evaluated approximately in terms of weighted interval end point values of the accelerations. This leads to the following approximate, but asymptotically correct expressions for small time increments,

$$\begin{aligned} \dot{\mathbf{u}}_{m+1} &= \dot{\mathbf{u}}_m + (1 - \gamma_N)h\ddot{\mathbf{u}}_m + \gamma_N h\ddot{\mathbf{u}}_{m+1} \\ \mathbf{u}_{m+1} &= \mathbf{u}_m + h\dot{\mathbf{u}}_m + (\tfrac{1}{2} - \beta_N)h^2\ddot{\mathbf{u}}_m + \beta_N h^2\ddot{\mathbf{u}}_{m+1} \end{aligned} \tag{3.11}$$

Here the parameters $0 < \gamma_N < 1$ and $0 < \beta_N < \frac{1}{2}$ are the forward weighting parameters, where full weight on the previous acceleration states $\ddot{\mathbf{u}}_m$ corresponds to $\gamma_N = 0$ and $\beta_N = 0$ and full forward weighting corresponds to $\gamma_N = 1$ and $\beta_N = \frac{1}{2}$. For linear systems the choice of these parameters and the relative time step length $\max(\omega_j)h$ affects the stability, the accuracy in system eigenfrequency reproductions and the numerical damping of the system. A commonly used setting is the so-called 'average acceleration' scheme with $\gamma_N = \frac{1}{2}$ and $\gamma_N = \frac{1}{4}$, for which the integration algorithm is stable for any relative time step length. By satisfying the equations of motion at t_{m+1}, the following equation for the current acceleration

states $\ddot{\mathbf{u}}_{m+1}$ is obtained,

$$\begin{aligned}\left(\mathbf{M}+\gamma h\mathbf{D}+\beta h^2\mathbf{K}\right)\ddot{\mathbf{u}}_{m+1} \;=\; & \mathbf{f}_{m+1}-\mathbf{D}\left(\dot{\mathbf{u}}_m+(1-\gamma_N)h\ddot{\mathbf{u}}_m\right)\\ & -\mathbf{K}\left(\mathbf{u}_m+h\dot{\mathbf{u}}_m+(\tfrac{1}{2}-\beta_N)h^2\ddot{\mathbf{u}}_m\right)\end{aligned} \tag{3.12}$$

For linear systems a convenient procedure for computing the current states involves the introduction of a set of prediction terms $\{\dot{\mathbf{u}}^*_{m+1},\, \mathbf{u}^*_{m+1}\}$ in which the last terms in (3.11a) and (3.11b) are neglected. Equation (3.12) gives the current acceleration states $\ddot{\mathbf{u}}_{m+1}$ and $\dot{\mathbf{u}}_{m+1}$ and $\mathbf{u}_{m+1}$ are then found by providing the last terms in (3.11),

$$\begin{aligned}\dot{\mathbf{u}}_{m+1} &= \dot{\mathbf{u}}^*_{m+1}+\gamma_N h\ddot{\mathbf{u}}_{m+1}\\ \mathbf{u}_{m+1} &= \mathbf{u}^*_{m+1}+\beta_N h^2\ddot{\mathbf{u}}_{m+1}\end{aligned} \tag{3.13}$$

The Newmark integration procedure as used in the present application is summarized in Table 3.2. In the present case the rotor equations of motion (3.9) are nonlinear due to the geometric stiffness term which depends on the current stress state $\boldsymbol{\sigma}_{m+1}$. Furthermore the apparent inertial terms are non-constant for non-constant angular velocity $\boldsymbol{\omega}$ and angular acceleration $\boldsymbol{\alpha}$ of the rotor coordinate system, and the aerodynamic terms depend on current angular velocity $\boldsymbol{\omega}$ and the current wind velocity field. In the present case the apparent inertial and aerodynamic matrices and load vectors are updated explicitly in the current time step, as these depend on prescribed operating conditions. When the equations of motion are solved for the current time step according to equations 3.10-3.12, this is done in a simple fixed point iteration procedure where the current stress field $\boldsymbol{\sigma}_{m+1}$ and consequently the geometric element stiffness matrices $\mathbf{K}_{g,m+1}$ is updated. For improved convergence speed the previous stress field $\boldsymbol{\sigma}_m$ is used as an initial guess.

Nodal section forces and moments are evaluated on local element basis according to (2.80). The element matrices in the local blade coordinate system are readily available, and so the local element states $\{\tilde{\mathbf{u}}_{m+1},\, \dot{\tilde{\mathbf{u}}}_{m+1},\, \ddot{\tilde{\mathbf{u}}}_{m+1}\}$ must be computed. This is done in a three-step procedure where the individual blade state vectors with respect to the rotor system are first extracted and then transformed into the local blade coordinate system by pre-multiplication with $\underline{\mathbf{R}}_k^T$. The local element states are finally extracted from the local blade state vectors. The procedure is shown in Table 3.2, in the steps 9a)-c).

3.2 Example: 8 m Prismatic Rotor Blade

The present finite beam element formulation is developed in order to capture the most important inertial and stiffness effects for rotating beams with small deformation-induced cross-section displacements and rotations. The formulation is linear for stationary operating conditions and non-linear under transient conditions. In the stationary case, modal analysis can be performed to obtain the information on the dynamic properties of the structure which is essential to controller calibration, and for investigation of transient performance the non-linear equations of motion can be integrated by the integration scheme summarized in Table 3.2. This section is devoted to an example which demonstrates how the model captures geometric and centrifugal stiffness effects, gyroscopic forces and the centrifugal and angular acceleration loads. A simple rotating beam with a small mass center offset is analyzed in terms of modal properties under different stationary angular velocities. Subsequently, the beam is subjected to a spin-up maneuver for transient response analysis. The blade geometry and operating conditions are inspired by Maqueda et al. [37].

TABLE 3.2: Integration of rotor equations of motion.

1) Initial conditions:

   $\mathbf{u}_0,\ \dot{\mathbf{u}}_0$

2) Time increment:

   $t_{m+1} = t_m + h$

3) Import global current operating conditions:

   $\boldsymbol{\theta}_{m+1},\quad \boldsymbol{\omega}_{m+1},\quad \boldsymbol{\alpha}_{m+1},\quad \mathbf{U}_{m+1}$

4) Compute local current operating conditions:

   $\tilde{\boldsymbol{\omega}}_{m+1,k} = \mathbf{R}_k^T \boldsymbol{\omega}_{m+1},\quad \tilde{\boldsymbol{\alpha}}_{m+1,k} = \mathbf{R}_k^T \boldsymbol{\alpha}_{m+1},\quad \tilde{\mathbf{U}}_{m+1,k} = \mathbf{R}_k^T \mathbf{U}_{m+1}$

5) Approximate internal section forces and moments:

   $[\,-\tilde{\mathbf{Q}}_a^T,\ -\tilde{\mathbf{M}}_a^T,\ \tilde{\mathbf{Q}}_b^T,\ \tilde{\mathbf{M}}_b^T\,]_{m+1}^T = [\,-\tilde{\mathbf{Q}}_a^T,\ -\tilde{\mathbf{M}}_a^T,\ \tilde{\mathbf{Q}}_b^T,\ \tilde{\mathbf{M}}_b^T\,]_m^T$

6) Assemble rotor:

   a) Local element matrices and load vectors:

      $\tilde{\mathbf{M}},\quad \tilde{\mathbf{D}}_{m+1},\quad \tilde{\mathbf{K}}_{m+1},\quad \tilde{\mathbf{f}}_{m+1}$

   b) Global rotor matrices and load vectors:

      $\mathbf{M},\quad \mathbf{D}_{m+1},\quad \mathbf{K}_{m+1},\quad \mathbf{f}_{m+1}$

7) Prediction step:

   $\dot{\mathbf{u}}_{m+1}^* = \dot{\mathbf{u}}_m + (1-\gamma) h \ddot{\mathbf{u}}_m$

   $\mathbf{u}_{m+1}^* = \mathbf{u}_m + h\dot{\mathbf{u}}_m + (\frac{1}{2} - \beta) h^2 \ddot{\mathbf{u}}_m$

8) Correction step:

   $\mathbf{M}_* = \mathbf{M} + \gamma h \mathbf{D}_{m+1} + \beta h^2 \mathbf{K}_{m+1}$

   $\ddot{\mathbf{u}}_{m+1} = \mathbf{M}_*^{-1}\big(\mathbf{f}_{m+1} - \mathbf{D}_{m+1}\mathbf{u}_m^* - \mathbf{K}_{m+1}\mathbf{u}_{m+1}^*\big)$

   $\dot{\mathbf{u}}_{m+1} = \dot{\mathbf{u}}_{m+1}^* + \gamma h \ddot{\mathbf{u}}_{m+1}$

   $\mathbf{u}_{m+1} = \mathbf{u}_{m+1}^* + \beta h^2 \ddot{\mathbf{u}}_{m+1}$

9) Section forces:

   a) Extract global blade states:

      $\mathbf{u}_{m+1,k},\quad \dot{\mathbf{u}}_{m+1,k},\quad \ddot{\mathbf{u}}_{m+1,k}$

   b) Rotate to local blade coordinate systems:

      $\tilde{\mathbf{u}}_{m+1,k} = \underline{\mathbf{R}}_k^T \mathbf{u}_{m+1,k},\quad \dot{\tilde{\mathbf{u}}}_{m+1,k} = \underline{\mathbf{R}}_k^T \dot{\mathbf{u}}_{m+1,k},\quad \ddot{\tilde{\mathbf{u}}}_{m+1,k} = \underline{\mathbf{R}}_k^T \ddot{\mathbf{u}}_{m+1,k}$

   c) Extract local element states:

      $\tilde{\mathbf{u}}_{m+1},\ \dot{\tilde{\mathbf{u}}}_{m+1},\ \ddot{\tilde{\mathbf{u}}}_{m+1}$

   d) Compute local element section forces and moments:

      $[\,-\tilde{\mathbf{Q}}_a^T,\ -\tilde{\mathbf{M}}_a^T,\ \tilde{\mathbf{Q}}_b^T,\ \tilde{\mathbf{M}}_b^T\,]_{m+1}^T =$

      $\tilde{\mathbf{M}}\ddot{\tilde{\mathbf{u}}}_{m+1} + \tilde{\mathbf{D}}_{m+1}\dot{\tilde{\mathbf{u}}}_{m+1} + \tilde{\mathbf{K}}_{m+1}\tilde{\mathbf{u}}_{m+1} - \tilde{\mathbf{f}}_{m+1}$

10) For improved accuracy on geometric stiffness re-run 6)-9).

11) Return to 2) or stop.

3.2.1 The Rotor Blade

The beam is shown in Fig. 3.1, and it consists of two prismatic parts. The primary part is a narrow rectangular cross-section profile, which provides the main stiffness of the beam. The secondary part is small compared to the primary part and it therefore has vanishing contribution to the overall stiffness of the beam.

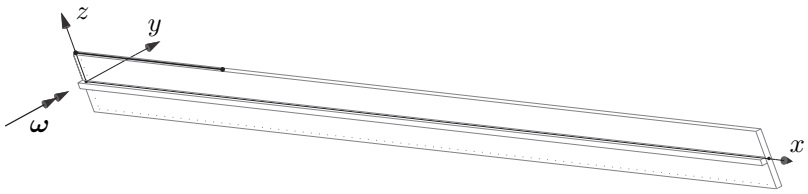

FIGURE 3.1: Cantilever beam with mass center offset.

One end of the beam is fixed at the origin of the rotating reference frame, i.e. $\mathbf{q}(0) = \mathbf{0}$ and $\mathbf{r}(0) = \mathbf{0}$, while the other end is free. The width and height of the primary cross-section part is $w_b = 0.035$m and $h_b = 0.35$m, and it is located such that the longitudinal line of symmetry coincides with reference axis x, while the cross section axes of symmetry are parallel to the y- and z-axis. The material is homogeneous and isotropic with mass density $\varrho = 2700\text{kg/m}^3$, modulus of elasticity $E = 72$GPa and Poisson ratio $\nu = 0.35$. The symmetric distribution of the homogeneous and isotropic material with respect to the y- and z-axis implies that the shear center and the elastic center coincide at the reference axis. The elastic and shear principal axes are furthermore parallel to the y- and z-axis.

The secondary part with the quadratic cross-section has width and height w_b and it is located adjacent to the main section, with its center of symmetry intersecting the y-axis. The material is homogeneous with mass density $\varrho = 7850\text{kg/m}^3$. The presence of this secondary part implies that the mass center G of the entire cross-section has coordinates $g_y \simeq -\frac{1}{4}w_b$ and $g_z = 0$, thus introducing a slight mass offset from the reference axis.

Inertial and axial elastic cross-section properties are determined according to the expressions in (2.16) and (2.29). Since the principal bending and shear axes are parallel to the y- and z-axis, no off-diagonal terms arise in the cross-section stiffness matrix $\mathbf{D}_c$. The shear stiffness components A^G_{yy} and A^G_{zz} are set to GA_0, where $G = \frac{1}{2}E/(1+\nu)$ is the shear modulus and $A_0 = \frac{5}{6}wh$ is the cross-section shear area, accounting for a non-uniform distribution of the shear stresses in the rectangular cross-section. The torsional stiffness is approximated by $K^G = \frac{1}{3}Ghw^3$. This holds for narrow cross-sections, i.e. $w_b \ll h_b$, where the contribution from shear stresses σ_{xz} to the torsional moment M_x can be neglected.

3.2.2 Modal Analysis

The present beam is rotated about the y-axis, i.e. $\boldsymbol{\omega} = [\,0,\, \omega_y,\, 0\,]^T$, and modeled using 8 elements of identical length. Solutions to the eigenvalue problem (2.88) are computed at stationary states $\boldsymbol{\alpha} = \mathbf{0}$ where the geometric stiffness matrix $\mathbf{K}_g$ is established according to the stress state from constant centrifugal forces $\mathbf{f}_C$ with 4 fixed point iterations on the internal stresses. The stress integral S^0 is approximated by $S^0 \simeq r_A^2 Q_x^0$, where the radius of gyration with respect to the shear center is evaluated as $r_A^2 = (I_{yy} + I_{zz})/(w_b h_b)$.

The first three eigenfrequencies are plotted as function of the rotational frequency in Fig. 3.2. The values are normalized with respect to the fundamental eigenfrequency at zero rotational velocity ω_1^0. The first two modes are the first and second bending modes in the y-direction

and the associated eigenfrequencies are seen to increase due to stiffening from the positive definite geometric stiffness contribution. The third mode is the first bending mode in the z-direction. This mode vibrates in the rotor plane whereby the negative definite centrifugal stiffness contribution is activated and counteracts the geometric stiffening. The eigenfrequency ω_3 hereby increases at a significantly slower rate than ω_1 and ω_2. In Krenk et al. [6] an approximate, explicit expression for the change of eigenfrequency with rotation speed is given, based on a perturbation analysis of the quadratic eigenvalue problem of size N associated with the equations of motion (2.76). Predicted values are shown by cross markers $\times$ and the analytical expression is seen to match the frequency developments very well.

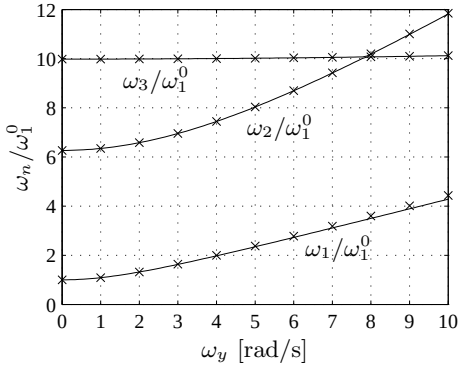

FIGURE 3.2: Structural eigenfrequencies $\omega_n/\bar{\omega}_1$ as function of angular velocity ω_y.

The complex-valued mode shape $\mathbf{u}_3$ for $\omega_y = 7$rad/s is shown in Fig. 3.3, where the real and imaginary values of the nodal displacements q_x, q_y, q_z and the torsional rotations r_x are plotted at the element nodes. The natural eigenfrequency is $\omega_3 = 23.76$rad/s. The normalization of the modes is chosen such that the largest value of q_z is purely imaginary and has the amplitude -1. The classic fundamental mode shape of a cantilever beam is recognized in Fig. 3.3a. The mass center G has an offset from the shear center A in the y-direction. This implies that for any vibration modes with a displacement component in the z-direction, this displacement will couple to torsion r_x. This is seen in Fig. 3.3b, where the torsional component r_x is shown. The scaling of the mode implies that the velocity $\dot{q}_z$ of the beam tip is purely real with a positive real part. The fact that the blade is traveling with a finite, positive in-plane velocity at the chosen phase in the modal oscillation means that gyroscopic forces, proportional to the velocity, are invoking compressive axial deformations of the beam, $q_x < 0$. These are shown in Fig. 3.3c, and the $-\pi/2$ phase lag to the displacement components is seen in terms of the purely real axial deformations q_x. The resulting component of the axial gyroscopic force-intensity of a cross-section is located in the mass center G of the cross-section. As the mass center has an offset in the y-direction from the elastic center C, bending moments about the z-axis are induced. This results in transverse displacements q_y, as shown in Fig. 3.3d. The deflection shape is almost identical to that of mode 2, as modes 2 and 3 have closely spaced eigenfrequencies at the current angular velocity.

3.2.3 Spin-Up Maneuver

The beam is subjected to a spin-up maneuver with a prescribed development of the rotation about the y-axis $\theta_y(t)$ given as

$$\theta_y(t) = \begin{cases} \frac{1}{3}\underline{\omega}_y\, t^3/t_1^2 & \text{for } 0 \le t \le t_1 \\ \underline{\omega}_y(t - \frac{2}{3}t_1) & \text{for } t > t_1 \end{cases} \tag{3.14}$$

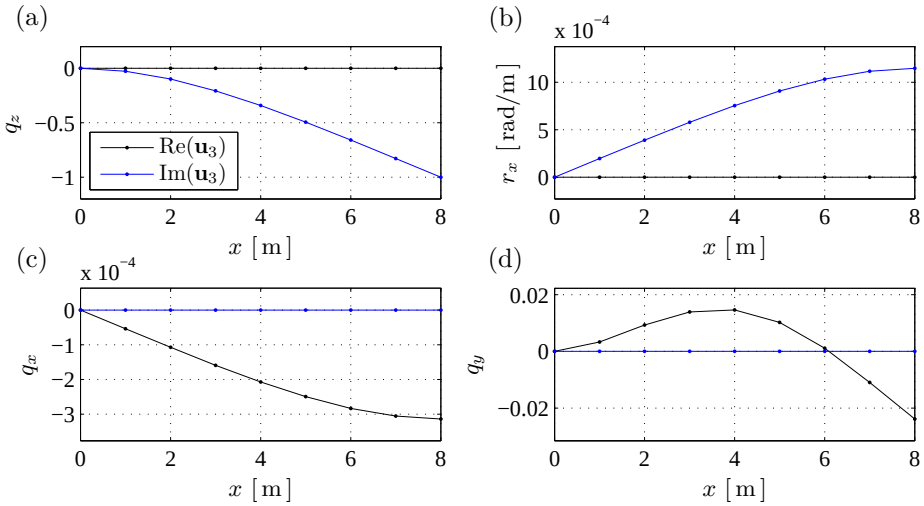

FIGURE 3.3: The complex-valued mode shape $\mathbf{u}_3$ for $\omega_y = 7$rad/s.

with $\underline{\omega}_y = 7\,\text{rad/s}$ and $t_1 = 1\,\text{s}$. The rotational velocity ω_y and angular acceleration α_y are shown in Fig. 3.4. The angular acceleration increases linearly until it reaches the peak value $\underline{\alpha}_y^1 = 14\text{rad/s}^2$ at $t_1 = 1$s, whereafter it is zero. The equations of motion (3.9) are solved using the Newmark integration method with the unconditionally stable 'average acceleration' scheme. The geometric stiffness $\mathbf{K}_g$ is updated between time instances using 4 iterations per time step. In the present case the time-step is $\Delta t = 0.0027$s, which corresponds to 15 time steps during one period of mode 6. The relatively high resolution is used in order to properly represent the strongly transient response after the deceleration at t_1.

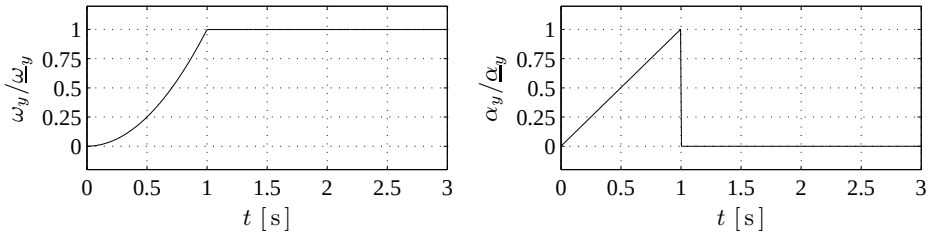

FIGURE 3.4: Angular velocity ω_y/ω_y^1 and angular acceleration α_y/α_y^1.

In Fig. 3.5a the dynamic and quasi-static in-plane beam end deflections q_z are shown, normalized with the beam height w_b. The quasi-static response is seen to follow the development of the angular acceleration $\alpha_y(t)$, which gives rise to angular acceleration forces $\mathbf{f}_G$ in the z-direction. When the angular acceleration is interrupted, the undamped system oscillates freely with mode 2 as the dominating mode. The dynamic and quasi-static axial section force Q_x at the fixed end of the beam is shown in Fig. 3.5b. The values are normalized with respect to the stationary axial force $\underline{Q}_x = \frac{1}{2}L^2\underline{\omega}_y^2 A^\varrho$ corresponding to stationary centrifugal forces at the constant rotational velocity $\underline{\omega}_y$. The high axial stiffness implies that the dynamic response is practically coinciding with the quasi-static response for $0\,\text{s} \le t \le 1\,\text{s}$. The oscillations of Q_x for $t > 1\,\text{s}$ are due to the gyroscopic forces proportional to the in-plane velocities $\dot{q}_z$.

In the present transient analysis the beam exhibits torsional deformations r_x and out-of-plane displacements q_y. These components are investigated in the following. In Fig. 3.6a

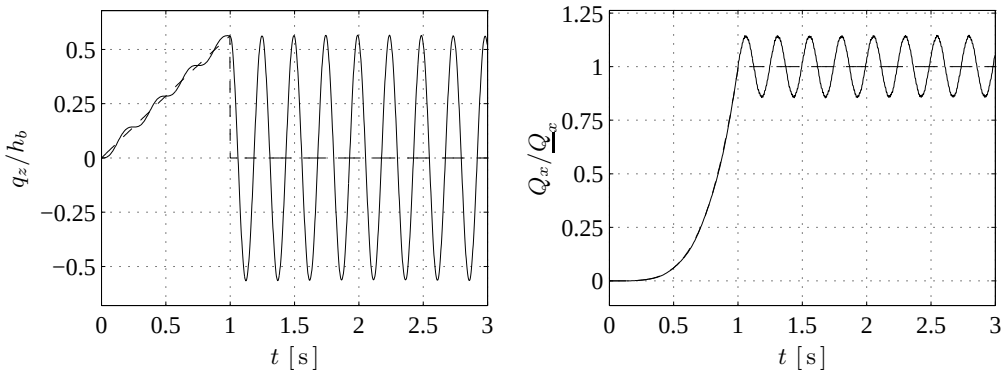

FIGURE 3.5: Dynamic and quasi-static responses. a) Free end displacements q_z. b) Fixed end axial force Q_x.

the torsional root moment M_x is shown, normalized with respect to the moment generated by the angular acceleration forces at $\underline{\alpha}_y$, which is given as $\underline{M}_x = \frac{1}{2}L^2 A^\varrho g_y \underline{\alpha}_y$. As the magnitude of α_y increases, angular acceleration forces are introduced.

During the first approximately 0.7 s this results in a negative (clockwise) torsional rotation r_x, with a corresponding negative moment M_x. Simultaneously, during the first 0.7 s, a positive shear force Q_z and a negative moment M_y appear due to the positive transverse displacements q_z. Corresponding changes in geometric stiffness arise in terms of the torsion-displacement derivative coupling (r_x, q_y') due to Q_z and in terms of the torsion derivative-rotation derivative coupling (r_x', r_z') due to M_y. These coupling effects have opposite direction, where the torsion-displacement coupling by Q_z is dominant in the present case. Thus, the negative rotation r_x invokes positive displacements q_y.

After approximately 0.7 s the centrifugal forces $\mathbf{f}_C$ evolve significantly, and the resulting centrifugal force has both an axial component Q_x and a transverse component Q_y, acting in the mass center. The transverse component demands negative displacements q_y, while Q_x has the opposite effect via the resulting bending moment about the z-axis. Here the latter component dominates and positive displacements q_y appear as shown in Fig. 3.6b. The torsion-displacement derivative coupling (r_x, q_y') due to Q_z implies that positive displacements q_y will induce a negative (clockwise) torsional rotation of the beam. This effect has opposite sign compared to the torsion induced by the angular acceleration forces and it is seen in Fig. 3.6a that the torsional root moment M_x starts to increase when the displacements q_y become significant due to the presence of centrifugal forces. The significant vibrations q_y for $t < 1$ are a combination of modes 1, 2 and 3 where mode 3 contributes due to the presence of non-working gyroscopic forces.

The modal analysis of the prismatic rotating beam shown in the present example has demonstrated in a simple way how direct analysis of complex-valued mode shapes provides a complete description of the modal dynamics of a rotating beam. It is furthermore demonstrated that the model captures tractable geometric and centrifugal stiffness effects, gyroscopic forces and the centrifugal and angular acceleration loads in a transient analysis. In the following section the element formulation is used to analyze the dynamics of a realistic wind turbine blade.

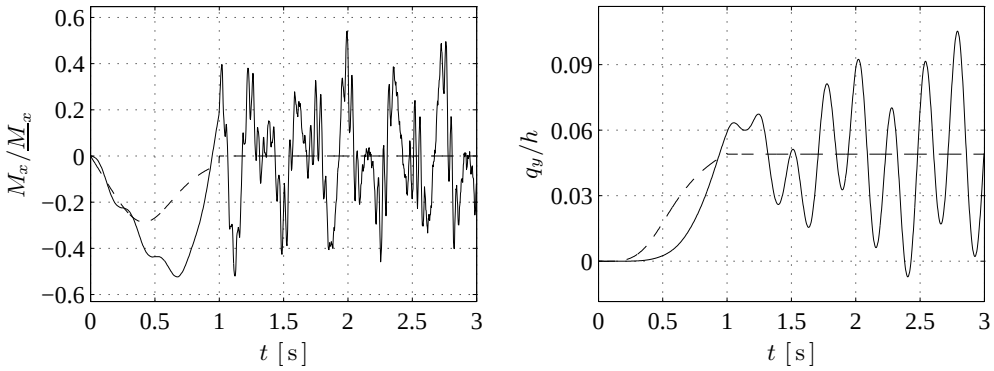

FIGURE 3.6: Dynamic and quasi-static responses. a) Root torsional moment M_x. b) Out-of-plane blade tip displacements q_y.

3.3 Example: Aeroelastic Analysis of a 42 m Wind Turbine Blade

This section introduces the wind turbine blade as an aeroelastic structural component and it is shown that the structure can be modeled by use of a limited number of beam elements according to the formulations given in Chapter 2. The analysis furthermore establishes a separation of flap-wise modes with strong aerodynamic damping and edge-wise modes with weak aerodynamic damping which motivates the development of the resonant vibration control method for e.g. edge-wise vibrations, given in Chapter 4.

3.3.1 Structural Properties

The primary objective of a wind turbine blade is to generate lift forces, of which the in-plane components provide a torque of the rotor about its main shaft. Due to the angular velocity of the rotor ω_y this generates a power source which is exploited by coupling a generator to the rotor shaft. The generator is designed to maintain a constant angular velocity of the rotor and the counter-torque provided by the generator is fundamentally provided by the resistance in any electrical circuit connected to the generator.

The primary objective of a wind turbine blade is to generate lift forces, of which the in-plane components provide a torque of the rotor about its main shaft. The shape of the blade reflects the need of aerodynamic performance, balanced by a necessary combination of structural stiffness and inertia. In Fig. 3.7a are shown the bending stiffnesses $\{EI_{flap}, EI_{edge}\}$ which correspond to bending about the local elastic principal axes which are approximately parallel and perpendicular to the local chord direction, respectively. The local increase in the edgewise bending stiffness around $x = 10\,\mathrm{m}$ is a result of the large chord length in this region. In Fig. 3.7b the cross-section mass density A^{ϱ} and the torsional inertia I^{ϱ} is shown. These fundamental structural properties illustrate that the blade is optimized for its function as a cantilever beam with a distributed load.

In order to maintain a small ratio between lift forces F_L and drag forces F_D it is beneficial to operate with small stationary angles of attack α_f, see e.g. Hansen [38]. For this reason, the chord twist β has large values near the blade root which are then reduced for increased profile distance to the axis of rotation. This creates a pre-twist of the blade. In Fig. 3.8a the chord twist angle β and the orientation of the principal axes β_{EI} are shown. The principal axes are seen to follow the chord twist angle closely.

As discussed in Sec. 2.2 the cross-section properties of wind turbine blades are typically

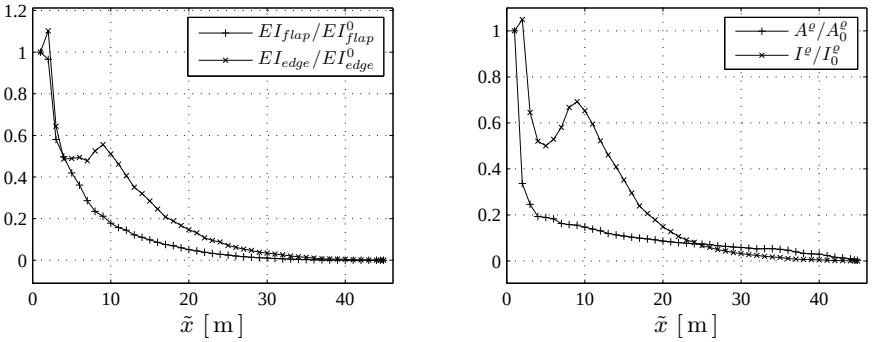

FIGURE 3.7: Principal flap/edge bending stiffnesses EI and inertial parameters A^e and I^e.

of general character due to e.g. the non-trivial geometry and non-homogeneous material composition. In Fig. 3.8b is shown the distances from the blade reference axis of the mass center g'_z, the elastic center c'_z and the shear center a'_z. The distances are measured along the chord and are positive towards the trailing edge. The values are normalized by the root chord C_0. The positions of these characteristic centers are seen to vary significantly over the length of the blade. The local discontinuities of the shear center positions are due to local changes in the shear web configuration.

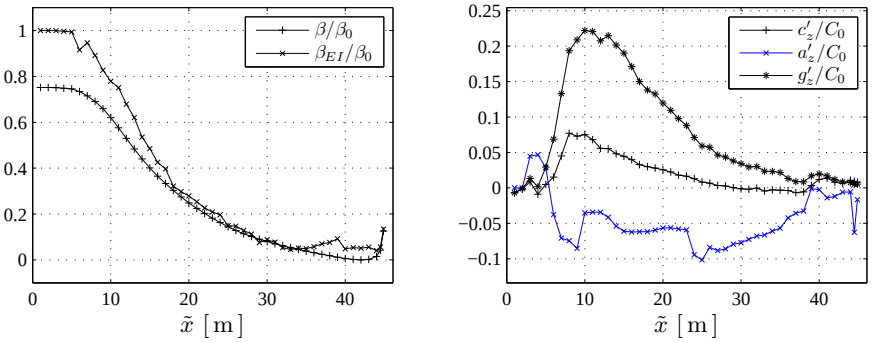

FIGURE 3.8: Chord angle β, principal axes angle β_c and z-coordinates of characteristic centers.

Typically wind turbines are operated at constant angular velocity within a given range of atmospheric mean wind speeds. In this range the power output of the turbine is kept constant, and in order to maintain a constant aerodynamic torque on the rotor, the blades are rotated about their longitudinal reference axes by an active pitch system. In Fig. 3.9 an example of an operating region is shown. The figure shows the stationary rotor angular velocity ω_y and active pitch angle β_p as function of mean wind speed U_y. The shown regime is a variant of that used by Østergaard et al. [39]. It is seen that the operating regime involves significant variations in rotor angular velocity and blade pitch angles.

The significant changes in blade cross-section parameters throughout the blade length implies that the blade is modelled effectively with a finite element formulation that accounts for non-constant cross-section properties, internal stresses and aerodynamic forces. In the next section a static analysis of a single wind turbine blade is performed and modeling convergence is investigated.

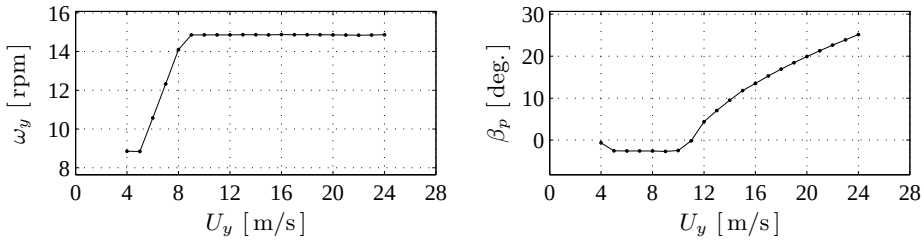

FIGURE 3.9: Rotational velocity ω and pitch angle as function of wind speed U_y.

3.3.2 Static Analysis

The wind turbine blade is in the case of stationary operation loaded by constant centrifugal and aerodynamic forces. The aerodynamic lift and drag forces depend on the angular velocity of the rotor $\boldsymbol{\omega}$, the mean wind speed U_y and the resulting inflow angles due to the blade pitch angle β_p and the chord twist angles $\beta(x)$. In Fig. 3.10a the resulting inflow speeds $\tilde{U}(x)$ are shown for stationary operation at 12 m/s and 20 m/s and in Fig. 3.10b the resulting inflow angles $\alpha_U(x) - \beta(x)$ are shown. In both figures the values are normalized with respect to the root values. The inflow angles are within the region of ± 10 degrees for approximately $\tilde{x} > \frac{1}{3}L$, where L is the blade length. In this region it is reasonable for typical aerodynamic profiles to assume that the flow around the profile is laminar, which implies that the stationary aerodynamic lift is proportional to the inflow angle. For an incompressible fluid the lift coefficient can be shown to be $C_L = 2\pi$ for thin aerodynamic profiles, and conventional profiles have been shown experimentally to come close to this value [23]. Fig. 3.10 hereby demonstrates that the stationary lift formulation in Sec. 2.3 is reasonable for the present application.

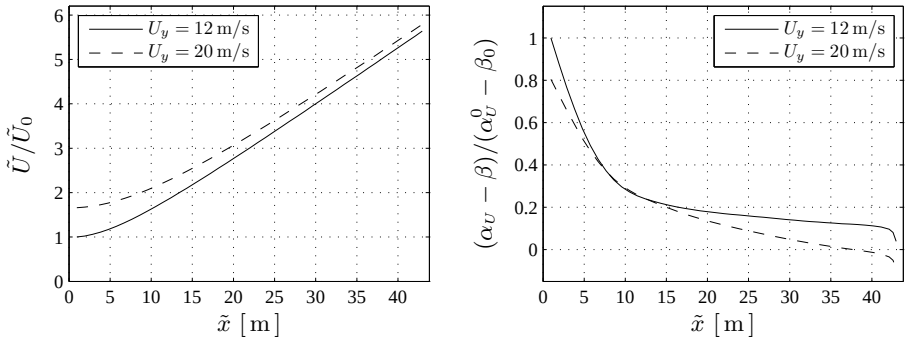

FIGURE 3.10: Local inflow velocity $\tilde{U}$ and inflow angle $\alpha_U - \beta$.

The stationary structural response for the 42 m blade operating at the mean wind speed $U_y = 12$ m/s is shown in Fig. 3.11 in terms of nodal displacements q_y and q_z extracted from the rotor displacement vector $\mathbf{u}$ which is defined in the rotor coordinate system. The values are normalized with respect to the maximum blade tip deflection, q_y^L. The blade is rotating with $\omega_y = 1.57$ rad/s corresponding to 15 rpm, and it has the coning angle $\gamma_1 = -6^o$ and the pitch angle $\beta_1 = 4.4^o$, corresponding to Svendsen et al. [18]. The lift center D is assumed to be located on the chord, one quarter of the chord length from the leading edge of the profile. The aerodynamic lift component F_L gives rise to significant out-of plane displacements q_y and somewhat smaller in-plane deflections q_z, as seen in Fig. 3.11a and b. The in-plane deflections q_z represent the part of the aerodynamic lift which generates rotor

torque, whereas the out-of-plane displacements q_y is an aerodynamic bi-product.

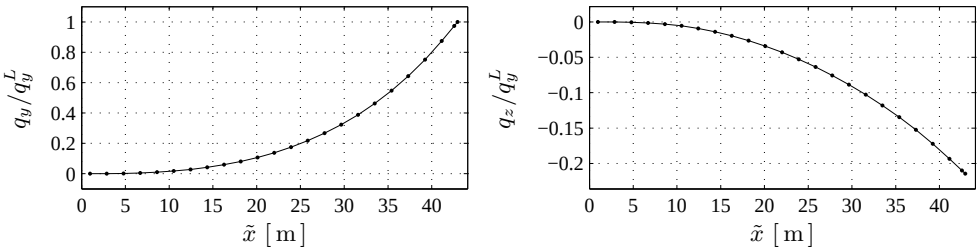

FIGURE 3.11: Normalized nodal displacements and rotations at $U_y = 12\,\mathrm{m/s}$.

The influence of the discretization level, i.e. the number of elements used in the representation of the blade, is investigated in the following. Also, the importance of the number of fixed point iterations for the non-linear geometric stiffness effect is investigated. In Fig. 3.12, 14 different blade discretization choices are shown. Each line represents the blade data points, shown as filled dots and the chosen nodes shown as circles. The number of elements in the individual discretizations is shown on the left.

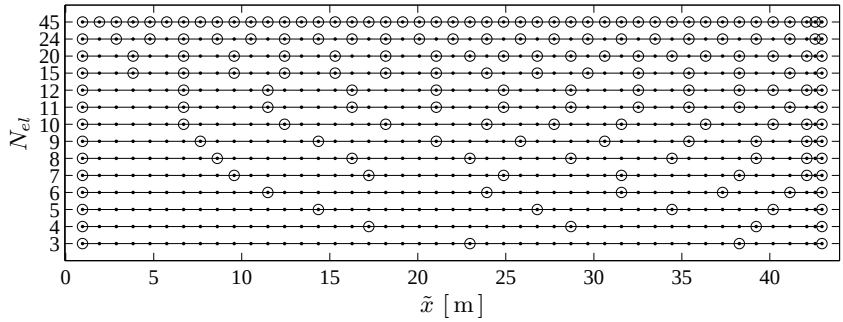

FIGURE 3.12: Node distributions for discretization convergence analysis.

The convergence of the static response is evaluated for the different discretizations shown in Fig. 3.12. The response is evaluated in terms of the resulting blade tip displacement $\|\mathbf{q}_{N_{el}}\|$ where the index N_{el} denotes the number of elements in the blade. For each discretization level the error measure ϵ_q, defined as

$$\epsilon_q = \frac{\|\mathbf{q}_{N_{el}}\| - \|\mathbf{q}_{45}\|}{\|\mathbf{q}_{45}\|} \cdot 100\% \tag{3.15}$$

is computed. The error measure ϵ_q gives the relative difference between $\|\mathbf{q}_{N_{el}}\|$ and the reference value $\|\mathbf{q}_{45}\|$ in which the number of nodes is equal to the number of data points. The error ϵ_q is plotted in Fig. 3.13a where it is seen to be generally decreasing with the number of elements. The error is below 1.0 % for 5 elements or more, thus the model is characterized as rapidly converging with regards to static deflections.

In the investigation leading to the results in Fig. 3.13a the geometric stiffness is established by using $N_{it} = 4$ fixed point iterations. The convergence of the static response with respect to the number of iterations N_{it} is investigated in the following. The error measure ϵ_{it} is defined as

$$\epsilon_{it} = \frac{\|\mathbf{q}_{N_{el}}\| - \|\mathbf{q}^8_{N_{el}}\|}{\|\mathbf{q}^8_{N_{el}}\|} \cdot 100\% \tag{3.16}$$

where the reference value $\|\mathbf{q}^{s}_{N_{el}}\|$ corresponds to the resulting blade tip displacement for a blade modeled with N_{el} elements and the geometric stiffness is established in $N_{it} = 8$ iterations. The development of the error ϵ_{it} is shown in Fig. 3.13b for $N_{el} = \{4, 8, 15, 45\}$ elements. The error is seen to be monotonously decreasing and the deviation from the reference value is in all cases below 0.1 % for $N_{it} = 3$ or more. The monotonous decrease in the error demonstrates that the formulation for the geometric stiffness via initial stresses is robust and rapidly converging in the present application.

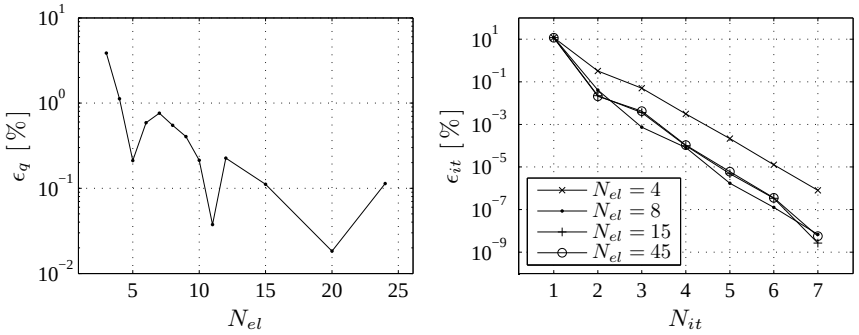

FIGURE 3.13: a) Displacement convergence with discretization level. b) Displacement convergence with geometric stiffness iterations.

The results in the present section demonstrate that the element formulation is robust and rapidly converging in terms of discretization and fixed point iteration of the geometric stiffness. The investigations have so far only considered the stationary static response. In the following section the performance of the model is investigated in the case of modal analysis.

3.3.3 Modal Analysis

When the eigenvalue problem (2.88) is solved the solution quality can be evaluated by the dimensionless error measure $\epsilon_{\mathbf{u}_j}$, defined as

$$\epsilon_{\mathbf{u}_j} = \frac{\| \left(\mathbf{K} + \lambda_j \mathbf{D} + \lambda_j^2 \mathbf{M} \right) \mathbf{u}_j \|}{\| \mathbf{K} \mathbf{u}_j \|} \tag{3.17}$$

where index j denotes the eigensolution number. The numerator should be equal to zero, however this is rarely fulfilled by the numerical solution of the eigenvalue problem. In Fig. 3.14 the error measures for the first four eigensolutions $\{\epsilon_{\mathbf{u}_1}, \epsilon_{\mathbf{u}_2}, \epsilon_{\mathbf{u}_3}, \epsilon_{\mathbf{u}_4}\}$ are plotted as function of the number of elements in the model N_{el}. The eigenvalue problem is solved with the built-in solver `eig` of the commercial programming environment MATLAB®, version R2010a. The error is seen to generally increase with the number of elements, i.e. the solution quality is reduced with the size of the problem (2.88). The solution quality is considered acceptable in the entire region. For simpler systems the error is in the author's experience however typically smaller than 10^{-9}.

Within the limits of the numerical solution of the eigenvalue problem, the solution of the eigenfrequencies ω_j and damping ratios ζ_j should converge with increasing discretization level. This is investigated by the eigenfrequency error measure ϵ_ω and the damping ratio error measure ϵ_ζ, defined as

$$\epsilon_{\omega_j} = \frac{\| \omega_j - \omega_j^{25} \|}{\omega_j^{25}} \cdot 100\,\%, \quad \epsilon_{\zeta_j} = \frac{\| \zeta_j - \zeta_j^{25} \|}{\| \zeta_j^{25} \|} \cdot 100\,\% \tag{3.18}$$

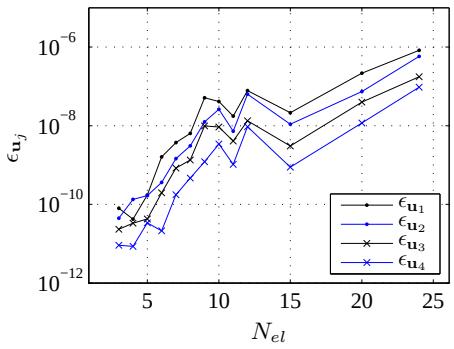

FIGURE 3.14: Eigensolution error $\epsilon_{\mathbf{u}_j}$ for modes 1-4.

where ω_j^{25} and ζ_j^{25} are the reference values for a discretization of the blade with 25 elements. The eigenfrequency error measures for the first four modes $\{\epsilon_1, \epsilon_2, \epsilon_3, \epsilon_4\}$ are plotted in Fig. 3.15a. The errors are seen to exhibit an overall decrease with N_{el} for approximately $N_{el} \leq 10$, and for $N_{el} = 5$ elements or more, the eigenfrequency errors are below 1.0 %, which must be characterized as a rapid convergence. The damping ratio error measures are plotted in Fig. 3.15b and the convergence of these values is seen to be less pronounced. It is however clear that the errors $\{\epsilon_{\zeta_1}, \epsilon_{\zeta_2}\}$ of the two first modes are below 5 % which is considered a satisfactory result for the present purpose. It has not been clarified why the damping ratios have a less pronounced convergence than the eigenfrequencies. The eigenfrequencies represent the balance between modal stiffness and mass, whereas the damping ratios arise from the aerodynamic formulation. Thus, the explanation is probably to be found in the aerodynamic formulation.

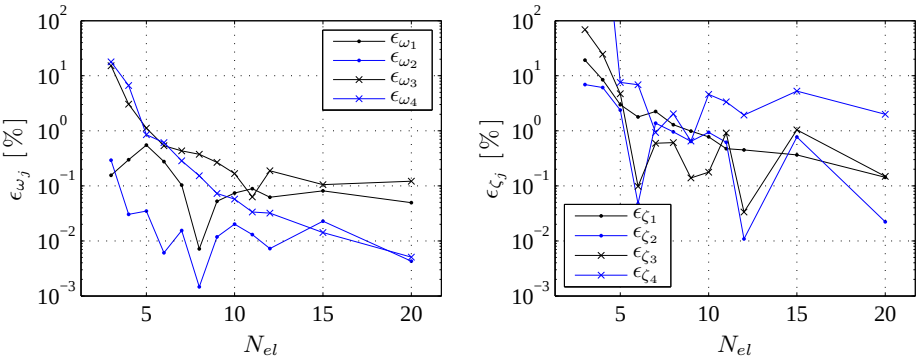

FIGURE 3.15: Eigenfrequency and damping convergence error for modes 1-4.

In the following the first two vibration modes of an isolated 42 m blade are presented for the stationary operating conditions corresponding to a mean wind $U_y = 12$ m/s and an angular velocity of 15 rpm as introduced in the previous section. The first blade vibration mode $\mathbf{u}_1$ is termed the first 'flap-wise' mode, and it is dominated by bending about the weak axis of the blade, corresponding to dominant local displacements $\tilde{q}_y$. This type of mode is strongly damped due to the significant modal velocities $\dot{\tilde{q}}_z$ generated in the rear aerodynamic center H, see e.g. (2.48). The mode has the eigenfrequency $\omega_1 = 6.150$ rad/s and the relatively high damping ratio $\zeta_1 = 0.418$.

The second vibration mode of the blade $\tilde{\mathbf{u}}_2$ is termed the first 'edge-wise' mode, as it is dom-

inated by bending about the strong axis of the blade, corresponding to local displacements $\tilde{q}_z$. Vibrations in the edge-wise direction only have small influence on the relative inflow angle, and so this type of mode typically has weak aerodynamic damping. The mode has the eigenfrequency $\omega_2 = 9.161\,\text{rad/s}$ and the damping ratio $\zeta_2 = 0.007$, which is recognized as a relatively low value, as expected. This result corresponds qualitatively to experimental and theoretical results for pitch-regulated wind turbines of comparable size, [2, 3]. In practice the damping ratio will be somewhat higher than predicted here due to the presence of intrinsic structural damping and non-linear aerodynamic effects which are not represented.

The mode shape $\tilde{\mathbf{u}}_2$ corresponding to the local blade coordinate system is shown in Fig. 3.16, in which the mode shape is scaled by phase and amplitude such that the local edge-wise blade tip displacement $\tilde{q}_z$ is purely real with unit amplitude. The real and imaginary values of $\tilde{q}_z$ are plotted in Fig. 3.16a and the typical vibration mode of a cantilever beam is immediately recognized. The flap-wise displacements $\tilde{q}_y$ are shown in Fig. 3.16b where significant real and imaginary components are present. In the present scaling of the mode shape the imaginary part represents a part of the flapwise displacements which have a $\pi/2$ phase difference to the edge-wise displacements. This implies that when the blade oscillates in mode 2, the cross-sections follow elliptical trajectories in the local cross-section plane $\{\tilde{y}, \tilde{z}\}$. This elliptical motion is caused by the linear, velocity-proportional aerodynamic forces which are performing a finite amount work on the blade. For the present mode the work is dissipative, corresponding to damping of the system. For completeness the torsional components $\tilde{r}_x$ are plotted in Fig. 3.16c and the axial components $\tilde{q}_x$ are plotted in Fig. 3.16d. The blade is seen to exhibit relatively small couplings to these components in edge-wise vibration and the axial compression measured in the reference axis is dominated by the bending-induced displacements due to the offset of the elastic center from the blade reference axis.

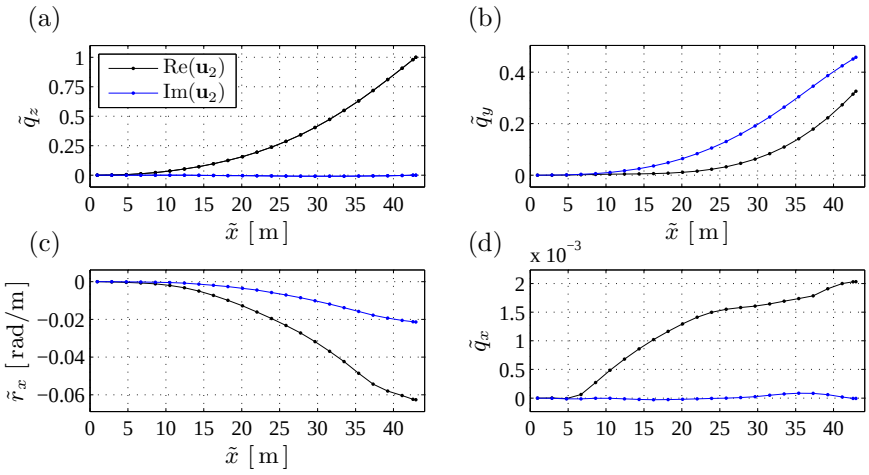

FIGURE 3.16: The edgewise vibration mode $\tilde{\mathbf{u}}_2$ in local coordinates for $U_y = 12\,\text{m/s}$.

As shown in Fig. 3.9 the turbine rotor is subjected to signification changes in operation conditions within a typical operation regime. This will affect the modal properties of the blades. In Fig. 3.17a the development of the first two blade eigenfrequencies is shown according to the operation points in Fig. 3.9. The values are normalized with respect to the eigenfrequencies in the initial point of operation with $U_y = 4\,\text{m/s}$. The first mode is seen to exhibit an increase in eigenfrequency of more than 10 %. This is primarily due to the fact that the mode is dominated by out-of-rotor-plane displacement components q_z for which the geometric stiffening is not counteracted by centrifugal softening. The fact that

the frequency change does not completely follow the change in rotor angular velocity is a consequence of structural and aerodynamic changes due changes of the pitch angles β_p and the increase in the mean wind speed U_y. Mode 2 displays a more ambiguous trend in terms of eigenfrequency development. This is primarily due to the fact that geometric stiffness effects are counteracted by centrifugal softening effects, leaving the more complex interplay between aerodynamic stiffness effects and structural changes due to pitch angles to determine the modal eigenfrequency. The relative developments of the damping ratios $\{\zeta_1, \zeta_2\}$ are shown in Fig. 3.17b. The damping ratio ζ_1 of the strongly damped mode 1 is seen to remain more or less constant within the operating regime when compared to the development of ζ_2. This damping ratio undergoes large relative changes and is seen to become negative in a small range of wind speeds around 9 m/s. In commercial wind turbines it is ensured that all vibration modes are positively damped, by e.g. accounting for the previously mentioned effects of the intrinsic structural damping and non-linear aerodynamic effects.

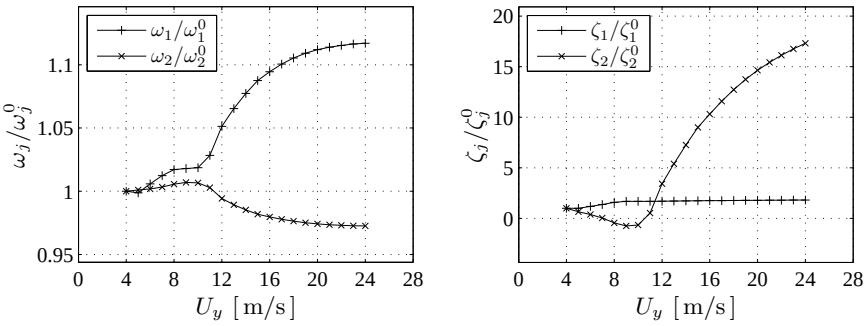

FIGURE 3.17: Blade eigenfrequencies ω_j and damping ratios ζ_j as function of wind speed U_y.

In Section 3.3.3 and the present section it has been shown that a typical wind turbine blade can be effectively modeled by the present beam element formulation, both in terms of static and modal analysis. It has furthermore been illustrated how the geometric stiffness formulation captures frequency changes of the blade within a representative operating regime and that the aerodynamic formulation produces the well-known separation of flap-wise modes with strong aerodynamic damping and edgewise modes with weak aerodynamic damping.

3.4 Dynamics of Three-Bladed Rotors

The present linearized wind turbine blade model has identified the edge-wise blade vibration modes as weakly damped. Thus, the fundamental motivation for developing an active modal vibration control method for wind turbine rotors has been established within the present finite element framework, and it corresponds qualitatively to experimental and theoretical results for pitch-regulated wind turbines of comparable size. When considering vibration control of flexible structures it is of great importance that the dynamics of the structure in question are well represented, as this allows an optimized structure/controller interaction to be constructed. For this reason the dynamics of three-bladed rotors are treated in detail the present section, where in particular the concepts of 'collective' and 'whirling' modes are discussed. These concepts are well-known from helicopter application, Coleman [40], and wind turbine stability analysis based on assumed mode shapes, Hansen [41, 42].

3.4.1 Vibration Modes

The vibrations of three-bladed rotors can be organized into groups of 3 related vibration modes, in which the local deformations of the three blades are quite similar. Each modal group is an extension of a single corresponding vibration mode of an isolated blade, e.g. the first edge-wise vibration mode which was studied in Section 3.2. When three blades are coupled via a flexible rotor shaft the three identical blade modes couple and form a group consisting of three distinctly different vibration modes. An example is shown in Fig. 3.18 of the first in-plane vibration modes of a rotor with simple, prismatic blades. The mode shapes are scaled such that the blade tip displacement of blade 1 is purely real, and local non-zero blade velocities are indicated with arrows. The first mode is the collective mode in which the blades oscillate in phase and activate the torsional flexibility of the rotor shaft. The next two modes are the forward and the backward whirling modes, respectively. These two modes have identical eigenfrequencies corresponding to a double root in the solution of the eigenvalue problem (2.88). The blades oscillate with mutual phase lags of $\alpha = \frac{2}{3}\pi$ with the sequential blade orders 1-2-3 and 1-3-2 relative to the angular velocity $\boldsymbol{\omega}$ of the rotor.

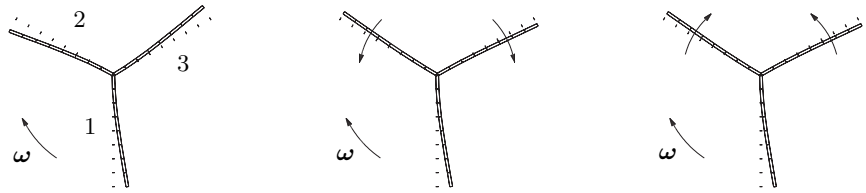

FIGURE 3.18: The first in-plane vibration modes of a rotating rotor. a) Collective motion. b) Forward whirling. c) Backward whirling.

In the case of a non-rotating rotor the vibration modes will be purely real, i.e. all modal blade vibrations will be in phase. The two whirling modes then take the form of 'clapping' modes where two blades perform a balanced vibration in counter-phase with the third blade. The purely real modes of a non-rotating rotor can be reproduced by proper combination of the complex whirling modes. This implies that the following complex representation of the rotor modes is valid also for the non-rotating case.

For increasing torsional stiffness of the rotor support, the modal blade displacements of the collective mode and the whirling modes tend to become identical. As explained by Krenk in [6], the periodic vibration of a single blade $\mathbf{u}_k$, $k = 1, 2, 3$, where k denotes blade number, due to modal energy in a given mode shape group can be expressed as a general complex Fourier series in terms of modal blade vibrations $\mathbf{u}^j$, where j denotes mode number, i.e. $j = 1, 2, 3$ or $j = 4, 5, 6$ etc. depending on the modal group in question. The Fourier series representation is also known as the Coleman transformation [40] and can be written as

$$\mathbf{u}_k = \sum_{k=1}^{N_b} \exp\left(2\pi i \, \tfrac{(j-1)(k-1)}{N_b}\right) \mathbf{u}^j \,, \quad k = 1, ..., N_b \tag{3.19}$$

where $N_b = 3$ in the case of three blades. For $N_b = 3$ the series (3.19) can be written in matrix format as

$$\begin{bmatrix} \mathbf{u}_1 \\ \mathbf{u}_2 \\ \mathbf{u}_3 \end{bmatrix} = \begin{bmatrix} 1 & 1 & 1 \\ 1 & e^{i\alpha} & e^{2i\alpha} \\ 1 & e^{2i\alpha} & e^{4i\alpha} \end{bmatrix} \begin{bmatrix} \mathbf{u}^1 \\ \mathbf{u}^2 \\ \mathbf{u}^3 \end{bmatrix} \tag{3.20}$$

Due to the fact that the angle α designates one third of a revolution around the unit circle,

the Fourier representation (3.20) can be written in the slightly different form

$$\begin{bmatrix} \mathbf{u}_1 \\ \mathbf{u}_2 \\ \mathbf{u}_3 \end{bmatrix} = \begin{bmatrix} 1 & 1 & 1 \\ 1 & e^{i\alpha} & e^{-i\alpha} \\ 1 & e^{-i\alpha} & e^{i\alpha} \end{bmatrix} \begin{bmatrix} \mathbf{u}^1 \\ \mathbf{u}^2 \\ \mathbf{u}^3 \end{bmatrix} \tag{3.21}$$

From this format it can be directly established that the resulting motion of the three blades is the sum of a collective blade motion and two whirling motions. This is seen by writing (3.21) as the sum

$$\begin{bmatrix} \mathbf{u}_1 \\ \mathbf{u}_2 \\ \mathbf{u}_3 \end{bmatrix} = \begin{bmatrix} 1 \\ 1 \\ 1 \end{bmatrix} \mathbf{u}^1 + \begin{bmatrix} 1 \\ e^{i\alpha} \\ e^{-i\alpha} \end{bmatrix} \mathbf{u}^2 + \begin{bmatrix} 1 \\ e^{-i\alpha} \\ e^{i\alpha} \end{bmatrix} \mathbf{u}^3 \tag{3.22}$$

The first term represents the collective blade motion and the last two terms represent the backward and forward whirling modes, respectively.

In a transient load case of a wind turbine rotor, all terms in (3.22) will be present in the structural response. As shown in Section 3.3 the edge-wise vibration modes are subject to weak aerodynamic damping, and this makes these modes an obvious target for resonant vibration control. Due to the inherent difference in natural frequency between the collective and the whirling modes, two separate resonant controllers with different frequency calibrations are required in order to perform a full and optimal control of the first edge-wise vibration mode group. It is therefore necessary to be able to filter out the collective blade motion and the whirling blade motion, respectively, from any measured broad-band rotor response. For this purpose the collective blade motion $\mathbf{u}^1$ is conveniently seen to correspond exactly to the mean value of the three physical blade responses $\mathbf{u}_j$,

$$\mathbf{u}^1 = \tfrac{1}{3}\big(\mathbf{u}_1 + \mathbf{u}_2 + \mathbf{u}_3\big) \tag{3.23}$$

which follows directly from summation over $\mathbf{u}^j$ in (3.21). Thus, the collective mode can be observed directly as the mean value of the three blade responses. The signal associated with a pair of whirling modes is identified by subtracting the mean blade response from the full blade response,

$$\begin{bmatrix} \mathbf{u}'_1 \\ \mathbf{u}'_2 \\ \mathbf{u}'_3 \end{bmatrix} = \begin{bmatrix} \mathbf{u}_1 \\ \mathbf{u}_2 \\ \mathbf{u}_3 \end{bmatrix} - \begin{bmatrix} 1 \\ 1 \\ 1 \end{bmatrix} \mathbf{u}^1 = \frac{1}{3} \begin{bmatrix} 2\mathbf{u}_1 - \mathbf{u}_2 - \mathbf{u}_3 \\ -\mathbf{u}_1 + 2\mathbf{u}_2 - \mathbf{u}_3 \\ -\mathbf{u}_1 - \mathbf{u}_2 + 2\mathbf{u}_3 \end{bmatrix} \tag{3.24}$$

which produces the 'deviatoric' blade deformations $\mathbf{u}'_k$. As noted by Krenk [43] the concept of a deviatoric part of a response is similar to the concept of deviatoric stresses in continuum mechanics, see e.g. Timoshenko & Goodier [44]. The identification of the signals representing the collective mode (3.23) and the whirling modes (3.24) is applied directly in the controller formulation in Chapter 4.

In the next section the dynamics of whirling in three-bladed rotors are discussed. The analysis is based on the first in-plane forward whirling mode of a rotor with simple, prismatic blades of homogenous material and no coning. However, the principles apply generally, not least to the first edge-wise whirling modes of a wind turbine rotor as will be demonstrated in Section 3.5.

3.4.2 Dynamics of Whirling

Whirling is a gyroscopic phenomenon occurring in rotating structures, e.g. transmission shafts or bladed rotors. As seen above, whirling modes come in pairs of forward and backward whirling and the difference between the two lies in the sign of the phase lag between gyroscopic and inertial forces. The interplay between the gyroscopic and inertial forces is

conveniently analyzed by a full complex representation of the blade displacement components. In Fig. 3.19 the local in-plane blade tip displacements $\{\tilde{q}_z^1, \tilde{q}_z^2, \tilde{q}_z^3\}$ and their velocity and acceleration counterparts are plotted in the complex plane for the forward whirling mode. The mode is scaled in terms of phase and amplitude such that the tip displacement of blade 1 is purely imaginary with negative unit amplitude. For progressing time the points are rotated counter-clockwise as indicated in the figure, and this corresponds to the blades passing through identical states in the sequential order 1-2-3 with a phase difference of $\frac{2}{3}\pi$. The chosen scale of the mode implies that the velocity of blade 1 is purely real and positive.

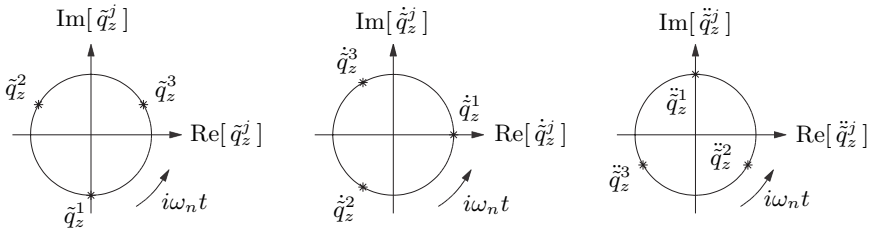

FIGURE 3.19: Local forward whirling blade tip displacements, velocities and accelerations.

In Fig. 3.20 the real parts of the structural displacements are plotted. Blade 1 is seen to be undeformed while blades 2 and 3 have negative and positive local displacements, respectively. The direction of the angular velocity of the rotor ω_y is shown in the figure, and the aforementioned sequential order 1-2-3 of identical blade states propagates in the same circular direction. This explains the term 'forward whirling' whereas 'backward whirling' corresponds to the sequential order 1-3-2 for the present case.

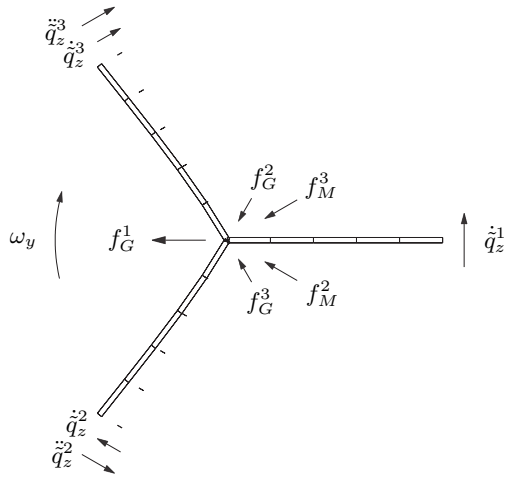

FIGURE 3.20: Forward whirling with local blade velocities and accelerations and resulting hub forces.

The real parts of blade tip velocities $\{\dot{\tilde{q}}_z^1, \dot{\tilde{q}}_z^2, \dot{\tilde{q}}_z^3\}$ and accelerations $\{\ddot{\tilde{q}}_z^1, \ddot{\tilde{q}}_z^2, \ddot{\tilde{q}}_z^3\}$ are depicted in Fig. 3.20 by vector representations indicating directions and amplitudes. Also, the gyroscopic blade root forces $\{f_G^1, f_G^2, f_G^3\}$ as well as the acceleration-proportional inertial forces $\{f_M^2, f_M^3\}$ are plotted. The gyroscopic forces are parallel with the local blade axes and due to the symmetry of the system these have a common resultant purely in the opposite direction of the reference axis of blade 1. The flexible support of the rotor is deformed under this

loading, by which the gyroscopic coupling of the blades is established. The acceleration-proportional blade root forces are symmetric about the axis of blade 1 and perpendicular to their local blade axes. In the case of forward whirling these contribute positively to the gyroscopic resultant whereas the contribution is negative for backward whirling. Thus, forward whirling will be the mode which produces the dominating in-plane loads of the main rotor shaft.

A simple example is given in the following to demonstrate the effects described above. A rotor is modeled using three rectangular, prismatic 8 m blades of homogeneous material. The blade have the cross-section width $w_b = 0.035\,\mathrm{m}$ and the cross-section heights $h_b = 0.200\,\mathrm{m}$, material density $\varrho = 2700\,\mathrm{kg/m^2}$, elastic modulus $E = 72\,\mathrm{GPa}$ and a Poisson ratio of $\nu = 0.35$. The blades are oriented such that in-plane displacements correspond to bending purely about the strong blade axes, and the local blade reference axis coincides with the longitudinal axis of symmetry. No aerodynamics are included. The eigenvalue problem (2.88) is solved for stationary rotation at the angular velocity $\omega_y = 5\,\mathrm{rad/s}$ and modes 5 and 6 are the forward and backward whirling modes respectively, with the eigenfrequencies $\{\omega_5, \omega_6\} = \{16.5105\,\mathrm{rad/s}, 16.5110\,\mathrm{rad/s}\}$. The fourth decimal reveals that the numerical solution of the eigenvalue problem does not produce eigenfrequencies which are exactly equal. Mode 4 is the first 'collective' in-plane vibration mode, in which all blades oscillate in phase, and it has the eigenfrequency $\omega_4 = 16.0163\,\mathrm{rad/s}$. Modes 1-3 are the first out-of-plane collective and whirling modes.

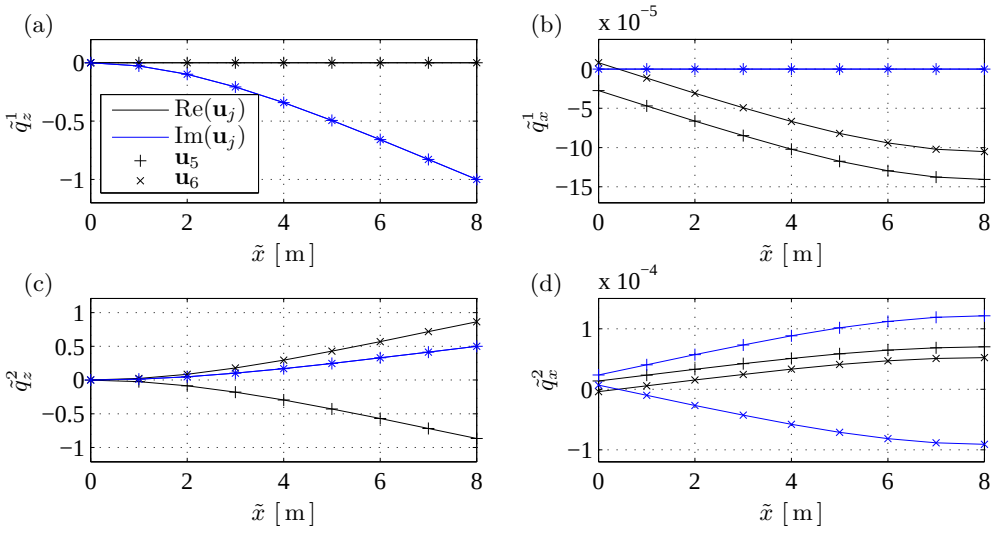

FIGURE 3.21: Local in-plane ($\tilde{q}_z^j$) and axial ($\tilde{q}_x^j$) displacements for forward and backward whirling.

The mode shapes $\mathbf{u}_5$ and $\mathbf{u}_6$ are plotted together in Fig. 3.21 in terms of local deformations of blade 1 and the modes are scaled as in Fig. 3.19. The real parts are plotted in black and the imaginary parts are plotted in blue. Nodal values of $\mathbf{u}_5$ are indicated with $\times$ while nodal values of $\mathbf{u}_6$ are indicated with $+$. The in-plane displacements $\tilde{q}_z^1$ are seen in Fig. 3.21a to be identical for the two modes. In Fig. 3.21b the axial deformations $\tilde{q}_x^1$ of the two modes are seen to develop identically, but a constant offset is seen between them. This offset is due to the displacement of the rotor, which identifies the difference between forward and backward whirling. For completeness, the local displacements of $\tilde{q}_z^2$ and $\tilde{q}_x^2$ of blade 2 are shown in Fig. 3.21c and d. In both cases the displacements are seen to have the same phases and

amplitudes as shown in Fig. 3.19.

In the present example the dynamics of whirling have been introduced and the phenomenon has been illustrated in a simple example using the present element formulation. It is seen that e.g. the well-known first in-plane vibration mode of an isolated blade splits into three similar but not identical modes when three blades are combined in a flexible rotor. These modes are the collective mode and the forward and backward whirling modes. The weakly damped edgewise vibration modes of a wind turbine rotor have the same properties, as demonstrated in the following section.

3.5 Example: Simulation of 86 m Wind Turbine Rotor

The dynamic properties of a realistic, three-bladed wind turbine rotor incorporate the aerodynamic damping and whirling features described in the previous sections. This is illustrated in the present example for a symmetric rotor consisting of three blades of the kind introduced in Sec. 3.3. A modal analysis is performed, followed by simulation of a free-decay vibration history in combined forward and backward edge-wise whirling.

The three blades are connected to the end of a solid steel shaft of length $L_s = 0.2\,\mathrm{m}$ and diameter 0.5 m. This creates a flexible support with relatively high stiffness which entails that related vibration modes as presented in Sec. 3.4 remain closely spaced in frequency. This is chosen to underline the excellent filter performance of the control system in Chapter 4. In practice the rotor support constituted by the drive-train, tower and nacelle structure is somewhat more flexible, particularly in terms of torsional stiffness, see e.g. [3]. Furthermore the actual support is single-symmetric about the vertical and horizontal center lines through the rotor hub, respectively. In operation, this support becomes periodic and requires a full multi-body solution method for time simulation, see e.g. Shabana [45] or Géradin & Cardona [27], and e.g. a mean value Fourier representation with assumed blade modes for modal analysis [41, 42]. The present double-symmetric shaft support allows the analyses to be performed directly in the rotating frame of reference using the present finite element formulation. As it will be seen in Chapter 4 it is essential for the control system analysis that actual vibration modes for the closed-loop system consisting of both structure and controllers are available. Blade numbering and azimuthal positions correspond to Fig. 3.20.

3.5.1 Modal Analysis

For the present analysis the wind turbine rotor is modeled using $N_{el} = 8$ elements per blade. The eigenvalue problem (2.88) is solved for the stationary case with the constant wind speed $U_y = 12\,\mathrm{m/s}$ and the angular velocity $\omega_y = 1.57\,\mathrm{rad/s}$ of the rotor. The blades have the coning angles $\gamma_k = \gamma_c = -6.0^o$ and the blades are pitched with $\beta_k = \beta_p = 4.4^o$. Geometric stiffness effects from the stationary centrifugal load are established by $N_{it} = 4$ iterations. The eigenfrequencies and damping ratios of the first 12 modes are shown in Table 3.3. The first three modes correspond to flap-wise deflections where modes 1 and 2 are the forward and backward whirling modes and mode 3 is the collective 'umbrella' mode where the blades oscillate in and out of the rotor plane simultaneously. The three flap-wise modes are strongly damped as also seen for the isolated blade in Sec. 3.3.

Modes 4 to 6 are the first edge-wise vibration modes, which are of particular interest for the resonant vibration control theory presented in Chapter 4. Mode 4 is the collective vibration mode where the three blades perform simultaneous edge-wise displacement. In Fig. 3.22a the real part of the edge-wise blade tip displacements $\tilde{q}_z^k$ of the mode shape $\mathbf{u}_4$ are shown. The mode is initially scaled such that the tip displacement $\tilde{q}_z^1$ of blade 1 is purely real with unit amplitude. The mode is then scaled by the factor $e^{i\varphi}$ with $-\pi \leq \varphi \leq \pi$, whereby the

TABLE 3.3: Rotor eigenfrequencies and damping ratios.

j	1	2	3	4	5	6	7	8	9	10	11	12
ω_j	6.155	6.174	6.234	8.543	9.142	9.154	16.31	16.31	16.57	25.64	27.59	27.59
ζ_j	0.425	0.421	0.416	0.014	0.006	0.006	0.164	0.164	0.162	0.001	0.001	0.001

modal displacements of $\tilde{q}_z^k$ are illustrated for an entire oscillation. It is seen that the three local blade tip trajectories are identical in both phase and amplitude.

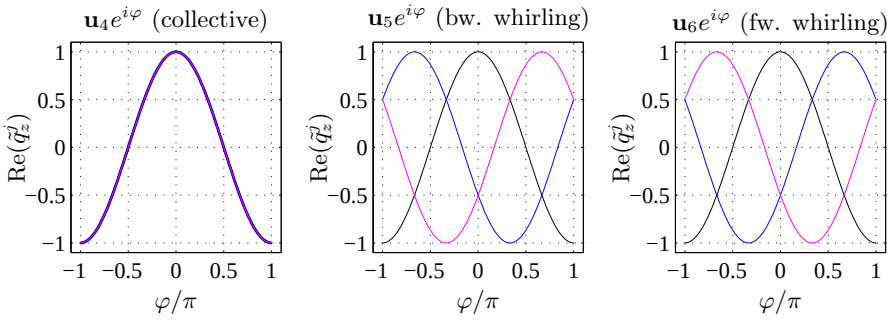

FIGURE 3.22: Edge-wise tip displacements in modes 4, 5 and 6. — $\tilde{q}_z^1$, — $\tilde{q}_z^2$, — $\tilde{q}_z^3$.

Modes 5 and 6 are the backward and forward whirling modes, respectively. The blade tip displacements of the two modes are plotted through one modal oscillation in Fig. 3.22b and c. As for mode 4 the two modes are scaled for purely real unit displacement of $\tilde{q}_z^1$. For both modes the amplitudes of blades 2 and 3 are seen to be identical to that of blade 1. Also, the mutual phase differences are seen to be exactly $\pm\frac{2}{3}\pi$. The phase orders identify $\mathbf{u}_5$ as the backward whirling mode and $\mathbf{u}_6$ as the forward whirling mode in the present case. Fig. 3.23 shows the shape of mode 5 for blade 1, from which the chosen element distribution is also seen. The eigenvalue problem is solved via the numerical solver `eig` provided by the commercial software MATLAB®. The whirling modes have almost identical eigenfrequencies. These are higher than the eigenfrequency of the collective mode, as this mode activates the torsional flexibility of the main shaft. The fact that the two eigenfrequencies are not completely identical is considered to be due to the presence of aerodynamic forces. This corresponds to the observations in e.g. [3]. The three modes are seen to be weakly damped, corresponding to the single blade analysis in Sec. 3.3. It has been observed that for increased flexibility of the rotor shaft, the eigenfrequencies of the two whirling modes are not significantly separated. However, the damping ratios of the two whirling modes may develop a significant separation.

The modes 7-9 are the second flap-wise whirling and collective modes. Due the dominating flap-wise motion these modes are seen to be significantly damped. Modes 10-12 are the second edge-wise collective and whirling modes, and the relation to the first edge-wise modes is clear from the low aerodynamic damping values. The linearized aerodynamic formulation is based on small velocities $\dot{\tilde{q}}_D$ compared to the relative flow speed $\tilde{U}_D$ in the chord direction. When analyzing the aerodynamic damping ratio of higher modes it must be taken into account that this assumption will at some point reach the limit of applicability.

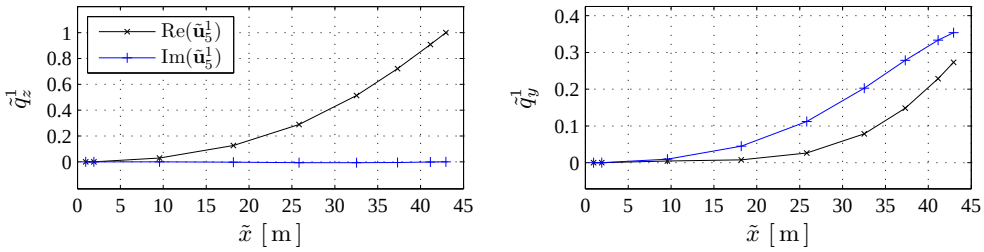

FIGURE 3.23: The edge-wise backward whirling mode $\mathbf{u}_5^1$ for blade 1 with respect to the local blade coordinate system.

3.5.2 Free Vibration

In this section a simple example of simulated transient rotor behavior is given. The purpose is to extend the introduction to the edge-wise whirling modes and to show that these are correctly reproduced by the time integration algorithm given in Table 3.2. The time step h is selected such that mode 16 of the coupled structure is resolved with 10 points per period, corresponding to $h = 0.023\,\mathrm{s}$. In each time instant the geometric stiffness matrix $\mathbf{K}_g$ is established using four iterations of internal stresses in the dynamic equilibrium of (2.76). The rotor angular velocity is held constant at $\omega_y = 1.57\,\mathrm{rad/s}$ and the blade pitch angles are held constant at $\beta_p = 4.4^o$.

The initial conditions of the free vibration history are chosen such that the edge-wise forward and backward whirling modes are initiated with relatively high energy levels. Blade numbering and azimuthal angles in the rotor coordinate system is identical to the rotor shown in Fig. 3.20. The initial conditions of the rotor correspond to the stationary centrifugal and aerodynamic load case which is used as basis for the modal analysis above, supplemented by a constant external load. The external load corresponds to a somewhat realistic situation where blade 2 and blade 3 are connected by a taut string attached in the local blade radii $\tilde{x}/L = 0.87$. The load vector is defined by specifying the loads $Q_z^{2,3} = \pm 10^4\,\mathrm{kNm}$ in the corresponding nodes. The transient response is initiated by 'cutting the string', modeled by setting the two nodal forces to zero, $Q_z^{2,3} = 0$, during the course of a single time step.

The structural response is shown in Fig. 3.24a in terms of the three in-plane blade tip responses in the rotor system q_z^k. At $t = 0.2\,\mathrm{s}$ the string is cut and blades 2 and 3 are seen to start oscillating about a new equilibrium, corresponding to the remaining stationary centrifugal and aerodynamic load. Blade 1 is seen to be almost unaffected by the abrupt load change.

In Fig. 3.24b the local edge-wise tip responses $\tilde{q}_z^k$ are shown. These are evaluated by premultiplication of the blade state vectors $\mathbf{u}_k$ by $\underline{\mathbf{R}}_k^T$ defined in (3.7). The rotor symmetry is evident when observing the local blade states, as these have identical stationary equilibria under pure centrifugal and aerodynamic load. Thus, the behavior of the blades is directly comparable when observed in the local blade coordinate systems. Blades 2 and 3 are seen to perform a 'clapping' motion which can be shown to correspond to a symmetric energy distribution between the forward and backward whirling modes. In the present case the initial 'string' load does not purely excite the first edge-wise vibration modes, by which the observed clapping motion is not perfectly symmetric.

The energy density spectrum $S_q^2(\omega)$ of the local edge-wise displacements $\tilde{q}_z^2$ of blade 2 is shown in Fig. 3.25. The spectrum is normalized with its maximum value S_q^0 corresponding

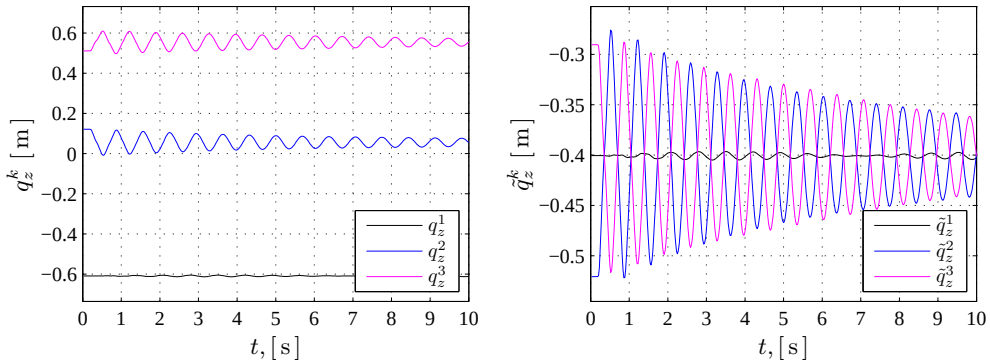

FIGURE 3.24: Rotor in-plane q_z^k and local edge-wise $\tilde{q}_z^k$ blade tip displacements.

to the non-zero mean component of the response. In the plot the eigenfrequencies of the first 12 modes are marked by the vertical dotted lines. The energy of the dynamic response is clearly seen to be concentrated on the first and second edge-wise whirling modes.

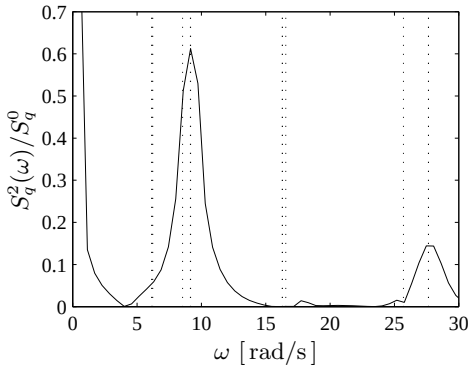

FIGURE 3.25: Energy density spectrum $S_q^2(\omega)$ of edge-wise displacements q_z^2.

As discussed in Sec. 3.4.2 the whirling modes introduce in-plane loads of the rotor transmission shaft. These are investigated in the following. Nodal section forces and moments of blade k in the rotor coordinate system $[\,\mathbf{Q}_k^T,\,\mathbf{M}_k^T\,]^T$ are evaluated by the rotation

$$\begin{bmatrix}\mathbf{Q}_k\\ \mathbf{M}_k\end{bmatrix} = \begin{bmatrix}\mathbf{R}_k & \mathbf{0}\\ \mathbf{0} & \mathbf{R}_k\end{bmatrix}\begin{bmatrix}\tilde{\mathbf{Q}}_k\\ \tilde{\mathbf{M}}_k\end{bmatrix} \tag{3.25}$$

where $\mathbf{R}_k$ is defined in (3.3). The resulting in-plane forces acting on the rotor shaft $\{Q_x^s, Q_z^s\}$ are determined as the sums of the corresponding nodal root forces of the three blades. The symmetric combination of forward and backward whirling which generates the 'clapping' vibration pattern generates an oscillating force at the whirling eigenfrequency in the x-direction, when blades 2 and 3 are the active blades. In Fig. 3.26a the forces $\{Q_x^s, Q_z^s\}$ are shown as function of time and both Q_x^s and Q_z^s are seen to oscillate at the first edge-wise whirling frequency after the initial decay of higher modes. The non-zero in-plane forces Q_z^s are related to the velocity-proportional aerodynamic forces. These are anti-symmetric due to the anti-symmetric velocities of blade 2 and 3. In Fig. 3.26b the in-plane shaft forces are plotted together in the $\{Q_x^s, Q_z^s\}$-plane as function of time where the start point is marked with an asterisk $*$ and the end point is marked with a cross $\times$. Upon the release of the system

the resulting in-plane force is seen to quickly engage in an elliptical clock-wise motion. The Q_x^s-components are due to the gyroscopic forces and acceleration-proportional inertial forces of the whirling modes and the Q_z^s components arise from the aerodynamic damping term. The simulation end point $\times$ is taken when the displacements of blade 2 and 3 are close to zero, corresponding the blades moving at the maximal local velocities. This is seen in Fig. 3.26a and to correspond to a maximum of Q_z^s.

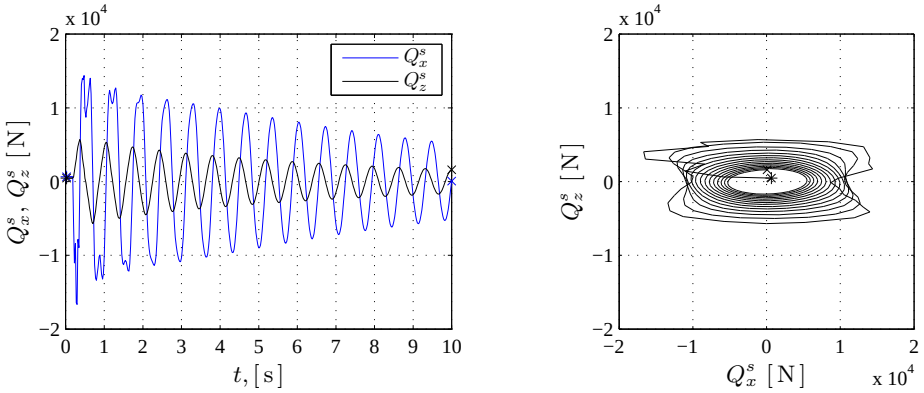

FIGURE 3.26: Global blade root section forces Q_x^s and Q_z^s.

The present section concludes the fundamental structural and aerodynamic analysis of the three-bladed wind turbine rotor. By a simple example it has been illustrated that the three-bladed wind turbine rotor model with symmetric pitch and coning angles and the non-symmetric aerodynamic formulation reproduces the weakly damped edge-wise vibration modes in a time integration of the equations of motion. Due to the presence of gyroscopic forces these modes are divided into a collective mode in which the blades oscillate in phase, and into the forward and backward whirling modes.

Chapter 4

Resonant Vibration Control of Beams and Rotors

In this chapter the basic idea of the resonant controller and its expansion to flexible multi-degree-of-freedom systems is given. Subsequently the formats for application to stationary systems and gyroscopics systems are given, accompanied by application to an isolated 42 m blade and an 86 m wind turbine rotor.

4.1 Basic Idea of the Resonant Controller

In this section the basic format of a resonant vibration controller for an undamped single-degree-of-freedom system is introduced. Also, the expansion to multi-degree-of-freedom systems is briefly discussed. The format is adopted from Krenk & Høgsberg [15, 16] where also the calibration scheme for the controller parameters is developed. The basic single-degree-of-freedom system is shown in Fig. 4.1a, with mass m, stiffness k and displacement x.

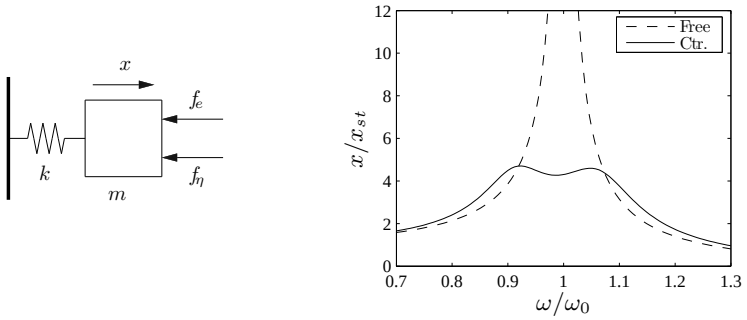

Figure 4.1: Basic, active resonant vibration control. a) Single-degree-of-freedom system. b) Frequency response.

If the free structural system is subjected to a broad band external force f_e, resonant amplification of the response occurs near the structural eigenfrequency $\omega_0 = k/m$. This amplification is shown with a dashed line in Fig. 4.1b where the stationary response amplitude x corresponding to a harmonic load of the form $f_e(t) = f_e e^{i\omega t}$ is shown, normalized with the static response x_{st}.

The fundamental objective of the resonant controller is to reduce the dynamic amplification of the structural response near ω_0 by actively applying a load f_η to the structure. For this purpose the controller is defined as a second order filter with a natural frequency ω_s close to the structural eigenfrequency ω_0. The independent controller state variable is excited by a sensor filter, transferring structural feedback in terms of e.g. displacement x or acceleration $\ddot{x}$, and the controller affects the structure via an actuator filter transferring the physical load. This creates a closed-loop system where resonant structural activity invokes resonant controller activity. By including a damping term in the controller transfer function, the mechanical energy of the coupled system can be effectively dissipated and structural displacements significantly reduced. For optimal calibration of the controller properties, the

targeted structural mode splits into two equally damped modes, closely spaced around the original structural frequency ω_0. The frequency response of a coupled system with an optimally calibrated controller is shown in Fig. 4.1b in terms of the fully drawn curve. The equal damping of the two emanating modes is seen to produce two identical resonant peaks with low amplification.

The coupled equations of motion for the single-degree-of-freedom system and the resonant controller are shown in (4.1) and (4.2). The equations are shown in the frequency domain, corresponding to a harmonic load $f_e(t) = f_e e^{i\omega t}$ with associated stationary response $x(t) = xe^{i\omega t}$. The structural equation of motion is

$$G^s_{xx}(\omega)x + G^s_{x\eta}(\omega)\eta = f_e/m \tag{4.1}$$

where $G_{xx}(\omega) = \omega_0^2 - \omega^2$ is the transfer function of the free, undamped structure and $G^s_{x\eta}(\omega)$ is the actuator feedback transfer function. Thus, the controller feedback is given as $f_\eta = G^s_{x\eta}(\omega)\eta$ where η is the controller state variable. This variable is governed by the equation

$$G^s_{\eta x}(\omega)x + G^s_{\eta\eta}(\omega)\eta = 0 \tag{4.2}$$

where $G^s_{\eta x}(\omega)$ is the sensor transfer function and $G^s_{\eta\eta}(\omega)$ is the second order controller transfer function, defined as

$$G^s_{\eta\eta}(\omega) = \omega_s^2 - \omega^2 + 2i\zeta_s\omega_s\omega \tag{4.3}$$

where ω_s is the controller eigenfrequency and ζ_s is the controller damping ratio. Krenk & Høgsberg [15, 16] define the following sensor and actuator transfer functions for a controller with acceleration feedback,

$$G^s_{\eta x}(\omega) = \omega^2, \quad G^s_{x\eta}(\omega) = \alpha_s\omega_s^2 + \beta_s 2i\zeta_s\omega_s\omega \tag{4.4}$$

The sensor feedback transfer function $G^s_{\eta x}(\omega)$ is seen to be a differential operator and the actuator transfer function $G^s_{x\eta}(\omega)$ is a linear filter with the two gain parameters α_s and β_s. In [15, 16] a displacement-based feedback system is also defined, which is not included here. For both acceleration and displacement feedback an optimal and explicit calibration scheme is developed in [15, 16]. The derivation is performed in two steps. The optimal controller frequency ω_s is initially identified by requiring equal damping of the two emanating modes. The remaining parameters are then determined by invoking a characteristic restriction on the dip in dynamic amplification close to ω_0, which has the effect of flattening and thereby lowering the entire resonant plateau of the coupled system. The optimal parameters are explicitly given as

$$\alpha_s = \frac{2\zeta_s^2}{1 - 2\zeta_s^2}, \quad \beta_s = \alpha_s, \quad \omega_s = \frac{\omega_0}{1 + \alpha_s} \tag{4.5}$$

The acceleration feedback filters (4.3) and (4.4) are equivalent to those of the passive, mechanical tuned mass damper [8, 46] when the gain parameters α_s, β_s are equal to the mass ratio between structure and damper. As shown in [46] the resulting damping ratios $\Delta\zeta$ become close to half the damping ratio of the damper, i.e. for a desired additional damping ratio $\Delta\zeta$ the basic controller damping ratio is chosen as $\zeta_s = 2\Delta\zeta$.

The resonant controller format can be applied to multi-degree-of-freedom systems. The format used in the present case is given in the frequency domain as

$$\big(\mathbf{K} + i\omega 2\mathbf{G} - \omega^2\mathbf{M}\big)\mathbf{u} + \mathbf{f}_\eta = \mathbf{f}_e \tag{4.6}$$

where $\mathbf{f}_\eta$ represents the imposed load from the actuator system. When the resonant control format is applied to a multi-degree-of-freedom system for vibration suppression of selected

modes, a number of physical considerations concerning the interplay between the control system and the modal dynamics of the flexible structure comes into play. One is that the sensor/acutator system must be positioned such that good controllability and observability is obtained for the targeted mode. For the present collocated format these two concepts are represented in the term modal connectivity. Also, it is necessary to minimize the controller connectivity to other modes, as these will otherwise disturb the calibration and operation of the controller. The resonant characteristic of the resonant controller provides and effective decoupling from other modes when these are well separated in frequency from the targeted mode. In this case the response of higher modes will be limited in the resonant region of the targeted mode, and their contribution can be approximated and included by a quasi-static approximation, see Preumont [35] and Krenk & Høgsberg [15, 16]. Also, a geometric decoupling from other modes can be obtained in systems where mode shapes are geometrically orthogonal, e.g. for beam bending modes about the strong and weak axis, respectively. In the case of gyroscopic systems, and in particular three-bladed rotors, modes arise which are closely spaced both frequency-wise and geometrically. These are discussed in Chapter 3 as the groups consisting of one collective vibration mode and the backward and forward whirling modes. In addition to the considered modal decoupling methods for rotating beams, optimal resonant control of the three-bladed rotor modes requires an additional decoupling scheme based on the mean and deviatoric blade deformation patterns described in Chapter 3. In Sec. 4.2 resonant vibration control of rotating beams is discussed and in Sec. 4.3 resonant vibration control of three-bladed rotors is discussed.

4.2 Control of Rotating Beams

In this section an overview of the controller format for control of non-rotating multi-degree-of-freedom structures is given, followed by an example where the method is applied to an isolated wind turbine blade. The blade is rotating, which gives rise to an eigenfrequency change compared to the stand-still situation, necessary for the controller tuning. As the blade is isolated the gyroscopic effects play a minor role, and the calibration according to the method for non-rotating structures proves effective. To illustrate that two modes can be addressed simultaneously with two different controller systems with associated sensor/actuator pairs, both the first flap-wise and the first edge-wise mode is controlled.

4.2.1 Controller Format

For a system with multiple controllers with associated sensor/actuator pairs, the combined actuator force $\mathbf{f}_\eta$ takes the form

$$\mathbf{f}_\eta = \mathbf{w}_1\eta_1 G^1_{x\eta}(\omega) + \mathbf{w}_2\eta_2 G^2_{x\eta}(\omega) + ... \tag{4.7}$$

where the first term is the actuator feedback from controller 1, the second term is that from controller 2 etc. The vectors $\mathbf{w}_k$ are the physical connectivity vectors of the collocated sensor/actuator pairs. A method for establishing the connectivity vector for a three-dimensional beam is given in Appedix C. The components η_k are the controller states and $G^k_{x\eta}(\omega)$ are the actuator feedback transfer function, corresponding to $G^s_{x\eta}(\omega)$ for the basic case. Each controller state is governed by the equation

$$G^k_{\eta\eta}(\omega)\eta_k + G^k_{\eta x}(\omega)\mathbf{w}_k^T\mathbf{u} \tag{4.8}$$

where $\mathbf{w}_k^T\mathbf{u}$ provides a scalar feedback from the structural deformation state. For an active strut positioned as in Fig. 1.2, i.e. in the axial direction with a finite distance to the elastic center, this feedback represents a combined state of axial blade deformation and bending. The controller filter is defined as the second order filter

$$G^k_{\eta\eta}(\omega) = \omega_k^2 - \omega^2 + 2i\zeta_k\omega_k\omega \tag{4.9}$$

which corresponds to the filter $G^s_{\eta\eta}(\omega)$ for the basic controller. For a system with acceleration feedback the sensor and actuator transfer functions are defined as

$$G^k_{\eta x}(\omega) = \omega^2, \quad \omega^2_{k,n}|\nu_k|^2 G^k_{x\eta}(\omega) = \alpha_k \omega_k^2 + \beta_k 2i\zeta_k \omega_k \omega \tag{4.10}$$

corresponding to (4.4). The eigenfrequency of the targeted modes are denoted as $\omega_{k,n}$ where k refers to controller number and n refers to mode number. The scaling of the actuator feedback function involves the connectivity factor $\nu_k = \mathbf{w}_k \mathbf{u}_n$ which represents the modal deformation of actuator k due to the its targeted mode n with mode shape $\mathbf{u}_n$. The scaling $\omega^2_{k,n}$ is due to a convenient scaling of mode shapes with respect to structural stiffness, as discussed in Krenk et al. [6]. The calibration of the multi-degree-of-freedom controller is based on a modal form of the coupled set of equations consisting of the structural equations of motion, i.e. (4.6) combined with (4.7) and the controller equations (4.8). The modal form includes the flexibility of the higher modes at the position of the sensor/actuator pair, via the quasi-static approximation of the structural admittance matrix (2.94). This leads to the quasi-static background flexibility factor κ_k,

$$\kappa_k = \frac{\mathbf{w}_k^T \mathbf{K}^{-1} \mathbf{w}_k}{|\nu_k|^2} - 1 \tag{4.11}$$

which represents the background flexibility of higher modes. In the ideal case of perfectly decoupled modal connectivity, i.e. with distributed controller forces proportional to the targeted mode shape, the quasi-static response is completely dominated by the targeted mode, which implies that $\kappa_k = 0$.

The resonant modal equations of the coupled system including the correction for background flexibility of higher modes take a form similar to (4.1) and (4.2), where the controller transfer function is modified by a term involving the sensor and actuator transfer functions, and which is proportional to the background flexibility parameter κ_k. This produces a cubic form of the resulting controller filter, which can be approximated by a quadratic, or second order, filter in the resonant region of the controller. By direct comparison with the basic parameter calibration (4.5) an explicit set of optimal parameters for the multi-degree-of-freedom controller is obtained. These parameters are given in Table 4.1 where indices k refer to the present application. Indices c and w refer to the parameters for control of collective and whirling modes in a three-bladed rotor, as presented in Sec. 4.3.

TABLE 4.1: Calibration with gain parameter α_s.

	$\alpha_{k,c,w}$	$\beta_{k,c,w}$	$\left(\frac{\omega}{\omega_n}\right)^2_{k,c,w}$	$\left(\zeta\frac{\omega}{\omega_n}\right)_{k,c,w}$
Basic	α_s	α_s	$\frac{1}{(1+\alpha_s)^2}$	$\sqrt{\frac{\alpha_s}{2(1+\alpha_s)^3}}$
Full	α_s	$\frac{\alpha_s}{1+\kappa\alpha_s}$	$\frac{1}{1-\frac{\kappa\alpha_s}{(1+\alpha_s)^2}}\,\frac{1}{(1+\alpha_s)^2}$	$\frac{1+\kappa\alpha_s}{1-\frac{\kappa\alpha_s}{(1+\alpha_s)^2}}\sqrt{\frac{\alpha_s}{2(1+\alpha_s)^3}}$

4.2.2 Example: Control of 42 m Wind Turbine Blade

This section exemplifies the resonant vibration control method by application of to the 42 m wind turbine blade presented in Chapter 3. The coupled equations of motion are given in detail in Svendsen et al. [17, 18]. Two separate controllers are applied to the blade, where

one targets the first flap-wise mode and the other targets the first edge-wise mode. The first flap-wise mode has significant aerodynamic damping, and in practical wind turbine application it would therefore be more relevant to target only edge-wise modes. However, the present example illustrates that it is possible to target several modes with individual control systems and obtain close to optimal controller calibration with the present method.

Two active struts are applied to the wind turbine blades as shown in Fig. 4.2. The struts are positioned close to the blade root where curvatures due to bending are largest. This maximizes the modal connectivities. The positions correspond to strut lengths $L_k = 6.0\,\mathrm{m}$, in positions between the first two element nodes as shown in [17]. Each strut is positioned such that the axis of the strut is parallel with the local blade axis $\tilde{x}$, in the distance $R_k = 0.70\,\mathrm{m}$ from the axis. This defines a circumference of possible strut positions, defined by the angles θ_k measured from the $\tilde{y}$-axis.

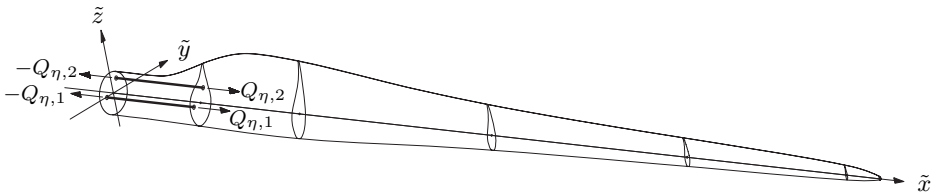

FIGURE 4.2: The 42 m wind turbine blade with two active strut controllers.

In the positioning of the sensor/actutator pairs the objective is generally to obtain a high modal connectivity while minimizing the background flexibility of higher modes, within the constraints of practical implementation. When a single controller is applied to a beam this is a relatively straightforward procedure, as the mode shapes of the free structure provide a good approximation of the resulting mode shapes in the controlled structure. This allows a direct procedure of application based on maximizing ν while minimizing κ. However, when multiple controllers are applied, the interaction between these must be accounted for. The explicit calibration procedure of Table 4.1 directly provides the optimal parameters for a chosen position of a single controller, and the resulting properties of the full, coupled system including all controllers can be directly evaluated by modal analysis. Thus, a simple parameter study for different combinations of controller positions can be performed and the optimal combination identified. This is done here with circumferential strut positions θ_1 and θ_2 as variables and the result is seen in Fig. 4.3. The following error measure is used. When the resonant controller is optimally tuned, the targeted mode splits into two new modes with identical damping ratios $\zeta_{n,1}$ and $\zeta_{n,2}$. The calibration error ε is defined as the relative deviation of e.g. $\zeta_{n,1}$ from the mean value of the two damping ratios. This error measure reflects the lack of symmetry in the frequency response curve seen in Fig. 4.1. It is seen in Fig. 4.3 that the calibration errors ε_k have a common region in which they are both minimized, namely for $\theta_1/\pi \simeq 1.0$ and $\theta_2/\pi \simeq 0.25$. These positions are depicted in Fig. 4.2 and the result corresponds well to the intuitive notion that controller 1, targeting the flap-wise mode should impose bending moments about the $\tilde{z}$-axis while controller 2, targeting the edge-wise mode should impose bending moments about the $\tilde{y}$-axis. However, the interaction of the two controllers is also clear when comparing to the optimal position for edge-wise mode controller operating 'alone', Svendsen et al. [18]. In this case the controller position is somewhat closer to $\theta/\pi \simeq 0.5$, i.e. pure bending about the $\tilde{y}$-axis.

The controller tuning parameters and resulting damping ratios of the coupled system are given in Table 4.2 for the rotating blade with angular velocity $\omega_y = 1.57\,\mathrm{rad/s}$. Close to optimal parameters for the two modes are obtained. The basic controller calibration leads

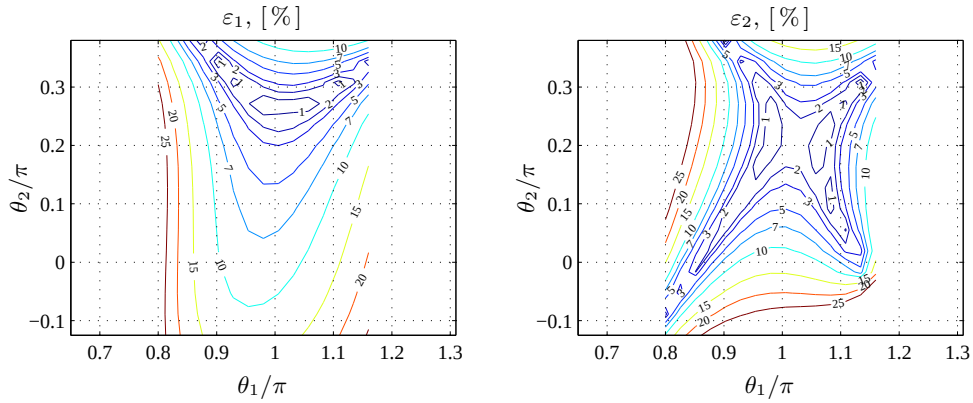

FIGURE 4.3: Calibration errors for varying controller position angle.

to controller frequencies ω_k which are slightly lower than those of the target modes, and the quasi-static correction has the opposite effect. In the present case the active controller frequencies become slightly larger than those of the free structure. The values $\kappa_1 = 14.1$ and $\kappa_2 = 10.1$ can be directly compared to the examples in Krenk & Høgsberg [15] where $\kappa = 23.5$ is obtained in the control of a very flexible cable, and $\kappa = 4.0$ is obtained in the control of a cantilever beam. The present results are seen to be located somewhat in between. The higher amount of background noise in the present case is somewhat related to the structural complexity of the wind turbine blade, where the effect of pre-twist as described in Chapter 3 plays a significant role, as it implies elastic coupling between flap-wise and edge-wise blade motion over the stretch of the sensor/actuator pairs.

TABLE 4.2: Control parameters, $\Delta\zeta_k = 0.06$.

n	κ_k	α_k	β_k	ω_k/ω_n	ζ_k	$\zeta_{n,1}$	$\zeta_{n,2}$	ϵ_n [%]
1	14.1	0.0297	0.0209	1.25	0.219	0.0619	0.0609	0.81
2	10.1	0.0297	0.0228	1.15	0.184	0.0599	0.0614	1.21

In Fig. 4.4a is shown the dynamic amplification of flap-wise blade tip displacements for the fully coupled system loaded by a harmonic force, proportional to the flap-wise mode shape of the free structure. The free response shows a distinct peak near the eigenfrequency of the free flap-wise mode. In the controlled case, this peak takes a form similar to that in Fig. 4.1, which indicates the almost optimal controller tuning. In Fig. 4.4b similar results are shown for the edge-wise displacements, for the blade loaded by a harmonic force proportional to the edge-wise mode. As seen Table 4.2 the calibration of the controller for this mode is slightly less optimal than the other mode, and this is seen in the controlled curve as a small non-symmetry. For practical use, the calibration is fully satisfactory is both cases.

4.3 Control of Three-Bladed Rotors

In this section an overview of the controller format for control of three-bladed rotors is given. In Krenk et al. [6] an example of application of the controller system to the three-bladed rotor presented in Chapter 3 is given, which is here supplemented with a discussion of e.g. controller positioning issues.

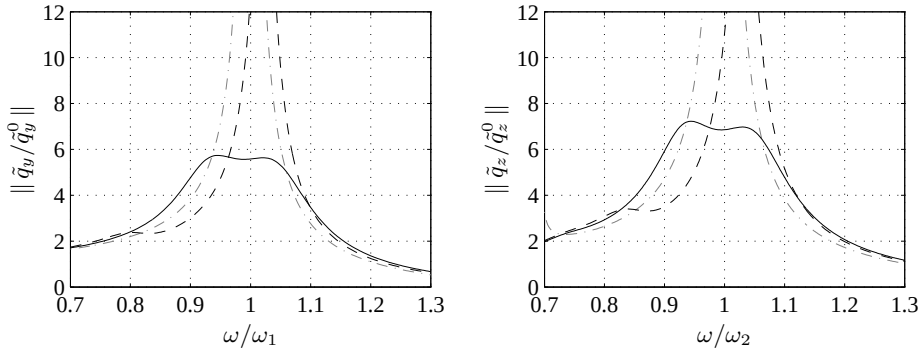

FIGURE 4.4: Dynamic amplification. a) Flap-wise tip displacement. b) Edge-wise tip displacement. -·-·- Free. —— Controlled. - - - $\kappa_k = 0$.

4.3.1 Controller Format

The controller format is developed with the purpose of adding damping to a given group of vibration modes. This group is assumed to consist of a collective mode, where all three blades move in phase, and a forward and a backward whirling mode where the blades oscillate with mutual phase lags of $\frac{2}{3}\pi$. Due to high degree of similarity of the three modes, these are addressed by a single set of three sensor/actuator pairs, one pair in each blade. This is shown in Fig. 1.3. The controller feedback is defined in terms of two distinctly different contributions,

$$\mathbf{f}_\eta = \mathbf{w}_c \eta_c G^c_{x\eta}(\omega) + \mathbf{W}\boldsymbol{\eta}\, G^w_{x\eta}(\omega) \tag{4.12}$$

The first term is a single-state controller, intended to address the collective mode. The term consists of the controller state η_c, the actuator transfer function $G^c_{x\eta}(\omega)$ and the controller connectivity vector $\mathbf{w}_c$. The second term in the actuator feedback (4.12) addresses the forward and backward whirling modes. As discussed in Section 3.4, a whirling mode consists of a uniform wave-like propagation of identical blade displacement fields. The three blades vibrate with mutual phase lags of $\frac{2}{3}\pi$ and the direction of the wave-propagation relative to the angular velocity of the rotor distinguishes the forward and backward whirling modes. In order to address whirling motion in a three-bladed rotor, three independent blade controller state variables are necessary for collocated identification and actuation of the two waveforms. The three controller states are organized in the controller state vector $\boldsymbol{\eta} = [\,\eta_1,\, \eta_2,\, \eta_3\,]^T$ where the numbering reflects the blade association of each controller state. The collocated sensor/actuator feedback for the whirling mode controller is imposed by the connectivity matrix $\mathbf{W}$. The connectivity vector $\mathbf{w}_c$ and the connectivity matrix $\mathbf{W}$ define linear combinations of the three scalar blade deformation signals,

$$\mathbf{w}_c = \tfrac{1}{3}(\mathbf{w}_1 + \mathbf{w}_2 + \mathbf{w}_3), \quad \mathbf{W} = [\,\mathbf{w}_1 - \mathbf{w}_c, \mathbf{w}_2 - \mathbf{w}_c, \mathbf{w}_3 - \mathbf{w}_c\,] \tag{4.13}$$

where $\mathbf{w}_c$ extracts the mean blade deformation signal and $\mathbf{W}$ extracts the three deviatoric blade signals. These two filters reflect the fundamental properties of the collective mode versus the whirling modes as described in Sec. 3.4 and provides an exact separation of of the two mode types.

The collective and the whirling controllers have transfer functions corresponding to (4.9) and (4.10) and the collective controller state is governed by an equation corresponding to (4.8). Thus, the modal equations describing the coupled system of the rotor and the collective controller can be established in the same way as for the control systems in the previous section, and the calibration follows directly from Table 4.1. The whirling controller states $\boldsymbol{\eta}$ are governed by a set of three equations. From this set of equations it is directly seen

that these states have constant relative amplitudes proportional to the modal connectivity of the associated sensor/actuator pairs, $\boldsymbol{\eta} \propto \boldsymbol{\nu}_w$, where the modal connectivities are given as $\boldsymbol{\nu}_w = \mathbf{W}^T \mathbf{u}_w$. This proportionality allows the coupled system of the multi-degree-of-freedom structural equations and the multi-component controller equations to be collapsed into scalar modal equations analogous to those of the basic resonant system. Thus, also in this case optimal calibration is as given in Table 4.1.

The establishment of the modal equations for the rotor system is based on the frequency response format (2.97) for gyroscopic systems. In this framework the expression for the background flexibility parameter of the collective mode controller κ_c takes the same form as for the non-rotating system (4.11). The background flexibility parameter of the whirling mode controller κ_w however takes a slightly different form,

$$\kappa_w = \frac{\bar{\boldsymbol{\nu}}_w^T \boldsymbol{\kappa}_w \boldsymbol{\nu}_w}{\nu_w^4} = \frac{\bar{\boldsymbol{\nu}}_w^T \mathbf{W}^T \mathbf{K}^{-1} \mathbf{W} \boldsymbol{\nu}_w}{\nu_w^4} - 1 \tag{4.14}$$

which involves the Hermitian transpose of the modal connectivity vector $\boldsymbol{\nu}_w$. The structure and normalization of κ_w corresponds to (4.11), and so these quantities are directly comparable. This will be seen from the following example.

4.3.2 Example: Control of 86 m Wind Turbine Rotor

In this example the resonant control system presented in Sec. 4.3 is applied to the 86 m wind turbine rotor introduced in Sec. 3.5. The coupled equations of motion are given in detail in Krenk et al. [6]. The objective is to add damping to the first group of edge-wise bending modes, i.e. modes 4-6 in Table 3.3. The sensor/actuator system consists of active struts with acceleration sensors attached as shown in Figs. 1.2 and 1.3. The control system is calibrated by the procedure in Table 4.1, including the effect of the background flexibility. The controller is designed to introduce the desired additional damping ratio to the collective mode $\Delta\zeta_c = 0.06$ and the additional damping ratio $\Delta\zeta_w = 0.06$ to the whirling modes. The tuning for the whirling modes is based on the properties of mode 5, i.e. the backward whirling mode. As discussed in Sec. 3.5 the frequencies of the two whirling modes are not completely identical due to the presence of aerodynamic forces. The theory of the resonant controller is developed for purely gyroscopic, three-bladed rotors. The non-symmetric and non-conservative properties of the aerodynamic terms break the symmetric and skew-symmetric form of the undamped part of (2.85). However, the effects are relatively small and as demonstrated in the present example, the resonant controller tuning is robust and exhibits excellent performance for the damped aeroelastic system.

The example features an initial study on controller positioning and calibration, based on modal analysis of the closed-loop equations of motion, according to the theory given in Sec. 2.5. It is shown that proper physical positioning and a quite accurate estimate of the eigenfrequencies of the targeted modes are important to the quality of the calibration. To illustrate the fundamental function of the controller, the rotor response corresponding to the non-zero initial conditions introduced in Sec. 3.5 is simulated.

Each strut is positioned such that the axis of the strut is parallel with the local blade axis $\tilde{x}$, in the distance $R_s = 0.80\,\mathrm{m}$ from the axis. The actuator has the length $L_s = 7.7\,\mathrm{m}$ and is positioned between element nodes 2 and 3 in Fig. 3.23. The physical position of the collocated sensor/actuator pairs influences the modal controllability of the controller and the amount of background 'noise' at the controller position due to the flexibility of higher modes. The influence of the angle θ_s is illustrated in Fig. 4.5a. It is seen from Fig. 4.5a that a unique position for optimal damping of the three modes is not defined. This is due to the

differences in mode shapes. However, within the region $0.44 < \theta_s/\pi < 0.46$ very accurate calibration of both the collective and the whirling mode controllers can be obtained using a shared set of sensor/actuator pairs. It is seen from Fig. 4.5b that optimal calibration is closely related to minimizing the modal background flexibility, expressed in terms of κ_c^4 and $\kappa_w^{5,6}$. It is further noted that in the quasi-static approximation (2.97) leading to the expressions for $\kappa_{c,w}$ the dynamic responses of lower modes, here corresponding to modes 1,2,3 are simply omitted. The fact that these modes are flap-wise, i.e. geometrically almost orthogonal to the targeted edge-wise modes explains why this approximation works well in the present case.

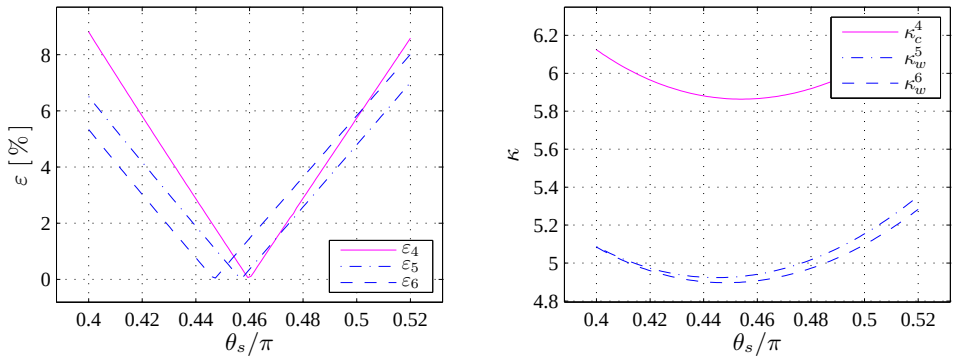

FIGURE 4.5: Controller positioning. a) Calibration error. b) Background flexibility parameters.

An important prerequisite for optimal calibration of the resonant controller is a good estimate of the eigenfrequency of the targeted mode ω_n. In Fig. 4.6 is shown the calibration errors obtained for a slightly erroneous eigenfrequency estimate ω_n^ε. It is seen that the calibration error increases linearly with the relative eigenfrequency error, and an error ratio of $\omega_n^\varepsilon/\omega_n = 2\,\%$ yields calibration errors in the region of $\varepsilon_j \simeq 10\,\%$. As indicated in Fig. 3.17 significant changes in modal rotor properties can be expected with practical operation regimes. It may therefore be relevant to employ a continuous update of controller properties accordingly. Given the fully active nature of the control system and the explicit calibration procedure, this should not involve significant practical challenges.

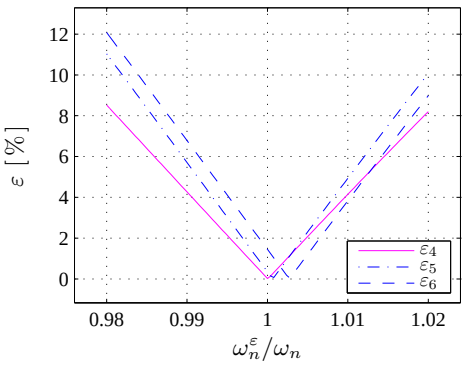

FIGURE 4.6: Calibration error for imposed eigenfrequency error.

The controller parameters are given in Table 4.3 for the strut position $\theta_s/\pi = 0.46$. With

$\kappa_c^4 = 5.9$ and $\kappa_w^5 = 5.9$ the relative background flexibility of higher modes is around half the value of that for the edge-wise controller of the single blade, where $\kappa_2 = 10.1$. This illustrates both that the filter (4.13) is very effective and that controller positioning and size can also make a difference when it comes to reducing background flexibility noise. The latter effect is here due to the fact that the active struts attached to the rotor are 28 % longer and have radial distances to the center axis which are 14 % larger than for the single blade.

TABLE 4.3: Control parameters, $\Delta\zeta_{4,5} = 0.06$.

	$\alpha_{c,w}$	$\beta_{c,w}$	$\omega_{c,w}$	$\zeta_{c,w}$	κ
Collective	0.0297	0.0253	9.075	0.1541	5.867
Whirling	0.0297	0.0259	9.564	0.1482	4.941

Blade tip amplifications in the edgewise direction are plotted in Fig. 4.7 for harmonic loading of the three controlled modes. The blades have identical frequency responses to the applied load and so only the response of one blade is shown in each figure. It is seen that the calibration including the correction for background flexibility leads to almost optimal response curves. When the quasi-static correction is not included, the reduction in performance becomes clear. The controller frequency is seen to be too low, by which the highest of the two emanating modes is not properly addressed. However, due to the lower background flexibility in the rotor case than in the single blade case, the effect of using $\kappa_{c,w} = 0$ is less critical in the rotor case.

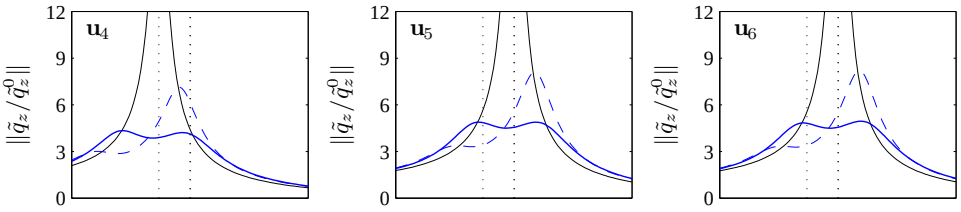

FIGURE 4.7: Modal dynamic amplification. Upper row: Blade tip responses; free: thin full line; controlled: thick full line; dashed: controlled ($\kappa_{w,c} = 0$).

The simulated response in Sec. 3.5 is dominated by an almost symmetric combination of the first edge-wise backward and forward whirling modes. In following the same initial conditions are prescribed for the controlled rotor. This allows a representation of the basic function of the whirling mode controller. The time integration is performed using the same settings as in Sec. 3.5.

In Fig. 4.8a the controlled edgewise blade tip responses $\tilde{q}_z^k$ are shown with full lines and the free response of blade 2 is shown with a dashed line for comparison. The vibration amplitudes of the two active blades are seen to be rapidly damped compared to the free response. The whirling mode controller effectively handles a response of combined backward and forward whirling. This is due to the fact that the filtering (4.13) extracts the 'deviatoric' blade signals which incorporate both whirling modes. In Fig. 4.8b the actuator forces $\tilde{Q}_\eta^k$ are plotted. It is seen that only $\tilde{Q}_\eta^2$ and $\tilde{Q}_\eta^3$ have significant activity, corresponding to the activity in blade 2 and 3. This demonstrates that the three controller states of $\boldsymbol{\eta}$ are fully independent, despite the fact that the calibration of the whirling mode controller is based on a scalar modal equation in which the three states are collapsed into the equivalent component η_w, see [6]. The gradual increase of the controller activity during approximately the first 1.2 s reflects

the 'inertia' of the second order filter, which limits the response rate of the controller. This is a natural feature of the resonant controller which ensures the focus of actuator efforts in the frequency domain. The advantage of the active controller is that this inertial effect 'comes for free', as it can in principle be realized by very lightweight actuator systems.

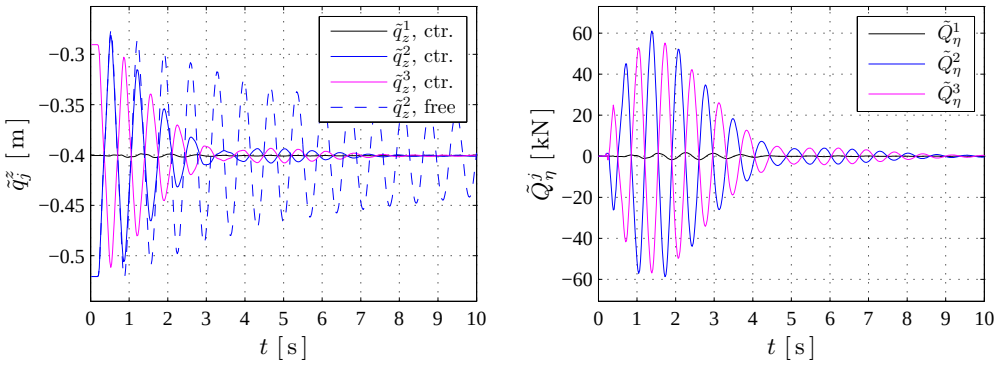

FIGURE 4.8: Local edgewise blade tip displacements $\tilde{q}_j^z$ and actuator forces $\tilde{Q}_\eta^j$.

The bending moment in blade 2 about the local $\tilde{y}$-axis $\tilde{M}_y$, at the root-wise end of the active strut is plotted in Fig. 4.9a. Again, the vibration amplitudes associated with the two active blades are seen to be rapidly damped. Also, the bending moment imposed by the actuator $\tilde{M}_\eta^2 = \tilde{Q}_\eta^2 \tilde{k}_z$ is plotted. It is seen that the bending moment imposed by the controller is small compared to the total bending moment in the blade. This relative difference in amplitude is a general feature of the optimally tuned resonant controller, and the effect is equivalent to harmonic loading where large dynamic amplification is obtained at resonance. The local trailing edge and leading edge material strains at the same location are plotted in Fig. 4.9b. In spite of significant actuator forces, the material strain at the position of the actuator is reduced in the controlled case. This is due to the fact that the optimally tuned resonant controller deploys actuator force for maximal energy dissipation. This occurs at peak velocities where structural displacements vanish.

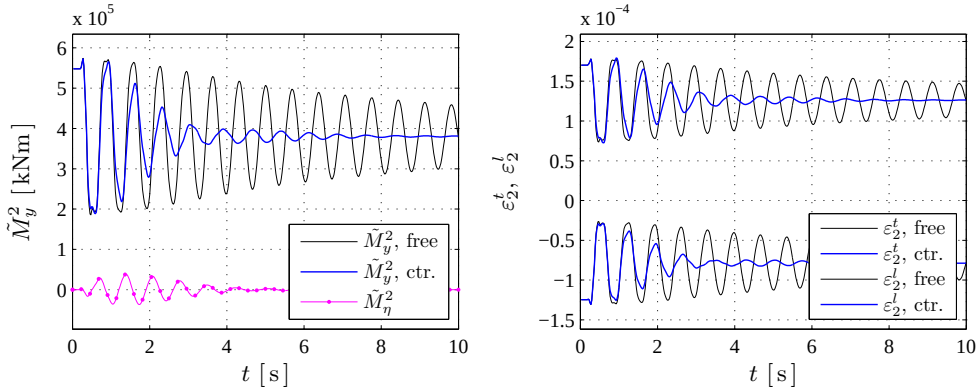

FIGURE 4.9: Structural load at the root-wise actuator end of blade 2. a) Local edgewise bending moments. b) Trailing and leading edge strains.

In Krenk et al. [6] a simulated wind field with realistic stochastic properties is applied to the present rotor with the same configuration. When subjected to a turbulent wind field, the

rotor response is highly transient and several vibration modes participate in the response. Significant dynamic components of the first edge-wise collective and whirling modes are present in the local edge-wise blade displacements and the potential of significantly reducing associated fatigue loading is clear. From time series and frequency spectra it is seen that the control system effectively reduces the amplitudes of the targeted modes, while leaving the remaining modes of the rotor virtually unaffected. These very low spill-over effects are obtained due the focused frequency-wise tuning of the control system, geometric decoupling via sensor/actuator positioning and the exact filtering of collective and whirling modes. The implication is that the active, resonant rotor control method can be employed to obtain effective damping of e.g. edge-wise vibration modes.

Chapter 5

Conclusions

The cost of energy produced by a modern, three-bladed wind turbine is related to the lifetime of the machine, and it is therefore of practical interest to consider methods for fatigue load reduction. The edge-wise vibration modes are typically subject to low aerodynamic damping and therefore a source of fatigue loads. This thesis presents a framework for structural modeling, analysis and active vibration damping of rotating wind turbine blades and rotors.

A structural rotor model is developed in terms of finite beam elements in a rotating frame of reference. The element comprises a representation of general, varying cross-section properties and assumes small cross-section displacements and rotations, by which the associated elastic stiffness and inertial terms are linear. The formulation consistently describes all inertial terms, including centrifugal softening and gyroscopic forces. Aerodynamic lift forces are assumed to be proportional to the relative inflow angle, which also gives a linear form with equivalent stiffness and damping terms. Geometric stiffness effects including the important stiffening from tensile axial stresses in equilibrium with centrifugal forces are included via an initial stress formulation. The element provides an accurate representation of the eigenfrequencies and whirling modes of the gyroscopic system, and identifies lightly damped edge-wise modes.

By adoption of a method for active, collocated resonant vibration of multi-degree-of-freedom systems it is demonstrated that the basic modes of a wind turbine blade can be effectively addressed by an in-blade 'active strut' actuator mechanism. The importance of accounting for background mode flexibility is demonstrated. Also, it is shown that it is generally possible to address multiple beam modes with multiple controllers, given that these are geometrically well separated.

For active vibration control in three-bladed wind turbine rotors the present work presents a resonance-based method for groups of one collective and two whirling modes. The controller introduces a dual system targeting the collective mode and the combined whirling modes respectively, via a shared set of collocated sensor/actuator pairs. The collective mode controller is decoupled from the whirling mode controller by an exact linear filter and an explicit procedure for optimal calibration of the controller gains is established. The control system is applied to an 86 m wind turbine rotor by means of active strut actuator mechanisms. The prescribed additional damping ratios are reproduced almost identically in the targeted modes and the observed spill-over to other modes is very limited and generally stabilizing. It is shown that physical controller positioning for reduced background noise is important to the calibration. By simulation of the rotor response to both simple initial conditions and a stochastic wind load it is demonstrated that the amplitudes of the targeted modes are effectively reduced, while leaving the remaining modes virtually unaffected. The actuator forces are shown to be generally beneficial to material strains and the requirements to the sensor/acutator system produced by the present simulation example can be met by existing technologies. Thus, the presented design method provides a consistent theoretical basis for active modal damping and fatigue load reduction in three-bladed wind turbine rotors.

Bibliography

[1] E. A. Bossanyi, Individual blade pitch control for load reduction, *Wind Energy*, 6 (2003) 119–128.

[2] Riziotis, V.A., Voutsinas, S.G., Politis, E.S., Chaviaropoulos, P.K., Aeroelastic stability of wind turbines: the problem, the methods and the issues, *Wind Energy*, 7 (2004) 373–392.

[3] M. H. Hansen, K. Thomsen, P. Fuglsang, Two methods for estimating aeroelastic damping of operational wind turbine modes from experiments, *Wind Energy*, 9 (2006) 179–191.

[4] T. K. Barlas, G. A. M. van Kuik, A comparison of smart rotor control approaches using trailing edge flaps and individual pitch control, *Progress in Aerospace Sciences*, 46 (2010) 1–27.

[5] P. B. Andersen, L. Henriksen, M. Gaunaa, C. Bak, T. Buhl, Deformable trailing edge flaps for modern megawatt wind turbine controllers using strain gauge sensors, *Wind Energy*, 13 (2010) 193–206.

[6] S. Krenk, M. N. Svendsen, J. Høgsberg, Resonant vibration control of three-bladed rotors, *Submitted*, (2011).

[7] A. Preumont, B. de Marneffe, A. Deraemaeker, F. Bossens, The damping of a truss structure with a piezoelectric transducer, *Computers and Structures*, 86 (2008) 227–239.

[8] J. Ormondroyd, J. P. Den Hartog, The theory of the dynamic vibration absorber, *Transactions of the ASME*, 50 (1928) 9–22.

[9] L. Meirovitch, Control of spinning flexible spacecraft by modal synthesis, *Acta Astronautica*, 4 (1977) 985–1010.

[10] M. J. Balas, Feedback control of flexible systems, *IEEE Transactions on Automatic Control*, 23 (1978) 673–679.

[11] S. C. Choi, J. S. Park, J. H. Kim, Vibration control of pre-twisted rotating composite thin-walled beams with piezoelectric fiber composites, *Journal of Sound and Vibration*, 300 (2007) 176–196.

[12] Y. A. Khulief, Vibration suppression in rotating beams using active modal control, *Journal of Sound and Vibration*, 242 (2001) 681–699.

[13] C. D. Shete, N. K. Chandiramani, L. I. Librescu, Optimal control of a pretwisted shearable smart composite rotating beam, *Acta Mechanica*, 191 (2007) 37–58.

[14] N. K. Chandiramani, Active control of a piezo-composite rotating beam using coupled plant dynamics, *Journal of Sound and Vibration*, 329 (2010) 2716–2737.

[15] S. Krenk, J. Høgsberg, Optimal resonant control of flexible structures, *Journal of Sound and Vibration*, 323 (2009) 530–554.

[16] S. Krenk, J. Høgsberg, Resonant damping of flexible structures, *COMPDYN 2009, ECCOMAS Thematic Conference on Computational Methods in Structural Dynamics and Earthquake Engineering* (2009).

[17] M. N. Svendsen, S. Krenk, J. Høgsberg, Resonant vibration control of rotating beams, *Journal of Sound and Vibration*, (2010), (doi:10.1016/j.jsv.2010.11.008).

[18] M. N. Svendsen, S. Krenk, J. Høgsberg, Resonant vibration control of wind turbine blades, *TORQUE 2010: The Science of Making Torque from Wind*, 543–553, June 28–30, Creete, Greece, 2010.

[19] M. Géradin, D. Rixen, *Mechanical Vibrations*, second ed., Wiley, Chichester, 1997.

[20] A. Kawamoto, S. Krenk, A. Suzuki, M. Inagaki, Flexible body dynamics in a local frame with explicitly predicted motion, *International Journal for Numerical Methods in Engineering*, 81 (2010) 246–268.

[21] S. Krenk, Element stiffness matrix for beams with with general cross-section properties, *Technical University of Denmark*, Department of Mechanical Engineering, (2006).

[22] S. Krenk, *Lectures on Thin-Walled Beams*, 3'rd ed., Technical University of Denmark, Department of Mechanical Engineering, 2001.

[23] Y. C. Fung, *An Introduction to the Theory of Aeroelasticity*, Dover, Mineola, New York, 1993.

[24] J. W. Larsen, S. R. K. Nielsen, S. Krenk, Dynamic stall model for wind turbine airfoils, *Journal of Fluids and Structures*, 23 (2007) 959–982.

[25] M. H. Hansen, Aeroelastic instability problems for wind turbines, *Wind Energy*, 10 (2007) 551–557.

[26] J. H. Argyris, An excursion into large rotations, *Computer Methods in Applied Mechanics and Engineering*, 32 (1982) 85–155.

[27] M. Géradin, A. Cardona, *Flexible Multibody Dynamics*, John Wiley & Sons, Chicester, 2001.

[28] S. Krenk, *Non-linear Modeling and Analysis of Solids and Structures*, Cambridge University Press, Cambridge, 2009.

[29] H. Ziegler, *Principles of Structural Safety*, Blaisdell Publishing Company, Waltham, Massachussets, 1968

[30] K. Washizu, *Variational Methods in Elasticity and Plasticity*, Pergamon Press, Oxford, 1968.

[31] V. Z. Vlasov, *Thin-walled Elastic Beams*, Israel Program for Scientific Translations, Jerusalem, 1961.

[32] D. H. Hodges, A. R. Atilgan, C. E. S. Cesnik, On a simplified strain energy function for geometrically nonlinear behaviour of anisotropic beams, *Composites Engineering*, 2 (1992) 513–526.

[33] T. J. R. Hughes, *The Finite Element Method, Linear Static and Dynamic Finite Element Analysis*, Dover, Mineola, New York, 2000.

[34] L. Meirovitch, A new method of solution of the eigenvalue problem for gyroscopic systems, *AIAA Journal*, 12 (1974) 1337–1342.

[35] A. Preumont, *Vibration Control of Active Structures, An Introduction*, second ed., Kluwer Academic Publishers, Dordrecht, 2002.

[36] N. M. Newmark, A method of computation for structural dynamics, *Journal of the Engineering Mechanics Division, ASCE*, 85 (1959) EM3 67–94.

[37] L. G. Maqueda, O. A. Bachau, A. A. Shabana, Effect of the centrifugal forces on the finite element eigenvalue solution of a rotating blade: a comparative study, *Multibody System Dynamics*, 19 (2008) 281–302.

[38] M. O. L. Hansen, *Aerodynamics of Wind Turbines*, London, 2000.

[39] K. Z. Østergaard, J. Stoustrup, P. Brath, Linear parameter varying control of wind turbines covering a both partial and full load conditions, *International Journal of Robust and Nonlinear Control*, 19 (2009) 92–116.

[40] R. P. Coleman, Theory of self-excited mechanical oscillations of hinged rotor blades, *National Advisory Committee for Aeronautics*, Advance Report 3G29, 1943.

[41] M. H. Hansen, Improved modal dynamics of wind turbines to avoid stall-induced vibrations, *Wind Energy*, 6 (2003) 179–195.

[42] M. H. Hansen, Aeroelastic stability analysis of wind turbines using an eigenvalue approach, *Wind Energy*, 7 (2004) 133–143.

[43] S. Krenk, *Private communication*, 2010.

[44] S. P. Timoshenko, J. N. Goodier, *Theory of Elasticity*, third ed., McGraw-Hill Kogakusha Ltd, Tokyo, 1970.

[45] A. A. Shabana, *Dynamics of Multibody Systems*, third ed., Cambridge University Press, Cambridge, 2005.

[46] S. Krenk, Frequency analysis of the tuned mass damper, *Journal of Appled Mechanics*, 72 (2005) 936–942.

[47] C. J. Goh, T. K. Caughey, On the stability problem caused by finite actuator dynamics in the collocated control of large space structures, *International Journal of Control*, 41 (1985) 787–802.

[48] S. Krenk, J. Høgsberg, Tuned mass absorbers on damped structures under random load, *Probabilistic Engineering Mechanics*, 23 (2008) 408–415.

[49] O. C. Zienkiewicz, R. L. Taylor, *The Finite Element Method. Vol. 1. Basic formulations and linear problems*, second ed., McGraw-Hill, London, 1971.

Appendix A

Matrices

This section provides the shape function matrices and the explicit forms of the area integrals associated with the inertial terms of the beam element formulation in Chapter 2.

A.1 Shape Functions

The shape function matrix $\mathbf{N}_x(x)$ is given as

$$\mathbf{N}_x(x) = \begin{bmatrix} N_1^a & 0 & 0 & 0 & 0 & 0 & N_1^b & 0 & 0 & 0 & 0 & 0 \\ 0 & N_q^a & 0 & 0 & 0 & N_r^a & 0 & N_q^b & 0 & 0 & 0 & -N_r^b \\ 0 & 0 & N_q^a & 0 & -N_r^a & 0 & 0 & 0 & N_q^b & 0 & N_r^b & 0 \\ 0 & 0 & 0 & N_1^a & 0 & 0 & 0 & 0 & 0 & N_1^b & 0 & 0 \\ 0 & 0 & 0 & 0 & N_1^a & 0 & 0 & 0 & 0 & 0 & N_1^b & 0 \\ 0 & 0 & 0 & 0 & 0 & N_1^a & 0 & 0 & 0 & 0 & 0 & N_1^b \end{bmatrix} \tag{A.1}$$

where the components are defined with respect to the coordinate s as

$$\begin{aligned} N_1^a(s) &= \tfrac{1}{2}(1-s), & N_1^b(s) &= \tfrac{1}{2}(1+s) \\ N_q^a(s) &= \tfrac{1}{4}(2+s)(s-1)^2, & N_q^b(s) &= -\tfrac{1}{4}(s-2)(1+s)^2 \\ N_r^a(s) &= \tfrac{1}{8}L(1+s)(s-1)^2, & N_r^b(s) &= -\tfrac{1}{8}L(s-1)(1+s)^2 \end{aligned} \tag{A.2}$$

The components of the derivative of the shape function matrix $\mathbf{N}_x'(x)$ are defined with respect to the coordinate s as

$$\begin{aligned} N_1^a(s)' &= -\tfrac{1}{2L}, & N_1^b(s)' &= \tfrac{1}{2L} \\ N_q^a(s)' &= \tfrac{3}{2L}(s-1)(1+s), & N_q^b(s)' &= -\tfrac{3}{2L}(s-1)(1+s) \\ N_r^a(s)' &= \tfrac{1}{4}(s-1)(1+3s), & N_r^b(s)' &= -\tfrac{1}{4}(1+s)(3s-1) \end{aligned} \tag{A.3}$$

The interpolation functions for nodal transverse displacement and bending rotation are shown in Fig. A.1 and the corresponding derivatives are shown in Fig. A.2.

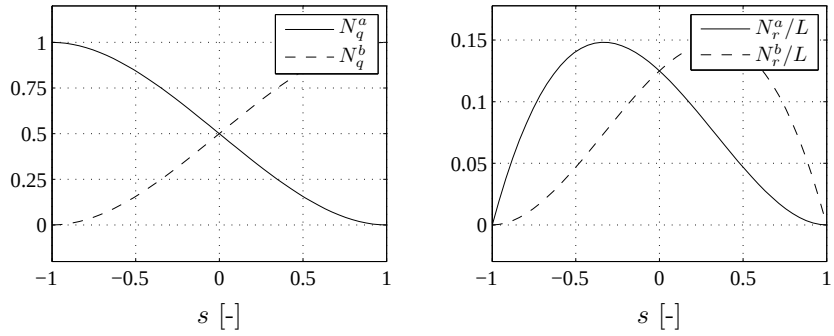

Figure A.1: Shape functions.

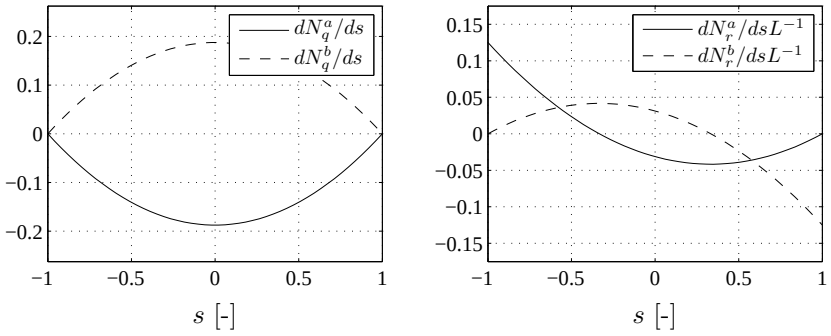

FIGURE A.2: Shape function derivatives.

A.2 Cross-section Inertia

The area integral associated with the uniform body acceleration matrix $\mathbf{M}_0$ is given as

$$\int_A \mathbf{N}_A \varrho dA = \begin{bmatrix} A^\varrho & 0 & 0 & 0 & S_z^\varrho & -S_y^\varrho \\ 0 & A^\varrho & 0 & -S_z^\varrho & 0 & 0 \\ 0 & 0 & A^\varrho & S_y^\varrho & 0 & 0 \end{bmatrix} \tag{A.4}$$

The area integral associated with the skew-symmetric gyroscopic matrix $\mathbf{G}$ is given as

$$\int_A \mathbf{N}_A^T \hat{\boldsymbol{\omega}} \mathbf{N}_A \varrho dA \; = \; \begin{bmatrix} 0 & -A^\varrho\omega_z & A^\varrho\omega_y & S_z^\varrho\omega_z + S_y^\varrho\omega_y & 0 & 0 \\ & 0 & -A^\varrho\omega_x & -S_y^\varrho\omega_x & S_z^\varrho\omega_x & -S_y^\varrho\omega_z \\ & & 0 & -S_z^\varrho\omega_x & -S_z^\varrho\omega_y & S_y^\varrho\omega_y \\ & & & 0 & -I_{zz}^\varrho\omega_z - I_{yz}^\varrho\omega_y & I_{yy}^\varrho\omega_y + I_{yz}^\varrho\omega_z \\ & \text{Skew-sym.} & & & 0 & 0 \\ & & & & & 0 \end{bmatrix} \tag{A.5}$$

The area integral associated with the centrifugal matrix $\mathbf{C}$ is given as

$$\int_A \mathbf{N}_A^T \hat{\boldsymbol{\omega}}^T \hat{\boldsymbol{\omega}} \mathbf{N}_A \varrho dA =$$

$$\begin{bmatrix} -S_y^\varrho\omega_x\omega_z & -A^\varrho\omega_x\omega_y & -A^\varrho\omega_x\omega_z \\ & -S_z^\varrho(\omega_x^2+\omega_z^2) + S_y^\varrho\omega_y\omega_z & -A^\varrho\omega_y\omega_z \\ & & A^\varrho(\omega_x^2+\omega_y^2) \\ & & \\ & \text{Sym.} & \\ & & \end{bmatrix}$$

$$\begin{bmatrix} A^\varrho(\omega_y^2+\omega_z^2) + S_z^\varrho\omega_x\omega_y & S_z^\varrho(\omega_y^2+\omega_z^2) & -S_y^\varrho(\omega_y^2+\omega_z^2) \\ -S_z^\varrho(\omega_x^2+\omega_z^2) + S_y^\varrho\omega_y\omega_z & -S_z\omega_x\omega_y & S_y^\varrho\omega_y\omega_x \\ S_y^\varrho(\omega_x^2+\omega_y^2) + S_z^\varrho\omega_y\omega_z & -S_z^\varrho\omega_x\omega_z & S_y^\varrho\omega_x\omega_z \\ I_{yy}^\varrho(\omega_x^2+\omega_y^2) + I_{zz}^\varrho(\omega_x^2+\omega_z^2) + 2I_{yz}\omega_y\omega_z & I_{zz}^\varrho\omega_x\omega_y - I_{yz}^\varrho\omega_x\omega_z & I_{yy}^\varrho\omega_x\omega_z - I_{yz}\omega_x\omega_y \\ & I_{zz}^\varrho(\omega_y^2+\omega_z^2) & -I_{yz}^\varrho(\omega_y^2+\omega_z^2) \\ & & I_{yy}^\varrho(\omega_y^2+\omega_z^2) \end{bmatrix}$$

(A.6)

The area integral associated with the centrifugal load vector $\mathbf{f}_C$ is given as

$$\int_A \mathbf{N}_A^T \hat{\boldsymbol{\omega}}^T \hat{\boldsymbol{\omega}} \mathbf{x} \varrho dA = \begin{bmatrix} xA^\varrho(\omega_z^2 + \omega_y^2) - S_y^\varrho \omega_y \omega_x - S_z^\varrho \omega_z \omega_x \\ S_y^\varrho(\omega_x^2 + \omega_z^2) - xA^\varrho \omega_x \omega_y - S_z^\varrho \omega_y \omega_z \\ S_z^\varrho(\omega_x^2 + \omega_y^2) - x\omega_x \omega_z - S_y^\varrho \omega_y \omega_z \\ (I_{zz}^\varrho - I_{yy}^\varrho)\omega_y \omega_z + I_{yz}^\varrho(\omega_y^2 - \omega_z^2) - xS_y^\varrho \omega_x \omega_z + I_{xz}^\varrho \omega_x \omega_y \\ xS_z^\varrho(\omega_y^2 + \omega_z^2) - I_{zz}^\varrho \omega_x \omega_z - I_{yz}^\varrho \omega_y \omega_x \\ -xS_y^\varrho(\omega_y^2 + \omega_z^2) + I_{yy}^\varrho \omega_x \omega_y + I_{yz}^\varrho \omega_x \omega_z \end{bmatrix} \tag{A.7}$$

The area integral associated with the angular acceleration load vector $\mathbf{f}_G$ is given as

$$\int_A \mathbf{N}_A^T \hat{\boldsymbol{\alpha}} \mathbf{x} \varrho dA = \begin{bmatrix} -S_y^\varrho \alpha_z + S_z^\varrho \alpha_y \\ xA^\varrho \alpha_z - S_z^\varrho \alpha_x \\ -xA^\varrho \alpha_y + S_y^\varrho \alpha_x \\ (I_{yy}^\varrho + I_{zz}^\varrho)\alpha_x - x(S_y^\varrho \alpha_y + S_z^\varrho \alpha_z) \\ I_{zz}^\varrho \alpha_y - I_{yz}^\varrho \alpha_z \\ I_{yy}^\varrho \alpha_z - I_{yz}^\varrho \alpha_y \end{bmatrix} \tag{A.8}$$

Appendix B

Alternative Beam Kinematics

A good intuitive understanding of beam kinematics can be obtained from a formulation based on cross-section displacements and rotations relative to the elastic center and the shear center. In this appendix the elastic cross-section flexibility matrix $\mathbf{C}$ and the geometric stress matrix $\mathbf{S}$ are defined on the basis of this formulation.

B.1 Kinematics with Shear and Elastic Center

The cross-section kinematics are now described in terms of the displacements $\hat{\mathbf{q}} = \left[\, \hat{q}_x,\ \hat{q}_y,\ \hat{q}_z \,\right]^T$ and the rotations $\hat{\mathbf{r}} = \left[\, \hat{r}_x,\ \hat{r}_y,\ \hat{r}_z \,\right]^T$ as shown in Fig. B.1a. The rotations $\hat{r}_y$ and $\hat{r}_z$ have axes through the y- and z-axis respectively, which pass through the elastic center C. The axis of torsional rotation $\hat{r}_x$ passes through the shear center A.

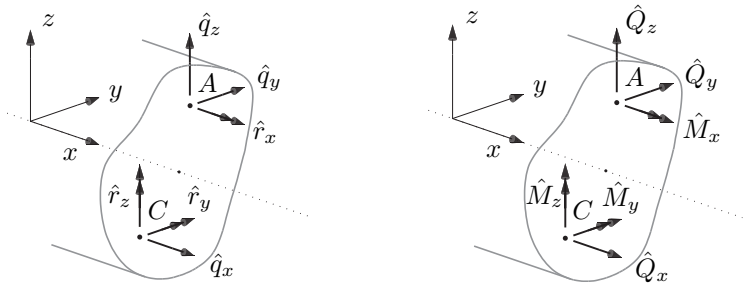

Figure B.1: a) Displacements $\hat{\mathbf{q}}$ and rotations $\hat{\mathbf{r}}$, b) Forces $\hat{\mathbf{Q}}$ and moments $\hat{\mathbf{M}}$.

The displacement field Δx can be written as

$$\Delta\mathbf{x} = \hat{\mathbf{N}}_A(y,z) \begin{bmatrix} \hat{\mathbf{q}} \\ \hat{\mathbf{r}} \end{bmatrix}, \quad \hat{\mathbf{N}}_A(y,z) = \begin{bmatrix} 1 & 0 & 0 & 0 & (z-c_z) & -(y-c_y) \\ 0 & 1 & 0 & -(z-a_z) & 0 & 0 \\ 0 & 0 & 1 & (y-a_y) & 0 & 0 \end{bmatrix} \tag{B.1}$$

with the shear center position vector $\mathbf{a} = [\, a_x,\, a_y,\, a_z \,]^T$ and the elastic center position vector $\mathbf{c} = [\, c_x,\, c_y,\, c_z \,]^T$. The displacements $\hat{\mathbf{q}}$ and rotations $\hat{\mathbf{r}}$ are related to the displacements $\mathbf{q}$ and rotations $\mathbf{r}$ at the element reference axis x by the transformation

$$\begin{bmatrix} \hat{\mathbf{q}} \\ \hat{\mathbf{r}} \end{bmatrix} = \hat{\mathbf{T}} \begin{bmatrix} \mathbf{q} \\ \mathbf{r} \end{bmatrix}, \quad \hat{\mathbf{T}} = \begin{bmatrix} 1 & 0 & 0 & 0 & c_z & -c_y \\ 0 & 1 & 0 & -a_z & 0 & 0 \\ 0 & 0 & 1 & a_y & 0 & 0 \\ 0 & 0 & 0 & 1 & 0 & 0 \\ 0 & 0 & 0 & 0 & 1 & 0 \\ 0 & 0 & 0 & 0 & 0 & 1 \end{bmatrix} \tag{B.2}$$

This allows the displacement field Δx to be written in terms of the element displacements $\mathbf{q}$ and rotations $\mathbf{r}$

$$\Delta\mathbf{x} = \mathbf{N}_A(y,z) \begin{bmatrix} \mathbf{q} \\ \mathbf{r} \end{bmatrix} \tag{B.3}$$

where the interpolation matrix $\mathbf{N}_A(y,z)$ is defined as

$$\mathbf{N}_A(y,z) = \hat{\mathbf{N}}_A(y,z)\hat{\mathbf{T}} \tag{B.4}$$

B.2 Elastic Stiffness

The forces $\hat{\mathbf{Q}} = [\,\hat{Q}_x,\,\hat{Q}_y,\,\hat{Q}_z\,]^T$ and moments $\hat{\mathbf{M}} = [\,\hat{M}_x,\,\hat{M}_y,\,\hat{M}_z\,]^T$ as shown in Fig. B.1 are energetically conjugate with the displacements $\hat{\mathbf{q}}$ and rotations $\hat{\mathbf{r}}$. The forces are defined as $\hat{\mathbf{Q}} = \mathbf{Q}$ as given in (2.25). The moment $\hat{\mathbf{M}}$ are defined as

$$\hat{M}_x = \int_A \left[\,\sigma_{xz}(y-a_y) - \sigma_{xy}(z-a_z)\,\right] dA \tag{B.5}$$

$$M_y = \int_A \sigma_{xx}(z-c_z)\,dA, \quad M_z = -\int_A \sigma_{xx}(y-a_z)\,dA \tag{B.6}$$

The cross-section strains $\hat{\boldsymbol{\gamma}} = \hat{\mathbf{q}}'$ and curvatures $\hat{\boldsymbol{\kappa}} = \hat{\mathbf{r}}'$ relate to their conjugate forces $\hat{\mathbf{Q}}$ and moments $\hat{\mathbf{M}}$ via the stiffness relation

$$\begin{bmatrix}\hat{\mathbf{Q}}\\ \hat{\mathbf{M}}\end{bmatrix} = \hat{\mathbf{D}}\begin{bmatrix}\hat{\boldsymbol{\gamma}}\\ \hat{\boldsymbol{\kappa}}\end{bmatrix} \tag{B.7}$$

where the associated cross-section flexibility matrix $\hat{\mathbf{D}}$ is given as

$$\hat{\mathbf{D}} = \begin{bmatrix} A^E & 0 & 0 & 0 & 0 & 0 \\ & \hat{A}^G_{yy} & A^G_{yz} & 0 & 0 & 0 \\ & & A^G_{zz} & 0 & 0 & 0 \\ & & & K^G & 0 & 0 \\ & \text{Sym.} & & & \hat{I}^E_{yy} & \hat{I}^E_{yz} \\ & & & & & \hat{I}^E_{zz} \end{bmatrix} \tag{B.8}$$

and the axial stiffness terms are given as

$$\hat{\mathbf{J}}_E = \begin{bmatrix} A^E & 0 & 0 \\ & \hat{I}^{\varrho}_{yy} & \hat{I}^E_{yz} \\ & & \hat{I}^E_{zz} \end{bmatrix} = \int_A \begin{bmatrix} 1 & 0 & 0 \\ & (y-c_y)(y-c_y) & (y-c_y)(z-c_z) \\ & & (z-c_z)(z-c_z) \end{bmatrix} E\,dA \tag{B.9}$$

Introducing the cross-section flexibility matrix $\hat{\mathbf{C}} = \hat{\mathbf{D}}^{-1}$, the complementary potential strain energy of the beam element can written as

$$U_e = \tfrac{1}{2}\int_L \left[\,\hat{\mathbf{Q}}^T,\ \hat{\mathbf{M}}^T\,\right]\hat{\mathbf{C}}\begin{bmatrix}\hat{\mathbf{Q}}\\ \hat{\mathbf{M}}\end{bmatrix} dx = \tfrac{1}{2}\int_L \left[\,\mathbf{Q}^T,\ \mathbf{M}^T\,\right]\mathbf{C}\begin{bmatrix}\mathbf{Q}\\ \mathbf{M}\end{bmatrix} dx \tag{B.10}$$

where the cross-section flexibility matrix is given as

$$\mathbf{C} = \left[\,(\hat{\mathbf{T}}^T)^{-1}\,\right]^T \hat{\mathbf{C}}\,\left[\,(\hat{\mathbf{T}}^T)^{-1}\,\right] \tag{B.11}$$

This expression establishes the cross-section flexibility matrix on the basis of the formulation of beam kinematics, which involves the positions of the shear center and the elastic center.

B.3 Geometric Stiffness

The potential energy associated with an initial stress distribution is given as [22],

$$\begin{aligned} U_g = \int_L \Big(\int_A \tfrac{1}{2}\sigma^0_{xx} \Big[\hat{q}'_y\hat{q}'_y + \hat{q}'_z\hat{q}'_z + \hat{r}'_x\hat{r}'_x\hat{S}^0 - \hat{q}'_y\hat{r}'_x(z-a_z) + \hat{q}'_z\hat{r}'_x(y-a_y) \Big] \, dA \\ + \hat{r}_x \int_A \Big[\sigma^0_{xy}\big(\hat{q}'_z + (y-a_y)\hat{r}'_x\big) - \sigma^0_{xz}\big(\hat{q}'_y - (z-a_z)\hat{r}'_x\big) \Big] \, dA \Big) \, dx \end{aligned} \tag{B.12}$$

By evaluation of the area integrals, the potential energy can be written in terms of cross-section forces and moments,

$$\begin{aligned} U_g = \int_L \Big(\tfrac{1}{2}\hat{q}'_y\hat{q}'_y\hat{Q}^0_x + \tfrac{1}{2}\hat{q}'_z\hat{q}'_z\hat{Q}^0_x + \hat{S}^0\hat{r}'_x\hat{r}'_x + \hat{Q}^0_y\hat{q}'_z r_x - \hat{Q}^0_z\hat{q}'_y r_x \\ + \hat{q}'_y\hat{r}'_x\big[-\hat{M}^0_y + \hat{Q}^0_x(a_z - c_z)\big] + \hat{q}'_z\hat{r}'_x\big[-\hat{M}^0_z - \hat{Q}^0_x(a_y - c_y)\big] \Big) \, dx \end{aligned} \tag{B.13}$$

The expression can be written in compact form as

$$U_g = \tfrac{1}{2}\int_L \big[\, \hat{\mathbf{q}}^T,\ \hat{\mathbf{r}}^T,\ \hat{\mathbf{q}}'^T,\ \hat{\mathbf{r}}'^T \,\big]\, \hat{\mathbf{S}} \begin{bmatrix} \hat{\mathbf{q}} \\ \hat{\mathbf{r}} \\ \hat{\mathbf{q}}' \\ \hat{\mathbf{r}}' \end{bmatrix} dx \tag{B.14}$$

where the stress matrix $\hat{\mathbf{S}}$ is defined as

$$\hat{\mathbf{S}} = \begin{bmatrix} 0 & 0 & 0 & 0 & 0 & 0 & 0 & 0 & 0 & 0 & 0 & 0 \\ & 0 & 0 & 0 & 0 & 0 & 0 & 0 & 0 & 0 & 0 & 0 \\ & & 0 & 0 & 0 & 0 & 0 & 0 & 0 & 0 & 0 & 0 \\ & & & 0 & 0 & 0 & 0 & -\hat{Q}^0_z & \hat{Q}^0_y & 0 & 0 & 0 \\ & & & & 0 & 0 & 0 & 0 & 0 & 0 & 0 & 0 \\ & & & & & 0 & 0 & 0 & 0 & 0 & 0 & 0 \\ & & & & & & 0 & 0 & 0 & 0 & 0 & 0 \\ & & & & & & & \hat{Q}^0_x & 0 & -\hat{M}^0_y + (a_z - c_z)\hat{Q}^0_x & 0 & 0 \\ & & & & & & & & \hat{Q}^0_x & -\hat{M}^0_z - (a_y - c_y)\hat{Q}^0_x & 0 & 0 \\ & & & \text{Sym.} & & & & & & \hat{S}^0 & 0 & 0 \\ & & & & & & & & & & 0 & 0 \\ & & & & & & & & & & & 0 \end{bmatrix} \tag{B.15}$$

The parameter $\hat{S}^0$, related to torsional instability, takes the form

$$\hat{S}^0 = \int_A \big[\, (y-a_y)^2 + (z-a_z)^2 \,\big]\sigma^0_{xx}\, dA \tag{B.16}$$

For prismatic beams the following relation is exact,

$$\begin{bmatrix} \hat{\mathbf{q}} \\ \hat{\mathbf{r}} \\ \hat{\mathbf{q}}' \\ \hat{\mathbf{r}}' \end{bmatrix} = \begin{bmatrix} \hat{\mathbf{T}} & \mathbf{0} \\ \mathbf{0} & \hat{\mathbf{T}} \end{bmatrix} \begin{bmatrix} \mathbf{q} \\ \mathbf{r} \\ \mathbf{q}' \\ \mathbf{r}' \end{bmatrix} \tag{B.17}$$

By substituting (B.17) into (B.14) and employing the shape function interpolation (2.41), the following form of the potential energy is obtained,

$$U_g = \tfrac{1}{2}\mathbf{u}^T\mathbf{K}_g\mathbf{u} \tag{B.18}$$

where the geometric stiffness matrix $\mathbf{K}_g$ is defined as

$$\mathbf{K}_g = \int_L \left[\mathbf{N}_x^T, \mathbf{N}_x'^T \right] \mathbf{S} \begin{bmatrix} \mathbf{N}_x \\ \mathbf{N}_x' \end{bmatrix} dx \tag{B.19}$$

and the stress matrix $\mathbf{S}$ is written as

$$\mathbf{S} = \begin{bmatrix} \hat{\mathbf{T}}^T & \mathbf{0} \\ \mathbf{0} & \hat{\mathbf{T}}^T \end{bmatrix} \hat{\mathbf{S}} \begin{bmatrix} \hat{\mathbf{T}} & \mathbf{0} \\ \mathbf{0} & \hat{\mathbf{T}} \end{bmatrix} \tag{B.20}$$

This expression establishes the geometric stiffness matrix on the basis of the formulation of beam kinematics, which involves the positions of the shear center and the elastic center.

Appendix C

Collocated Sensor/Actuator Connectivity

The present section describes how the physical blade connectivity vectors $\mathbf{w}_k$ can be defined for collocated sensor/actuator pairs. The cross-section attachment point K of a sensor/actuator mechanism has coordinates $\tilde{\mathbf{k}} = [\,\tilde{k}_x,\, \tilde{k}_y,\, \tilde{k}_z\,]^T$ which are given with respect to the local blade coordinate system, see Fig. C.1. The orientation of imposed actuator forces is defined by the vector $\tilde{\mathbf{e}}_q = [\,\tilde{e}_q^x,\, \tilde{e}_q^y,\, \tilde{e}_q^z\,]^T$ and the orientation of imposed moments is defined by the vector $\tilde{\mathbf{e}}_r = [\,\tilde{e}_r^x,\, \tilde{e}_r^y,\, \tilde{e}_r^z\,]^T$. The example in Fig. C.1 shows the orientation vectors of an actuator capable of imposing and axial force and a twisting moment in K. The collocated format implies that the associated sensors are capable of measuring axial displacement and torsional rotation in K.

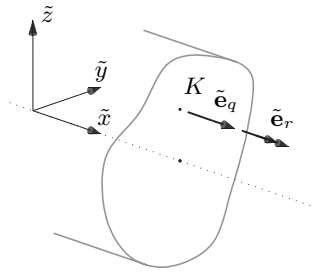

Figure C.1: Sensor/actuator attachment point K and orientation vectors $\tilde{\mathbf{e}}_q$ and $\tilde{\mathbf{e}}_r$.

The present control system relies on a single, scalar feedback q from each blade sensor system, defined as

$$q = \left[\, \tilde{\mathbf{e}}_q^T,\, \tilde{\mathbf{e}}_r^T \,\right] \begin{bmatrix} \tilde{\mathbf{q}}_K \\ \tilde{\mathbf{r}}_K \end{bmatrix} \tag{C.1}$$

which involves the displacements $\tilde{\mathbf{q}}_K$ and rotations in $\tilde{\mathbf{r}}_K$ in K. The displacements and rotations in K are energetically conjugate to the forces $\tilde{\mathbf{Q}}_K$ and moments $\tilde{\mathbf{M}}_K$ in K. Thus, these quantities relate to the corresponding nodal values via the same linear transformation,

$$\begin{bmatrix} \tilde{\mathbf{q}}_K \\ \tilde{\mathbf{r}}_K \end{bmatrix} = \mathbf{T}_K^T \begin{bmatrix} \tilde{\mathbf{q}} \\ \tilde{\mathbf{r}} \end{bmatrix}, \quad \begin{bmatrix} \tilde{\mathbf{Q}} \\ \tilde{\mathbf{M}} \end{bmatrix} = \mathbf{T}_K \begin{bmatrix} \tilde{\mathbf{Q}}_K \\ \tilde{\mathbf{M}}_K \end{bmatrix} \tag{C.2}$$

where the transformation matrix $\mathbf{T}_K$ is given as

$$\mathbf{T}_F = \begin{bmatrix} 1 & 0 & 0 & 0 & 0 & 0 \\ 0 & 1 & 0 & 0 & 0 & 0 \\ 0 & 0 & 1 & 0 & 0 & 0 \\ 0 & -\tilde{k}_z & \tilde{k}_y & 1 & 0 & 0 \\ \tilde{k}_z & 0 & 0 & 0 & 1 & 0 \\ -\tilde{k}_y & 0 & 0 & 0 & 0 & 1 \end{bmatrix} \tag{C.3}$$

Active struts inserted as shown in Fig. 1.3 would be attached by the ends at two separate cross-section in the points K_a and K_b where the indices designate the associated element

nodes. One displacement or acceleration sensor would be attached at each end of the strut, measuring the structural response in the axial direction of the strut. If the active strut is positioned in alignment with the local blade reference axis $\tilde{x}$, the associated orientation vectors are

$$\tilde{\mathbf{e}}_q^a = [\,1,\,0,\,0\,]^T, \quad \tilde{\mathbf{e}}_r^a = \mathbf{0}, \quad \tilde{\mathbf{e}}_q^b = [\,-1,\,0,\,0\,]^T, \quad \tilde{\mathbf{e}}_r^b = \mathbf{0} \tag{C.4}$$

The scalar blade feedback signal q is then defined as

$$q = q_a - q_b \tag{C.5}$$

which represents a state of combined bending and axial deformation if the sensor/actuator is positioned with a finite distance to the elastic center. By substituting the first equation of (C.2) into (C.1) and establishing the signal (C.5) the physical blade connectivity vectors with respect to the local blade coordinate system $\tilde{\mathbf{w}}_k$ take the form

$$\tilde{\mathbf{w}}_k = \begin{bmatrix} \ddots & & & & \\ & \mathbf{T}_K^a & & & \\ & & \ddots & & \\ & & & \mathbf{T}_K^b & \\ & & & & \ddots \end{bmatrix} \begin{bmatrix} \vdots \\ \tilde{\mathbf{e}}_q^a \\ \tilde{\mathbf{e}}_r^a \\ \vdots \\ \tilde{\mathbf{e}}_q^b \\ \tilde{\mathbf{e}}_r^b \\ \vdots \end{bmatrix} \tag{C.6}$$

where the transformation matrices are included as diagonal blocks in a null-matrix in positions corresponding to the attachment nodes, and the orientation vectors are located similarly in a null-vector. The physical blade connectivity vector with respect to the rotor coordinate system $\mathbf{w}_k$ is then obtained by rotation according to (3.7) and expansion to match the size of the rotor equation system.

Appendix D

Algorithms

The coupled model consisting of structure and controller is implemented in the commercial programming environment MATLAB®, version R2010a. In this appendix all implemented functions are printed and selected details are described. From the presented set of scripts and functions all presented simulation results can be reproduced, given the data of the 42 m wind turbine blade. The functions of the program are organized in four groups,

1. Primary model functions
2. Secondary model functions
3. Model analysis and controller calibration functions
4. Assembly functions

The first three groups relate to the theoretical expressions of the present thesis, and the general vector format is used directly in the implementation. The last group of functions handles model assembly. The functions can be found on the enclosed CD-ROM.

D.1 Element Integration

In Table D.1 the primary model functions are listed. The function `kc3ebeamflex.m` performs the numerical integration of the apparent inertial matrices $\mathbf{C}$, $\mathbf{G}$, $\dot{\mathbf{G}}$ and vectors $\mathbf{f}_C$, $\mathbf{f}_G$ for a given element. Selected details of this function are given in the following. The primary input to the function is the local angular velocity $\boldsymbol{\omega}$ and angular acceleration $\boldsymbol{\alpha}$, blade cross-section data via the variable `blade_data` and the nodal coordinates of the element `Xe` in the local blade coordinate system. The element nodes are placed at existing data points of the blade, see the main assembly and simulation file `rotor_control_16.m`. In line 27-34 of `kc3ebeamflex.m` the local coordinates of the data points within the element are determined.

Table D.1: Primary model functions.

File	Description
`kc3ebeamflex.m`	Inertial element matrices, $\mathbf{C}$, $\mathbf{G}$, $\dot{\mathbf{G}}$, $\mathbf{f}_C$, $\mathbf{f}_G$
`CaKafa3ebeamflex_02.m`	Aerodynamic element matrices, $\mathbf{K}_a$, $\mathbf{D}_a$, $\mathbf{f}_a$
`kg3ebeamflex.m`	Geometric element stiffness matrix, $\mathbf{K}_g$
`m3ebeamflex.m`	Element mass matrix, $\mathbf{M}$
`k3ebeamflex.m`	Element stiffness matrix, $\mathbf{K}_e$
`fr3beamflex.m`	Element reactions, $[\,\mathbf{Q}_a^T,\, \mathbf{M}_a^T,\, \mathbf{Q}_b^T,\, \mathbf{M}_b^T\,]^T$
`shaft.m`	Shaft element matrices, $\mathbf{K}_s$, $\mathbf{M}_s$

Within each interval between element data points, the integration points according to he chosen Lobatto quadrature rule s_m are then determined with associated weights w_m, see line 47-49. The subroutine `intval_Lobatto.m` is called for this purpose, and this routine belongs

to the group of secondary model files, see Table D.2. In line 52-80 of `kc3ebeamflex.m` cross-section inertial parameters $\mathbf{J}_\varrho$ are interpolated linearly between data points and evaluated at all integration coordinates. The cross-section inertial matrices (A.5)-(A.8) are then explicitly evaluated in all integration points, see line 83-174. Shape functions $\mathbf{N}$, evaluated in all integration points, are obtained via the secondary model function `shapefunctions.m`. The function returns matrices corresponding to the definition (A.1). The element integrals (2.18)-(2.22) are performed numerically according to (2.83)-(2.84) and the implementation in line 178-189 is seen to match exactly the theoretical format.

TABLE D.2: Secondary model functions.

File	Description
`Rmat.m`	Rotation matrix, $\mathbf{R}$
`intval_Lobatto.m`	Lobatto quadrature points and weights, s_m, w_m
`shapefunctions.m`	Shape functions, $\mathbf{N}$
`shapefunctions_d.m`	Shape function derivatives, $\mathbf{N}'$
`Cmat.m`	Cross-section flexibility in data points, $\mathbf{C}_s$
`WindInterpol.m`	3D interpolation of wind velocities in data points, $\mathbf{U}$

D.2 Rotor Assembly and Simulation

The three-bladed rotor is assembled in the main file `rotor_control_18.m`, see Table D.3. Also, the equations of motion (3.9) are simulated according to the procedure listed in Table 3.2. In the following, selected details of this script are given. The main file handles five general tasks:

1. Assembly of the stationary structural rotor equations of motion
2. Controller calibration
3. Assembly of the closed-loop equations of motion
4. Time integration of the closed-loop equations of motion

Assembly of the stationary structural terms (3.9) is performed in line 1-295. Initially the structural blade data is loaded and the distribution of element nodes over the data points is established, line 13-55. The orientation of the local blade axes in the rotor coordinate system is defined in line 57-69, including blade pitch, coning and azimuth angles (3.1). Rotation matrices are subsequently defined in line 71-95 according to (3.3) and (3.7), and the local blade angular velocities $\boldsymbol{\omega}_j$ are computed in line 97-110 according to (3.4).

Evaluation of aerodynamic matrices and vectors is performed in line 112-157. Relative wind speeds in the rotor coordinate system due to rotation are determined in all data points in line 129-131 and wind speeds relative to the local blade coordinate systems are computed by transformation in line 134. Transformation of local blade matrices and force vectors is performed in line 150-157 according to (3.8).

Initial assembly of structural terms is performed in line 159-214, followed by iterations on the geometric stiffness matrix $\mathbf{K}_g$ in line 217-283. The function `rotor_assem.m` used in line 224-228 to assemble full rotor matrices from blade matrices defined with reference to the rotor coordinate system. In line 238 the static equations of motion (3.9) are solved and the three blade responses are extracted individually in line 242 by the function `bladedofs.m`. The local blade responses are computed by pre-multiplication with the rotation matrix $\underline{\mathbf{R}}_k$

defined in (3.7). Local nodal section forces and moments are computed in line 255-261 via the function `fr3beamflex.m` which employs equation 2.80 on local element level. It is noted that for this purpose, local element matrices e.g. element mass matrices in the variable `Me1`, are continuously kept available in the system memory. With local nodal element section forces and moments available, the geometric stiffness matrices are evaluated in line 263-269. When the geometric stiffness is sufficiently accurate, all terms of the equations of motion (3.7) for the stationary case are available and a modal analysis can be performed, line 296. The function `evp_02.m` solves the state-space eigenvalue problem (2.88), sorts the solution and extracts all eigenfrequencies ω_j, damping ratios ζ_j and associated structural eigenvectors $\mathbf{u}_j$, omitting the complex conjugate solutions.

As the modal properties of the stationary rotor have been determined, controller application and calibration can be performed. This is implemented in line 302-394. The identical local positions of the three sensor/actuator pairs are defined in line 303-308. Nodal attachment points, the distance from the blade reference axis `Rf` and the angular position measured from the local y-axis `aa` defines the spatial coordinates of attachment points. The vector `e` is the orientation of local measurement, according to (C.4). In line 318-321 the physical connectivity vectors $\mathbf{w}_k$ are obtained via the function `convec.m` and the filtered connectivity matrices $\mathbf{w}_c$ and $\mathbf{W}$ are evaluated in line 310-316. The controller tuning is performed in line 325-394. Optimal parameters for the collective controller are obtained from the function `colcal_02.m` and optimal parameters for the whirling mode controller are obtained from the function `whirlcal_02.m`. The equations of motion for the closed-loop system are assembled in line 397-415. Time simulation of the equations of motion according to Table 3.2 is performed in line 424-780.

TABLE D.3: Controller calibration and model analysis functions.

File	Description
`rotor_control_18.m`	Assembly and simulation
`convec.m`	Sensor/actuator connectivity vectors, $\mathbf{w}_k$
`colcal_02.m`	Collective mode controller
`whirlcal_02.m`	Whirling mode controller
`evp_02.m`	Solve eigenvalue problem

TABLE D.4: Assembly functions.

File	Description
`c3beamflex_02.m`	Assembly of aerodynamic terms
`assmk.m`	Element matrix assembly
`insetup.m`	Assembly of inertial terms
`fesetup_01.m`	Assembly of blade mass and elastic stiffness matrices
`m3beamflex.m`	Assembly of blade mass matrix
`k3beamflex_01.m`	Assembly of blade elastic stiffness matrix
`rotor_assem.m`	Assembly of rotor from blade and shaft matrices
`bladedofs.m`	Extraction of blade-wise rotor d.-o.-f.'s
`kg3beamflex_01.m`	Assembly of blade geometric stiffness matrix

P1

(Journal paper)

Resonant vibration control of rotating beams

Journal of Sound and Vibration
(doi:10.1016/j.jsv.2010.11.008)

Journal of Sound and Vibration 330 (2011) 1877–1890

Contents lists available at ScienceDirect

Journal of Sound and Vibration

journal homepage: www.elsevier.com/locate/jsvi

Resonant vibration control of rotating beams

Martin Nymann Svendsen *, Steen Krenk, Jan Høgsberg

Department of Mechanical Engineering, Technical University of Denmark, DK-2800 Lyngby, Denmark

ARTICLE INFO

Article history:
Received 3 March 2010
Received in revised form
29 October 2010
Accepted 9 November 2010
Handling Editor: D.J. Wagg
Available online 4 December 2010

ABSTRACT

Rotating structures, like e.g. wind turbine blades, may be prone to vibrations associated with particular modes of vibration. It is demonstrated, how this type of vibrations can be reduced by using a collocated sensor–actuator system, governed by a resonant controller. The theory is here demonstrated by an active strut, connecting two cross-sections of a rotating beam. The structure is modeled by beam elements in a rotating frame of reference following the beam. The geometric stiffness is derived in a compact form from an initial stress formulation in terms of section forces and moments. The stiffness, and thereby the natural frequencies, of the beam depend on the rotation speed and the controller is tuned to current rotation speed to match the resonance frequency of the selected mode. It is demonstrated that resonant control leads to introduction of the intended level of damping in the selected mode and, with good modal connectivity, only very limited modal spill-over is generated. The controller acts by resonance and therefore has only a moderate energy consumption, and successfully reduces modal vibrations at the resonance frequency.

1. Introduction

Vibrations in rotating structures is a naturally occurring phenomenon in for example wind turbine and helicopter rotors, turbo machinery and rotating space structures. These vibrations are often dominated by a single or a few lightly damped modes, and these vibrations typically require additional damping, introduced e.g. by passive or active damping devices. The present paper deals with the introduction of additional damping into these vibration modes for rotating beams, using an active resonant control strategy, which targets a specific mode by inherent resonant behavior close to the eigenfrequency of the particular mode.

The 'independent modal space control' formulation by Meirovitch [1] was one of the early works addressing vibrations in flexible structures via their modal energy distribution. A theoretical form was given for an actuator force distribution for adding damping to one or more specific modes, without changing the characteristics of the other modes. Balas [2] gave the modal approach a more practical form by developing a feedback controller with a finite number of discrete sensors and actuators. This work also introduced the use of modal state observers and tuning of modal actuator gains according to the theory of optimal linear quadratic control. Furthermore, the issues of modal observability and controllability, and the associated notion of spill-over and instability effects, were addressed. In practice, sensor and actuator systems may have non-ideal dynamic properties, leading to possible system instabilities. This was investigated by Goh and Caughey [3] for collocated control systems with second-order actuator dynamics. For instance, a piezoelectric sensor/actuator pair with high-frequency dynamics was applied for modal vibration control by Baz and Poh [4], using a modified version of the independent modal space control theory, where the structural properties of the piezoelectric material were taken into account. Recent investigations on vibration control of rotating beams have primarily focused on the use of novel smart materials, implementing well established control algorithms, such as direct velocity feedback [5] or optimal linear quadratic control based on either modal states [6] or physical system states [7].

* Corresponding author. Tel.: +45 4525 1377.
E-mail address: mns@mek.dtu.dk (M.N. Svendsen).

0022-460X/$ - see front matter © 2010 Elsevier Ltd. All rights reserved.
doi:10.1016/j.jsv.2010.11.008

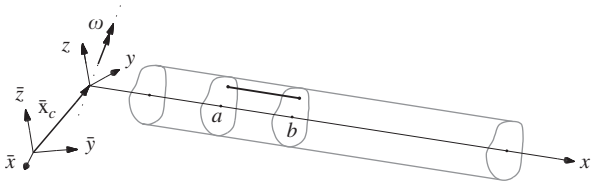

Fig. 1. Inertial and local frames for a flexible beam with an active strut controller.

The present work develops the resonant control principle of Krenk and Høgsberg [8,9] in the context of rotating structures. The resonant control is based on collocated sensor–actuator pairs, governed by a controller which implements a resonance tuned to the natural frequency of the mode(s) in question. In the case of rotating structures the actuator typically acts 'internally' e.g. in the form of an active strut, connecting two cross-sections of a beam, see e.g. Preumont et al. [10]. When attached between two cross-sections, as illustrated in Fig. 1, local bending moments can be applied to extract energy from transverse vibrations. The introduction of the resonant device leads to a split of the original mode into two modes with closely spaced frequencies, and it has been demonstrated that optimal damping properties are obtained when these two modes have identical damping ratio [8,9]. The theoretical basis of resonant control is developed for an idealized single-degree-of-freedom model structure. In flexible structures, like the present application to beams, the sensor will record additional motion from other modes. This additional motion is non-resonant, and can be compensated for in the calibration of the resonant controller via a quasi-static correction of the parameter expressions for single-degree-of-freedom systems.

The present work introduces a three-dimensional, two-node finite element model for rotating beams with general cross-section properties. The beam element is described in a local rotating frame of reference, fixed to the element reference axis as illustrated in Fig. 1. Displacements and rotations are assumed to be small, and beam kinematics is described by the motion of the cross-section planes via three translation components and three rotation components. The stiffness matrices are derived from complementary energy [11]. A central point is the inclusion of geometric stiffness, i.e. the apparent stiffness introduced by the stress state in the structure. In the present formulation the geometric stiffness is derived by rewriting the linearized theory of initial stresses [12] in integrated form in terms of section forces and moments [13]. The structural equations of motion are established from Lagrange's equations defined in terms of nodal system states, and the kinetic energy is described in terms of absolute velocities in the local reference frame. This allows a consistent energy-based derivation of the dynamic equations of motion, including centrifugal and gyroscopic forces, angular acceleration terms and inertial reaction forces.

The paper is organized as follows. In Section 2 the beam kinematics are defined and the kinetic energy is established. A linearized form of the potential strain energy and the potential energy associated with initial stresses is developed in Section 3, and structural equations of motion are derived from Lagrange's equations in Section 4. In Section 5 the resonant controller with acceleration feedback is defined and the explicit tuning procedure is presented. The performance of the resonant controller is demonstrated in Section 6 via a numerical example, where to controllers are fitted in a modern large scale wind turbine blade and tuned to address the first and second vibration modes, respectively.

2. Beam kinematics and inertial effects

In order to obtain a consistent representation of the inertial properties of a body, a suitable kinematic representation must be established. In the following a convenient description of beam kinematics is presented. The format is employed in a derivation of the kinetic energy, from where the characteristic inertial terms are extracted. The derivation follows Kawamoto et al. [14], where a formulation for isoparametric elements is established. In the present case nodal rotations are a fundamental part of the kinematic description, necessitating extension of the formulation in [14] to Hermitian shape functions.

2.1. Beam element representation

In Fig. 1 the flexible beam is shown in the inertial frame of reference $\{\bar{x},\bar{y},\bar{z}\}$ and the local frame of reference $\{x, y, z\}$. The beam is initially straight and has the local x-axis as longitudinal reference axis. The coordinates of a point in the undeformed beam are represented in the local frame by the position vector $\mathbf{x}=[x, y, z]^{\mathrm{T}}$. The displacement of the point $\mathbf{x}$ due to beam deformation is denoted $\Delta\mathbf{x}=[\Delta x,\Delta y,\Delta z]^{\mathrm{T}}$, and the total position of a point in the deformed state is

$$\mathbf{x}_t=\mathbf{x}+\Delta\mathbf{x} \tag{1}$$

Cross-sections of the deformed beam are defined as planar thin slices of the beam, orthogonal to the reference axis x. Cross-sections are assumed to remain planar under beam deformation. The displacement field $\Delta\mathbf{x}$ of a cross-section intersecting the reference axis at the point $[x, 0, 0]^{\mathrm{T}}$ is represented via the linearized interpolation (2) over the undeformed cross-section,

$$\Delta\mathbf{x}=\mathbf{N}_A(y,z)\begin{bmatrix}\mathbf{q}(x)\\ \mathbf{r}(x)\end{bmatrix},\quad \mathbf{N}_A(y,z)=\begin{bmatrix}1&0&0&0&z&-y\\0&1&0&-z&0&0\\0&0&1&y&0&0\end{bmatrix} \tag{2}$$

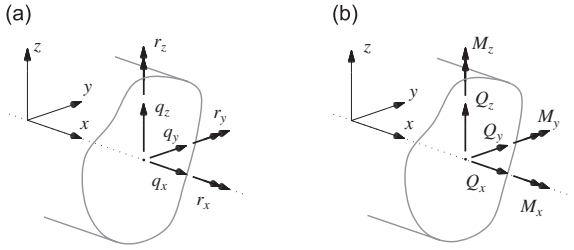

Fig. 2. (a) Displacements **q** and rotations **r** and (b) Forces **Q** and moments **M**.

where $\mathbf{q}=[q_x, q_y, q_z]^{\mathrm{T}}$ are displacements and $\mathbf{r}=[r_x, r_y, r_z]^{\mathrm{T}}$ are rotations with respect to the reference axes in the local frame, as indicated in Fig. 2a. The linearized format of the area interpolation matrix $\mathbf{N}_A$ assumes small cross-section rotations **r**.

In order to obtain a discrete finite element formulation, cross-section displacements and rotations along the element reference axis are interpolated by nodal displacements and rotations $\mathbf{u}^{\mathrm{T}}=[\mathbf{q}_a^{\mathrm{T}}, \mathbf{r}_a^{\mathrm{T}}, \mathbf{q}_b^{\mathrm{T}}, \mathbf{r}_b^{\mathrm{T}}]$ and the longitudinal interpolation functions $\mathbf{N}_x(x)$,

$$\begin{bmatrix}\mathbf{q}(x)\\ \mathbf{r}(x)\end{bmatrix}=\mathbf{N}_x(x)\mathbf{u} \tag{3}$$

The subscripts *a* and *b* indicate the two element nodes. The deformed position field $\mathbf{x}_t$ may then be written as

$$\mathbf{x}_t=\mathbf{x}+\mathbf{N}_A(y,z)\mathbf{N}_x(x)\mathbf{u} \tag{4}$$

whereby the interpolation of the deformation field $\Delta\mathbf{x}$ is separated into a local cross-section area interpolation $\mathbf{N}_A(y,z)$ and a length-wise interpolation $\mathbf{N}_x(x)$.

2.2. Kinetic energy

The kinetic energy associated with rigid-body motion and motion due to deformation of the beam is given by the volume integral

$$T=\frac{1}{2}\int_V \mathbf{v}_t^{\mathrm{T}}\mathbf{v}_t\varrho\ \mathrm{d}V \tag{5}$$

where $\mathbf{v}_t$ is the absolute velocity of a point in the local frame of reference and $\varrho=\varrho(x,y,z)$ is the mass density. The center of the local frame of reference is located in $\overline{\mathbf{x}}_c$. The orientation is determined by the rotation matrix **R**, corresponding to the finite rotation $\boldsymbol{\theta}=[\theta_x,\theta_y,\theta_z]^{\mathrm{T}}$ about an arbitrary axis, Argyris [15]. In the present case the axis of rotation is assumed to intersect the center of the local reference frame. The deformed position with respect to the inertial frame $\overline{\mathbf{x}}_t$ can then be written as

$$\overline{\mathbf{x}}_t=\overline{\mathbf{x}}_c+\mathbf{R}\mathbf{x}_t \tag{6}$$

The absolute velocity $\overline{\mathbf{v}}_t$ is found by differentiation of $\overline{\mathbf{x}}_t$ with respect to time,

$$\overline{\mathbf{v}}_t=\overline{\mathbf{v}}_c+\mathbf{R}\dot{\mathbf{x}}_t+\dot{\mathbf{R}}\mathbf{x}_t \tag{7}$$

where $\overline{\mathbf{v}}_c=\dot{\overline{\mathbf{x}}}_c$ is the velocity of the local reference frame. The absolute velocity in the local frame of reference $\mathbf{v}_t$ is found by pre-multiplication with $\mathbf{R}^{\mathrm{T}}$,

$$\mathbf{v}_t=\mathbf{R}^{\mathrm{T}}\overline{\mathbf{v}}_t=\mathbf{v}_c+\dot{\mathbf{x}}_t+\hat{\boldsymbol{\omega}}\mathbf{x}_t \tag{8}$$

The first term represents the velocity of the moving frame with respect to the local orientation and the second term represents the local velocity due to deformation. The last contribution represents the rotational velocity of the local frame of reference, where the skew-symmetric matrix $\hat{\boldsymbol{\omega}}$, denoting the vector product $\boldsymbol{\omega}\times$, is defined as

$$\hat{\boldsymbol{\omega}}=\boldsymbol{\omega}\times\ =\mathbf{R}^{\mathrm{T}}\dot{\mathbf{R}}=\begin{bmatrix}0 & -\omega_z & \omega_y\\ \omega_z & 0 & -\omega_x\\ -\omega_y & \omega_x & 0\end{bmatrix} \tag{9}$$

Thus, $\hat{\boldsymbol{\omega}}\mathbf{x}_t=\boldsymbol{\omega}\times\mathbf{x}_t$, where $\boldsymbol{\omega}=\dot{\boldsymbol{\theta}}$ is the angular velocity of the local frame of reference.

2.3. Inertial matrices

When inserting (4) into (8) the interpolated velocity field $\mathbf{v}_t$ appears as

$$\mathbf{v}_t=\mathbf{v}_c+\mathbf{N}_A\mathbf{N}_x\dot{\mathbf{u}}+\hat{\boldsymbol{\omega}}\mathbf{x}+\hat{\boldsymbol{\omega}}\mathbf{N}_A\mathbf{N}_x\mathbf{u} \tag{10}$$

where arguments of the interpolation arrays have been omitted for brevity. Substitution of (10) into (5) leads to the following expression for the kinetic energy:

$$T=\frac{1}{2}\dot{\mathbf{u}}^{\mathrm{T}}\mathbf{M}\dot{\mathbf{u}}+\mathbf{v}_c^{\mathrm{T}}\mathbf{M}_0\dot{\mathbf{u}}+\dot{\mathbf{u}}^{\mathrm{T}}\mathbf{G}\mathbf{u}+\mathbf{v}_c^{\mathrm{T}}\mathbf{G}_0\mathbf{u}+\frac{1}{2}\mathbf{u}^{\mathrm{T}}\mathbf{C}\mathbf{u}+\mathbf{u}^{\mathrm{T}}\mathbf{f}_C+\dot{\mathbf{u}}^{\mathrm{T}}\mathbf{f}_G^*+\frac{1}{2}m\mathbf{v}_c^{\mathrm{T}}\mathbf{v}_c+\frac{1}{2}\int_V\mathbf{x}^{\mathrm{T}}\hat{\boldsymbol{\omega}}^{\mathrm{T}}\hat{\boldsymbol{\omega}}\mathbf{x}\varrho\,\mathrm{d}V+\frac{1}{2}\int_V\mathbf{v}_c^{\mathrm{T}}\hat{\boldsymbol{\omega}}\mathbf{x}\varrho\,\mathrm{d}V \tag{11}$$

This expression consists of a set of well-defined contributions to the kinetic energy in the form of characteristic inertial terms. $\mathbf{M}$ is the classic symmetric mass matrix associated with motion due to deformation of the body,

$$\mathbf{M}=\int_L\mathbf{N}_x^{\mathrm{T}}\left(\int_A\mathbf{N}_A^{\mathrm{T}}\mathbf{N}_A\varrho\,\mathrm{d}A\right)\mathbf{N}_x\,\mathrm{d}x \tag{12}$$

The volume integral is separated into a local area integral and an integral over the element length. The area integral can be written explicitly as

$$\int_A\mathbf{N}_A^{\mathrm{T}}\mathbf{N}_A\varrho\,\mathrm{d}A=\begin{bmatrix}A^\varrho & 0 & 0 & 0 & S_z^\varrho & -S_y^\varrho\\ & A^\varrho & 0 & -S_z^\varrho & 0 & 0\\ & & A^\varrho & S_y^\varrho & 0 & 0\\ & & & I^\varrho & 0 & 0\\ & \text{Sym.} & & & I_{zz}^\varrho & -I_{zy}^\varrho\\ & & & & 0 & I_{yy}^\varrho\end{bmatrix} \tag{13}$$

where the weighted area, section moments and moments of inertia are defined by

$$\begin{bmatrix}A^\varrho & S_y^\varrho & S_z^\varrho\\ & I_{yy}^\varrho & I_{yz}^\varrho\\ & & I_{zz}^\varrho\end{bmatrix}=\int_A\begin{bmatrix}1 & y & z\\ & yy & yz\\ & & zz\end{bmatrix}\varrho\,\mathrm{d}A \tag{14}$$

and $I^\varrho=I_{yy}^\varrho+I_{zz}^\varrho$. The remaining inertial vectors and matrices introduced in (11) are defined in the following. Inertial forces due to uniform body accelerations $\mathbf{a}_c=\ddot{\mathbf{x}}_c$ enter via the matrix

$$\mathbf{M}_0=\int_L\mathbf{N}_x^{\mathrm{T}}\left(\int_A\mathbf{N}_A\varrho\,\mathrm{d}A\right)\mathbf{N}_x\,\mathrm{d}x \tag{15}$$

where the area integral can be written explicitly in terms of the mass density A^ϱ and the first-order moments S_α^ϱ. The skew-symmetric gyroscopic coupling matrix is given as

$$\mathbf{G}=\int_L\mathbf{N}_x^{\mathrm{T}}\left(\int_A\mathbf{N}_A^{\mathrm{T}}\hat{\boldsymbol{\omega}}\mathbf{N}_A\varrho\,\mathrm{d}A\right)\mathbf{N}_x\,\mathrm{d}x \tag{16}$$

which is composed of products between the angular velocity components $[\omega_x,\omega_y,\omega_z]$ and the parameters in (14). The term $\mathbf{v}_c^{\mathrm{T}}\mathbf{G}_0\mathbf{u}$ represents the kinetic energy associated with gyroscopic forces due to a uniform velocity of the rotating frame. These forces are not present in the equations of motion in the local frame, thus $\mathbf{G}_0$ is not given here. The centrifugal stiffness enters through the centrifugal matrix

$$\mathbf{C}=\int_L\mathbf{N}_x^{\mathrm{T}}\left(\int_A\mathbf{N}_A^{\mathrm{T}}\hat{\boldsymbol{\omega}}^{\mathrm{T}}\hat{\boldsymbol{\omega}}\mathbf{N}_A\varrho\,\mathrm{d}A\right)\mathbf{N}_x\,\mathrm{d}x \tag{17}$$

which is symmetric, but not necessarily positive definite because displacements within the plane of rotation may lead to increased negative centrifugal forces, hence reducing the effective structural stiffness. The centrifugal forces are defined as

$$\mathbf{f}_C=\int_L\mathbf{N}_x^{\mathrm{T}}\left(\int_A\mathbf{N}_A^{\mathrm{T}}\hat{\boldsymbol{\omega}}^{\mathrm{T}}\hat{\boldsymbol{\omega}}\mathbf{x}\varrho\,\mathrm{d}A\right)\mathrm{d}x \tag{18}$$

where several products within the area integral contain the factor x, representing the distance from the cross-section reference point to the intersection between the rotation axis and the beam reference axis. In Section 4 the equation of motion is derived from Lagrange's equations, where the forces due to angular acceleration $\boldsymbol{\alpha}=\dot{\boldsymbol{\omega}}$ enter via the time derivative of $\mathbf{f}_G^*$. These forces can therefore be computed by the integral

$$\mathbf{f}_G=\int_L\mathbf{N}_x^{\mathrm{T}}\left(\int_A\mathbf{N}_A^{\mathrm{T}}\hat{\boldsymbol{\alpha}}\mathbf{x}\varrho\,\mathrm{d}A\right)\mathrm{d}x \tag{19}$$

The last three terms in (11) represent the kinetic energy associated with a uniform translational velocity and angular velocity of the undeformed structure. Here m is the mass of the beam element, while the last two terms represent rotational and gyroscopic inertia, respectively. These constant terms do not produce contributions to the equations of motion in the local frame of reference.

The gyroscopic and centrifugal matrices are time dependent, as the angular velocity $\boldsymbol{\omega}$ may vary in time. In time simulations, these matrices as well as the centrifugal and angular acceleration force vectors must be updated accordingly.

This may be done by explicit evaluation of area integrals based on the constant cross-section parameters (14) and prescribed or predicted angular velocities and accelerations, followed by numerical evaluation of the length-wise integrals (16)–(19).

3. Beam stiffness effects

The elastic and geometric stiffness contributions to the equations of motion are established from the variation of the structural potential energy U. The potential energy is here evaluated as the sum $U = U_e + U_g$ of the potential strain energy U_e and the potential energy U_g associated with deformation of a body with internal stresses $\boldsymbol{\sigma}$. The variation of the potential energy can be written as

$$\frac{\partial U}{\partial \mathbf{u}^{\mathrm{T}}} = \mathbf{g}(\mathbf{u}) \tag{20}$$

which is fundamentally a nonlinear function of the system states $\mathbf{u}$. Assuming small deformations and linear elastic material properties, the variation of the potential strain energy can be written as a linear function in $\mathbf{u}$, with the elastic stiffness matrix $\mathbf{K}_e$ as proportionality factor. As discussed by Washizu [12], the variation of the potential strain energy associated with internal stresses can be linearized by considering the internal stress field as a constant initial stress field $\boldsymbol{\sigma}^0$ which resides in the undeformed structure and is independent of changes in $\mathbf{u}$. Application of these linearizations of the elastic and geometric stiffness gives the following linearized form of the variation of the potential energy:

$$\mathbf{g}(\mathbf{u}) \simeq (\mathbf{K}_e + \mathbf{K}_g(\boldsymbol{\sigma}^0))\mathbf{u} \tag{21}$$

where $\mathbf{K}_g(\boldsymbol{\sigma}^0)$ is the geometric stiffness matrix based on an initial state of stress $\boldsymbol{\sigma}^0$.

3.1. Elastic stiffness matrix

The elastic stiffness matrix is established from the complementary potential energy following [11]. The flexibility of a two-node beam element with six degrees of freedom per node can be obtained from six independent deformation modes, corresponding to a set of end loads in static equilibrium. Since the static fields are independent of the beam configuration, the flexibility method allows an exact lengthwise integration of the potential strain energy in beams with general and varying cross-section properties. This differentiates the method from classical stiffness methods based on approximate interpolation of kinematic fields.

The static field consists of cross-section forces $\mathbf{Q}=[Q_x, Q_y, Q_z]^{\mathrm{T}}$ and moments $\mathbf{M}=[M_x, M_y, M_z]^{\mathrm{T}}$, as illustrated in Fig. 2b. The associated deformations are described in terms of generalized strains $\boldsymbol{\gamma} = \mathbf{q}'$ and curvatures $\boldsymbol{\kappa} = \mathbf{r}'$, where the superscript $'$ denotes lengthwise differentiation $\mathrm{d}/\mathrm{d}x$. The component γ_x is the axial strain, while γ_y and γ_z are the shear strains. The rate of twist is denoted κ_x, while κ_y, κ_z are the curvatures associated with bending. The assumption of planar cross-sections corresponds to assuming homogeneous St. Venant torsion, with identical cross-sectional warping along the beam. For thin-walled beams this assumption is often reasonable for beams with closed cross-sections [17].

In the case of linear material properties, the cross-section forces and moments are energetically conjugate to the generalized strains and curvatures via the non-singular cross-section stiffness matrix $\mathbf{D}$,

$$\begin{bmatrix} \mathbf{Q} \\ \mathbf{M} \end{bmatrix} = \mathbf{D} \begin{bmatrix} \boldsymbol{\gamma} \\ \boldsymbol{\kappa} \end{bmatrix} \tag{22}$$

For an isotropic material the stiffness matrix $\mathbf{D}$ is given in terms of cross-section moments weighted with the elastic modulus E or the shear modulus G similar to the weighting with ϱ for the inertial parameters in (14). While the axial parameters weighted by E are given explicitly by area integrals similar to their inertial equivalents, the shear parameters typically require the shear stress distribution

$$\mathbf{D} = \begin{bmatrix} A^E & 0 & 0 & 0 & S_y^E & S_z^E \\ & A_{yy}^G & A_{yz}^G & 0 & 0 & 0 \\ & & A_{zz}^G & 0 & 0 & 0 \\ & & & K^G & 0 & 0 \\ & \text{Sym.} & & & I_{yy}^E & I_{yz}^E \\ & & & & & I_{zz}^E \end{bmatrix} \tag{23}$$

In the general case of anisotropic non-homogeneous material properties the matrix $\mathbf{D}$ may be determined by numerical methods, see e.g. Hodges et al. [16].

The potential strain energy of a beam element is given by integration of the cross-section energy density,

$$U_e = \frac{1}{2}\int_L [\boldsymbol{\gamma}^{\mathrm{T}},\ \boldsymbol{\kappa}^{\mathrm{T}}]\mathbf{D}\begin{bmatrix} \boldsymbol{\gamma} \\ \boldsymbol{\kappa} \end{bmatrix} \mathrm{d}x = \frac{1}{2}\int_L \begin{bmatrix} \mathbf{Q}^{\mathrm{T}},\ \mathbf{M}^{\mathrm{T}} \end{bmatrix} \mathbf{C} \begin{bmatrix} \mathbf{Q}^{\mathrm{T}} \\ \mathbf{M}^{\mathrm{T}} \end{bmatrix} \mathrm{d}x \tag{24}$$

The first integral utilizes a description of the kinematic field and the associated cross-section stiffness, while the second integral brings the static field and the associated cross-section flexibility into play, introducing the flexibility matrix $\mathbf{C} = \mathbf{D}^{-1}$. In a beam without external loads the internal normal force, the shear forces and the torsional moment are constant, while

bending moments vary linearly. Thus, the desired distribution of the internal forces along the beam element can be parameterized in terms of the element mid point values $\mathbf{Q}_c$ and $\mathbf{M}_c$. Substitution of the parametric representation of $\mathbf{Q}$ and $\mathbf{M}$ in terms of $\mathbf{Q}_c$ and $\mathbf{M}_c$ into (24) yields

$$U_e = \frac{1}{2}\left[\mathbf{Q}_c^{\mathrm{T}},\ \mathbf{M}_c^{\mathrm{T}}\right]\mathbf{H}\begin{bmatrix}\mathbf{Q}_c\\ \mathbf{M}_c\end{bmatrix} \tag{25}$$

where the element flexibility matrix $\mathbf{H}$ represents the integral of the elastic energy density associated with cross-section flexibility and the desired distribution of the static fields. By inversion of the element flexibility matrix and appropriate transformation from the constant mid point internal forces and moments into nodal displacements and rotations $\mathbf{u}$, the potential energy can be written as

$$U_e = \frac{1}{2}\mathbf{u}^{\mathrm{T}}\mathbf{K}_e\mathbf{u} \tag{26}$$

defining the elastic element stiffness matrix $\mathbf{K}_e$. This matrix is symmetric and positive definite and is given explicitly in [11].

3.2. Geometric stiffness matrix

A theory for linearized stability analysis based on initial stresses was formulated by Vlasov [17], who used direct vector arguments to obtain the equilibrium conditions in differential equation format. This form does not immediately lead to a symmetric matrix formulation of the finite element equations, and it appears to be more convenient to combine the continuum format of the linearized initial stress problem [12] with the displacement field used in the beam theory, Krenk [13]. In this formulation the additional contribution to the energy functional from the initial stress is obtained on the basis of a general three-dimensional state of stress with initial normal stress σ^0_{xx} and initial shear stresses σ^0_{xy},σ^0_{xz}, corresponding to the basic assumptions of beam theory. The effect of the initial stress on the equilibrium conditions is represented via the change of orientation of the initial state of stress, expressed via the lengthwise derivative of the transverse displacements $(q_y'-r_x'z, q_z'+r_x'y)$. Hereby the initial stresses, that were in equilibrium in the undeformed state, produce additional terms in the equilibrium equations. The corresponding quadratic energy functional is

$$U_g = \int_L \left\{ \int_A \frac{1}{2}\left[(q_y'-r_x'z)^2+(q_z'+r_x'y)^2\right]\sigma^0_{xx}\,\mathrm{d}A - r_x\int_A \frac{1}{2}\left[(q_y'-r_x'z)\sigma^0_{xz}-(q_z'+r_x'y)\sigma^0_{xy}\right]\mathrm{d}A\right\}\mathrm{d}x \tag{27}$$

The original formulation also includes the effect of externally applied distributed loads, an effect not included here. By evaluation of the area integrals the potential energy is expressed in terms of initial section forces $\mathbf{Q}^0$ and moments $\mathbf{M}^0$. The contribution to the potential energy from the initial stress is hereby expressed in the following matrix format:

$$U_g = \frac{1}{2}\int_L \left[\mathbf{q}^{\mathrm{T}},\ \mathbf{r}^{\mathrm{T}},\ \mathbf{q}'^{\mathrm{T}},\ \mathbf{r}'^{\mathrm{T}}\right]\mathbf{S}\begin{bmatrix}\mathbf{q}\\ \mathbf{r}\\ \mathbf{q}'\\ \mathbf{r}'\end{bmatrix}\mathrm{d}x \tag{28}$$

where the initial stress matrix $\mathbf{S}$ is given as

$$\mathbf{S} = \begin{bmatrix}
0 & 0 & 0 & 0 & 0 & 0 & 0 & 0 & 0 & 0 & 0 & 0\\
 & 0 & 0 & 0 & 0 & 0 & 0 & 0 & 0 & 0 & 0 & 0\\
 & & 0 & 0 & 0 & 0 & 0 & 0 & 0 & 0 & 0 & 0\\
 & & & 0 & 0 & 0 & 0 & -Q_z^0 & Q_y^0 & a_zQ_z^0+a_yQ_y^0 & 0 & 0\\
 & & & & 0 & 0 & 0 & 0 & 0 & 0 & 0 & 0\\
 & & & & & 0 & 0 & 0 & 0 & 0 & 0 & 0\\
 & & & & & & 0 & 0 & 0 & 0 & 0 & 0\\
 & & & & & & & Q_x^0 & 0 & -M_y^0 & 0 & 0\\
 & & & & & & & & Q_x^0 & -M_z^0 & 0 & 0\\
 & & & \text{Sym.} & & & & & & S^0 & 0 & 0\\
 & & & & & & & & & & 0 & 0\\
 & & & & & & & & & & & 0
\end{bmatrix} \tag{29}$$

The parameter $S^0 = \int_A (y^2+z^2)\sigma^0_{xx}\,\mathrm{d}A$ must generally be evaluated numerically, but explicit approximations can be made in certain cases. The cross-section displacements $\mathbf{q}$ and rotations $\mathbf{r}$, and the corresponding derivatives $\mathbf{q}'$ and $\mathbf{r}'$ are interpolated

as defined in (3), i.e. in terms of shape functions $\mathbf{N}_x$ and nodal degrees of freedom $\mathbf{u}$,

$$\begin{bmatrix} \mathbf{q} \\ \mathbf{r} \\ \mathbf{q}' \\ \mathbf{r}' \end{bmatrix} = \begin{bmatrix} \mathbf{N}_x \\ \mathbf{N}_x' \end{bmatrix} \mathbf{u} \tag{30}$$

This leads to the following compact form of the potential energy:

$$U_g = \frac{1}{2}\mathbf{u}^{\mathrm{T}}\mathbf{K}_g\mathbf{u} \tag{31}$$

where the geometric element stiffness matrix $\mathbf{K}_g$ is defined as

$$\mathbf{K}_g = \int_L [\mathbf{N}_x^{\mathrm{T}},\ \mathbf{N}_x'^{\mathrm{T}}]\ \mathbf{S}\ \begin{bmatrix} \mathbf{N}_x \\ \mathbf{N}_x' \end{bmatrix} \mathrm{d}x \tag{32}$$

The geometric stiffness matrix is symmetric, but not necessarily positive definite, as e.g. compressive axial stresses introduce negative restoring forces when rotated outwards under beam bending. This effect is represented by the axial section force Q_x^0 appearing in the diagonal of the initial stress matrix $\mathbf{S}$. The off-diagonal moments M_y^0 and M_z^0 in $\mathbf{S}$ introduce a similar effect where opposing beam sides are softened and stiffened by axial stresses, respectively. Initial shear forces couple transverse displacements and torsion and directly influence torsional stiffness in the case of a shear center offset.

4. Structural equations of motion

As the kinetic energy (11) and the potential energy contributions (26) and (31) have now been established, the equations of motion in the local frame of reference can be derived from Lagrange's equations. These are given in terms of the nodal state space variables $\mathbf{u}$ and $\dot{\mathbf{u}}$,

$$\frac{\mathrm{d}}{\mathrm{d}t}\left(\frac{\partial T}{\partial \dot{\mathbf{u}}^{\mathrm{T}}}\right) - \frac{\partial T}{\partial \mathbf{u}^{\mathrm{T}}} + \frac{\partial U}{\partial \mathbf{u}^{\mathrm{T}}} = \mathbf{f}_e \tag{33}$$

where $\mathbf{f}_e$ is an external force vector. The contribution to the equations of motion from inertial forces is obtained by evaluating the first two terms of (33). Substitution of (11) gives

$$\frac{\mathrm{d}}{\mathrm{d}t}\left(\frac{\partial T}{\partial \dot{\mathbf{u}}^{\mathrm{T}}}\right) - \frac{\partial T}{\partial \mathbf{u}^{\mathrm{T}}} = \mathbf{M}\ddot{\mathbf{u}} + \mathbf{M}_0^{\mathrm{T}}\mathbf{a}_c + 2\mathbf{G}\dot{\mathbf{u}} + (\dot{\mathbf{G}} - \mathbf{C})\mathbf{u} - \mathbf{f}_C + \mathbf{f}_G \tag{34}$$

The centrifugal forces and the inertial forces due to angular acceleration impose body forces and contributions to the structural stiffness. In the present application no initial stresses are present in the undeformed structure. For large rotational velocities perpendicular to the beam axis, centrifugal forces may produce axial stresses of significant magnitude relative to the geometric stiffness effects. The corresponding structural deformations are however relatively small, and in the present application the associated geometric stiffness effects are therefore approximated via the initial stress formulation. This means that the initial stresses $\boldsymbol{\sigma}^0$ are replaced by stresses $\boldsymbol{\sigma}$ based on an equilibrium state at current time. Hereby, the variation of the potential energy can be written as

$$\frac{\partial U}{\partial \mathbf{u}^{\mathrm{T}}} \simeq (\mathbf{K}_e + \mathbf{K}_g(\boldsymbol{\sigma}))\mathbf{u} \tag{35}$$

In a time integration procedure the geometric stiffness at a given time step is initially computed based on the internal forces from the equilibrium state of the previous time step. For most practical applications this explicit approach will give satisfactorily results. However, for improved accuracy a simple iteration loop within each time step can be implemented.

Substitution of the inertial terms (34) and the stiffness terms (35) into (33) gives the complete set of linearized equations of motion,

$$\mathbf{M}\ddot{\mathbf{u}} + 2\mathbf{G}\dot{\mathbf{u}} + \mathbf{K}\mathbf{u} = \mathbf{f}_e + \mathbf{f}_C - \mathbf{f}_G \tag{36}$$

where $\mathbf{K}$ is the equivalent element stiffness matrix,

$$\mathbf{K} = \mathbf{K}_e + \mathbf{K}_g + \dot{\mathbf{G}} - \mathbf{C} \tag{37}$$

The section forces $\mathbf{f}_r$ are evaluated on element level as

$$\mathbf{f}_r = \mathbf{M}\ddot{\mathbf{u}} + 2\mathbf{G}\dot{\mathbf{u}} + \mathbf{K}\mathbf{u} - (\mathbf{f}_e + \mathbf{f}_C - \mathbf{f}_G) \tag{38}$$

The section force vector is organized as $\mathbf{f}_r^{\mathrm{T}} = [\mathbf{Q}_a^{\mathrm{T}}, \mathbf{M}_a^{\mathrm{T}}, \mathbf{Q}_b^{\mathrm{T}}, \mathbf{M}_b^{\mathrm{T}}]$, where subscripts a and b refer to the first and second node of the beam element, respectively.

4.1. Modal analysis for stationary rotation

For stationary rotation with $\boldsymbol{\alpha}=\mathbf{0}$ the system matrices of (36) are constant. If the effect of the constant centrifugal force is furthermore included only in terms of initial stresses corresponding to local equilibrium, the homogeneous part of (36) describes a linear system with natural eigenfrequencies and associated eigenvectors. The equations of motion can be written in state space format [18,19],

$$\begin{bmatrix}\mathbf{M} & \mathbf{0}\\ \mathbf{0} & \mathbf{K}\end{bmatrix}\begin{bmatrix}\ddot{\mathbf{u}}\\ \dot{\mathbf{u}}\end{bmatrix}+\begin{bmatrix}2\mathbf{G} & \mathbf{K}\\ -\mathbf{K} & \mathbf{0}\end{bmatrix}\begin{bmatrix}\dot{\mathbf{u}}\\ \mathbf{u}\end{bmatrix}=\mathbf{0} \tag{39}$$

Introducing the state vector $\mathbf{z}^{\mathrm{T}}=[\dot{\mathbf{u}}^{\mathrm{T}},\mathbf{u}^{\mathrm{T}}]$, the system (39) takes the first-order form

$$\mathbf{A}\dot{\mathbf{z}}+\mathbf{B}\mathbf{z}=\mathbf{0} \tag{40}$$

For $\boldsymbol{\alpha}=\mathbf{0}$ the equivalent stiffness matrix $\mathbf{K}$ is symmetric and positive definite. Consequently, $\mathbf{A}$ is positive definite and symmetric, whereas $\mathbf{B}$ is skew-symmetric. In the associated eigenvalue problem this leads to purely imaginary eigenvalues, appearing in conjugate pairs with associated complex-valued eigenmodes. The eigenvalue problem for gyroscopic systems was originally solved by Meirovitch [18], where the problem was divided into the solution of two real-valued problems in standard form. Here the eigenvalue problem (40) is solved directly using standard numerical techniques and the resulting complex-valued mode shapes are interpreted directly.

5. Resonant controller format and tuning

As the dynamic equations of motion (36) for the rotating beam are now defined, the application of the resonant controller to the structural system can be addressed. In this section the filters of the controller are defined as transfer functions in the frequency domain, and a format for representing the physical interaction between the structure and the controller sensor/actuator pairs is developed. Finally, the tuning procedure for a system with acceleration feedback is presented. Details about the tuning procedure are given in [8,9].

The objective of the controller is to extract energy from the selected mode by imposing a specifically tuned resonant force to the structure. Actuator feedback is represented by the force vector $\mathbf{f}_\eta$, and the resulting structural equations of motion become

$$\mathbf{M}\ddot{\mathbf{u}}+2\mathbf{G}\dot{\mathbf{u}}+\mathbf{K}\mathbf{u}=\mathbf{f}_e+\mathbf{f}_C-\mathbf{f}_G+\mathbf{f}_\eta \tag{41}$$

The resonant controller is conveniently defined in the frequency domain. The beam is assumed to rotate with constant angular velocity $\boldsymbol{\omega}$, i.e. $\boldsymbol{\alpha}=\mathbf{0}$ and $\mathbf{f}_G=\mathbf{0}$. Deformations due to the constant centrifugal force are neglected, while maintaining the associated contribution to the geometric stiffness. For a harmonic external force $\mathbf{f}_e$ with angular frequency ω, a stationary solution $\mathbf{u}e^{\mathrm{i}\omega t}$, where i is the imaginary unit, is assumed for the system (41). The equations of motion in the frequency domain can be written as

$$(\mathbf{K}+2\mathrm{i}\omega\mathbf{G}-\omega^2\mathbf{M})\mathbf{u}=\mathbf{f}_e+\mathbf{f}_\eta \tag{42}$$

Following the approach in [8,9] the controller forces $\mathbf{f}_\eta$ are introduced as

$$\mathbf{f}_\eta=-G_{q\eta}(\omega)\mathbf{w}\eta \tag{43}$$

where $G_{q\eta}(\omega)$ is the actuator feedback transfer function and $\mathbf{w}$ is the controller connectivity vector, representing the physical attachment of the controller to the beam structure. The variable η is the controller state, governed by the feedback equation,

$$G_{\eta\eta}(\omega)\eta=-G_{\eta q}(\omega)q \tag{44}$$

where $G_{\eta\eta}(\omega)$ is the controller transfer function and $G_{\eta q}$ is the sensor feedback transfer function. The controller transfer function is a second-order filter representing the inherent resonant properties of the device. The scalar quantity q represents the structural displacement over the actuator,

$$q=\mathbf{w}^{\mathrm{T}}\mathbf{u} \tag{45}$$

The fact that the controller is collocated results in both the sensor and actuator feedback being defined in terms of the controller connectivity vector $\mathbf{w}$. In the case of an active strut, acceleration feedback can be measured by accelerometers aligned with the axial direction of the active strut, or by filtered feedback from an axial displacement gauge.

5.1. Controller definition and tuning

According to [8,9] the resonant controller operating with acceleration feedback on a flexible, multi-degree-of-freedom structure is defined by the following transfer functions:

$$G_{\eta\eta}(\omega)=\omega_\eta^2-\omega^2+2\mathrm{i}\zeta_\eta\omega_\eta\omega,\quad G_{\eta q}(\omega)=-\omega^2,\quad G_{q\eta}(\omega)=\frac{1}{v_1^2}(\alpha_\eta\omega_\eta^2+\beta_\eta 2\mathrm{i}\zeta_\eta\omega_\eta\omega) \tag{46}$$

The principle of a resonant device dates back to the tuned mass damper originally introduced by Ormondroyd and Den Hartog [20]. It should be noted that (46) reproduces the equations of a mechanical tuned mass damper, with frequency ω_η and damping ratio ζ_η, when the actuator gains α_η and β_η are equal to the mass ratio. In the case of resonant control with acceleration feedback α_η and β_η are tuning parameters in the actuator feedback transfer function $G_{q\eta}(\omega)$. The sensor feedback transfer function $G_{\eta q}(\omega)$ is seen to be a differential operator generating accelerations.

The particular tuning of the controller follows the procedure in [8,9], where an explicit scheme determines the parameters ω_η, ζ_η, α_η and β_η according to a desired additional modal damping ratio $\Delta\zeta$. The identification of optimal values for the parameters consists of an isolated single-mode analysis followed by a quasi-static correction for background modes in a multi-degree-of-freedom structure. When a resonant controller is applied to a single-degree-of-freedom system, the system mode splits into two modes. Optimal resonant control should therefore introduce equal modal damping to the two modes. This defines the optimal filter frequency ω_c. The remaining parameters are then determined so that the dynamic amplification has a flat plateau between the two involved resonance frequencies. This two step procedure yields the following set of optimal parameters for a single-degree-of-freedom system:

$$\zeta_c = 2\Delta\zeta, \quad \beta_c = \frac{2\zeta_c^2}{1-2\zeta_c^2}, \quad \alpha_c = \beta_c, \quad \omega_c = \frac{\omega_n}{1+\beta_c} \tag{47}$$

The performance of the resonant controller is affected by the presence of additional structural flexibility from higher modes at the location of the controller. This flexibility is represented by the modal quasi-static flexibility parameter κ_n,

$$\kappa_n = \left(\frac{\omega_n}{\nu_n}\right)^2 \mathbf{w}^{\mathrm{T}}\mathbf{K}^{-1}\mathbf{w} - 1 \tag{48}$$

which in normalized form represents the additional or excess flexibility contained in the higher modes at sensor/actuator location. This expression contains the nodal connectivity parameter ν_n, which represents the magnitude of the mode shape over the controller,

$$\nu_n = \mathbf{w}^{\mathrm{T}}\mathbf{u}_n \tag{49}$$

where $\mathbf{u}_n$ is the targeted mode shape. The modal connectivity factor enters the formulation by its squared value. When ν_n is complex it is multiplied by the complex conjugate ν_n^* in order to obtain the real-valued square of the local mode shape amplitude. Both parameters κ_n and ν_n provide useful information for comparative studies on controller placement. One would normally seek to minimize 'background noise' represented by κ_n while maximizing nodal connectivity ν_n.

When including the quasi-static correction for the flexibility of higher modes in the sensor feedback, and then establishing an equivalence between the modal equation of the targeted mode and the optimal single-mode equations, the following expressions are obtained for the control parameters:

$$\alpha_\eta = \beta_c, \quad \beta_\eta = \frac{\beta_c}{1+\kappa_n\beta_c}, \quad \omega_\eta^2 = \frac{\omega_c^2}{1-\dfrac{\kappa_n\beta_c}{(1+\beta_c)^2}}, \quad \zeta_\eta = \frac{\omega_\eta}{\omega_c}(1+\kappa_n\beta_c)\zeta_c \tag{50}$$

The formulas (47)–(50) constitute the complete parameter tuning, when the controller/structure connection has been chosen. The background correction only accounts for modes with higher frequencies than the targeted mode, and thus the current derivation of (48)–(50) implicitly assumes that the background correction does not include contributions from lower-frequency modes. In practice individual targeted modes will be near-orthogonal to some of the components of the quasi-static correction, and the full correction can be used e.g. for a set of modes containing lowest flap-wise and lowest edge-wise mode.

5.2. Closed-loop system equations

The system equations for a rotating beam structure including the closed-loop sensor/actuator feedback are obtained by substituting (43) and (45) into (42) and (44) and finally inserting the transfer functions (46). The corresponding time-domain equations can then be written as

$$\begin{bmatrix} \mathbf{M} & \mathbf{0} \\ -\mathbf{w}^{\mathrm{T}} & 1 \end{bmatrix}\begin{bmatrix} \ddot{\mathbf{u}} \\ \ddot{\eta} \end{bmatrix} + \begin{bmatrix} 2\mathbf{G} & \dfrac{\beta_\eta}{\nu_n^2}2\zeta_\eta\omega_\eta\mathbf{w} \\ \mathbf{0} & 2\zeta_\eta\omega_\eta \end{bmatrix}\begin{bmatrix} \dot{\mathbf{u}} \\ \dot{\eta} \end{bmatrix} + \begin{bmatrix} \mathbf{K} & \dfrac{\alpha_\eta}{\nu_n^2}\omega_\eta^2\mathbf{w} \\ \mathbf{0} & \omega_\eta^2 \end{bmatrix}\begin{bmatrix} \mathbf{u} \\ \eta \end{bmatrix} = \begin{bmatrix} \mathbf{f}_e + \mathbf{f}_C - \mathbf{f}_G \\ 0 \end{bmatrix} \tag{51}$$

Introducing the augmented system state vector

$$\mathbf{u}_\eta = [\mathbf{u}^{\mathrm{T}}, \eta]^{\mathrm{T}} \tag{52}$$

Eq. (51) take the compact form

$$\mathbf{M}_\eta\ddot{\mathbf{u}}_\eta + \mathbf{D}_\eta\dot{\mathbf{u}}_\eta + \mathbf{K}_\eta\mathbf{u}_\eta = \begin{bmatrix} \mathbf{f}_e + \mathbf{f}_C - \mathbf{f}_G \\ 0 \end{bmatrix} \tag{53}$$

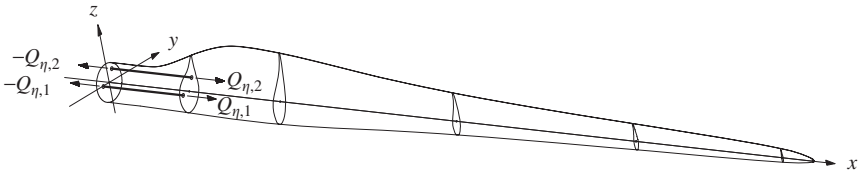

Fig. 3. The 42 m wind turbine blade with two active strut controllers.

This format is convenient for modal analysis of the controlled system and time simulation using e.g. classical linear Newmark integration. Multiple controllers are represented by further augmentation of the structural equations of motion.

6. Active damping of a rotating wind turbine blade

Modern wind turbine blades are large rotating pre-twisted beam-like structures, typically with low structural damping. When operating in turbulent aerodynamic conditions, several of the lower modes may be excited, yielding significant fatigue loading. This section considers the resonant control of a realistic 42 m wind turbine blade by two active strut controllers, designed to damp the first and second blade vibration modes, respectively.

6.1. *The* 42 m *wind turbine blade*

The blade is shown in the local frame of reference $\{x, y, z\}$ in Fig. 3. The inhomogeneous cross-section properties of the composite blade structure are described by the equivalent parameters introduced in the matrix $\mathbf{D}$ in (23). The pitch axis is chosen as the x-axis, and the elastic, the shear and the mass centers are generally not coinciding. The elastic and inertial cross-section properties are interpolated linearly along the pitch axis between 46 sections with a detailed cross-section description.

A modern wind turbine has continuously varying operating conditions, depending on the current mean wind speed. In this example a mean wind speed of 12 m/s is assumed, and two operating conditions are considered: the blade at turbine standstill with $\|\boldsymbol{\omega}\| = 0$ rad/s, and the normal operating condition with $\|\boldsymbol{\omega}\| = 1.57$ rad/s, corresponding to approximately 15 rpm. To maintain the desired performance of the wind turbine the blades may be rotated about the pitch axis. In the present case this rotation angle is assumed to be -4.4°. Furthermore, the blade is slightly inclined relative to the axis of rotation, and for the present blade this coning angle is 6.0°. This gives a local angular velocity of the blade of $\boldsymbol{\omega} = \|\boldsymbol{\omega}\|[-0.105, 0.992, 0.0758]^{\mathrm{T}}$, where the ω_y-component is clearly dominating.

The blade is modeled using 15 elements, where transverse displacements are interpolated using cubic Hermitian shape functions, while rotations and axial displacements are interpolated by linear shape functions. Numerical integration of the polynomials along the longitudinal pitch axis is performed by Lobatto quadrature, see e.g. [21]. Modal analysis is performed by solving the eigenvalue problem (40), where the geometric effects of internal stresses due to stationary rotation are included.

The mode shapes $\mathbf{u}_1$ and $\mathbf{u}_2$ are shown in Fig. 4 for $\|\boldsymbol{\omega}\| = 1.57$ rad/s in the local frame of reference. Due to the gyroscopic forces the vibration modes are complex-valued, and the figure shows both the real (+) and the imaginary ($\times$) parts. The displacements shown in Fig. 4a correspond to the first flapwise mode, dominated by bending about the weak axis of the blade.

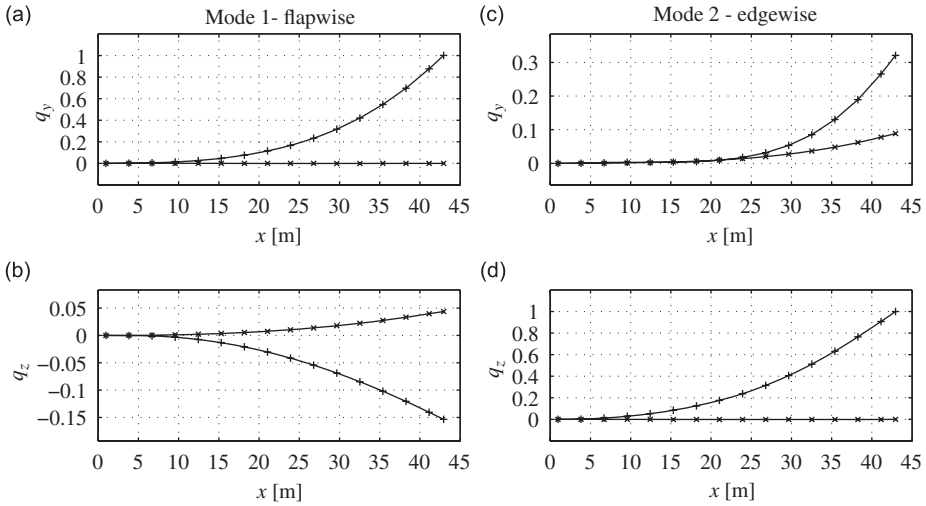

Fig. 4. Mode shapes $\mathbf{u}_1$ and $\mathbf{u}_2$ for $\|\boldsymbol{\omega}\| = 1.57$ rad/s. – + – Re($\mathbf{u}_n$). – $\times$ – Im($\mathbf{u}_n$).

Table 1
Controller tuning.

$\|\boldsymbol{\omega}\|$	n	v_{nn}^2	κ_n	α_η	β_η	ω_η/ω_n	ζ_η	$\zeta_{n,1}$	$\zeta_{n,2}$	ε_n (%)
0	1	5.90e−9	14.0	0.0297	0.0210	1.24	0.217	0.0619	0.0609	0.82
	2	1.66e−8	10.3	0.0297	0.0227	1.15	0.186	0.0603	0.0608	0.42
1.57	1	6.55e−9	14.1	0.0297	0.0209	1.25	0.219	0.0619	0.0609	0.81
	2	1.70e−8	10.1	0.0297	0.0228	1.15	0.184	0.0599	0.0614	1.21

Because of the pretwist of the blade, small displacements in the z-direction also occur as shown in Fig. 4b. The imaginary components represent the phase difference between q_y and q_z, corresponding to an elliptical vibration path in the cross-sectional plane. The second mode is the first edgewise mode, which is dominated by bending about the strong axis, as shown in Fig. 4c and d.

At standstill the first two eigenfrequencies are $\omega_1 = 5.93$ rad/s and $\omega_2 = 9.08$ rad/s, while at $\|\boldsymbol{\omega}\| = 1.57$ rad/s the eigenfrequencies are $\omega_1 = 6.29$ rad/s and $\omega_2 = 9.09$ rad/s. The geometric effect from internal axial stresses in equilibrium with stationary centrifugal forces is generally to increase blade stiffness, thus eigenfrequencies increase with rotational velocity. For the natural frequency ω_1 of the flapwise mode this yields an increase of 6.1 percent, whereas for the edgewise mode the centrifugal softening almost compensates for the stiffening by geometric stiffness, and the increase of ω_2 is only 0.1 percent.

6.2. Controller positioning and tuning

Two active strut controllers with acceleration feedback are attached to the blade, tuned individually to introduce additional damping $\Delta\zeta = 0.06$ to modes 1 and 2, respectively. The location of the two struts is indicated in Fig. 3. The active struts have the lengths $L_1 = L_2 = 6.00$ m, and they are located at the root of the blade between nodes 1 and 3 of the finite element model. This location gives almost optimal modal connectivity since the beam curvature is largest at the root. The struts are located inside the blade and parallel to the pitch axis, and both struts have an offset relative to the pitch axis of 0.700 m. The positions of the two controllers are finally determined by the two angles θ_1 and θ_2 in the cross-sectional plane relative to the local y-axis. In the present application the inertia forces from the physical actuator mass will be negligible compared to the controller forces. The structural properties of the actuator are therefore not included in the structural model.

A robust position strategy should maximize the modal connectivities $v_{11} = \mathbf{w}_1^{\mathrm{T}}\mathbf{u}_1$ and $v_{22} = \mathbf{w}_2^{\mathrm{T}}\mathbf{u}_2$, while minimizing the corresponding cross-modal connectivities $v_{12} = \mathbf{w}_1^{\mathrm{T}}\mathbf{u}_2$ and $v_{21} = \mathbf{w}_2^{\mathrm{T}}\mathbf{u}_1$. These two objectives do not necessarily share optima, and minimizing v_{12} and v_{21} typically provides the best results. In the case of perfectly decoupled strut locations $v_{12} = v_{21} = 0$ and the two emanating modes are equally damped, i.e. the deviation $\varepsilon_n = (\zeta_{n,1} - \zeta_{n,2})/\zeta_{n,1}$ becomes zero. The sensor/actuator pair is here positioned according to $\{\theta_1/\pi, \theta_2/\pi\} = \{1.00, 0.25\}$ as illustrated in Fig. 3. For $\|\boldsymbol{\omega}\| = 1.57$ rad/s the associated deviations are $\{\varepsilon_1, \varepsilon_2\} = \{0.81$ percent, 1.21 percent$\}$ which represents a very accurate combined controller tuning. In Table 1 the tuning parameters of the two controllers are shown for standstill and operation. In all cases the explicit tuning procedure is seen to produce close to optimal controller tuning, where almost exactly the intended amount of damping is added to the targeted modes, when the quasi-static parameter correction (50) is included.

Changes in structural properties associated with changes in rotational speed affect the optimal values of tuning parameters. Fig. 5 shows the development of controller frequencies ω_η as a function of rotational speed $\|\boldsymbol{\omega}\|$, normalized with the initial values at standstill, ω_η^0. The frequency $\omega_{\eta 1}$ is seen to increase, following the increase in ω_1. A slight decrease of $\omega_{\eta 2}$ is seen, due to the small increase in modal connectivity v_{22} and decrease in background flexibility κ_2.

Fig. 6a shows the dynamic amplification of local blade tip displacements q_y for harmonic loading of mode 1, with $\|\boldsymbol{\omega}\| = 1.57$ rad/s. The dash-dotted line shows the free response, and the full curve shows the controlled response. The nearly

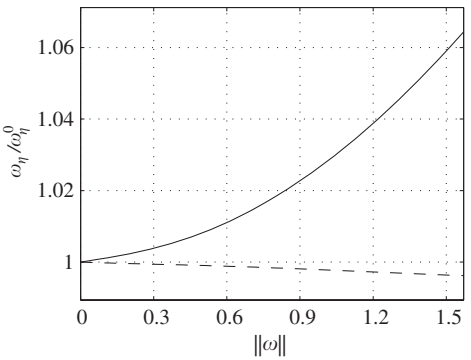

Fig. 5. Optimal controller frequencies. — $\omega_{\eta 1}/\omega_{\eta 1}^0$. - - - $\omega_{\eta 2}/\omega_{\eta 2}^0$.

symmetrical 'shoulders' of the full curve illustrates the almost optimal tuning of the controller. The dashed curve represents the dynamic amplification for a damped system where the correction for background modal flexibility is omitted, i.e. $\kappa_1 = 0$. It is seen that the damping performance of the controller in this case is lost, which illustrates the importance of the quasi-static correction. Fig. 6b shows the dynamic amplification of the local tip displacement q_z at harmonic loading of mode 2, and the results are similar to those in Fig. 6a for mode 1.

The relatively high value $\kappa_1 = 14.1$ corresponds to a significant presence of higher modes at the location of controller 1. This entails some spill-over to these modes, and the added damping to the following two flapwise modes with deflection in the y-direction is $\{\zeta_5,\zeta_7\} = \{0.0159,0.0232\}$. With $\kappa_2 = 10.1$ for controller 2 the spill-over to higher modes is somewhat smaller. The added damping to the following higher modes in the z-direction are $\{\zeta_6,\zeta_8\} = \{0.0058,0.0052\}$. It is seen that limited spill-over can be attained when modal background interference is limited. The general implication is that when mentionable spill-over is inevitable, it always provides positive contributions. A rigorous proof of the latter has not been found, however it is likely to exist due to the collocated nature of the design.

6.3. Simulated structural response

To demonstrate the controller performances in a realistic setting, free and controlled structural response is simulated for a turbulent wind field with realistic stochastic properties. The wind is simulated as a discrete, unidirectional velocity field, where the spatial correlation is established via a Karhunen–Loeve expansion based on independent temporal processes.

The equations of motion (53) are solved using the Newmark integration method with the unconditionally stable 'average acceleration' scheme with parameters $\gamma = \frac{1}{2}$ and $\beta = \frac{1}{4}$, see e.g. [19]. The geometric stiffness $\mathbf{K}_g$ is updated between time instances in a single-step procedure, where the section forces from the most recent equilibrium state are used to compute $\mathbf{K}_g$. For small time-steps h relative to the period of the highest important vibration mode T_n this approximation is sufficiently accurate, and in the present case T_6/h=10. A small amount of algorithmic α-damping with $\alpha = 0.04$ is included to model light structural damping.

In Fig. 7a the local blade tip response q_y is shown, where the free response is shown by the dashed curve and the controlled response is shown by the full curve. The free response has a quasi-static 'mean' component following the resulting blade lift force, superimposed by oscillations at the natural frequency ω_1. In the controlled case the oscillations at ω_1 are seen to be significantly reduced by the controller, while the 'mean' response remains unaffected. Similarly, free and controlled blade tip

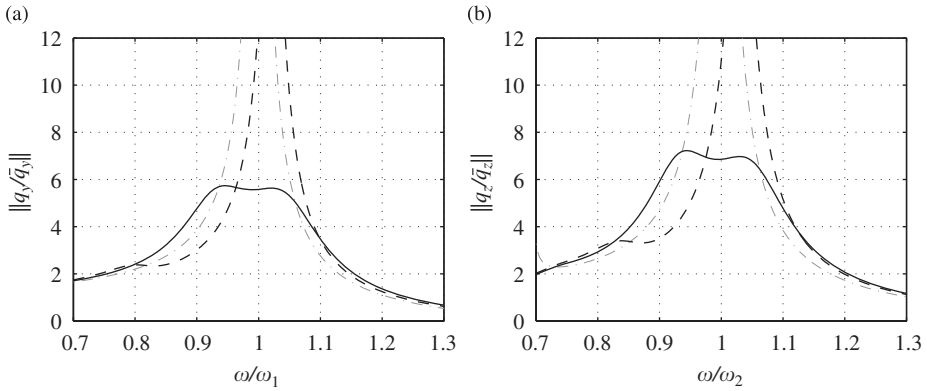

Fig. 6. Dynamic amplification: (a) Flapwise tip displacement $\|q_y/\bar{q}_y\|$ and (b) Edgewise tip displacement $\|q_z/\bar{q}_z\|$. - · - · - Free. — Controlled. - - - $\kappa_n = 0$.

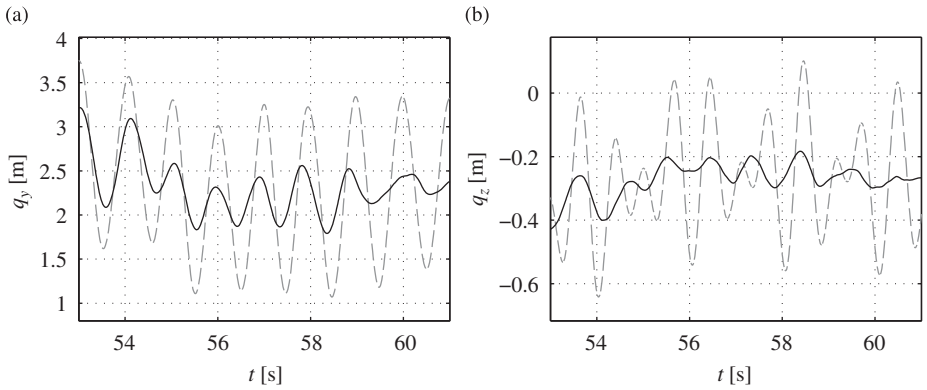

Fig. 7. Simulated displacement response at blade tip: (a) Flapwise displacements q_y and (b) Edgewise displacements q_z.

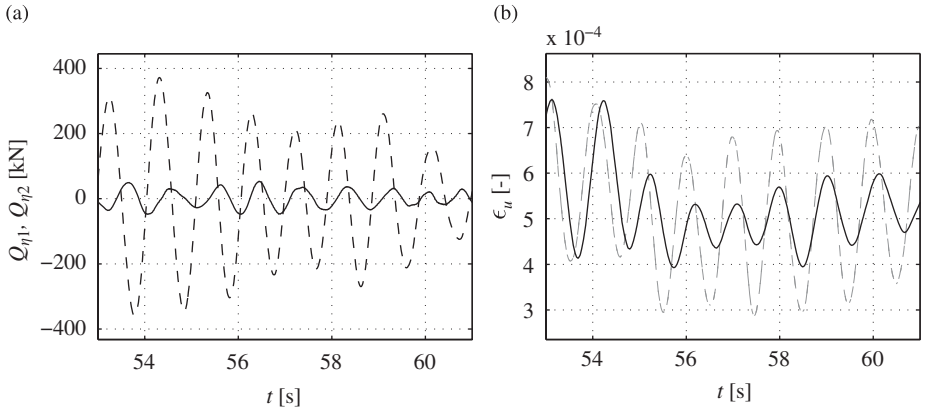

Fig. 8. (a) Actuator forces. - - - $Q_{\eta 1}$. — $Q_{\eta 2}$ and (b) Blade root surface strain ε_u. - - - Free. — Controlled.

response q_z are shown in Fig. 7b. Oscillations at both ω_1 and ω_2 are present because the relatively active flapwise mode 1 has significant components also in the z-direction. It is seen that vibration amplitudes at both ω_1 and ω_2 are effectively reduced, while maintaining the 'mean' response path.

Actuator forces $Q_{\eta 1}$ and $Q_{\eta 2}$ are shown in Fig. 8a. The large vibration amplitude of mode 1 compared to mode 2 is reflected by the difference in force amplitudes. Both actuators operate almost harmonically corresponding to their controller frequencies, with $\omega_{\eta 2}$ being slightly larger than $\omega_{\eta 1}$. This demonstrates the narrow frequency bands of the controller operation. Furthermore, both actuator forces are zero mean processes, reflecting the controller filtering of the quasi-static structural motion.

The purpose of vibration control in flexible structures is often to reduce material loading in terms of peak- or recurring stress magnitudes. The largest material loading from vibrations in mode 1 are the axial strains ε_u at the outer side surfaces of the blade root. These are plotted in Fig. 8b, calculated for the left (upwind) side where material elongation is induced. It is seen that the actuator forces reduce the material strains at all times, also locally at the actuator location.

7. Conclusion

It has been demonstrated that a collocated resonant controller, here used for an active strut with acceleration feedback, is effective and robust in providing a specified level of modal damping for a selected mode. It is furthermore shown that it is possible to position and tune multiple controllers with associated sensor/actuator pairs for effective, simultaneous damping of multiple modes.

The performance of the resonant control principle is demonstrated in the relevant and realistic setting of a modern, large scale wind turbine blade. The strongly varying structural composition and the inertial rotation effects create vibration modes with complex elastic and gyroscopic couplings. Still, accurate and stable modal damping is obtained and oscillating strain amplitudes are generally reduced.

A compact formulation for three-dimensional, two-node finite beam elements in a rotating frame of reference has been established. In this formulation, general, varying inertial and elastic properties are accounted for via energy formulations, and geometric stiffness effects are represented via a linearized initial stress formulation. The element allows for high-accuracy modeling of structures with complex geometry and material properties, and the linearized format permits modal analysis in operational states of rotation. Relevant investigations can be performed for complex structures operating e.g. under aerodynamic loads, where the effects of centrifugal stiffening and elastic or geometric torsion-bending couplings play an important role.

The present combination of the generalized finite beam element model and the explicit procedure for application and tuning of active, collocated resonant controllers represents a compact theoretical basis for effective and robust damping of modal vibrations in rotating beam structures.

References

[1] L. Meirovitch, Control of spinning flexible spacecraft by modal synthesis, *Acta Astronautica* 4 (1977) 985–1010.
[2] M.J. Balas, Feedback control of flexible systems, *IEEE Transactions on Automatic Control* 23 (1978) 673–679.
[3] C.J. Goh, T.K. Caughey, On the stability problem caused by finite actuator dynamics in the collocated control of large space structures, *International Journal of Control* 41 (1985) 787–802.
[4] A. Baz, S. Poh, Performance of an active control system with piezoelectric actuators, *Journal of Sound and Vibration* 126 (1988) 327–343.
[5] S.C. Choi, J.S. Park, J.H. Kim, Vibration control of pre-twisted rotating composite thin-walled beams with piezoelectric fiber composites, *Journal of Sound and Vibration* 300 (2007) 176–196.
[6] Y.A. Khulief, Vibration suppression in rotating beams using active modal control, *Journal of Sound and Vibration* 242 (2001) 681–699.
[7] C.D. Shete, N.K. Chandiramani, L.I. Librescu, Optimal control of a pretwisted shearable smart composite rotating beam, *Acta Mechanica* 191 (2007) 37–58.
[8] S. Krenk, J. Høgsberg, Optimal resonant control of flexible structures, *Journal of Sound and Vibration* 323 (2009) 530–554.

[9] S. Krenk, J. Høgsberg, Resonant damping of flexible structures, *COMPDYN 2009, ECCOMAS Thematic Conference on Computational Methods in Structural Dynamics and Earthquake Engineering*, 2009.
[10] A. Preumont, B. de Marneffe, A. Deraemaeker, F. Bossens, The damping of a truss structure with a piezoelectric transducer, *Computers and Structures* 86 (2008) 227–239.
[11] S. Krenk, *Element Stiffness Matrix for Beams with General Cross-section Properties*, Technical University of Denmark, Department of Mechanical Engineering, 2006.
[12] K. Washizu, *Variational Methods in Elasticity and Plasticity*, Pergamon Press, Oxford, 1968.
[13] S. Krenk, *Lectures on Thin-Walled Beams*, third ed., Technical University of Denmark, Department of Mechanical Engineering, 2001.
[14] A. Kawamoto, S. Krenk, A. Suzuki, M. Inagaki, Flexible body dynamics in a local frame with explicitly predicted motion, *International Journal for Numerical Methods in Engineering* 81 (2010) 246–268.
[15] J.H. Argyris, An excursion into large rotations, *Computer Methods in Applied Mechanics and Engineering* 32 (1982) 85–155.
[16] D.H. Hodges, A.R. Atilgan, C.E.S. Cesnik, On a simplified strain energy function for geometrically nonlinear behaviour of anisotropic beams, *Composites Engineering* 2 (1992) 513–526.
[17] V.Z. Vlasov, *Thinwalled Elastic Beams*, Israel Program for Scientific Translations, Jerusalem, 1961.
[18] L. Meirovitch, A new method of solution of the eigenvalue problem for gyroscopic systems, *AIAA Journal* 12 (1974) 1337–1342.
[19] M. Géradin, D. Rixen, *Mechanical Vibrations*, second ed., Wiley, Chichester, 1997.
[20] J. Ormondroyd, J.P. Den Hartog, The theory of the dynamic vibration absorber, *Transactions of the ASME* 50 (1928) 9–22.
[21] T.J.R. Hughes, *The Finite Element Method, Linear Static and Dynamic Finite Element Analysis*, Dover, Mineola, New York, 2000.

P2

(Conference paper)

Resonant vibration control of wind turbine blades

TORQUE 2010: The Science of Making Torque from Wind
June 28–30, Creete, Greece, 2010, 543–553

Resonant Vibration Control of Wind Turbine Blades

Martin Nymann Svendsen[a,b] mns@mek.dtu.dk
Steen Krenk[a] sk@mek.dtu.dk
Jan Høgsberg[a] jhg@mek.dtu.dk

Department of Mechanical Engineering[a],
Technical University of Denmark, DK-2800 Lyngby, Denmark

Vestas Wind Systems A/S[b]
Hedeager 42, DK-8200 Aarhus N, Denmark

Abstract

The paper deals with introduction of damping to specific vibration modes of wind turbine blades, using a resonant controller with acceleration feedback. The wind turbine blade is represented by three-dimensional, two-node finite elements in a local, rotating frame of reference. The element formulation accounts for arbitrary mass density distributions, general elastic cross-section properties and geometric stiffness effects due to internal stresses. A compact, linear formulation for aerodynamic forces with associated stiffness and damping terms is established and added to the structural model. The efficiency of the resonant controller is demonstrated for a representative turbine blade exposed to turbulent wind loading. It is found that the present explicit tuning procedure yields close to optimal tuning, with very limited modal spill-over and effective reduction of the vibration amplitudes.

Keywords: Resonant control, rotating beam elements, aeroelastic beam elements, edgewise damping.

1 Introduction

Vibrations in rotating or idling wind turbine blades is a common phenomenon due to the relatively large and slender proportions of modern blades. Flapwise vibration modes are typically well-damped by aerodynamic forces, while edgewise vibration modes may have low aerodynamic damping ratios. Therefore, the present paper considers introduction of damping to specific edgewise vibration modes in the wind turbine blade, using an active collocated resonant control strategy.

The present work adopts a recently developed design procedure for resonant control systems, [1, 2]. The controller is governed by a set of second-order filters with either displacement or acceleration sensor feedback. The controller is assumed to be collocated, i.e. sensors and actuators are assumed to operate in pairs with shared physical points of attachment. Actuator feedback can e.g. take the form of forces, applied either from an external source at a single discrete point or from internal devices with two distinct attachment points. An example of an internal device is the active strut, which is a one-dimensional device capable of generating an axial force [3]. When attached between two cross-sections of e.g. a wind turbine blade, as illustrated in Fig. 1, local bending moments can be applied to extract energy from edgewise blade vibrations.

In the adopted scheme [1,2] the controller parameters are tuned according to the observation that optimal damping of the targeted mode is established for equal damping of the two closely spaced modes that replace the original mode when the controller is introduced into the system. An explicit quasi-static correction of controller parameters accounts for the additional flexibility from the higher modes of the structure.

A compact formulation for three-dimensional, two-node finite beam elements in a rotating frame of reference is adopted [4]. In this formulation general inertial and elastic properties of the beam can be accounted for through the formulation of kinetic and complementary elastic energy [5]. Furthermore, geometric stiffness effects are introduced by a linearized initial stress formulation [6].

In order to investigate the controller performance on an aeroelastic wind turbine blade, the aerodynamic forces on the beam elements are introduced in a state-proportional format. The formulation is based on the relative inflow angles [7, 8], and varying locations of the aerodynamic centers and the shear center are accounted for. The resulting aeroelastic model allows for direct finite element-based eigensolution analysis and time simulation of the rotating aeroelastic beam structure.

The performance of the resonant controller is

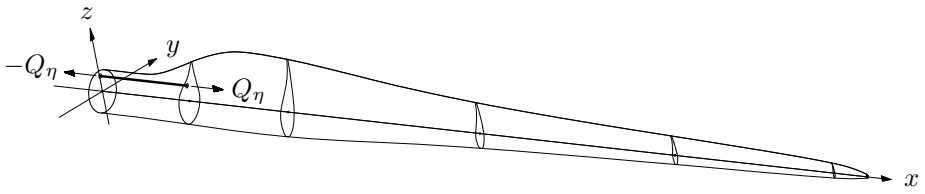

Figure 1: An active strut applied to a wind turbine blade.

finally demonstrated in terms of a $42\,\mathrm{m}$ wind turbine blade, where the aim is to provide a desired level of additional damping of the first edgewise vibration mode. The example blade incorporates representative structural and aerodynamic properties of a MW turbine blade but is modelled with a reduced structural damping in order to better illustrate the qualities of the resonant control. The active device is an active strut with acceleration feedback. The actuator is located at the root of the blade where the controllability of the critical mode is large, and it is demonstrated that the properly tuned controller yields a significant reduction of the edgewise vibrations of the blade for realistic turbulent wind loading.

2 Rotating beam element

The turbine blade is modeled by three-dimensional two-node finite beam elements in a rotating frame of reference [4]. The frame rotates about its origin described by the angular velocity vector $\boldsymbol{\omega}^T = [\,\omega_x,\,\omega_y,\,\omega_z\,]$ and the associated angular acceleration $\boldsymbol{\alpha} = \dot{\boldsymbol{\omega}}$. Cross-sections remain planar and the kinematics of the beam are described through the cross-section displacements $\mathbf{q}^T = [\,q_x,\,q_y,\,q_z\,]$ and rotations $\mathbf{r}^T = [\,r_x,\,r_y,\,r_z\,]$ with respect to the element reference axes $\{x,\,y,\,z\}$. In the present formulation the pitch axis of the blade defines the longitudinal axis x, as shown in Fig. 1. Nodal values of the cross-section displacements and rotations are organized in the vector $\mathbf{u}^T = [\,\mathbf{q}_a^T,\,\mathbf{r}_a^T,\,\mathbf{q}_b^T,\,\mathbf{r}_b^T\,]$, where subscripts a and b denote the two element nodes. Substitution of kinetic and elastic energy into Lagrange's equations leads to the following format of the element equations of motion,

$$\mathbf{M}\ddot{\mathbf{u}} + 2\mathbf{G}\dot{\mathbf{u}} + \mathbf{K}\mathbf{u} = \mathbf{f}_e + \mathbf{f}_C - \mathbf{f}_G \qquad (1)$$

where $\mathbf{M}$ is the mass matrix associated with motion in the local frame of reference, $\mathbf{f}_e$ is the external force vector, $\mathbf{G}(\boldsymbol{\omega})$ is the skew-symmetric gyroscopic coupling matrix, $\mathbf{f}_C(\boldsymbol{\omega})$ is the centrifugal force and $\mathbf{f}_G(\boldsymbol{\alpha})$ is the angular acceleration force. The stiffness matrix $\mathbf{K}$ is given as

$$\mathbf{K} = \mathbf{K}_e + \mathbf{K}_g + \dot{\mathbf{G}} - \mathbf{C} \qquad (2)$$

The elastic stiffness matrix $\mathbf{K}_e$ is derived from a formulation of the complementary elastic energy [5], accounting for lengthwise variation of elastic properties of the cross-sections. The centrifugal stiffness effect is contained in the symmetric matrix $\mathbf{C}(\boldsymbol{\omega})$, and implies apparent softening of the beam. This softening is balanced by the corresponding geometric stiffening of the beam, represented in (2) by the geometric stiffness matrix $\mathbf{K}_g(\boldsymbol{\sigma})$. In the present case the geometric stiffness matrix $\mathbf{K}_g$ follows from a formulation of the potential energy associated with an initial stress state $\boldsymbol{\sigma}^0$ [6]. This formulation is based on an initial stress field $\boldsymbol{\sigma} = \boldsymbol{\sigma}^0$ in the undeformed beam. Hereby the associated geometric stiffness matrix becomes constant, once the initial stresses have been determined. In the present case this assumption is relaxed by replacing the initial stresses with the stresses obtained from an equilibrium state at current time. In time simulations the equilibrium state can be established based on the internal stresses from the previous time step, or by a few iteration loops within the present time step. The internal stress state is expressed by the section forces $\mathbf{Q}^T = [\,Q_x,\,Q_y,\,Q_z\,]$ and moments $\mathbf{M}^T = [\,M_x,\,M_y,\,M_z\,]$, which are contained in the element vector $\mathbf{f}_r^T = [\,\mathbf{Q}_a^T,\,\mathbf{M}_a^T,\,\mathbf{Q}_b^T,\,\mathbf{M}_b^T\,]$, and the section forces can then be determined via the equilibrium equation on element level as

$$\mathbf{f}_r = \mathbf{M}\ddot{\mathbf{u}} + 2\mathbf{G}\dot{\mathbf{u}} + \mathbf{K}\mathbf{u} - (\mathbf{f}_e + \mathbf{f}_C - \mathbf{f}_G) \qquad (3)$$

The section forces $\mathbf{Q}$ and moments $\mathbf{M}$ are energetically conjugate to the displacements $\mathbf{q}$ and the rotations $\mathbf{r}$. Internal axial forces Q_x due to the centrifugal forces $\mathbf{f}_C$ generate the well-known centrifugal stiffening effect, while internal shear forces $Q_y,\ Q_z$ and bending moments $M_y,\ M_z$ generate bending/torsion couplings.

For stationary rotation with $\boldsymbol{\alpha} = \mathbf{0}$ the system matrices of (1) are constant. If the effect of the centrifugal force is included only in terms of the resulting initial stresses, the homogeneous part of (1) describes a linear system with natural eigenfrequencies and associated eigenvectors. For a rotor system with cantilever blades, $\mathbf{K}$ and $\mathbf{M}$ are symmetric and positive definite, while $\mathbf{G}$ is skew-symmetric. In a state-space formulation this leads to purely imaginary eigenval-

ues, appearing in conjugate pairs with associated complex-valued eigenmodes [9].

3 Aerodynamic effects

In this section a formulation for the state-proportional aerodynamic forces is developed. A constant aerodynamic forcing term $\mathbf{f}_a$ arises corresponding to the undeformed structural geometry, while a stiffness term $\mathbf{K}_a\mathbf{u}$ and a damping term $\mathbf{D}_a\dot{\mathbf{u}}$ arise from deformation-induced changes in inflow angle.

3.1 Angle of attack

Figure 2 illustrates a typical operational position of a wind turbine profile. The profile is shown with a combined pitch and twist angle β in the positive direction, and a direction of the relative wind flow speed W corresponding to a positive flow angle α_W. The profile chord is indicated by the dotted line.

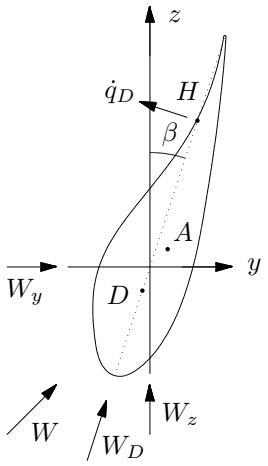

Figure 2: Airfoil and flow velocities.

Aerodynamic lift is assumed to be proportional to the inflow angle α, defined as

$$\alpha = \alpha_f + \alpha_K + \alpha_D \tag{4}$$

where α_f is the inflow angle component in the undeformed position of the aerodynamic profile, α_K is the inflow angle component due to twist of the profile and α_D is the relative inflow angle component due to the transverse velocity of the profile. The spatial position of the profile is expressed by $\mathbf{x}^T = [\,x,\, y,\, z\,]$, which defines the profile intersection with the element reference axis.

The mean wind flow angle α_W is given by the relation

$$\tan\alpha_W = W_y/W_z \tag{5}$$

where W_y is the atmospheric wind speed in the y-direction and $W_z = \|\boldsymbol{\omega} \times \mathbf{x}\|$ is the profile velocity due to the angular blade velocity. The mean inflow angle α_f may then be written as

$$\alpha_f = \alpha_W - \beta + \alpha_0 \tag{6}$$

where α_0 represents a constant lift contribution due to profile camber.

The inflow angle component due to cross-section torsion α_K is written as

$$\alpha_K = r_x \tag{7}$$

where r_x is the torsional degree of freedom. This part of the aerodynamic inflow angle is proportional to the state deformation and therefore results in an aerodynamic stiffness term.

The last term of (4) is based on the relative inflow angle generated by the characteristic profile velocity $\dot{q}_D$, perpendicular to the chord as shown in Fig. 2. For airfoils with rotational oscillations, $\dot{q}_D$ is measured at the rear aerodynamic center H, located on the chord one quarter of the chord length from the trailing edge [10]. This leads to the following expression for $\dot{q}_D$,

$$\dot{q}_D = \dot{q}_z \sin\beta - \dot{q}_y \cos\beta + \dot{r}_x h \tag{8}$$

where h is the chordwise distance between the shear center A with coordinates $\mathbf{a}^T = [\,a_x,\, a_y,\, a_z\,]$ and the rear aerodynamic center H with coordinates $\mathbf{h}^T = [\,h_x,\, h_y,\, h_z\,]$,

$$h = \|\mathbf{h}\| - \frac{\mathbf{h}^T\mathbf{a}}{\|\mathbf{h}\|} \tag{9}$$

The shear center is defined as the point in a cross-section where a shear force will not introduce torsion. The cross-section rotates about the shear center when subjected to a torsional moment.

The relative inflow angle component α_D can be determined from the relation $\sin\alpha_D = \dot{q}_D/W_D$, where

$$W_D = W\cos(\alpha_W - \beta) \tag{10}$$

is the flow speed parallel to the chord. For small angles, i.e. $\dot{q}_D \ll W_D$, the following approximation can be made,

$$\alpha_D \simeq \frac{1}{W_D}\big(\dot{q}_z \sin\beta - \dot{q}_y \cos\beta + \dot{r}_x h\big) \tag{11}$$

Substitution of (6), (7) and (11) into (4) gives the following expression for the inflow angle α,

$$\begin{aligned}\alpha = {} & \alpha_W + \beta + \alpha_0 + r_x \\ & + \frac{1}{W_D}\big(\dot{q}_z \sin\beta - \dot{q}_y \cos\beta + \dot{r}_x h\big)\end{aligned} \tag{12}$$

The last part of the aerodynamic inflow angle is proportional to the velocity states, hence representing aerodynamic damping.

3.2 Aerodynamic element forces

The aerodynamic pressure distribution is assumed to correspond to a resulting lift force F_L, perpendicular to the flow angle α_W, and a resulting drag force F_D, parallel to the flow angle α_W. The two forces are assumed to act through the aerodynamic center D with coordinates $\mathbf{d}^T = [\, d_x,\, d_y,\, d_z \,]$. For a thin flat plate the aerodynamic center is located one quarter of the plate width from the leading edge. The aerodynamic forces F_L and F_D are organized in the vector $\mathbf{F}_W$ and given as

$$\mathbf{F}_W = \begin{bmatrix} F_L \\ F_D \end{bmatrix} = \tfrac{1}{2}\varrho_a C W^2 \alpha \begin{bmatrix} C'_L \\ C'_D \end{bmatrix} \qquad (13)$$

where ϱ_a is the air mass density, C is the chord length, and C'_L, C'_D are lift and drag curve inclinations. The wind velocity W relative to the aerodynamic profile is given as

$$W = \sqrt{W_y^2 + W_z^2} \qquad (14)$$

By insertion of (12) into (13) the following expression for $\mathbf{F}_W$ can be written,

$$\mathbf{F}_W = \mathbf{F} + \mathbf{A}_K \begin{bmatrix} \mathbf{q} \\ \mathbf{r} \end{bmatrix} + \mathbf{A}_D \begin{bmatrix} \dot{\mathbf{q}} \\ \dot{\mathbf{r}} \end{bmatrix} \qquad (15)$$

where the matrices $\mathbf{A}_K$ and $\mathbf{A}_D$ are given in Appendix A. Aerodynamic forces $\mathbf{Q}_a$ and moments $\mathbf{M}_a$ acting at the element reference axis are written as

$$\begin{bmatrix} \mathbf{Q}_a \\ \mathbf{M}_a \end{bmatrix} = \mathbf{T}\mathbf{R}\mathbf{F}_W \qquad (16)$$

Here $\mathbf{R}$ is a transformation matrix for rotation of $\mathbf{F}_W$ into equivalent forces in D aligned with the element coordinate system, and $\mathbf{T}$ is a transformation matrix that establishes the equivalent forces and moments at the reference axis. The matrices $\mathbf{R}$ and $\mathbf{T}$ are given in Appendix A.

Element nodal forces and moments are obtained by the virtual work δV expressed in terms of the conjugate virtual displacements $\delta\mathbf{q}$ and rotations $\delta\mathbf{r}$,

$$\delta V = \int_L \left[\, \delta\mathbf{q}^T,\ \delta\mathbf{r}^T \,\right]^T \begin{bmatrix} \mathbf{Q}_a \\ \mathbf{M}_a \end{bmatrix} dx \qquad (17)$$

The displacement field is interpolated via nodal degrees of freedom $\mathbf{u}$ and shape functions $\mathbf{N}(x)$, such that

$$\begin{bmatrix} \mathbf{q} \\ \mathbf{r} \end{bmatrix} = \mathbf{N}(x)\mathbf{u} \qquad (18)$$

Inserting (18) into (17) leads to the following expression for the virtual work,

$$\delta V = \delta\mathbf{u}^T \int_L \mathbf{N}^T \begin{bmatrix} \mathbf{Q}_a \\ \mathbf{M}_a \end{bmatrix} dx \qquad (19)$$

Substitution of (15) into (16), followed by substitution into (19) implies that the virtual work by the external load can be written as $\delta V = \delta\mathbf{u}^T\mathbf{f}$, whereby the resulting force vector can be identified as

$$\mathbf{f} = \mathbf{f}_a + \mathbf{K}_a\mathbf{u} + \mathbf{D}_a\dot{\mathbf{u}} \qquad (20)$$

where the aerodynamic force vector $\mathbf{f}_a$, the aerodynamic stiffness matrix $\mathbf{K}_a$ and the aerodynamic damping matrix $\mathbf{D}_a$ are given in Appendix A.

The aerodynamic stiffness matrix is not necessarily positive definite. Thus, aerodynamic stiffness effects may reduce or increase structural eigenfrequencies. The aerodynamic damping matrix is non-symmetric, and thus the classic modal decoupling via orthogonal eigenmodes does not apply directly. This implies that modes may be energetically coupled, i.e. vibration energy may be transferred between modes. Finally, the damping matrix is not necessarily positive definite, which means that the vibration modes may be negatively damped.

4 Resonant vibration control

In this section the filters of the resonant controller are defined as transfer functions in the frequency domain, and the tuning procedure for a system with acceleration feedback is presented. Details about the tuning procedure are given in [1, 2].

4.1 Controller format

The objective of the controller is to extract modal energy by imposing a specifically tuned resonant force to the structure. Actuator feedback is represented by the force vector $\mathbf{f}_\eta$, and the resulting structural equations of motion become

$$\begin{aligned} \mathbf{M}\ddot{\mathbf{u}} + \mathbf{D}\dot{\mathbf{u}} + \mathbf{K}\mathbf{u} = \\ \mathbf{f}_e + \mathbf{f}_C - \mathbf{f}_G + \mathbf{f}_a + \mathbf{f}_\eta \end{aligned} \qquad (21)$$

The system (21) is the complete representation of the aeroelastic beam, where the system damping matrix $\mathbf{D}$ is the sum of the gyroscopic matrix $\mathbf{G}$ and the aerodynamic damping matrix $\mathbf{D}_a$,

$$\mathbf{D} = 2\mathbf{G} - \mathbf{D}_a \qquad (22)$$

and where the system stiffness matrix $\mathbf{K}$ is

$$\mathbf{K} = \mathbf{K}_e + \mathbf{K}_g + \dot{\mathbf{G}} - \mathbf{C} - \mathbf{K}_a \qquad (23)$$

The resonant controller is conveniently defined in the frequency domain. The beam is assumed to rotate with constant angular velocity $\boldsymbol{\omega}$, i.e. $\boldsymbol{\alpha} = \mathbf{0}$ and $\mathbf{f}_G = \mathbf{0}$. Deformations due to the

constant centrifugal force are neglected, while maintaining the associated contribution to the geometric stiffness. For a harmonic external force $\mathbf{f}_e$ with angular frequency ω, a stationary solution $\mathbf{u}e^{i\omega t}$, where i is the imaginary unit, is assumed for the system (21). The equations of motion in the frequency domain can be written as

$$\left(\mathbf{K} + i\omega\mathbf{D} - \omega^2\mathbf{M}\right)\mathbf{u} = \mathbf{f}_e + \mathbf{f}_\eta \qquad (24)$$

Following [1, 2] the controller forces $\mathbf{f}_\eta$ are defined as

$$\mathbf{f}_\eta = -G_{q\eta}(\omega)\mathbf{w}\eta \qquad (25)$$

where $G_{q\eta}(\omega)$ is the actuator feedback transfer function and $\mathbf{w}$ is the controller connectivity vector, representing the physical attachment of the controller to the beam structure. The variable η is the controller state, governed by the feedback equation,

$$G_{\eta\eta}(\omega)\eta = -G_{\eta q}(\omega)q \qquad (26)$$

where $G_{\eta\eta}(\omega)$ is the controller transfer function and $G_{\eta q}(\omega)$ is the sensor feedback transfer function. The controller transfer function is a second order filter representing the inherent resonant properties of the device. The scalar quantity q represents the structural displacement over the actuator,

$$q = \mathbf{w}^T\mathbf{u} \qquad (27)$$

The fact that the controller is collocated results in both the sensor and actuator feedback being defined in terms of the controller connectivity vector $\mathbf{w}$. A general procedure for defining $\mathbf{w}$ for three-dimensional finite beam elements is given in [4].

4.2 Definition and tuning of filters

According to [1, 2], the resonant controller operating with acceleration feedback is defined by the transfer functions

$$\begin{aligned} G_{\eta\eta}(\omega) &= \omega_\eta^2 - \omega^2 + 2i\zeta_\eta\omega_\eta\omega, \\ G_{\eta q}(\omega) &= -\omega^2, \\ G_{q\eta}(\omega) &= \left(\alpha_\eta\omega_\eta^2 + \beta_\eta 2i\zeta_\eta\omega_\eta\omega\right)/\nu_1^2 \end{aligned} \qquad (28)$$

Here ζ_η, ω_η, α_η and β_η are tuning parameters defined by the explicit tuning procedure given in Appendix B.

The controller tuning is based on an initial tuning for an equivalent single-degree-of-freedom system with the properties of the targeted structural mode. Subsequently a correction is performed to account for the additional structural flexibility from background modes. This additional flexibility is represented by the modal quasi-static flexibility parameter κ_n,

$$\kappa_n = \left(\frac{\omega_n}{\nu_n}\right)^2 \mathbf{w}^T\mathbf{K}^{-1}\mathbf{w} - 1 \qquad (29)$$

This expression contains the nodal connectivity parameter ν_n, which represents the magnitude of the mode shape over the controller,

$$\nu_n = \mathbf{w}^T\mathbf{u}_n \qquad (30)$$

where $\mathbf{u}_n$ is the targeted mode shape.

By introduction of the augmented state vector $\mathbf{u}_\eta = [\,\mathbf{u}^T,\, \eta]^T$, the linear closed-loop system equations for free vibrations can be written as

$$\mathbf{M}_\eta\ddot{\mathbf{u}}_\eta + \mathbf{D}_\eta\dot{\mathbf{u}}_\eta + \mathbf{K}_\eta\mathbf{u}_\eta = \begin{bmatrix} \mathbf{f}_C + \mathbf{f}_G + \mathbf{f}_a \\ 0 \end{bmatrix} \qquad (31)$$

where the external force $\mathbf{f}_e$ is omitted. The augmented matrices $\mathbf{M}_\eta$, $\mathbf{D}_\eta$ and $\mathbf{K}_\eta$ are given in Appendix C.

5 Control of edgewise vibrations

In this section an example is given of resonant vibration control of the first edgewise mode of a $42\,\mathrm{m}$ wind turbine blade under typical operating conditions. The blade has structural and aerodynamic properties which are to a reasonable extent similar to those of commercial products. The controller is an active strut with acceleration feedback, attached as shown in Fig. 1.

The example is organized as follows. The turbine blade is presented in Sec. 5.1 in terms of selected structural properties and modal characteristics under the considered operating conditions. In Sec. 5.2 the application and tuning of the controller is described, and the controller performance is illustrated in Sec. 5.3 via time simulation of blade response under realistic, turbulent aerodynamic loading.

5.1 The 42 m wind turbine blade

The $42\,\mathrm{m}$ wind turbine blade is shown in Fig. 1. The blade is a pre-twisted composite structure with material orientations balanced for equivalent isotropic cross-section properties.

Structural properties are given in 46 points along the blade reference axis. In Fig. 3 the distribution of the chord-wise coordinates of the mass center $\bar{g}_C$, the elastic center $\bar{c}_C$, the shear center $\bar{a}_C$ and the aerodynamic center $\bar{d}_C$ are shown. The values are normalized with respect to the root diameter C_0, e.g. $\bar{g}_C = g_C/C_0$, and positive in the direction of the trailing edge. It is seen that cross-section properties vary significantly along the reference axis, and that the

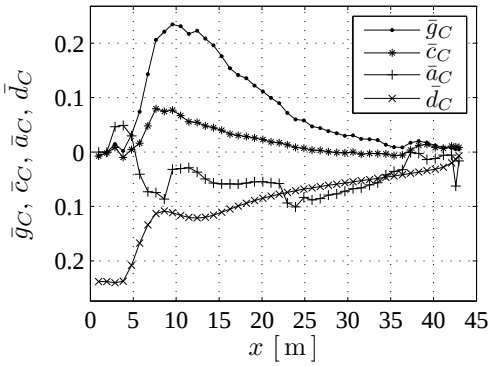

Figure 3: Characteristic coordinates.

mass center, the shear center and the aerodynamic center are generally not coinciding.

The modal characteristics of the blade are determined for the stationary operating conditions with $W_y = 12\,\mathrm{m/s}$, $||\boldsymbol{\omega}|| = 1.57\,\mathrm{rad/s}$ corresponding to $15\,\mathrm{rpm}$, and $\beta_p = 4.4°$. The blade has a coning angle of $\gamma = 6.0°$ relative to the rotor plane.

The blade is modeled using 15 elements, whereby each element spans approximately three data points, of which two are located at the element ends. Cross-section properties are interpolated linearly between data points. Hermitian shape functions are used for interpolation of transverse displacements and linear functions are used for interpolation of axial displacements and rotations. The integrals $(\mathrm{A}.5)$ are evaluated numerically by Lobatto quadrature [11], which takes end-point values into account.

Geometric stiffness effects are determined according to the section forces and moments introduced by centrifugal and aerodynamic forces. Centrifugal forces lead to internal axial forces, which generate a stiffening of the blade. Aerodynamic forces lead to internal shear forces and bending moments, by which bending/torsion couplings arise. The eigenfrequency of flapwise modes is generally increased due to the geometric stiffening, whereas this effect is to a large extent counteracted by centrifugal softening in the case of edgewise modes.

Due to the aerodynamic damping term, relatively large damping ratios are found for flapwise modes, e.g. $\zeta_1 = 0.462$ and $\zeta_3 = 0.164$ for the first two, while relatively low damping values are found for the edgewise modes, e.g. $\zeta_2 = 0.007$ and $\zeta_4 = 0.001$ for the first two. In practice, edgewise damping ratios are somewhat higher due to e.g. intrinsic material damping, not represented here.

The first edgewise mode has the eigenfrequency $\omega_2 = 9.17\,\mathrm{rad/s}$ corresponding to $1.46\,\mathrm{Hz}$, and the mode shape $\mathbf{u}_2$ shown in Fig. 4 in terms of local degrees of freedom. The local degrees of freedom refer to the original element coordinate system as shown in Fig. 1, which follows the elements through rotation according to the pitch and coning angles. The mode is normalized such that the largest real part of the local displacement component q_z equals 1 in Fig. 4a. Here the typical vibration mode of a cantilever beam is recognized.

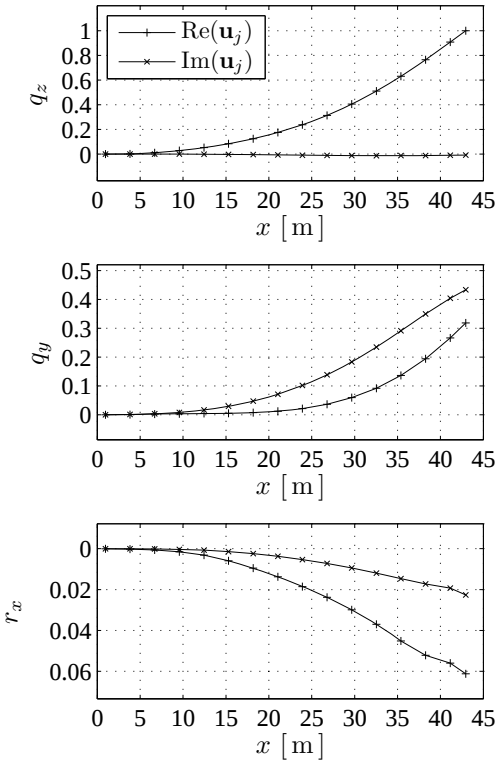

Figure 4: Mode shape $\mathbf{u}_2$ for $W_y = 12\,\mathrm{m/s}$.

In Fig. 4b the flapwise displacement component q_y of $\mathbf{u}_2$ is shown. It is seen that both a real part in phase with q_z and an imaginary part with a $\pi/2$ phase difference to q_z is present. The in-phase part represents an elastic (q_y, q_z)-coupling due to the pre-twist of the blade. The part of q_y which is $\pi/2$ out of phase with q_z is generated by gyroscopic forces and aerodynamic damping forces, of which the aerodynamic contribution is predominant in the present case.

The modal torsional rotation components r_x are shown in Fig. 4c. The real components are generated by the shear- and mass centers being non-coinciding, and this presence of torsion results in aerodynamic stiffening of the vibration mode. The imaginary components of r_x are generated by the shear- and aerodynamic centers being non-coinciding, whereby aerodynamic damping forces induce torsional moments.

5.2 Controller Application and Tuning

The first edgewise vibration mode has been shown to have a low aerodynamic damping ratio. In this section a collocated active strut with acceleration feedback is applied to the turbine blade in order to introduce additional damping into this particular mode. The choice of physical placement and the explicit tuning of the controller is based on the modal characteristics shown in the previous section.

The first edgewise vibration is primarily a bending mode in the local z-direction, in which the largest curvatures occur at the fixed end of the blade. Thus, for optimized modal controllability and observability, the active strut is fitted at the blade root with a finite distance in the local z-direction to the elastic center. Bending moments can hereby be induced to control the dominant components of the addressed mode. The attachment points are denoted V_1 and V_2, where V_1 is located at the root cross-section with local coordinates $[\,v_x^1,\, v_y^1,\, v_x^1\,] = [\,1.00,\, 0.05,\, 0.70\,]\,\mathrm{m}$ and V_2 is located $6.00\,\mathrm{m}$ into the blade, i.e. with local coordinates $[\,v_x^2,\, v_y^2,\, v_x^2\,] = [\,7.00,\, 0.05,\, 0.70\,]\,\mathrm{m}$. Thus, the length of the active strut is $6.00\,\mathrm{m}$. The finite, positive components v_y^1, v_y^2 are chosen due to the inclined modal cross-section vibration path induced by the components q_y of mode 2.

A few of the higher vibration modes of the free structure are negatively damped by aerodynamic forces. In order to stabilize these modes in time integration, a moderate amount of Rayleigh damping and algorithmic α-damping is added to the system. This increases the 'inherent' damping ratio of mode 2 in the uncontrolled reference system to $\zeta_2 = 0.009$.

The controller is tuned according to the modal properties under the stationary operating conditions of $W_y = 12\,\mathrm{m/s}$, $||\boldsymbol{\omega}|| = 1.57\,\mathrm{rad/s}$ corresponding to $15\,\mathrm{rpm}$ and $\beta_p = 4.4°$. The desired additional amount of damping is set to $\Delta\zeta = 0.060$. The physical connection of the controller defines the modal connectivity parameter ν_2 and the modal quasi-static flexibility parameter κ_2, and the controller parameters are subsequently determined according to the formulas (B.1)-(B.4). The resulting values are given in Table 1.

When the controller is applied, the targeted mode splits into two new, closely spaced modes. For optimal tuning the two modes have equal damping ratios $\zeta_{n,1}$ and $\zeta_{n,2}$. In the present case the deviations of $\zeta_{2,1}$ and $\zeta_{2,2}$ from the mean value $\bar{\zeta}_2 = (\zeta_{2,1} + \zeta_{2,2})/2$ are $\pm 0.92\%$. The blade tip displacement frequency response in the local z-direction according to simultaneous unit tip loads in the y- and z-directions is shown in Fig. 5. The two vertical dotted lines indicate the eigenfrequencies ω_1 and ω_2 of the uncontrolled system. The uncontrolled frequency response is seen to have a significant resonant peak at ω_2, whereas the controlled system is clearly reduced. The slightly sub-optimal tuning results in the small lack of symmetry of the two damped response peaks.

Table 1: Controller parameters.

$\zeta_c \cdot 10^{-1}$	1.200	$\beta_c \cdot 10^{-2}$	2.965
ω_c	8.902	$\alpha_c \cdot 10^{-2}$	2.965
κ_2	7.231	$\beta_\eta \cdot 10^{-2}$	2.442
$\lvert\nu_2\rvert^2 \cdot 10^{-8}$	2.360	$\alpha_\eta \cdot 10^{-2}$	2.965
ω_η	9.967	$\zeta_{2,1} \cdot 10^{-2}$	6.625
$\zeta_\eta \cdot 10^{-1}$	1.632	$\zeta_{2,2} \cdot 10^{-2}$	6.747

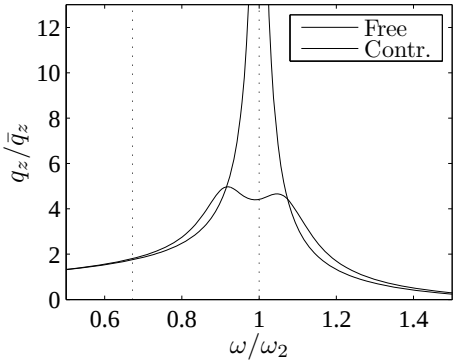

Figure 5: Edgewise tip displacement frequency response to flap- and edgewise load.

The present limitation of the controller tuning quality is due to the complex structural configuration of the turbine blade. The significant blade twist implies that modes generally consist of displacements in both the y- and z-directions. Thus, structural feedback will in principle contain unwanted contributions from all structural modes. Similarly, controller feedback will, in principle, induce a general excitation of structural modes. However, a key property of the controller is the very limited amount of modal spill-over. This is due to the narrow, frequency-wise band of actuator forces due to the inherent resonant nature of the controller. Table 2 shows the first four eigenfrequencies and damping ratios of the free and controlled system. A small amount of spill-over in terms of added damping is seen to the second edgewise mode (mode 4), while the flapwise modes (modes 1 and 3) are practically unaffected by the controller.

The mean added damping is $\bar{\zeta}_2 - \zeta_2^{fr} = 0.058$,

Table 2: Eigenfrequencies and damping ratios.

n	ζ_n^{fr}	ζ_n^{ctr}	ω_n^{fr}	ω_n^{ctr}
1	0.464	0.463	6.12	6.16
2,1	0.009	0.066	9.17	8.38
2,2	-	0.068	-	9.76
3	0.167	0.167	16.6	16.6
4	0.007	0.019	27.7	28.1

which is somewhat smaller than the desired value, $\Delta\zeta = 0.060$. This is due to the fact that the effect of a local damper can not be added directly for damped structures. An accurate formula for the combined effect has been given in [12].

In the simpler case of prismatic beams with complex dynamic properties, close to optimal tuning can be obtained [4]. For the present purpose the tuning quality is however highly satisfactory. This is further demonstrated in the following section.

5.3 Controlled System Response

In the following the controller performance is demonstrated via time simulation of free and controlled blade responses. The blade is subjected to a realistic $600\,\mathrm{s}$ turbulent wind field with the average wind speed $\bar{W}_y = 12\,\mathrm{m/s}$. Full spatial correlation of wind velocities is assumed for simplicity.

The simulation is performed with prescribed angular velocity $\boldsymbol{\omega}$ and angular acceleration $\boldsymbol{\alpha}$. A spin-up sequence during the first three seconds accelerates the blade from a complete rest to the angular velocity $||\boldsymbol{\omega}|| = 1.57\,\mathrm{rad/s}$ corresponding to $15\,\mathrm{rpm}$, which is kept constant at this level for the remaining simulation time. The blade pitch is kept constant at $\beta_p = 4.4°$, regardless of wind speed fluctuations.

In Fig. 6 sequences of the local edgewise blade tip displacements q_z are shown. The time scale is normalized with the period of mode 2, T_2. In the free response, significant oscillations at the frequency of mode 2 are seen. In the controlled response these oscillations are reduced, while the quasi-static 'mean' vibration path is practically unchanged. This demonstrates the frequency-specific targeting of controller forces obtained in the controller tuning.

The local flapwise displacements q_y are shown in Fig. 7. It is seen that the free and controlled responses are almost identical. This demonstrates the specific kinematic targeting of controller forces, achieved by placement of the controller such that bending moments are primarily induced about the principal axes about which

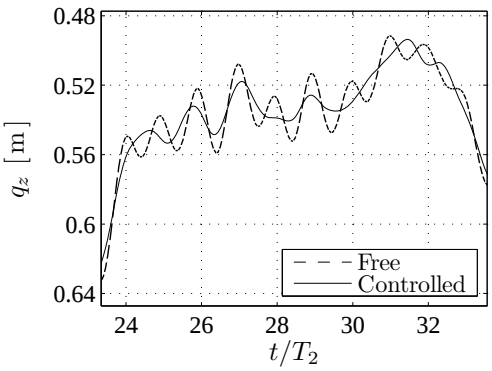

Figure 6: Edgewise tip displacements.

cross-sections rotate to generate displacements in the z-direction. The blade pre-twist implies that the orientation of principal axes varies along the beam, and particularly, over the extension of the controller.

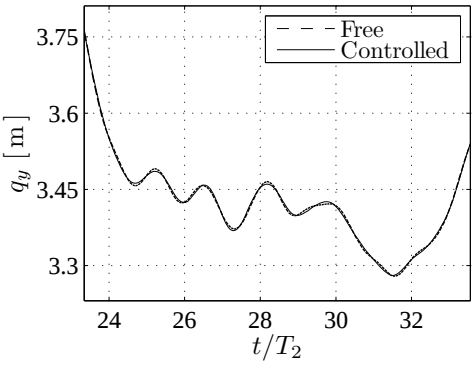

Figure 7: Flapwise tip displacements.

One objective of actively adding damping to one or more specific modes may be to reduce material damaging from cyclic loading. Displacements generated by mode 2 induce the largest material strains ε_u on the surface of the blade root, near the intersections between the surface and the local z-axis. In Fig. 8 the root surface strains ε_u are plotted. The root surface strains are here determined as $\varepsilon_u = Q_x/A^E + \frac{1}{2}s_z M_y/I_{yy}^E$, where A^E is the axial cross-section stiffness, I_{yy}^E is the cross-section bending stiffness about the y-axis and s_z is the distance from the element reference axis to the intersection between the blade surface and the the local z-axis in the positive direction.

The values of ε_u are positive, corresponding to elongation. It is seen that the amplitude of variations in surface strains due to vibrations in mode 2 are significantly reduced by the controller. Furthermore, the shown strains are determined at a physical location close to the active device where significant axial control forces Q_η are applied.

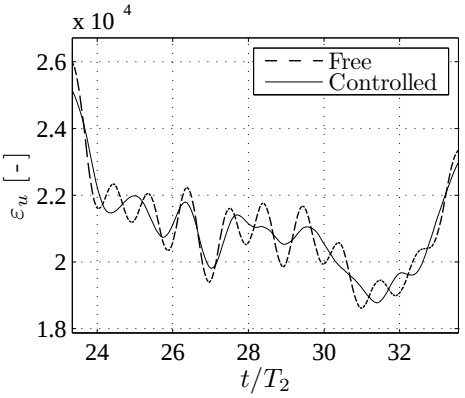

Figure 8: Root surface strains ε_u.

This illustrates one of the key features of the resonant controller, namely that the forces induced by the controller are always beneficial in terms of material loading, compared to those induced by vibrations in the targeted mode.

The necessary actuator forces for the resonant controller in the present application can be generated by standard, commercial electric linear servo actuators. The performance of these actuator systems is typically defined in terms of maximum continuous or peak axial force versus axial controller velocity. The axial controller velocity is shown in Fig. 9, and the values have been found to be well within the capable range of available products.

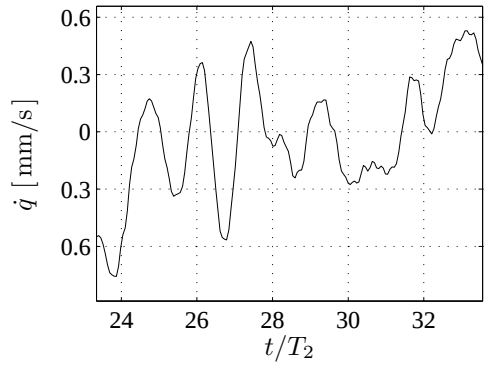

Figure 9: Controller velocity $\dot{q}$.

Figure 10 shows the controller axial force Q_η. The force is seen to operate at a frequency close to ω_2. This demonstrates the resonant, narrow band operating region of the controller. It is furthermore noted that the actuator feedback operates about a zero mean value. This is due to the acceleration feedback, by which the controller is not affected by a static mean deflection of the structure. For wind turbine blades this feature becomes relevant, as different mean aerodynamic blade loads are associated with different operation states. A concern in this matter then falls upon the ability of actuator systems to operate with the required stroke amplitudes. In the present case the following key actuator parameters are found: Maximum force $|Q_\eta|^{max} = 14.7\,\mathrm{kN}$, maximum velocity $|\dot{q}|^{max} = 1.52\,\mathrm{mm/s}$ and maximum stroke $|q|^{max} = 4.90\,\mathrm{mm}$. These values are within the range of commercially available actuators, such as electric linear servo drives or electro-hydraulic linear actuators with pistons driven by pressurized oil.

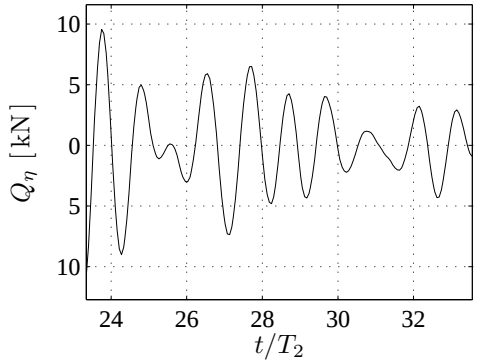

Figure 10: Controller force Q_η.

Requirements to the acceleration sensor are not presented here. Standard sensor systems are available which easily accommodate the scale of the present problem, both in terms of frequency resolution and tolerated levels of operation. The controller sensitivity towards noise from global blade accelerations is furthermore minimized by the fact that relative structural accelerations are measured.

The present study of requirements to the active device indicates that practical implementation of the resonant control method towards edgewise vibrations in wind turbine blades is well within range. In a more design oriented analysis, finite dynamics of the actuator and its mechanical connection should be taken into account when tuning the control parameters.

6 Conclusion

It has been demonstrated that a collocated resonant controller with acceleration feedback, here used for an active strut with acceleration feedback, is effective and robust in providing additional damping to a selected vibration mode of a wind turbine blade.

Close to optimal tuning with very limited modal spill-over is obtained from the explicit tuning procedure, despite the complex elastic, gyroscopic and aerodynamic couplings in the dynamics of the flexible structure.

The time simulation of the turbine blade demonstrates that the active controller effec-

tively reduces the otherwise significant vibration amplitudes in the targeted edgewise mode, while being always beneficial in terms of material loading, both globally and locally.

While mode 2 is damped, the remaining vibration modes are practically unaffected. The insignificant spill-over demonstrates that controller efforts are effectively limited to the intended purpose. The found requirements to the active device indicate that implementation of the resonant control method towards edgewise vibrations in wind turbine blades is well within practical range.

The structural model adopts a formulation for three-dimensional, two-node finite beam elements in a local, rotating frame of reference. The element allows for high-accuracy modeling of structures with arbitrary mass distributions, general elastic properties and geometric stiffness effects due to internal stresses. Here a compact formulation for state-proportional aerodynamic forces on the same element type has been established. In this formulation, varying locations of the aerodynamic centers and the shear center are accounted for, and the resulting aerodynamic stiffness and damping terms can be added directly to the structural model. The resulting model allows for direct, finite element-based eigensolution analysis and time simulation of rotating, aeroelastic beam structures.

The present combination of the aeroelastic blade model with the explicit procedure for application and tuning of active, collocated resonant controllers represents a compact theoretical basis for effective and robust damping of modal vibrations in wind turbine blades.

References

[1] S. Krenk, J. Høgsberg, Optimal resonant control of flexible structures, *Journal of Sound and Vibration*, 323 (2009) 530–554.

[2] S. Krenk, J. Høgsberg, Resonant damping of flexible structures, *COMPDYN 2009, ECCOMAS Thematic Conference on Computational Methods in Structural Dynamics and Earthquake Engineering* (2009).

[3] A. Preumont, B. de Marneffe, A. Deraemaeker, F. Bossens, The damping of a truss structure with a piezoelectric transducer, *Computers & Structures*, 86 (2008) 227–239.

[4] M. N. Svendsen, S. Krenk, J. Høgsberg, Resonant vibration control of rotating beams, *To be published*, (2010).

[5] S. Krenk, *Element stiffness matrix for beams with general cross-section properties*, Technical University of Denmark, Department of Mechanical Engineering, (2006).

[6] S. Krenk, *Lectures on thin-walled beams*, Technical University of Denmark, Department of Mechanical Engineering, (2006).

[7] J. W. Larsen, S. R. K. Nielsen, S. Krenk, Dynamic stall model for wind turbine airfoils, *Journal of Fluids and Structures*, 23 (2007) 959–982.

[8] M. H. Hansen, Aeroelastic instability problems for wind turbines, *Wind Energy*, 10 (2007) 551–557.

[9] M. Géradin, D. Rixen, *Mechanical Vibrations*, second ed., Wiley, Chichester, 1997.

[10] Y. C. Fung, *An Introduction to the Theory of Aeroelasticity*, Dover, Mineola, New York, 1993.

[11] T. J. R. Hughes, *The Finite Element Method, Linear Static and Dynamic Finite Element Analysis*, Dover, Mineola, New York, 2000.

[12] S. Krenk, J. Høgsberg, Tuned mass absorbers on damped structures under random load, *Probabilistic Engineering Mechanics*, 23 (2008) 408–415.

A Aerodynamic terms

$$\mathbf{A}_K = \tfrac{1}{2}\varrho_a C W^2 \begin{bmatrix} 0 & 0 & 0 & C'_L & 0 & 0 \\ 0 & 0 & 0 & C'_D & 0 & 0 \end{bmatrix} \quad (A.1)$$

$$\mathbf{A}_C = \tfrac{1}{2}\varrho_a C \tfrac{W^2}{W_D} \begin{bmatrix} 0 & -C'_L\cos(\beta) & C'_L\sin(\beta) & C'_L h & 0 & 0 \\ 0 & -C'_D\cos(\beta) & C'_D\sin(\beta) & C'_D h & 0 & 0 \end{bmatrix} \quad (A.2)$$

$$\mathbf{R} = \begin{bmatrix} 0 & 0 \\ \cos\alpha_W & \sin\alpha_W \\ -\sin\alpha_W & \cos\alpha_W \end{bmatrix} \quad (A.3)$$

$$\mathbf{T} = \begin{bmatrix} 1 & 0 & 0 \\ 0 & 1 & 0 \\ 0 & 0 & 1 \\ 0 & -d_z & d_y \\ d_z & 0 & 0 \\ -d_y & 0 & 0 \end{bmatrix} \quad (A.4)$$

$$\begin{aligned} \mathbf{f}_a &= \int_L \mathbf{N}^T\mathbf{T}\mathbf{R}\mathbf{F}dx, \\ \mathbf{K}_a &= \int_L \mathbf{N}^T\mathbf{T}\mathbf{R}\mathbf{A}_K dx, \\ \mathbf{D}_a &= \int_L \mathbf{N}^T\mathbf{T}\mathbf{R}\mathbf{A}_D dx \end{aligned} \quad (A.5)$$

B Controller tuning

$$\zeta_c = 2\Delta\zeta, \quad \beta = \frac{2\zeta_c^2}{1-2\zeta_c^2}, \tag{B.1}$$

$$\alpha_\eta = \beta, \quad \beta_\eta = \frac{\beta}{1+\kappa_n\beta}, \tag{B.2}$$

$$\omega_\eta^2 = \frac{1}{1-\dfrac{\kappa_n\beta}{(1+\beta)^2}}\left(\frac{\omega_n}{1+\beta}\right)^2, \tag{B.3}$$

$$\zeta_\eta = \frac{1}{\omega_\eta\left(1+\kappa_n\beta\right)\left(1-\dfrac{\kappa_n\beta}{\left(1+\beta\right)^2}\right)}\frac{\zeta_c\omega_n}{1+\beta} \tag{B.4}$$

C Closed-loop system matrices

$$\mathbf{M}_\eta = \begin{bmatrix} \mathbf{M} & \mathbf{0} \\ -\mathbf{w}^T & 1 \end{bmatrix} \tag{C.1}$$

$$\mathbf{D}_\eta = \begin{bmatrix} \mathbf{D} & \dfrac{\beta_\eta}{\nu_n^2}2\zeta_\eta\mathbf{w} \\ \mathbf{0} & 2\zeta_\eta\omega_\eta \end{bmatrix} \tag{C.2}$$

$$\mathbf{K}_\eta = \begin{bmatrix} \mathbf{K} & \dfrac{\alpha_\eta}{\nu_n^2}\omega_\eta^2\mathbf{w} \\ \mathbf{0} & \omega_\eta^2 \end{bmatrix} \tag{C.3}$$

P3

(Journal paper)

Resonant vibration control of three-bladed wind turbine rotors

Submitted
January 2011

Resonant Vibration Control of Three-Bladed Wind Turbine Rotors

S. Krenk[†], M.N. Svendsen[†,‡] and J. Høgsberg[†]

[†]Department of Mechanical Engineering,
Technical University of Denmark, DK-2800 Lyngby, Denmark

[‡]Vestas Wind Systems A/S,
Hedeager 42, DK-8200 Aarhus N, Denmark

Abstract. Rotors with blades as e.g. in wind turbines are prone to vibrations due to the flexibility of the blades and the support. In the present paper a theory is developed for active control of a combined set of vibration modes in three-bladed rotors. The control system consists of identical collocated actuator-sensor pairs on each of the blades and targets a set of three modes constituting a collective mode with identical motion of all the blades, and two independent whirling modes, in which a relative motion pattern moves forward or backward over the rotor. The natural frequency of the collective mode is typically lower than the frequency of the whirling modes due to support flexibility. The control signals from the blades are combined into a mean signal, addressing the collective mode, and three components from which the mean signal has be subtracted, addressing the pair of whirling modes. The response of the actuators is tuned to provide resonant damping of the collective mode and the whirling modes by using the separate resonance characteristics of the collective and the whirling modes. In the calibration of the control parameters it is important to account for the added flexibility of the structure due to influence of other non-resonant modes. The efficiency of the method is demonstrated by application to a rotor with 42 meter blades, where the sensor-actuator system is implemented in the form of an axial extensible strut near the root of each blade. The load is provided by a simple but fully three-dimensional correlated wind velocity field. It is shown by numerical simulations that the active damping system can provide a significant reduction in the response amplitude of the targeted modes, while applying control moments to the blades that are about one order of magnitude smaller than the moments from the external load.

Nomenclature

$\mathbf{A}, \mathbf{B}$	=	state-space matrices
$\mathbf{C}$	=	centrifugal stiffness matrix
$\mathbf{D}_a$	=	aerodynamic damping matrix
$\mathbf{F}$	=	state-space force
$\mathbf{f}$	=	total force
$\mathbf{f}_e$	=	external force
$\mathbf{f}_c$	=	centrifugal forces
$\mathbf{f}_g$	=	gyroscopic forces
$\mathbf{f}_\eta$	=	control force
$\mathbf{G}$	=	gyroscopic stiffness matrix
$g_\alpha, g_\beta, g_\zeta, g_\omega$	=	effective system control parameters
$G^c(\omega), G^w(\omega)$	=	control filter for collective and whirling modes
i	=	complex imaginary unit

$\mathbf{K}$	=	total stiffness matrix
$\mathbf{K}_a$	=	aerodynamic stiffness matrix
$\mathbf{K}_e$	=	elastic stiffness matrix
$\mathbf{K}_g$	=	geometric stiffness matrix
$\mathbf{M}$	=	mass matrix
q_j	=	modal amplitude of $\mathbf{z}_j$
$\mathbf{R}$	=	wind field covariance matrix
$t, \Delta t$	=	time and simulation time increment
$\mathbf{u}_j$	=	displacements of mode j
$\mathbf{u}_{(k)}$	=	displacements of blade k
V	=	mean wind speed
$\mathbf{v}$	=	turbulent wind component
$\mathbf{v}_C, \mathbf{v}_B, \mathbf{v}_F$	=	Collective, and forward and backward whirling modes
$\mathbf{v}_{(j)}$	=	displacements Fourier coefficients
$\mathbf{W}$	=	controller connectivity for whirling modes
$\mathbf{w}_c$	=	controller connectivity for collective mode
$\mathbf{w}_j$	=	controller connectivity arrays
$\mathbf{x}_j, \mathbf{y}_j$	=	real and imaginary part of $\mathbf{z}_j$
$\mathbf{z}$	=	state-space vector
$\mathbf{z}_j$	=	state-space vector of mode j

Greek

α	=	angle between blades, $\alpha = 120^\circ$
α_c, α_w	=	control parameter of collective and whirling modes
β_c, β_w	=	control parameter of collective and whirling modes
κ_c, κ_w	=	quasi-static correction parameter for collective and whirling modes
λ	=	wind field length-scale
λ_j	=	eigenvalue of mode j
ν_c, ν_w	=	connectivity parameter for collective and whirling modes
$\Omega, \mathbf{\Omega}$	=	angular frequency of rotor
ω_c, ω_w	=	controller frequency of collective and whirling modes
ω_j	=	angular frequency of mode j
σ_v^2	=	along-wind velocity variance
$\boldsymbol{\xi}_n$	=	simulated white-noise sequence
ζ_c, ζ_w	=	control damping parameter of collective and whirling modes

Subscripts

c	=	collective mode
j	=	mode number
n	=	time increment index
u	=	structure variable index
w	=	whirling mode
η	=	control variable index

1. Introduction

A central design problem for rotors with blades such as e.g. in wind turbines and helicopters is the question of vibrations due to the flexibility of the blades and the support. The vibration modes involve coupling between the individual blades and also depend on the rotation frequency and the aerodynamic loads, see e.g. [1] and [2]. Efficient control and damping of the vibrations in this type of rotors must take account of these factors. The present paper develops a theory for control based on vibration resonance for three bladed wind turbine rotors. The control scheme only requires a

single sensor/actuator pair for each blade. However, both sensor and actuator thereby interacts with parts of the motion of the rotor that is not associated with the targeted mode(s), and it is an essential feature of the control scheme to account for this so-called 'background flexibility' of the rotor in the design of the control algorithm relating the sensor and actuator signals. In the present paper the control system is implemented in the form of an active strut connecting two blade cross-sections close to the root of the blade, but alternative implementations, e.g. in the form of active surface coatings are also possible using the same algorithm.

The present introduction combines a brief review of the current state of vibration problems and control methods for edge-wise vibrations of wind turbine rotors, a discussion of the particular features of vibrations of three-bladed rotors, and a summary of the equations of motion for the dynamics of the rotor. Section 2 gives a concise presentation of modal analysis of gyroscopic systems with complex valued mode shapes, and in particular develops a compact approximate response representation in terms of a resonant contribution from the targeted mode plus a quasi-static correction to be used for representation of the 'background flexibility'. The control system and its calibration are presented in Sections 3 and 4, demonstrating how the sensor/actuator signals from the three blades are combined to address the specifically targeted rotor modes. Finally Section 5 illustrates the ability of the present method to substantially reduce the lowest group of edge-wise vibration modes in a typical wind turbine rotor with 86 m diameter, subjected to a simulated stochastic turbulent wind field.

1.1. *Current status*

With the increasing size of wind turbine rotors, now in the diameter range of 80–120 m, dynamic effects become more and more important. A general survey of the main combined structural and aerodynamic aspects has been given by Hansen et al. [1], where it is demonstrated that a particular issue is the edge-wise vibrations of the rotor. These vibrations are typically associated with low structural as well as low aerodynamic damping, even including the possibility of instability for some combinations of blade properties and operating conditions. The problem was discussed by Thomsen et al. [3], who presented damping results obtained by a method in which the rotor shaft is excited by a harmonic load generated by an eccentric mass rotating in the fixed nacelle of the wind turbine. In this frame the angular frequencies of the forward and backward whirling modes are separated by twice the angular frequency of the rotor, and thus the loading primarily excites the forward or backward whirling edge-wise vibration mode, depending on the selected frequency of excitation. The results indicate a damping ratio of the order $\zeta_F \simeq 0.015$ for forward whirling and $\zeta_B \simeq 0.006$ for backward whirling. A closer analysis of the vibration modes and frequencies of the rotor was subsequently carried out by Hansen [4], and the results suggest that the higher damping of the forward whirling mode for this particular rotor may be due to coupling with a flap-wise vibration mode with higher damping. Analyses carried out by Riziotis et al. [5] indicate similar damping ratio for the forward and backward edge-wise vibration modes, and give low or

even negative values, depending on the operating conditions. Later work by Hansen et al. [6] also indicates very low damping of the edge-wise vibration modes.

Undesirable vibrations are typically associated with unavoidable excitation of one or more structural vibration modes, typically with low damping. A classic approach to control of these undesirable vibrations is the so-called modal control, see e.g. Meirovitch [7]. The basic idea of modal control is to introduce a sufficient number of sensors to characterize the targeted modal response(s), and then to use this information to distribute appropriate loads to these modes via a suitable number of distributed actuators. The control parameters defining the linear relations between the sensor and actuator signals are typically determined from a quadratic functional that constitutes a weighted average of the desired goal and the associated cost of the control. This takes the form of an optimization problem, and this type of control is therefore often termed 'optimal control'. This type of control has been applied to rotating beams e.g. by Khulief [8], Chandiramani et al. [9] and Shete et al. [10]. The advantage of the optimal control formalism is its stringent mathematical basis. However, it makes use of a distributed set of sensors as well as actuators, and in the context of a full wind turbine rotor in operating conditions, issues of the optimal form of the quadratic functional and the modal representation and its truncation may present problems. A preliminary study relating to multi-sensor/actuator control of a wind turbine blade has recently been presented by Rice and Verhaegen [11].

In recent years there has been a considerable research interest in so-called 'smart control' of wind turbine rotors, and a recent survey has been given by Barlas and Kuik [12]. A central aspect of smart control of wind turbine rotors is the design of novel actuation mechanisms. Concepts that are currently considered include an active blade tip with controllable motion, controlled flaps [2], material configurations that couple extension and twist or bending and twist, taps mounted near the trailing edge, and variable shape concepts where the camber or the trailing edge can be controlled, see e.g. [13, 14]. The present paper makes use of a variant of 'smart control' in which a local curvature can be introduced close to the blade root by an active strut that serves both as sensor and actuator. The control scheme addresses the group of edge-wise vibration modes, but is different in concept from modal control. In modal control several sensors are used to identify the modal response, and similarly several actuators are used to provide a corresponding modal load. In the present concept only a single sensor/actuator pair is used in each blade, and the modal part of the response is identified by use of a simple quasi-static correction term that does not require knowledge of other mode shapes. The control algorithm operates on a resonance principle that makes use of the frequency of the targeted mode(s). The combination of resonant control and a suitable correction for background flexibility has shown promise for control of single-mode vibrations of buildings and cable supported structures [15, 16]. In the present context the theory is extended to gyroscopic systems with complex modes, and a decomposition technique for a group of modes of the rotor.

1.2. *Vibrations of three-bladed rotors*

In rotors with identical blades the vibration modes occur in groups. The properties relating to the periodic nature of the modes with respect to the blade number suggests a Fourier representation of the motion of the individual blades, here denoted $\mathbf{u}_{(k)}$, $k = 0, \cdots, N-1$. The general complex Fourier representation has the form

$$\mathbf{u}_{(k)} \;=\; \sum_{j=0}^{N-1} \exp\left(2\pi i\, \frac{kj}{N}\right) \mathbf{v}_{(j)}\,, \quad k = 0, \cdots, N-1\,, \tag{1}$$

where $\mathbf{v}_{(j)}$ represents the Fourier component vector associated with a single blade. A vibration with frequency ω is represented by including a time factor $\mathrm{e}^{i\omega t}$, and the instantaneous displacements are given by the real part of the representation. When used in connection with bladed rotors this representation is often called the Coleman transformation [17]. Fourier representations also find application to other types of periodic structures, see e.g. [18].

For a three-bladed rotor the Fourier relation (1) can be expressed in matrix form as

$$\begin{bmatrix} \mathbf{u}_{(1)} \\ \mathbf{u}_{(2)} \\ \mathbf{u}_{(3)} \end{bmatrix} \;=\; \begin{bmatrix} 1 \\ 1 \\ 1 \end{bmatrix} \mathbf{v}_C \;+\; \begin{bmatrix} 1 \\ \mathrm{e}^{\,i\alpha} \\ \mathrm{e}^{-i\alpha} \end{bmatrix} \mathbf{v}_B \;+\; \begin{bmatrix} 1 \\ \mathrm{e}^{-i\alpha} \\ \mathrm{e}^{\,i\alpha} \end{bmatrix} \mathbf{v}_F \tag{2}$$

with $\alpha = 2\pi/3$. In this representation $\mathbf{v}_C$ represents a collective mode, in which each of the blades have identical motion $\mathbf{u}_{(j)} = \mathbf{v}_C$. When the time dependence of a vibration is represented by the exponential factor $\mathrm{e}^{i\omega t}$ the complex exponentials in the Fourier representation (2) simply represent a shift in the phase angle. It is seen that the mode associated with $\mathbf{v}_B$ corresponds to 'backward whirling', in which the blade sequence 1–3–2 occurs with a phase delay of $\alpha = 2\pi/3$, while the mode associated with $\mathbf{v}_F$ corresponds to 'forward whirling', in which the sequence is 1–2–3. Figure 1 illustrates the collective mode, and the backward and forward whirling modes. The blades without arrows are in their maximum displacement state, while the arrows indicate the velocity of the other blades.

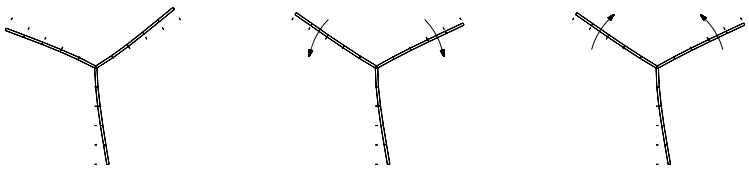

FIGURE 1. Collective, backward and forward vibration modes of a three-bladed rotor.

If the shaft rotates with constant angular velocity about a fixed direction in space, each of the three modes have the same frequency as that of an individual blade. However, in the context of wind turbines the shaft has torsional flexibility, and therefore the frequency of the collective mode is typically lower than the frequencies of the corresponding whirling modes. Motion of the shaft and aerodynamic effects will typically lead to a small difference in the two whirling frequencies.

1.3. *Equations of motion*

In the present paper the analysis is performed on a full rotor model in which the vector $\mathbf{u}$ contains all degrees-of-freedom of the structural model. While detailed analysis propellers and helicopter rotors may require use of a fully non-linear kinematic formulation, see e.g. [19], wind turbine rotors in operational conditions can typically be analyzed with a partially non-linear theory, in which accurate representation of the centrifugal forces is essential, [1]. In the rotating frame of reference the discretized equations of motion can be written in the standard form, see e.g. [20],

$$\mathbf{M}\ddot{\mathbf{u}} + 2\mathbf{G}\dot{\mathbf{u}} + \mathbf{K}\mathbf{u} = \mathbf{f}\,. \tag{3}$$

The mass matrix is $\mathbf{M}$, while $2\mathbf{G}$ is the skew-symmetric gyroscopic matrix and $\mathbf{K}$ is the linearized stiffness matrix. In the present problem the stiffness matrix consists of four contributions: the elastic stiffness matrix $\mathbf{K}_e$, the geometric stiffness matrix $\mathbf{K}_g$ arising from the stiffening effects of tension stresses, the negative stiffness $\mathbf{C}$ generated by the direct effect of the centrifugal force, and in the case of variable angular velocity the angular acceleration stiffness $\dot{\mathbf{G}}$,

$$\mathbf{K} = \mathbf{K}_e + \mathbf{K}_g - \mathbf{C} + \dot{\mathbf{G}}. \tag{4}$$

The total force vector

$$\mathbf{f} = \mathbf{f}_e + \mathbf{f}_c - \mathbf{f}_g \tag{5}$$

contains the external load $\mathbf{f}_e$, the centrifugal forces $\mathbf{f}_c$, and the gyroscopic forces $-\mathbf{f}_g$. A detailed derivation of the terms appearing in the equation of motion (3) in the form of a finite element model with specialized beam elements is given in [21].

2. Vibrations of the Rotor

The control concept developed in this paper is based on resonant interaction between the rotor and the controller, and it is therefore necessary first to establish some general properties of vibrations of the rotor without the controller. This section gives a concise presentation of the theory and properties of the dynamics of gyroscopic systems that are needed in the subsequent development of the structural control.

2.1. *Undamped gyroscopic vibrations*

The additional damping to be introduced by the controller is needed because of small or negative damping of the mode(s) in question. The calibration is therefore based on the corresponding undamped vibrations. The undamped modes and the corresponding vibration frequencies are found from the assumption of the existence of vibrations with the format

$$\mathbf{u}(t) = \mathbf{u}_j \exp(\lambda_j t)\,. \tag{6}$$

where $\mathbf{u}_j$ is typically a complex mode-shape vector, and the parameter λ_j determines the time dependence. When this solution is substituted into the homogeneous form of the equation of

motion (3) the following quadratic eigenvalue problem is obtained

$$[\,\mathbf{M}\lambda_j^2 \,+\, 2\mathbf{G}\lambda_j \,+\, \mathbf{K}\,]\,\mathbf{u}_j \,=\, \mathbf{0}. \tag{7}$$

In the case of non-gyroscopic motion $\mathbf{G} = \mathbf{0}$, and the equation reduces to a linear eigenvalue problem in λ_j^2.

The gyroscopic eigenvalue problem is conveniently solved by forming an expanded eigenvalue problem for the state-space variables, here collected in the state-space vector

$$\mathbf{z}^T \,=\, [\,\dot{\mathbf{u}}^T,\, \mathbf{u}^T\,]. \tag{8}$$

The equations of motion are typically expressed in the state-space format

$$\begin{bmatrix} \mathbf{M} & \mathbf{0} \\ \mathbf{0} & \mathbf{K} \end{bmatrix} \begin{bmatrix} \ddot{\mathbf{u}} \\ \dot{\mathbf{u}} \end{bmatrix} + \begin{bmatrix} 2\mathbf{G} & \mathbf{K} \\ -\mathbf{K} & \mathbf{0} \end{bmatrix} \begin{bmatrix} \dot{\mathbf{u}} \\ \mathbf{u} \end{bmatrix} = \begin{bmatrix} \mathbf{f} \\ \mathbf{0} \end{bmatrix}, \tag{9}$$

where a velocity identity has been introduced in a form involving the effective stiffness matrix $\mathbf{K}$, [22, 23, 20]. This format can be expressed in compact form as the set of linear first order equations

$$\mathbf{A}\dot{\mathbf{z}} \,+\, \mathbf{B}\mathbf{z} \,=\, \mathbf{F}\,. \tag{10}$$

with the $2n \times 2n$ matrices

$$\mathbf{A} \,=\, \begin{bmatrix} \mathbf{M} & \mathbf{0} \\ \mathbf{0} & \mathbf{K} \end{bmatrix}, \qquad \mathbf{B} \,=\, \begin{bmatrix} 2\mathbf{G} & \mathbf{K} \\ -\mathbf{K} & \mathbf{0} \end{bmatrix}, \tag{11}$$

and the expanded load vector

$$\mathbf{F}^T \,=\, [\,\mathbf{f}^T,\, \mathbf{0}\,]. \tag{12}$$

The matrix $\mathbf{A}$ is symmetric, while $\mathbf{B}$ is skew-symmetric, when the system is undamped.

Free vibrations are now represented in the expanded format as

$$\mathbf{z}(t) \,=\, \mathbf{z}_j \exp(\lambda_j t)\,, \tag{13}$$

where the eigenvalues and eigenvectors follow from the linear eigenvalue problem of the extended equations of motion (10),

$$\big[\,\mathbf{B} \,+\, \lambda_j \mathbf{A}\,\big]\,\mathbf{z}_j \,=\, \mathbf{0}\,. \tag{14}$$

Alternative forms of the expanded linear eigenvalue problem exist, e.g. in terms of real vectors [22, 23, 20] or in a hybrid state-space form in terms of the local displacements and global velocities, where the last equation is a momentum balance expressed in terms of the mass matrix, [24]. However, in the present application the complex form of the mode shape vectors $\mathbf{u}_j$ in connection with the classic state-space format is convenient.

It is important for the present problem that the eigenvalues of an undamped gyroscopic system are imaginary. This is most simply demonstrated by writing the state-space eigenvector $\mathbf{z}_j$ of the expanded eigenvalue problem (14) in terms of its real and imaginary parts, $\mathbf{z}_j = \mathbf{x}_j + i\mathbf{y}_j$. Pre-multiplication of the expanded eigenvalue equation with $\bar{\mathbf{z}}_j^T$ gives the following expression for the eigenvalue

$$\lambda_j = -\,\frac{\bar{\mathbf{z}}_j^T \mathbf{B}\mathbf{z}_j}{\bar{\mathbf{z}}_j^T \mathbf{A}\mathbf{z}_j} = -\,\frac{2i\,\mathbf{x}_j^T \mathbf{B}\mathbf{y}_j}{\mathbf{x}_j^T \mathbf{A}\mathbf{x}_j + \mathbf{y}_j^T \mathbf{A}\mathbf{y}_j}\,, \tag{15}$$

where the last form follows from the symmetry of $\mathbf{A}$ and anti-symmetry of $\mathbf{B}$. It follows immediately from this formula that the eigenvalue λ_j is imaginary, and thus can be expressed in

terms of the real valued angular frequency ω_j as $\lambda_j = i\omega_j$. It furthermore follows that if $\mathbf{u}_j$, λ_j constitute an eigen-pair, so does the complex conjugate pair $\bar{\mathbf{u}}_j$, $\bar{\lambda}_j = -i\omega_j$. It follows from the quadratic eigenvalue equation (7) that except for the very special case $\mathbf{G}\mathbf{u}_j = \mathbf{0}$, the eigenvector $\mathbf{u}_j$ is complex.

2.2. *Frequency response analysis*

A solution is now sought to the expanded non-homogeneous dynamic equation of motion (10) in the form of an expansion in the $2n$ expanded mode shape vectors $\mathbf{z}_j$,

$$\mathbf{z}(t) \;=\; \sum_{j=1}^{2n} \mathbf{z}_j \, q_j(t). \tag{16}$$

Let the time dependence be harmonic and of the form $\exp(\lambda t) = \exp(i\omega t)$. Substitution of the expansion (16) into the equation of motion (10) then gives

$$\sum_{j=1}^{2n} \big(\mathbf{B} + \lambda\mathbf{A}\big)\mathbf{z}_j \, q_j \;=\; \mathbf{F}. \tag{17}$$

Pre-multiplication by $\bar{\mathbf{z}}_k^T$ gives

$$\sum_{j=1}^{2n} \bar{\mathbf{z}}_k^T \big(\mathbf{B} + \lambda\mathbf{A}\big)\mathbf{z}_j \, q_j \;=\; \bar{\mathbf{z}}_k^T\mathbf{F} \;=\; \bar{\lambda}_k \bar{\mathbf{u}}_k^T\mathbf{f}, \tag{18}$$

where the reduction of the load term follows from the state-space representation of the response (8) and the load (12).

It follows from the linear eigenvalue problem (14) that the eigenvectors $\mathbf{z}_j$ can be normalized to satisfy the orthogonality relation

$$\bar{\mathbf{z}}_k^T \mathbf{A}\, \mathbf{z}_j \;=\; 2\delta_{kj}. \tag{19}$$

An additional set of orthogonality then follows from the eigenvalue equations (14) in the form

$$\bar{\mathbf{z}}_k^T \mathbf{B}\, \mathbf{z}_j \;=\; -2\lambda_j \, \delta_{kj}. \tag{20}$$

In these relations the factor 2 has been introduced to provide a smooth transition to the classic non-gyroscopic solution for $\Omega \to 0$.

The orthogonality relations (19) and (20) reduce the response equation (18) to the following set of equations for the individual component amplitudes q_k,

$$2(\lambda - \lambda_k)\, q_k \;=\; \bar{\lambda}_k \bar{\mathbf{u}}_k^T\mathbf{f}. \tag{21}$$

This relation determines the displacement amplitudes as

$$q_k \;=\; \frac{1}{2}\,\frac{\bar{\lambda}_k}{\lambda - \lambda_k}\,\bar{\mathbf{u}}_k^T\mathbf{f} \;=\; \frac{1}{2}\,\frac{\omega_k}{\omega_k - \omega}\,\bar{\mathbf{u}}_k^T\mathbf{f}. \tag{22}$$

Substitution of these response amplitudes into the state-space expansion (16) gives

$$\begin{bmatrix} \dot{\mathbf{u}} \\ \mathbf{u} \end{bmatrix} \;=\; \tfrac{1}{2}\sum_{j=1}^{2n} \begin{bmatrix} \lambda_j\mathbf{u}_j \\ \mathbf{u}_j \end{bmatrix} \frac{\omega_j}{\omega_j - \omega}\,\bar{\mathbf{u}}_j^T\mathbf{f}. \tag{23}$$

The displacement response follows from the lower part of this state-space relation in the form

$$\mathbf{u} \,=\, \tfrac{1}{2}\sum_{j=1}^{2n} \frac{\omega_j}{\omega_j - \omega}\, \mathbf{u}_j \bar{\mathbf{u}}_j^T \mathbf{f}. \tag{24}$$

In this representation each of the $2n$ eigenvector–eigenvalue pairs of the extended eigenvalue problem are represented by an individual term. However, when $\mathbf{u}_j$ and $\lambda_j = i\omega_j$ constitute an eigenpair, the combination of $\bar{\mathbf{u}}_j$ and $\bar{\lambda}_j = -i\omega_j$ also constitute a pair. Thus, the frequency response can be represented by the n-term expansion

$$\mathbf{u} \,=\, \tfrac{1}{2}\sum_{j=1}^{n} \Big(\frac{\omega_j}{\omega_j - \omega}\, \mathbf{u}_j \bar{\mathbf{u}}_j^T \,+\, \frac{\omega_j}{\omega_j + \omega}\, \bar{\mathbf{u}}_j \mathbf{u}_j^T \Big)\, \mathbf{f}. \tag{25}$$

Both of the matrices appearing within the parenthesis are Hermitean, but for gyroscopic systems the eigenvectors are complex, and the two matrices are not identical. When combining the symmetric and skew-symmetric parts of the matrices, the following form of the solution is obtained

$$\mathbf{u} \,=\, \sum_{j=1}^{n} \Big[\frac{\omega_j^2}{\omega_j^2 - \omega^2}\, \tfrac{1}{2}\big(\mathbf{u}_j \bar{\mathbf{u}}_j^T + \bar{\mathbf{u}}_j \mathbf{u}_j^T \big) \,+\, \frac{\omega\, \omega_j}{\omega_j^2 - \omega^2}\, \tfrac{1}{2}\big(\mathbf{u}_j \bar{\mathbf{u}}_j^T - \bar{\mathbf{u}}_j \mathbf{u}_j^T \big) \Big]\, \mathbf{f}. \tag{26}$$

The first term in the quare brackets is real and symmetric, and corresponds to the non-gyroscopic case. The second term is skew-symmetric and imaginary, and is associated specifically with the gyroscopic case via the complex eigenvectors.

2.3. *Approximate frequency response formula*

The calibration of the control system is based on the idea of a resonant mode, supplemented by the quasi-static response from other modes with higher frequency. The idea of including the effect of the additional flexibility provided by the high-frequency modes in the form of a quasi-static approximation is classic within structural dynamics, see e.g. [25], and has been used successfully in connection with active vibration control of stationary structures, e.g. in [15, 16]. In a rotating frame with gyroscopic forces the mode shape vectors are complex, and the format of the frequency response is modified as seen in (25) and (26), and this leads to a need for modifying the quasi-static correction procedure.

The general frequency response formula (25) identifies a series expansion of the inverse of the frequency dependent response equation matrix,

$$[\,\mathbf{K} \,+\, 2i\omega\mathbf{G} - \omega^2\mathbf{M}\,]^{-1} \,=\, \tfrac{1}{2}\sum_{j=1}^{n} \Big(\frac{\omega_j}{\omega_j - \omega}\, \mathbf{u}_j \bar{\mathbf{u}}_j^T \,+\, \frac{\omega_j}{\omega_j + \omega}\, \bar{\mathbf{u}}_j \mathbf{u}_j^T \Big). \tag{27}$$

In particular, the limit $\omega = 0$ represents the static flexibility in the form of the expansion

$$\mathbf{K}^{-1} \,=\, \sum_{j=1}^{n} \tfrac{1}{2}\big(\mathbf{u}_j \bar{\mathbf{u}}_j^T \,+\, \bar{\mathbf{u}}_j \mathbf{u}_j^T \big). \tag{28}$$

Now, let ω_k be the frequency of the resonant mode. When contributions from the lower-frequency modes are neglected, and contributions from the higher-frequency modes are represented by their quasi-static equivalent, the expansion (27) takes the form

$$[\,\mathbf{K} \,+\, 2i\omega\mathbf{G} - \omega^2\mathbf{M}\,]^{-1} \,\simeq\, \tfrac{1}{2}\Big(\frac{\omega_k}{\omega_k - \omega}\, \mathbf{u}_k \bar{\mathbf{u}}_k^T \,+\, \frac{\omega_k}{\omega_k + \omega}\, \bar{\mathbf{u}}_k \mathbf{u}_k^T \Big) \,+\, \sum_{j=k+1}^{n} \tfrac{1}{2}\big(\mathbf{u}_j \bar{\mathbf{u}}_j^T \,+\, \bar{\mathbf{u}}_j \mathbf{u}_j^T \big). \tag{29}$$

The contribution from the resonant mode is now expressed in a form that emphasizes the Hermitean form of the original matrix around the resonance frequency ω_k,

$$\tfrac{1}{2}\Big(\frac{\omega_k}{\omega_k-\omega}\,\mathbf{u}_k\bar{\mathbf{u}}_k^T\,+\,\frac{\omega_k}{\omega_k+\omega}\,\bar{\mathbf{u}}_k\mathbf{u}_k^T\Big)\,=\,\frac{\omega_k^2}{\omega_k^2-\omega^2}\,\mathbf{u}_k\bar{\mathbf{u}}_k^T\,-\,\frac{\omega_k}{\omega_k+\omega}\,\tfrac{1}{2}\big(\mathbf{u}_k\bar{\mathbf{u}}_k^T-\bar{\mathbf{u}}_k\mathbf{u}_k^T\big). \tag{30}$$

In the present context the approximate response formulation is to be used in a frequency range around ω_k. In this range the first term in (30) dominates the second, which is therefore omitted in the final approximation

$$[\,\mathbf{K}\,+\,2i\omega\mathbf{G}-\omega^2\mathbf{M}\,]^{-1}\,\simeq\,\frac{\omega_k^2}{\omega_k^2-\omega^2}\,\mathbf{u}_k\bar{\mathbf{u}}_k^T\,+\,\sum_{j=k+1}^{n}\tfrac{1}{2}\big(\mathbf{u}_j\bar{\mathbf{u}}_j^T\,+\,\bar{\mathbf{u}}_j\mathbf{u}_j^T\big). \tag{31}$$

This approximation is mostly needed in connection with resonant response from one of the lower modes, and it is therefore convenient to eliminate the summation over the higher modes by use of (28), whereby

$$[\,\mathbf{K}\,+\,2i\omega\mathbf{G}-\omega^2\mathbf{M}\,]^{-1}\,\simeq\,\frac{\omega_k^2}{\omega_k^2-\omega^2}\,\mathbf{u}_k\bar{\mathbf{u}}_k^T\,+\,\Big[\,\mathbf{K}^{-1}\,-\,\sum_{j=1}^{k}\tfrac{1}{2}\big(\mathbf{u}_j\bar{\mathbf{u}}_j^T\,+\,\bar{\mathbf{u}}_j\mathbf{u}_j^T\big)\Big]. \tag{32}$$

It is seen that the modification due to the gyroscopic force term consists in using the Hermitean product of the complex modes in the resonant term, and the symmetrized product in the quasi-static correction.

2.4. *Change of eigenfrequencies with rotation speed*

In the present context it is of importance that the natural vibration frequencies change with the angular velocity of the rotor $\boldsymbol{\Omega}$. A simple estimate of the relative change of natural frequency can be obtained from a perturbation analysis of the quadratic eigenvalue problem (7). The non-rotating state $|\Omega|=0$ is used as reference state for a mode shape $\mathbf{u}_0$ with angular vibration frequency $\boldsymbol{\omega}_0$. A direct first order perturbation leads to the following form for the angular vibration frequency ω at the angular rotation frequency $\boldsymbol{\Omega}$

$$\frac{\omega^2}{\omega_0^2}=\frac{\mathbf{u}_0^T\mathbf{K}(\boldsymbol{\Omega})\mathbf{u}_0}{\mathbf{u}_0^T\mathbf{K_0}\mathbf{u}_0}\,=\,1\,+\,\frac{\mathbf{u}_0^T(\,\mathbf{K}_g\,-\,\mathbf{C}\,)_{|\Omega|=1}\,\mathbf{u}_0}{\mathbf{u}_0^T\mathbf{K}_0\mathbf{u}_0}\;\Omega^2\,, \tag{33}$$

where $\mathbf{K}(\boldsymbol{\Omega})$ is the effective stiffness matrix at the rotation frequency $\Omega=|\boldsymbol{\Omega}|$, while $\mathbf{K}_0$ is at standstill with $\Omega=0$. Thus, the formula (33) makes use of the ratio between the modal stiffness at the rotation frequency Ω and the modal stiffness at $\Omega=0$. The change of stiffness comes from the geometric stiffness matrix $\mathbf{K}_g$ and the centrifugal force matrix $\mathbf{C}$. Both of these components are quadratic in Ω, leading to the last expression. The change in natural frequency of a rotor due to the rotational stiffening effect is illustrated in [26]. In the present context for a wind turbine rotor the increase in geometric stiffness will typically outweigh the stiffness reduction from the centrifugal force matrix, leading to an increase of vibration frequency with increasing rotation speed. This is discussed and illustrated in the example in Section 5.

3. Control System

The vibration control is implemented via actuators which impose the control force vector $\mathbf{f}_\eta$ on the structure. After introduction of the control force the equation of motion (3) takes the form

$$\big(\mathbf{K} + 2i\omega\mathbf{G} - \omega^2\mathbf{M}\big)\mathbf{u} + \mathbf{f}_\eta = \mathbf{f}. \tag{34}$$

In the present context the control forces are intended to reduce the vibration intensity of a group of vibration modes such as the combined vibration in the first in-plane collective and associated forward and backward whirling modes discussed in Section 1 and illustrated in Fig. 1.

The natural frequency of the collective mode is typically smaller than the natural frequency of the two whirling modes due to the rotational flexibility of the drivetrain. Thus, resonant control, based on the natural frequencies of the modes, must address the whirling mode and the set of the two whirling modes separately. The control is implemented via identical collocated sensor/actuator pairs on each of the three blades. In its simplest form the sensor/actuator connects two degrees of freedom of a blade, typically by a vector of the form

$$\mathbf{w}_k = [\,0, \cdots, 1, 0, \cdots, -1, 0, \cdots]^T, \quad k = 1, 2, 3, \tag{35}$$

where the subscript $k = 1, 2, 3$ denotes the blade number, and the ± 1 coefficients form the difference between the two degrees of freedom of this blade.

3.1. *Feedback from collective mode*

The connectivity array of the collective mode is defined by the mean value of the corresponding arrays for the individual blades,

$$\mathbf{w}_c = \tfrac{1}{3}\big(\mathbf{w}_1 + \mathbf{w}_2 + \mathbf{w}_3\big). \tag{36}$$

This connectivity array defines an average over the three blades of the displacement difference registered by the sensor(s) on the individual blades. The averaged displacement $\mathbf{w}_c^T\mathbf{u}$ defines a control variable η_c for the collective mode by the frequency relation

$$G^c_{\eta u}(\omega)\mathbf{w}_c^T\mathbf{u} + G^c_{\eta\eta}(\omega)\eta_c = 0. \tag{37}$$

In this equation $G^c_{\eta\eta}(\omega)$ is a resonant second-order filter,

$$G^c_{\eta\eta}(\omega) = \omega_c^2 - \omega^2 + 2i\zeta_c\omega_c\omega. \tag{38}$$

Here ω_c is the controller frequency of the collective mode, which must be tuned to the natural frequency $\omega_{c,n}$ of the free collective vibration mode as in Section 4.1, where also the damping parameter ζ_c is calibrated. $G^c_{\eta u}(\omega)$ is a second-order filter, representing the coupling between the control variable and the structure. It may be chosen to implement acceleration feedback by

$$G^c_{\eta u}(\omega) = \omega^2. \tag{39}$$

Alternatively, displacement feedback may be implemented by selecting $G^c_{\eta u}(\omega) = \omega_c^2$, as discussed in [15]. Only acceleration feedback will be considered explicitly here.

A special case occurs if the displacement field is given completely by the collective mode shape $\mathbf{u}_c$ in the form $\mathbf{u} = \mathbf{u}_c q_c$, where q_c is the corresponding modal coordinate. In this case the frequency relation (37) takes the form

$$G^c_{\eta u}(\omega)\nu_c q_c + G^c_{\eta\eta}(\omega)\eta_c = 0, \tag{40}$$

where

$$\nu_c = \mathbf{w}_c^T \mathbf{u}_c \tag{41}$$

is the modal connectivity parameter of the collective mode, giving the displacement of the mode-shape vector over the controller. For flexible structures the control parameters should be calibrated from the full displacement vector $\mathbf{u}$ which contains additional contributions from other modes that are excited by the actuator forces. This is discussed in detail in Section 4, but first the feedback format of the whirling modes must be presented.

3.2. *Feedback from whirling modes*

The whirling modes involve different displacements in each of the blades, and therefore require a connectivity array with contributions from each of the blades. When the mean contribution from the collective mode is subtracted, the whirling mode connectivity array takes the form

$$\mathbf{W} = \tfrac{1}{3}[\,\mathbf{w}_1 - \mathbf{w}_c, \mathbf{w}_2 - \mathbf{w}_c, \mathbf{w}_3 - \mathbf{w}_c\,], \tag{42}$$

where each of the three columns correspond to one of the blades. There are three components in the representation of the whirling modes, and although the introduction of $\mathbf{w}_c$ leads to a linear relation between these components, the analysis is simplified by retaining three components in the analysis. In the case of the whirling modes the three displacement components are extracted in the form $\mathbf{W}^T\mathbf{u}$. These displacement components are related to the control variables $\boldsymbol{\eta} = [\,\eta_1, \eta_2, \eta_3]^T$ by the frequency relation

$$G^w_{\eta u}(\omega)\mathbf{W}^T\mathbf{u} + G^w_{\eta\eta}(\omega)\boldsymbol{\eta} = \mathbf{0}. \tag{43}$$

In this relation $G_{\eta\eta}(\omega)$ is a common scalar resonant second-order filter for the whirling modes,

$$G^w_{\eta\eta}(\omega) = \omega_w^2 - \omega^2 + 2i\zeta_w\omega_w\omega. \tag{44}$$

Here ω_w is the controller frequency of the whirling modes, which must be tuned to the natural frequency $\omega_{w,n}$ of the free whirling vibration modes, and ζ_w is the damping parameter for the whirling modes. The whirling modes will have acceleration feedback, represented by

$$G^w_{\eta u}(\omega) = \omega^2. \tag{45}$$

Also this can be changed to displacement feedback.

At whirling mode resonance the displacement field will be dominated by a combination of the whirling modes, combined in $\mathbf{u} = \mathbf{u}_w q_w$, where q_w is the modal coordinate. When this representation is substituted, the frequency relation (43) takes the form

$$G^w_{\eta u}(\omega)\mathbf{W}^T\mathbf{u}_w q_w + G^w_{\eta\eta}(\omega)\boldsymbol{\eta} = \mathbf{0}. \tag{46}$$

This relation determines the relative magnitude of the control variable components by $\boldsymbol{\eta} \propto \mathbf{W}^T\mathbf{u}_w$. Thus, a modal connectivity factor can be introduced for the three components of the whirling motion,

$$\boldsymbol{\nu}_w = \mathbf{W}^T\mathbf{u}_w. \tag{47}$$

The relation between the components of the control variables $\boldsymbol{\eta}$ can then be expressed in normalized form as

$$\boldsymbol{\eta} = \nu_w^{-1}\boldsymbol{\nu}_w\,\eta_w, \qquad \nu_w = (\bar{\boldsymbol{\nu}}_w^T\boldsymbol{\nu}_w)^{1/2}. \tag{48}$$

It is noted that if $\boldsymbol{\nu}_w$ corresponds to one of the whirling modes, e.g. forward whirling, the complex conjugate $\bar{\boldsymbol{\nu}}_w$ corresponds to the other, backward whirling. Thus, the two whirling modes are equally represented in the parameter ν_w.

Pre-multiplication of the three-component whirling mode feedback equation (46) by $\bar{\boldsymbol{\nu}}_w^T$ then reduces to the single scalar equation

$$G_{\eta u}^{w}(\omega)\nu_w q_w + G_{\eta\eta}^{w}(\omega)\eta_w = 0\,. \tag{49}$$

This equation is of the same form as the feedback equation (40) for the collective mode, and thus the calibration of the two sets of control parameters follow essentially the same procedure as described in Section 4.

3.3. *Control force equation*

The control force has components from both the collective and the whirling modes. These are filtered by the frequency functions $G_{u\eta}^{c}(\omega)$ and $G_{u\eta}^{c}(\omega)$, respectively. The system is designed as collocated, whereby the force components are generated by the same index arrays used to extract the control signal, and the controller force therefore has the form

$$\mathbf{f}_\eta \;=\; G_{u\eta}^{c}(\omega)\mathbf{w}_c\eta_c \;+\; G_{u\eta}^{w}(\omega)\,\mathbf{W}\boldsymbol{\eta}. \tag{50}$$

This representation is introduced into the equation of motion (34), and the total set of equations then consist of the structural equation of motion plus the equations (37) and (46) for the controller signals. The corresponding reduced control equations (40) and (49) are used for calibrating the controller functions $G_{\eta\eta}(\omega)$, $G_{\eta u}(\omega)$ and $G_{u\eta}(\omega)$ for the collective and the whirling modes as discussed in the next section.

4. Controller Calibration

The two components of the resulting control force (50), addressing the collective and the whirling modes, respectively, are calibrated individually in the following. The optimal control parameters for the basic calibration without the quasi-static correction for background flexibility are presented first, and then these results are modified to take the effect of background flexibility into account. The calibration is a generalization to complex modes of the procedure described in detail in [15, 16], which has been used for damping of a single wind turbine blade in [21].

4.1. *Basic calibration of collective mode*

The governing equations for the resonant control of the collective mode are obtained by combining the equation of motion (34), the control force described by the first term in (50), and the scalar filter equation in (40). In this initial calibration procedure the response is assumed to be fully described by the collective mode, $\mathbf{u} = \mathbf{u}_c q_c$, and the dynamic part of (32). Hereby, the homogeneous scalar equations governing the control of the collective mode can be written as

$$\begin{aligned} (\omega_{c,n}^2 - \omega^2)\,\nu_c\,q_c \,+\, \omega_{c,n}^2\,|\nu_c|^2 G_{u\eta}^c(\omega)\,\eta_c &= 0, \\ G_{\eta u}^c(\omega)\,\nu_c\,q_c \,+\, G_{\eta\eta}^c(\omega)\,\eta_c &= 0, \end{aligned} \tag{51}$$

where $|\nu_c| = (\bar{\nu}_c \nu_c)^{1/2}$ is the magnitude of the modal connectivity parameter ν_c. For acceleration feedback with $G_{\eta u}^c(\omega) = \omega^2$ the corresponding control function $G_{u\eta}^c(\omega)$ contains a constant and a linear term with gain parameters α_c and β_c, respectively,

$$\omega_{c,n}^2\,|\nu_c|^2 G_{u\eta}^c(\omega) \,=\, \alpha_c\,\omega_c^2 \,+\, \beta_c\,2i\zeta_c\omega_c\omega\,. \tag{52}$$

The normalization of $G_{u\eta}^c(\omega)$ by $\omega_{c,n}^2\,|\nu_c|^2$ is suggested by the second term of the first equation in (51), and the control variable then only appears in the combination η_c/ν_c. This leaves a formulation, in which α_c can be considered as a gain parameter of the controller, while the parameters ω_c, β_c and ζ_c should be determined to yield optimal control properties.

The coupled equations (51) are a generalized form of the frequency response equations of a tuned mass damper, analyzed in detail in [27]. The gain parameter α_c plays the role of the mass ratio in the tuned mass damper. The resonant control force splits the original single mode into two modes, and the optimal solution corresponds to equal damping of these two modes. This provides two equations, essentially determining the coupling coefficient β_c and the resonant controller frequency ω_c. The controller damping parameter ζ_c is then determined from the frequency response properties. This procedure results in the following optimal parameters in terms of the gain parameter α_c:

$$\beta_c \,=\, \alpha_c\,, \qquad \omega_c \,=\, \frac{\omega_{c,n}}{1+\alpha_c}\,, \qquad \zeta_c^2 \,=\, \frac{\alpha_c}{2(1+\alpha_c)}\,. \tag{53}$$

These expressions, corresponding to calibration without background flexibility, are summarized in the first row of Table 1.

Resonant control is typically advantageous when additional damping $\Delta\zeta$ is needed for lightly damped modes of the structures, such as e.g. the edgewise vibration modes of a wind turbine rotor. The present calibration procedure secures equal modal damping of the targeted mode, which in this case is the collective mode. For optimal calibration the two modes associated with the collective vibration form receives half of the damping ratio associated with the controller, [27],

$$\Delta\zeta_{c,n} \,\simeq\, \tfrac{1}{2}\,\zeta_c\,. \tag{54}$$

This means that the desired damping is obtained by choosing ζ_c as twice the desired additional damping for the targeted mode. The expression for ζ_c in (53) can then be solved for the gain parameters α, which finally determines the remaining control parameters α_c, β_c and ω_c. This

TABLE 1. Calibration with gain parameter α.

	$\alpha_{c,w}$	$\beta_{c,w}$	$\left(\dfrac{\omega}{\omega_n}\right)^2_{c,w}$	$\left(\zeta\,\dfrac{\omega}{\omega_n}\right)_{c,w}$
Basic	α	α	$\dfrac{1}{(1+\alpha)^2}$	$\sqrt{\dfrac{\alpha}{2(1+\alpha)^3}}$
Full	α	$\dfrac{\alpha}{1+\kappa\alpha}$	$\dfrac{1}{1-\dfrac{\kappa\alpha}{(1+\alpha)^2}}\,\dfrac{1}{(1+\alpha)^2}$	$\dfrac{1+\kappa\alpha}{1-\dfrac{\kappa\alpha}{(1+\alpha)^2}}\sqrt{\dfrac{\alpha}{2(1+\alpha)^3}}$

design sequence can also be applied for the control of the whirling modes, as demonstrated for the control of the wind turbine rotor in Section 5.

4.2. *Basic calibration of whirling modes*

For the whirling modes the control equations are obtained by combining the equation of motion (34), the control force described by the second term in (50), and the filter equation in (49). The response is in this case assumed to be represented by the whirling mode, $\mathbf{u} = \mathbf{u}_w q_w$, and again only the dynamic part of (32) is included. Hereby, the scalar equations for the control of the whirling modes can be written in normalized form as

$$\begin{aligned} (\omega_{w,n}^2 - \omega^2)\,\nu_w\,q_w \;+\; \omega_{w,n}^2\,\nu_w^2 G_{u\eta}^w(\omega)\,\eta_w &= 0, \\ G_{\eta u}^w(\omega)\,\nu_w\,q_w \;+\; G_{\eta\eta}^w(\omega)\,\eta_w &= 0, \end{aligned} \tag{55}$$

where the normalized scalar parameters ν_w and η_w are defined in (48). The format of the frequency function $G_{u\eta}^w(\omega)$ is identical to that in (52) for the collective mode,

$$\omega_{w,n}^2\,\nu_w^2\,G_{u\eta}^w(\omega) \;=\; \alpha_w\,\omega_w^2 \;+\; \beta_w\,2i\zeta_w\omega_w\omega. \tag{56}$$

With this normalization the equations only depend on the control variable in the combination η_w/ν_w. The governing equations for the whirling modes in (55)–(56) are equivalent to those in (51)–(52) for the collective mode. When α_w is taken as gain parameter in this case, the remaining parameters β_w, ω_w and ζ_w are given by the expressions in (53), when replacing the subscript c by w. Thus the first row in Table 1 applies to both the controllers of the collective and the whirling modes.

4.3. *Accounting for background flexibility*

In modal control of flexible structures the the sensors and actuators typically interact with deformations from non-targeted modes thereby contaminating the simple single mode control scheme. When using a small number of sensors/actuaors this effect can be an important aspect in the design of the control scheme, see e.g. [28]. In the analysis leading to the scalar equations (51) and (55) for the collective and whirling modes, respectively, the response is assumed to be fully represented by the targeted mode alone. However, in general the structural response contains contributions from all vibration modes of the system. The displacement generated by the control

variable η_c of the collective mode is determined from the equation of motion (34) with the force from the collective control given by the first term of (50),

$$\mathbf{u} \,=\, -\big[\mathbf{K} + 2i\omega\mathbf{G} - \omega^2\mathbf{M}\big]^{-1}\mathbf{w}_c G^c_{u\eta}(\omega)\,\eta_c. \tag{57}$$

The matrix inverse is now introduced by the approximation (32). In the present context all non-resonant modes are included in the quasi-static term, because the non-resonant lower modes are orthogonal or approximately orthogonal to the control force. Hereby the displacement of the collective sensor takes the form

$$\mathbf{w}_c^T\mathbf{u} \,=\, -\left(\frac{\omega_k^2}{\omega_k^2-\omega^2}\,|\nu_c|^2 \,+\, \mathbf{w}_c^T\mathbf{K}^{-1}\mathbf{w}_c \,-\, |\nu_c|^2\right) G^c_{u\eta}\,\eta_c\,. \tag{58}$$

The first term represents the dynamic response of the collective mode $\nu_c q_c$, while the two remaining terms constitute a correction for the quasi-static response of the non-resonant vibration modes. The response can be written in compact form as

$$\mathbf{w}_c^T\mathbf{u} \,=\, \nu_c\, q_c \,-\, \kappa_c\,|\nu_c|^2\, G^c_{u\eta}\,\eta_c\,, \tag{59}$$

where the factor

$$\kappa_c \,=\, \frac{\mathbf{w}_c^T\mathbf{K}^{-1}\mathbf{w}_c}{|\nu_c|^2} \,-\, 1 \tag{60}$$

represents the background flexibility from the non-resonant vibration modes. Substitution of (59) into (37) yields a modified filter equation

$$G^c_{\eta u}(\omega)|\nu_c|q_c + \Big[\, G^c_{\eta\eta}(\omega) \,-\, \kappa_c\,|\nu_c|^2\, G^c_{\eta u}(\omega)G^c_{u\eta}(\omega)\,\Big]\,\eta_c \,=\, 0, \tag{61}$$

which reduces to (49) for $\kappa_c = 0$. The introduction of the background flexibility leads to a modified interpretation of the control filter $G^c_{\eta\eta}(\omega)$ and thereby to a change in the calibration results. However, the calibration procedure is similar to the basic case and the expressions for the optimal control parameters, α_c, β_c, ω_c and ζ_c, are here only summarized in the bottom row of Table 1, where $\kappa = \kappa_c$ for the collective mode. It is seen that the expressions in the bottom row reduce to the expressions for the basic single mode calibration for $\kappa = 0$.

In the case of whirling modes the displacement generated by the control force takes a form similar to (57),

$$\mathbf{u} \,=\, -\big[\,\mathbf{K} + 2i\omega\mathbf{G} - \omega^2\mathbf{M}\,\big]^{-1}\mathbf{W}\,\boldsymbol{\eta}\,G^c_{u\eta}(\omega). \tag{62}$$

Introduction of the approximate representation (32) for the matrix inverse and identification of the dynamic modal response then gives the compact expression

$$\mathbf{W}^T\mathbf{u} \,=\, \boldsymbol{\nu}_w q_w \,-\, \boldsymbol{\kappa}_w G^w_{u\eta}\,\boldsymbol{\eta}_w\,, \tag{63}$$

where the correction matrix appears as

$$\boldsymbol{\kappa}_w \,=\, \mathbf{W}^T\mathbf{K}^{-1}\mathbf{W} \,-\, \tfrac{1}{2}\big(\boldsymbol{\nu}_w\bar{\boldsymbol{\nu}}_w^T \,+\, \bar{\boldsymbol{\nu}}_w\boldsymbol{\nu}_w^T\big)\,. \tag{64}$$

Substitution of the representation (63) into (43) yields a modified filter equation on scalar form

$$G^w_{\eta u}(\omega)\nu_w q_w + \Big[G^w_{\eta\eta}(\omega) \,-\, \kappa_w\,\nu_w^2\, G^w_{\eta u}G^w_{u\eta}\Big]\,\eta_c = 0\,, \tag{65}$$

where the scalar correction factor is given as

$$\kappa_w \;=\; \frac{\bar{\boldsymbol{\nu}}_w^T \boldsymbol{\kappa}_w \boldsymbol{\nu}_w}{\nu_w^4} \;=\; \frac{\bar{\boldsymbol{\nu}}_w^T \mathbf{W}^T \mathbf{K}^{-1} \mathbf{W} \boldsymbol{\nu}_w}{\nu_w^4} \;-\; 1\,. \tag{66}$$

It is noted that for undamped gyroscopic systems this scalar factor is real-valued. The modified filter equation (65) is equivalent to that in (61) for the collective mode, and the optimal control parameters for the whirling mode are given by the expressions in the bottom row of Table 1 with $\kappa = \kappa_w$.

4.4. *Implementation*

The equations of motion for the combined structure-control system are obtained by substitution of the control force expression (50) into the equation of motion (34). This equation must be supplemented by the equation (37) for the control of the collective mode and (43) for the whirling modes. The frequency functions defining the control are defined in (38), (39) and (52) for the collective mode, and in (44), (45) and (56) for the whirling modes.

The coupled equations of motion can be written in matrix form as

$$\mathbf{M}_*\ddot{\mathbf{u}}_* \;+\; \mathbf{D}_*\dot{\mathbf{u}}_* \;+\; \mathbf{K}_*\mathbf{u}_* \;=\; \mathbf{f}_*\,, \tag{67}$$

where the asterisk $*$ refers to an expanded format, where the augmented vector $\mathbf{u}_*$ contains both the structural and the control variables,

$$\mathbf{u}_*^T \;=\; [\,\mathbf{u}^T,\, \boldsymbol{\eta}^T,\, \eta_c\,]\,. \tag{68}$$

The vector $\boldsymbol{\eta}$ contains the three control variables addressing the whirling modes, while η_c is the scalar control variable for the collective mode. In the expanded format the system matrices are given as

$$\mathbf{M}_* = \begin{bmatrix} \mathbf{M} & \mathbf{0} & \mathbf{0} \\ -\mathbf{W}^T & \mathbf{I} & 0 \\ -\mathbf{w}_c^T & \mathbf{0} & 1 \end{bmatrix}, \quad \mathbf{D}_* = \begin{bmatrix} 2\mathbf{G} & g_\beta^w \mathbf{W} & g_\beta^c \mathbf{w}_c \\ \mathbf{0} & g_\zeta^w \mathbf{I} & \mathbf{0} \\ \mathbf{0} & \mathbf{0} & g_\zeta^c \end{bmatrix}, \quad \mathbf{K}_* = \begin{bmatrix} \mathbf{K} & g_\alpha^w \mathbf{W} & g_\alpha^c \mathbf{w}_c \\ \mathbf{0} & g_\omega^w \mathbf{I} & \mathbf{0} \\ \mathbf{0} & \mathbf{0} & g_\omega^c \end{bmatrix}. \tag{69}$$

The effective system parameters are defined as

$$g_\alpha \;=\; \frac{\alpha_\eta}{(\omega_n \nu)^2}\,\omega_\eta^2\,, \qquad g_\beta \;=\; \frac{\beta_\eta}{(\omega_n \nu)^2}\,2\zeta_\eta \omega_\eta\,, \qquad g_\zeta \;=\; 2\zeta_\eta \omega_\eta\,, \qquad g_\omega \;=\; \omega_\eta^2\,, \tag{70}$$

where superscripts c and w are implied, while $\omega_n \nu = \omega_{c,n}|\nu_c|$ for the control of the collective mode and $\omega_n \nu = \omega_{c,w}\nu_w$ for the whirling modes. The augmented force vector is $\mathbf{f}_*^T = [\,\mathbf{f}^T,\, \mathbf{0}^T,\, 0\,]$. It is noted that the present formulation does not include any delays in the controller system. However, in principle these effects can be included in the present format via additional differential relations, if needed.

5. Active Control of Wind Turbine Rotor

In this section the theory is illustrated by application to a three-bladed wind turbine rotor with a diameter of 86 m shown in Fig. 2 with an active strut mounted near the root of each blade. First the structural properties and dynamics of the rotor without control are presented. Then a controller system with a single active strut at the root of each blade is described and calibrated

according to the procedure in Section 4. Finally, the performance of the control is illustrated for response of the rotor to a wind field that is simulated by an autoregressive procedure outlined in Appendix A.

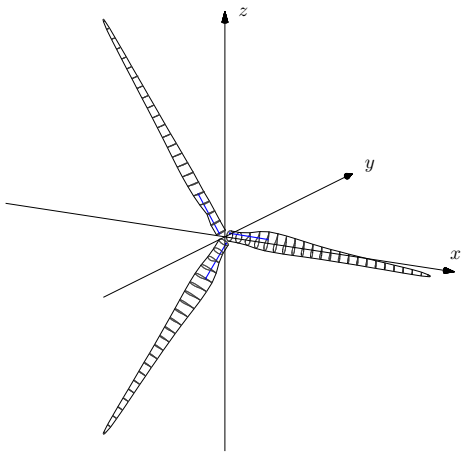

FIGURE 2. Three-bladed wind turbine rotor with actuator struts.

5.1. *The 86 m Wind Turbine Rotor*

The rotor consists of three identical 42 m blades. In Fig. 3 a blade is shown in the local blade coordinate system $\{\tilde{x}, \tilde{y}, \tilde{z}\}$. Each blade is equipped with a collocated sensor/actuator pair near the root, as shown in the figure. The structural properties of the free blade, i.e. with inactive controllers, correspond to a typical, modern wind turbine blade, [21]. The three blades are connected to the end of a solid steel shaft of length 0.2 m and diameter 0.5 m. The other end of the shaft is fixed in the rotating coordinate frame.

The rotor is modeled via a finite beam element formulation in the local, rotating frame of reference. Gyroscopic and centrifugal effects are represented, and the geometric stiffening effects due to the centrifugal blade loading are included via an initial stress formulation, [21]. Cross-section properties are provided at 46 sections along each blade. A linearized formulation of the aerodynamic forces on the blade is used, which includes a constant load term according to the undeformed blade position and velocity in the wind field and state-proportional terms representing relative inflow angle changes due to blade deformation, [29]. This formulation leads to an additional aerodynamic load vector $\mathbf{f}_a$ and the non-symmetric and non-positively definite stiffness and damping matrices $\mathbf{K}_a$ and $\mathbf{D}_a$. The aeroelastic equations of motion take the form

$$\mathbf{M}\ddot{\mathbf{u}} + (2\mathbf{G} - \mathbf{D}_a)\dot{\mathbf{u}} + (\mathbf{K} - \mathbf{K}_a)\mathbf{u} = \mathbf{f} + \mathbf{f}_a. \tag{71}$$

The properties of the aerodynamic terms break the symmetric and skew-symmetric form of the undamped system (9). However, the effects are relatively small and as demonstrated in the present example, the resonant controller tuning is robust and exhibits excellent performance for the damped aeroelastic system.

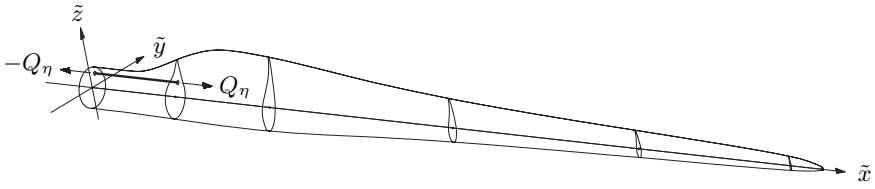

FIGURE 3. Rotor blade in the local coordinate system with an active strut attached at two cross-sections near the root.

The blades are modeled using $N_{el} = 8$ elements per blade of the type described in detail in [21], and the shaft is represented by a single element. The modal properties of the system (71) are obtained as a linear perturbation from a stationary state including structural forces with geometric stiffness, and centrifugal and aerodynamic forces. The modes and frequencies are obtained by solving the state-space eigenvalue problem (14), including the state-dependent aerodynamic terms. The eigenfrequencies ω_j and the aeroelastic damping ratios ζ_j are shown in Table 2. Modes 1-3 are the first flap-wise collective and whirling modes, that are dominated by displacements perpendicular to the rotor plane with local components $\tilde{q}_y$. The flap-wise modes are seen to be fairly strongly damped due to their significant impact on the flow pattern. Modes 4–6 constitute the first group of edge-wise vibration modes, with a collective mode 4, backward whirling in mode 5, and forward whirling in mode 6. These modes are seen to be weakly damped by aerodynamics, as they are dominated by displacements along the chord of the blade cross-sections. Modes 7–9 are the second flap-wise blade bending modes and modes 10–12 are the second edge-wise bending modes.

TABLE 2. Rotor eigenfrequencies and linear aerodynamic damping ratios.

j	1	2	3	4	5	6	7	8	9	10	11	12
ω_j	6.155	6.174	6.234	8.543	9.142	9.154	16.31	16.31	16.57	25.64	27.59	27.59
ζ_j	0.425	0.421	0.416	0.014	0.006	0.006	0.164	0.164	0.162	0.001	0.001	0.001

The rotor eigenfrequencies vary with the angular rotor velocity Ω, and for the present rotor the development is shown in Fig. 4 for modes 1, 4, 7 and 10. The values are obtained from

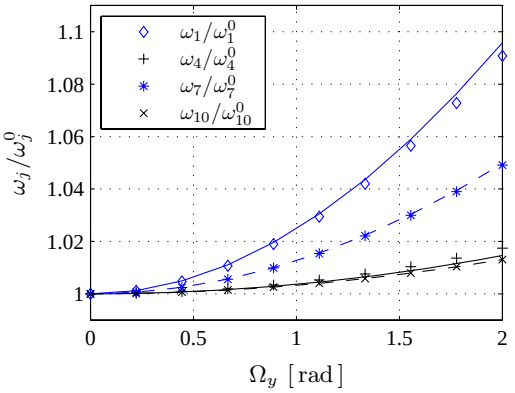

FIGURE 4. Eigenfrequencies as function of rotor angular velocity Ω_y. Markers from the eigenvalue problem (14), curves from the analytical expression (33).

solution of the eigenvalue problem (14) without aerodynamic terms and plotted as markers. The approximation (33) is plotted as curves and is seen to match the eigenvalue solution well. The flap-wise modes 1 and 7 are mostly out of the rotor plane and therefore only mobilize a small softening contribution from the centrifugal force load, and as a consequence the frequencies exhibit a substantial increase with rotor speed. In contrast the eigenfrequencies of the the edge-wise modes 4 and 10 are mainly in the rotor plane and exhibit a fairly modest increase due to the softening effect of the centrifugal load.

In the present example, the control system is designed to introduce additional damping into the first set of edge-wise bending modes, i.e. modes 4–6. The local components $\tilde{\mathbf{u}}_5^1$ of a single blade in backward whirling are shown in Fig. 5. The mode is normalized to a purely real blade tip displacement $\tilde{q}_z$ of unit magnitude. The mode is seen to be dominated by this component. The presence of significant imaginary components in the flap-wise direction $\tilde{q}_y$ is a combined effect of gyroscopic and aerodynamic damping forces and represents an elliptic modal blade motion in the local $\{\tilde{q}_y, \tilde{q}_z\}$-plane.

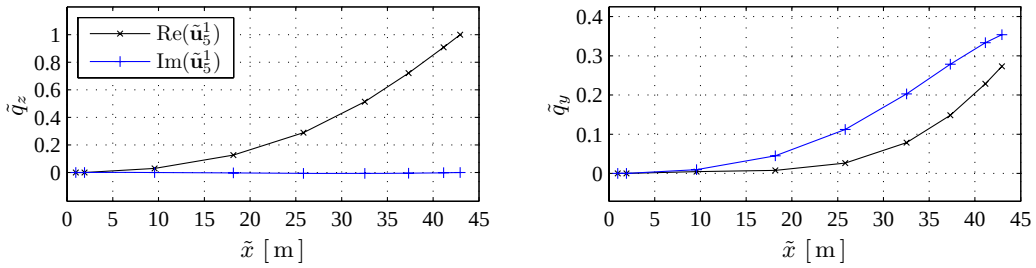

FIGURE 5. The edgewise backward whirling mode $\tilde{\mathbf{u}}_5^1$ for blade 1 with respect to the local blade coordinate system.

It is seen in Table 2 that the first edge-wise whirling modes have closely spaced eigenfrequencies. The frequency of the collective mode is close to the frequencies of the whirling modes due to the relatively high stiffness of the rotor shaft. In practice, the eigenfrequency of the collective mode is typically somewhat lower, due to the lower torsional stiffness of typical rotor shafts, [6]. The present configuration with a relatively stiff rotor shaft is chosen in order to demonstrate the ability of the present controller design to separate the collective mode from the whirling modes. Actual modal damping ratios are somewhat higher in practice than shown in Table 2. This is mainly due to structural intrinsic damping and non-linear aerodynamic effects which are not represented here. However, it is well established that edge-wise vibration modes tend to be weakly damped as discussed in Section 1.1.

5.2. *Controller Calibration*

The active strut shown in Fig. 3 is attached to the blade at two cross-sections with a distance of $L_s = 7.7\,\mathrm{m}$. A change of length of the strut introduces an eccentric axial force $\pm\tilde{Q}_\eta$ and thereby a local bending moment on these cross-sections. This actuator is well suited to control blade bending

modes, including in particular the first group of edge-wise vibration modes. For this purpose the eccentricity of the strut is chosen to impose bending moments about the local $\tilde{y}$-axis. The optimal polar angle between the $\tilde{z}$-axis and the direction to the strut is nearly the same for the three edge-wise modes, and the value $\theta_s/\pi = 0.46$ is chosen in all three blades to conserve symmetry.

The control system is calibrated by the procedure described in Section 4, including the effect of the background flexibility. The controller is designed to introduce the desired additional damping ratio to the collective mode $\Delta\zeta_c = 0.06$ and the additional damping ratio $\Delta\zeta_w = 0.06$ to the whirling modes. The resulting parameters are given in Table 3. The basic controller tuning involves a reduction of the controller frequencies $\omega_{c,w}$ relative to the modal eigenfrequency, while the quasi-static correction prescribes a relative increase. In the present case the resulting controller frequencies are slightly higher than the corresponding undamped structural frequencies, with $\omega_c/\omega_4 = 9.075/8.543 = 1.062$ and $\omega_w/\omega_5 = 9.564/9.142 = 1.046$. Also, the resulting controller damping ratios are seen to be slightly higher than the basic value of $\zeta_{c,w} \simeq 2\Delta\zeta_{4,5} = 0.12$.

TABLE 3. Control parameters for $\Delta\zeta_{4,5} = 0.06$.

	$\alpha_{c,w}$	$\beta_{c,w}$	$\omega_{c,w}$	$\zeta_{c,w}$	ν	κ
Collective	0.0297	0.0253	9.075	0.1541	1.374e-5	5.867
Whirling	0.0297	0.0259	9.564	0.1482	2.558e-5	4.941

The structural frequency response of the collective and the two whirling modes are shown in the upper part of Fig. 6. The dynamic amplification of a blade tip response is evaluated for a harmonic load proportional to the individual mode shape, $\mathbf{f} = \mathbf{u}_j e^{i\omega t}$. The free response, shown with a thin full line displays significant resonant amplification, while the damped response, shown with a thick full line displays equally damped modes with low dynamic amplification and the desired flat plateau at resonance. The dashed curves show the response obtained when the correction for quasi-static background flexibility is not included, i.e. with $\kappa_{c,w} = 0$. Clearly, this correction is decisive for optimal calibration of the present control system. The importance of the quasi-static correction is represented by the magnitude of the parameter κ, and examples in [16] for a building structure show the parameter range $\kappa \simeq 1$–10, depending on how directly the sensor/actuator pair is addressing the targeted mode.

The lower part of Fig. 6 shows the frequency responses of the imposed controller moments $\tilde{M}_\eta = \tilde{Q}_\eta \tilde{d}_z$, where $\tilde{d}_z$ is the local $\tilde{z}$-wise position coordinate of the sensor/actuator pair. The values are normalized with respect to the static blade root moments about the local $\tilde{y}$-axis $\tilde{M}_y^0$. The slightly inclined plateau is similar to the ideal optimal results presented in [15].

The response is calculated by use of the combined structure–controller equations (67). The eigenvalue problem associated with equation (67) is solved for the four possible combinations of active or in-active controllers and the associated modal properties of the closed-loop system are listed in Table 4. The modal properties for zero gain, $\alpha_c = \alpha_w = 0$ corresponds to $\Delta\zeta_{c,w} = 0$ and

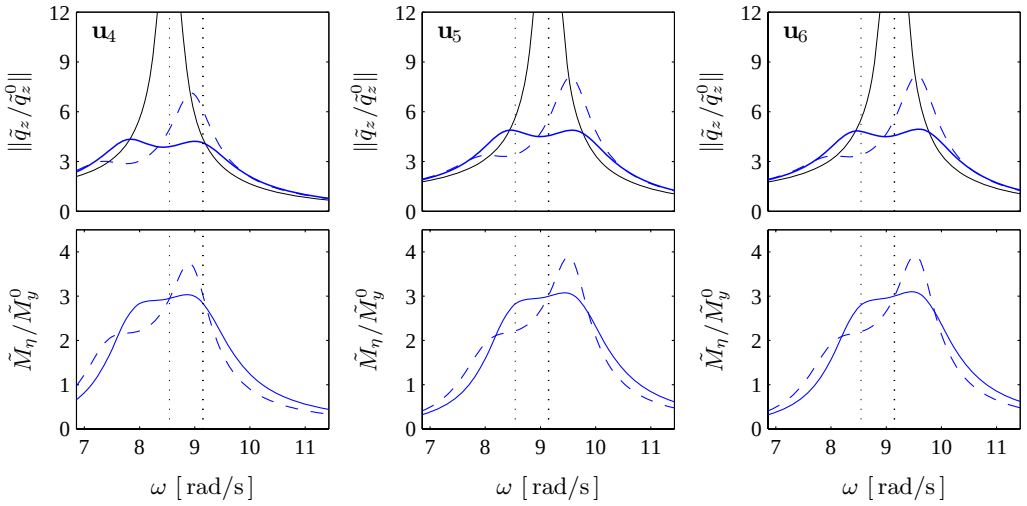

FIGURE 6. Modal dynamic amplification. Top: blade tip response; Bottom: normalized control moment. (Thin full line: free; Thick full line: control; Dashed: control with $\kappa_{w,c} = 0$.)

reproduce the eigenfrequencies and damping of the structural system (71). However, in this case the control variables appear in the form of the four new undamped modes 4, 6, 7 and 9.

The results in the three remaining column pairs correspond to an additional desired damping ratio of $\Delta\zeta = 0.06$ for the three cases: combined damping of collective and whirling modes, damping of collective mode alone, and damping of whirling modes alone. As mentioned in Section 4 the effect of the controller is to split an original undamped structural mode into two modes with equal damping but slightly different frequency. In the case where all three edge-wise modes are damped with the target $\Delta\zeta_c = \Delta\zeta_w = 0.06$ the collective mode splits into modes 4 and 7 with resulting total damping ratio 0.0682 and 0.0687, respectively. These damping ratios are nearly equal and correspond closely to the combination of structural and imposed damping derived theoretically in [30], by which $\zeta_{\text{total}} \simeq \frac{3}{4}\zeta_{\text{struct}} + \zeta_{\text{cont}} = \frac{3}{4}0.0137 + 0.06 = 0.0703$. Similarly the original two whirling modes split into modes 5, 6, 9, and 10 that have nearly equal total damping ratio in the range 0.0641–0.0654, corresponding closely to the theoretical value $\zeta_{\text{total}} \simeq \frac{3}{4}0.0057 + 0.06 = 0.0643$.

The case in which only the collective mode is controlled, $\Delta\zeta_c = 0.06$ and $\Delta\zeta_w = 0$, is shown in the third double-column. The collective mode is split into modes 4 and 5, and the total damping is identical to that of the combined damping case. In this case the whirling modes 7 and 10 are unaffected, and there are 3 undamped zero gain controller modes. Conversely, in the case of damping of only the whirling modes, $\Delta\zeta_c = 0$ and $\Delta\zeta_w = 0.06$, these modes retain the additional damping from the combined case, while the collective mode receives no additional damping. Thus, the results illustrate the complete decoupling of the collective mode from the whirling modes, and also demonstrate that the total damping conforms closely to the theoretical prediction. Furthermore, it is seen that the influence of the controller on the other modes, the so-called spill-over effect, is negligible.

TABLE 4. Rotor eigenfrequencies and damping ratios.

Mode	$\Delta\zeta_{c,w} = 0$		$\Delta\zeta_{c,w} = 0.06$		$\Delta\zeta_c = 0.06$		$\Delta\zeta_w = 0.06$	
j	ω_j	ζ_j	ω_j	ζ_j	ω_j	ζ_j	ω_j	ζ_j
1	6.1549	0.4249	6.1613	0.4242	6.1549	0.4249	6.1613	0.4242
2	6.1741	0.4207	6.1804	0.4200	6.1741	0.4207	6.1804	0.4200
3	6.2342	0.4157	6.2447	0.4152	6.2447	0.4152	6.2342	0.4157
4	8.5432	0.0000	7.7859	0.0690	7.7859	0.0690	8.3759	0.0649
5	8.5432	0.0137	8.3759	0.0649	9.1218	0.0690	8.3799	0.0656
6	9.1416	0.0000	8.3799	0.0656	9.1416	0.0000	8.5432	0.0137
7	9.1416	0.0000	9.1218	0.0690	9.1416	0.0000	8.5432	0.0000
8	9.1416	0.0057	9.4581	0.1482	9.1416	0.0057	9.4581	0.1482
9	9.1416	0.0000	9.7026	0.0645	9.1416	0.0000	9.7026	0.0645
10	9.1544	0.0056	9.7116	0.0637	9.1544	0.0056	9.7116	0.0637
11	16.3080	0.1642	16.3081	0.1642	16.3080	0.1642	16.3081	0.1642
12	16.3135	0.1642	16.3141	0.1642	16.3135	0.1642	16.3141	0.1642
13	16.5668	0.1623	16.5670	0.1622	16.5670	0.1622	16.5668	0.1623
14	25.6435	0.0012	25.8800	0.0081	25.8800	0.0081	25.6435	0.0012
15	27.5851	0.0006	27.9584	0.0110	27.5851	0.0006	27.9584	0.0110
16	27.5925	0.0004	27.9665	0.0108	27.5925	0.0004	27.9665	0.0108

5.3. *Wind Field Simulation*

The wind velocity field is simulated by the simple auto-regressive model presented in appendix A. The model generates correlated time histories corresponding to an approximate isotropic wind field at the points of the mesh shown in Fig. 7 consisting of 24 radial lines with 8 points in each. In the model a correlated wind velocity field is generated on a cross-section and propagated by a single-step recurrence relation. The model represents a spatial field of 'frozen turbulence', that is then convected downwind with the mean wind speed $V = 12\,\mathrm{m/s}$, [31]. The along-wind step size is taken as $\Delta y = 0.5\,\mathrm{m/s}$ to allow for a suitable frequency resolution of the wind field. Due to the approximate nature of the simulation model it must be calibrated at two sections separated by several of the intended simulation steps Δy. In the present example the integral length-scale of the wind field is $\lambda = 120\,\mathrm{m}$, and the model is calibrated by the correlation structure of two sections separated by the length-scale λ, as illustrated in Fig. 7.

The single-step model is approximate as discussed in the appendix. In the present context the main purpose is to enable a fair assessment of the reduction in the vibration level of the wind turbine rotor from its initial state without damping devices to the configuration with an axial sensor-actuator mounted close to the blade root. The two important features in this context are the axial correlation structure, which appears as spectral frequency content, and the transverse correlation determining the modal loads on the blades. An indication of the performance of the simulation method can be obtained from Fig. 8 showing the along-wind component correlation and the transverse component correlations for points separated by the along-wind distance y. The figure shows the theoretical correlation functions under the assumption of exponential or Airy

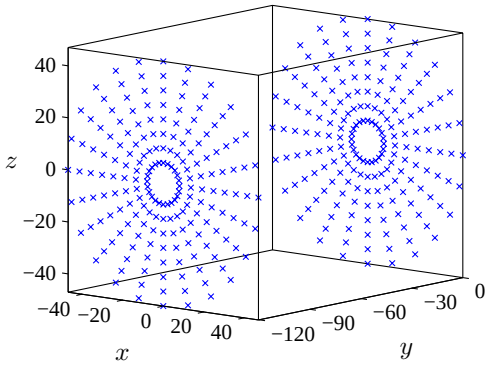

FIGURE 7. Points for wind field calibration, $\lambda = \Delta y = 120\,\mathrm{m}$.

function representation, respectively. The model was calibrated using the exponential representation of the correlation functions, and the figure shows the correlation functions of simulated records at point number 5 from the center in the horizontal line in the grid. It is seen that the transverse correlation function corresponds closely to the Airy function representation obtained from the von Kàrmàn spectral density function [32], while the axial component retains much of its exponential structure. The model shows a good conservation of the initial theoretical correlation structure in a cross section, and thus represents the modal loads rather well. The representation of the frequency behavior, corresponding to along-wind records, contains some approximation, but as the present application is related to the relative magnitude of resonant response at particular structural frequencies, the model is considered fully adequate in the present context.

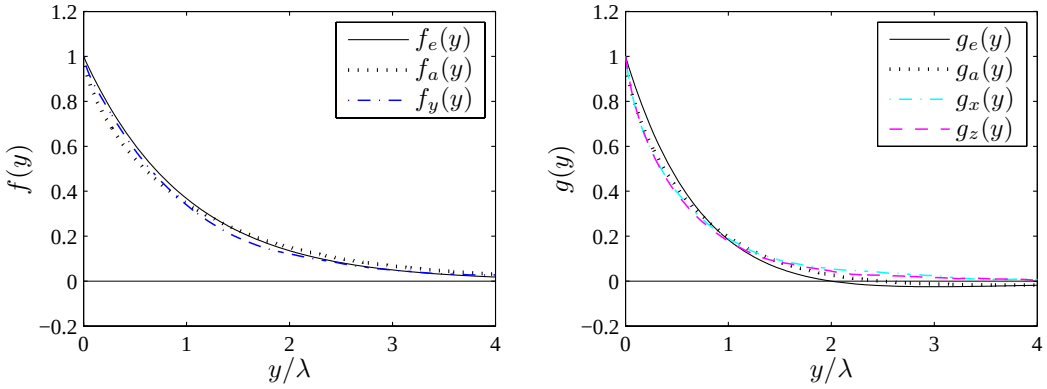

FIGURE 8. Simulated and theoretical autocorrelation functions.

5.4. *Simulated Structural Response*

The performance of the control system is evaluated from a simulated response of the rotor to the stochastic wind field introduced in the previous section. In the simulation the rotor angular velocity is held constant at $\Omega_y = 1.57\,\mathrm{rad/s}$ and the blade pitch angle is held constant at $\beta_p = 4.4^0$.

The structural response is obtained via a standard Newmark integration with the unconditionally stable 'average acceleration' scheme. The time step h is selected such that mode 16 of the coupled structure is resolved with 10 points per period, corresponding to $h = 0.023\,\mathrm{s}$. The wind field of frozen turbulence is convected with the mean velocity $V = 12\,\mathrm{m/s}$, which with simulation steps $\Delta y = 0.5\,\mathrm{m}$ corresponds to a sample frequency of 24 Hz.

The data points of the rotor blades follow helical trajectories through the grid of discrete frozen turbulence components. At all simulation time instants the three turbulence components are evaluated at the blade element data points by linear spatial interpolation. In each simulation time instant the associated aerodynamic load vector $\mathbf{f}_a$ and matrices $\mathbf{D}_a$, $\mathbf{K}_a$ are evaluated and the geometric stiffness matrix $\mathbf{K}_g$ is established using four iterations of internal stresses in the dynamic system equation (67).

The free response with $\Delta\zeta_c = \Delta\zeta_w = 0$ and the controlled response with $\Delta\zeta_c = \Delta\zeta_w = 0.06$ are simulated using the same wind field. Time histories for the in-plane and out-of-plane tip displacements $\tilde{q}_z^1$ and $\tilde{q}_y^1$ are shown in Fig. 9. The free edge-wise response in Fig. 9a is seen to have a highly active dynamic component near the eigenfrequency of the first edge-wise modes. This particular dynamic component is seen to be effectively reduced in the controlled case. Figure 9b shows the corresponding flap-wise tip response. It is seen that this part of the response is virtually unaffected by the controller. This is primarily due to the geometric decoupling of the controller from flap-wise blade motion, obtained via the positioning of the sensor/actuator pairs.

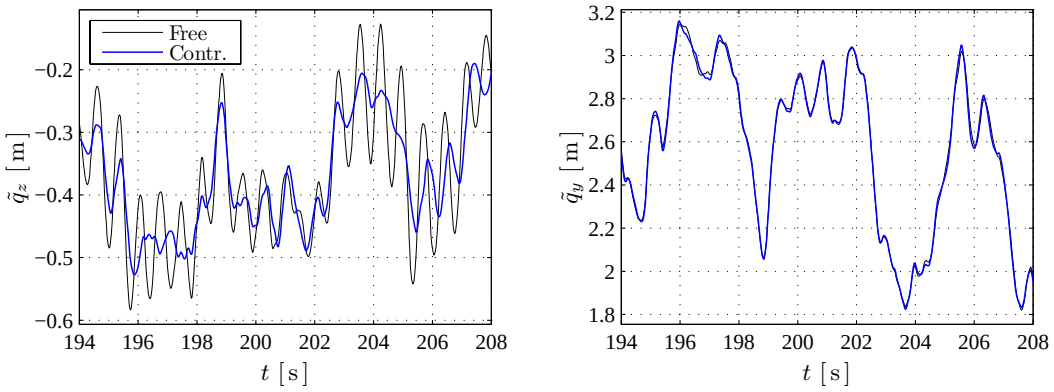

FIGURE 9. Local edge-wise $\tilde{q}_z$ and flap-wise $\tilde{q}_y$ blade tip displacements.

The resonance principle implemented in the controllers is clearly seen from the energy density spectra of the edge-wise blade responses $S_j^q(\omega)$ for each of the three blades $j = 1, 2, 3$, as shown in Fig. 10. The vertical lines indicate structural eigenfrequencies from Table 2, and two distinct peaks are seen located at the collective and the whirling mode free response frequencies. In the controlled case these local peaks in the spectral density are essentially eliminated, while leaving the remaining spectrum virtually unaffected. At the angular rotor velocity $\Omega_y = 1.57\,\mathrm{rad/s}$, marked with a dotted line, a distinct peak is seen, arising from the periodic motion of the rotor in the wind field, [33]. One revolution takes $T_\Omega = 4\,\mathrm{s}$, during which the convected turbulence travels

$T_\Omega V = 48\,\mathrm{m} = 0.4\lambda$. As seen in Fig. 8, significant correlation is present at this distance. This effect is also clearly visible in the response spectra shown in [1] and [6].

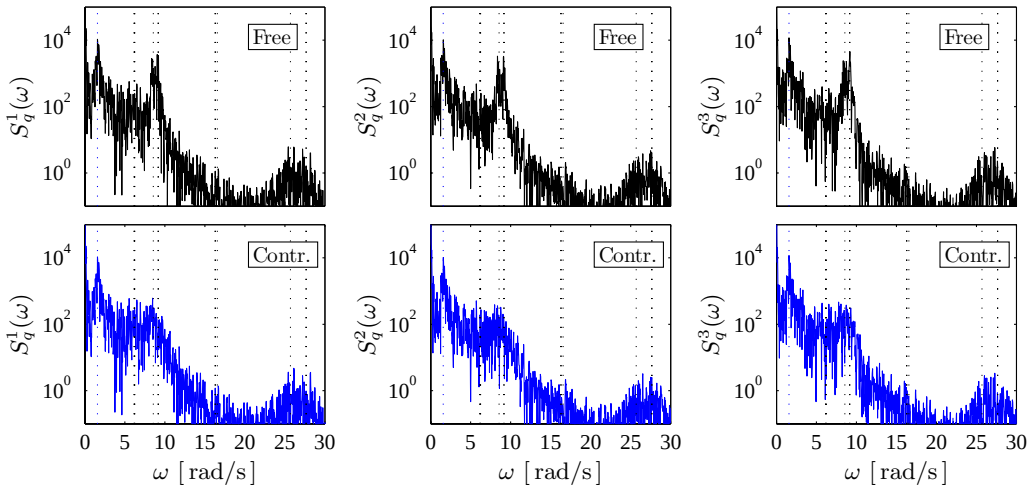

FIGURE 10. Energy spectrum $S_q^j(\omega)$ of edgewise blade tip displacements $\tilde{q}_z^j$.

The bending moment in a blade about the local $\tilde{y}$-axis $\tilde{M}_y$, at the innermost end of the active strut, located at node 2 in the present model, is plotted in Fig. 11a. Again, the edge-wise dynamic components are seen to be significantly reduced in the controlled case. Also, the bending moment imposed by the actuator $\tilde{M}_\eta = \tilde{Q}_\eta \tilde{d}_z$, where $\tilde{d}_z$ is the local $\tilde{z}$-wise position coordinate of the sensor/actuator pair, is plotted. It is seen that the bending moment imposed by the controller is small compared to the total bending moment in the blade. This relative difference in amplitude is a general feature of the optimally tuned resonant controller. The effect is equivalent to harmonic loading where large dynamic amplification is obtained at resonance. The local trailing edge material strains at the same location are plotted in Fig. 11b. In spite of significant actuator forces, the material strain at the position of the actuator is reduced in the controlled case. This is due to

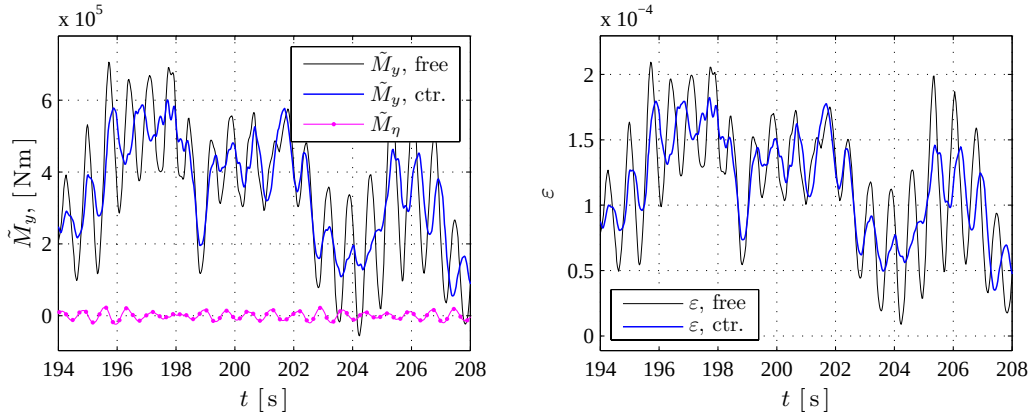

FIGURE 11. Structural load at root-end of actuator. a) Edgewise bending moments. b) Trailing edge strains.

the fact that the optimally tuned resonant controller deploys actuator force for maximal energy dissipation. This occurs at peak velocities where structural displacements vanish.

Both forward and backward whirling produce hub reaction forces perpendicular to the axis of rotation which must be balanced by the rotor shaft. To illustrate this effect the local blade root shear forces measured in the rotor coordinate system Q_x, Q_z are evaluated and the energy density spectra $S_Q^x(\omega)$, $S_Q^z(\omega)$ of the resulting rotor hub forces Q_x, Q_z are plotted in Fig. 12. In the free response this load appears as distinct peaks at the first edge-wise whirling frequencies. As seen from the controlled response the whirling controller effectively eliminates this component of the energy spectrum.

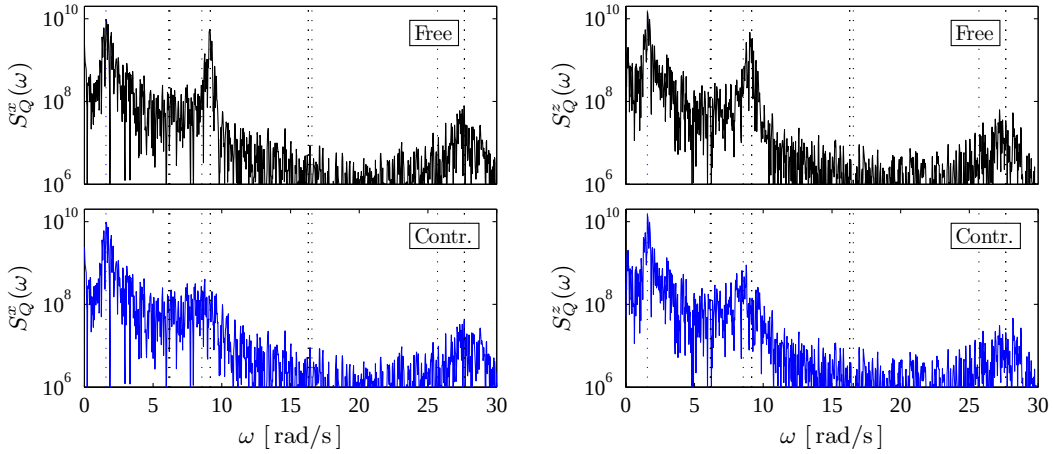

FIGURE 12. Energy density spectra $S_Q^x(\omega)$, $S_Q^z(\omega)$ of the rotor hub forces Q_x and Q_z.

A typical design factor for linear actuator systems is the required stroke velocity. A sample of the stroke velocity $\dot{q}_\eta$ is shown in Fig. 13a. In the present case the stroke velocities range within $\pm 4\,\mathrm{mm/s}$. The range of actuator forces Q_η in the present application is $\pm 60\,\mathrm{kN}$. Both requirements

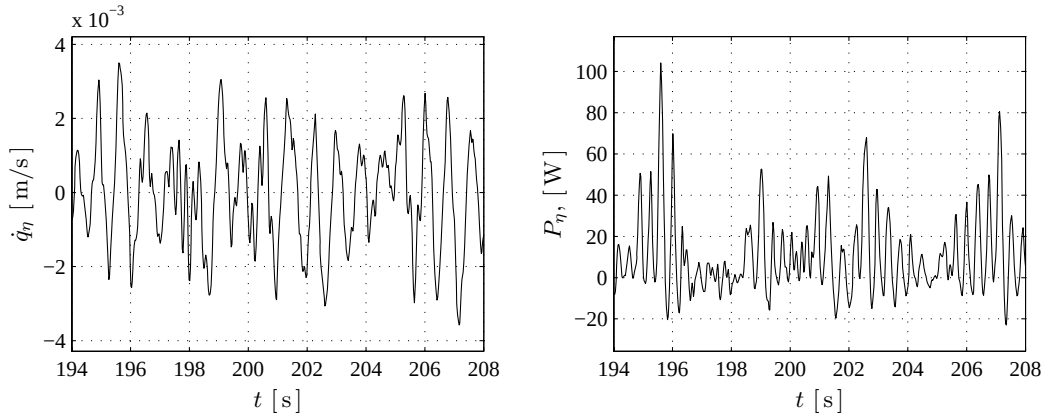

FIGURE 13. Actuator displacement velocity $\dot{q}_\eta$ and dissipative actuator power P_η.

are easily met by existing hydraulic actuators, and this technology is already widely used in the active pitch regulation systems of modern wind turbines.

The dissipative power of an actuator $P_\eta = Q_\eta \dot{q}_\eta$ is shown in Fig. 13. Occasional negative contributions are seen to occur, however the energy dissipation is generally positive. The continuous power consumption of the controller is in the range of 100 W which is insignificant compared to the mega-Watt power production capacity of modern wind turbines.

6. Conclusions

It has been known for the last decade that edge-wise vibrations of the blades in three-bladed rotors for wind turbines are potentially very lightly damped. These vibration modes occur in groups of three due to the three-fold symmetry of the rotor, and a method for control of such a group of vibration modes has been developed. The method makes use of collocated control via a single active strut with sensor/actuator capacity in each of the three blades. The controller system is based on the concept of resonance, generalizing the idea of the tuned mass damper. Thus, the combined information from the sensor in each of the three blades must be used to extract the relevant information about the current magnitude of the targeted modal response. When using the minimum number of sensor/actuator pairs – here three active struts for the group of three associated edge-wise vibration modes – it is unavoidable that the response also contains non-resonant contributions from other modes. The procedure developed here separates the response into that of the collective mode of the group, and the combined response from the pair of whirling modes in the group. For each of these two types of response a quasi-static correction is developed to account for the extra flexibility created by the non-resonant part of the response. In typical three-bladed wind turbine rotors the sensor/actuator struts can be mounted such that the effect is orthogonal or nearly orthogonal to the relevant group(s) of flap-wise vibration modes. Low-frequency tower modes will typically be separated frequency-wise from the targeted edge-wise vibration modes, and the quasi-static correction terms can therefore be expressed explicitly in terms of the stiffness matrix and the mode-shapes of the targeted modes, without need for a complete modal analysis of the system.

The calibration procedure makes use of a full eigenvalue analysis of the rotating blades with complex-valued mode-shapes. The full modal expansion in this case has $2N$ terms, each associated with a frequency factor $(\omega_j \pm \omega)^{-1}$, instead of the eigenvalue problem for non-rotating systems with an N-term solution with frequency factors $(\omega_j^2 - \omega^2)^{-1}$. It is demonstrated, how the general complex formulation can be used in an approximate form, that appears as a simple introduction of complex mode-shape vectors in the classic form for non-rotating structures. The resulting formulation is in terms of real-valued coefficients, permitting use of the optimal parameter formulae for non-rotating structures.

The performance of the resonant control procedure with three active struts has been investigated in relation to a wind turbine rotor with a diameter of 86 m, representative of current large-size

wind turbines. The analysis demonstrates as illustrated in Fig. 6 that the controller calibration is close to optimal, when the quasi-static correction is included, while omission of the effect of the additional quasi-static flexibility will result in a rather unbalanced calibration with reduced damping capacity. The introduction of a quasi-static correction leads to a controller format that is more general than that associated with a tuned mass absorber. While the tuned mass absorber is a purely passive device, the use of the generalized format may lead to a need for an active power supply as illustrated in Fig. 13b. However, the necessary power capacity is quite low compared to the dissipated power. The idea of the resonant control is to target one or more selected modes specifically, with the expectation that this will reduce oscillations occurring at the targeted frequencies. The effectiveness is clearly illustrated in the response records shown in Figs. 9 and 11. Thus, the resonant damping approach appears very suitable for reduction of the fatigue loading on wind turbine rotor blades. The use of a local active strut introduces local structural loads, but the records shown in Fig. 11 indicate that the local controller loads are modest relative to the effect of the direct structural loads.

Appendix A. Wind Field Simulation

A.1. *Isotropic wind field*

The turbulent wind field used in the present paper is represented in the form of isotropic incompressible turbulence as described by Batchelor [31]. The general form of the covariance between the turbulent velocity components at two points separated by the spatial vector $\mathbf{x}$ then is

$$\mathbf{R}(\mathbf{r}) \,=\, \mathrm{E}[\,\mathbf{v}(\mathbf{r}_0+\mathbf{r})\,\mathbf{v}(\mathbf{r}_0)^T\,] \,=\, \sigma_v^2\Big(\,[\,f(r)-g(r)\,]\frac{\mathbf{r}\,\mathbf{r}^T}{\mathbf{r}^T\mathbf{r}} \,+\, g(r)\Big), \tag{A.1}$$

where $r=|\mathbf{r}|$ is the distance between the two points, and σ_v^2 is the variance of a single component at a point. $f(r)$ and $g(r)$ are the lengthwise and transverse correlation function, respectively. It follows from incompressibility that they are related by

$$g(r) \,=\, f(r) \,+\, \frac{r}{2}\,\frac{d}{dr}f(r). \tag{A.2}$$

The covariance functions are described by the lengthwise spectral density function $F(k)$, where k is the wavenumber,

$$\sigma_v^2 f(r) \,=\, \int_{-\infty}^{\infty} F(k)\,\mathrm{e}^{ikr}\,dr. \tag{A.3}$$

Analytically tractable results are obtained when using the von Kàrmàn spectral density, [32],

$$\sigma_v^2 F(k) \,=\, \frac{1}{\sqrt{\pi}}\,\frac{\Gamma(\gamma)}{\Gamma(\gamma-\frac{1}{2})}\,\frac{\sigma_u^2\,\ell}{[\,1+(k\ell)^2]^\gamma}. \tag{A.4}$$

The Kolmogorov cascade theory implies that the exponent is $\gamma=5/6$. In this case the covariance functions can be expressed in terms of Airy functions [34], when introducing the non-linear variable transformation

$$z=\Big(\frac{3r}{2\ell}\Big)^{2/3}, \tag{A.5}$$

whereby

$$f(r)=\frac{\mathrm{Ai}(z)}{\mathrm{Ai}(0)}, \qquad g(r) \,=\, f(r) \,+\, \frac{z}{3}\,\frac{\mathrm{Ai}'(z)}{\mathrm{Ai}(0)}. \tag{A.6}$$

Here $\mathrm{Ai}(z)$ is the Airy function and $\mathrm{Ai}'(z)$ its derivative. A simpler approximate formulation is obtained by using $\gamma = 1$, whereby

$$f(r) = \mathrm{e}^{-r/\lambda}, \qquad g(r) \;=\; \big(\,1 - \frac{1}{2}\,\frac{r}{\lambda}\big)\,\mathrm{e}^{-r/\lambda}. \tag{A.7}$$

In this formulation λ is the integral spatial length-scale. When using the same integral length-scale in (A.6) it follows that $\ell = 1.339\lambda$. The Airy and exponential formats are compared in Fig. A.1, showing that the curves cross at $r \simeq \lambda$.

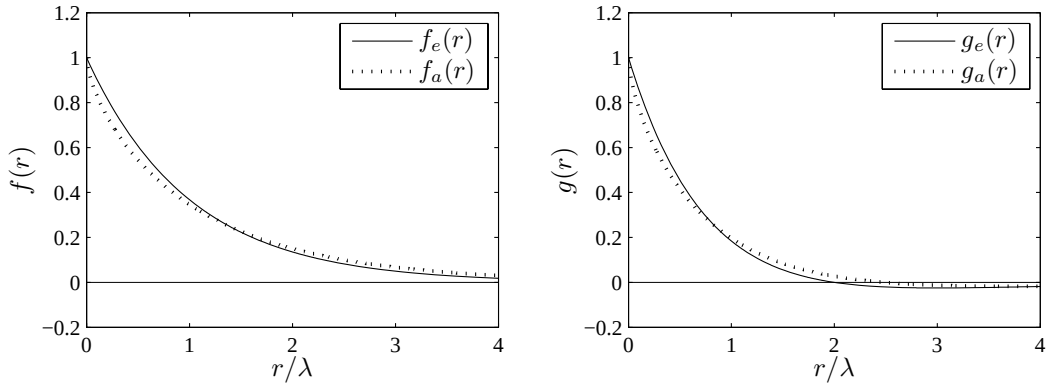

FIGURE A.1. Correlation functions $f(r)$ and $g(r)$: Airy (dots), Exponential (full).

A.2. *Autoregressive simulation*

In the present context, where the main purpose is to estimate the reduction of the resonant response, the turbulent wind field is simulated by use of an autoregressive model represented by the single-step recurrence relation

$$\mathbf{v}_n \;=\; \mathbf{A}\mathbf{v}_{n-1} \,+\, \mathbf{B}\boldsymbol{\xi}_{n-1}, \qquad n = 1, 2, \cdots \tag{A.8}$$

The array $\mathbf{v}_n$ contains the wind components at a chosen number of points in a transverse plane relative to the average wind, and $\boldsymbol{\xi}_n$ contains corresponding uncorrelated normally distributed variables,

$$\mathbf{v}_n \;=\; [\,v_1, v_2, \cdots, v_m\,]_n^T\,, \qquad \boldsymbol{\xi}_n \;=\; [\,\xi_1, \xi_2, \cdots, \xi_m\,]_n^T \tag{A.9}$$

The subscript n denotes the time $t_n = n\,\Delta t$, and each step in the recurrence corresponds to a time increment Δt. The relation between spatial coordinates and time is provided by the mean wind speed V via the hypothesis of convected 'frozen turbulence', [31]. Hereby the time increment Δt corresponds to the downwind distance

$$\Delta y = V\,\Delta t\,, \tag{A.10}$$

and time separation can be related to the spatial covariance function (A.1).

The chief advantage of the simple single-step algorithm (A.8) is the simple relation between the matrices $\mathbf{A}$, $\mathbf{B}$ and the covariance function describing the field,

$$\mathbf{R}_j \;=\; \mathrm{E}[\,\mathbf{v}_n \mathbf{v}_{n-j}^T\,] \qquad j = \cdots, -1, 0, 1, \cdots\,. \tag{A.11}$$

Although the single-step autoregressive model imposes severe constraints on the simulated field, it appears to capture the essential properties of the present problem sufficiently well.

For calibration over a single step the matrices $\mathbf{A}$ and $\mathbf{B}$ can be identified directly via conditional expected values in the stochastic wind field. The idea is to consider $\mathbf{v}_{n-1}$ known. Hereby the conditional expectation of $\mathbf{v}_n$ becomes

$$\mathrm{E}[\,\mathbf{v}_n|\,\mathbf{v}_{n-1}] \;=\; \mathbf{A}\mathbf{v}_{n-1}. \tag{A.12}$$

Thus, $\mathbf{A}$ is identified as the matrix in the conditional mean formula of a set of correlated stochastic variables, given by

$$\mathbf{A} \;=\; \mathbf{R}_1\mathbf{R}_0^{-1}. \tag{A.13}$$

The matrix $\mathbf{B}$ is determined by collecting the two response terms on the left side of the equation,

$$\mathbf{v}_n \;-\; \mathbf{A}\mathbf{v}_{n-1} \;=\; \mathbf{B}\boldsymbol{\xi}_{n-1}. \tag{A.14}$$

Both sides represent a normal vector variable with zero mean. When the vector $\mathbf{v}_{n-1}$ is assumed known, the covariance matrix of the right hand side corresponds to the conditional covariance of $\mathbf{v}_n$,

$$\mathrm{Cov}[\,\mathbf{v}_n\mathbf{v}_n^T|\,\mathbf{v}_{n-1}] \;=\; \mathbf{B}\,\mathrm{E}[\,\boldsymbol{\xi}_{n-1}\boldsymbol{\xi}_{n-1}^T]\,\mathbf{B}^T. \tag{A.15}$$

The vector $\boldsymbol{\xi}_{n-1}$ has independent normalized components, and thus the product $\mathbf{B}\mathbf{B}^T$ is the conditional covariance

$$\mathbf{B}\,\mathbf{B}^T \;=\; \mathrm{Cov}[\,\mathbf{v}_n\mathbf{v}_n^T|\,\mathbf{v}_{n-1}] \;=\; \mathbf{R}_0 \;-\; \mathbf{R}_1\mathbf{R}_0^{-1}\mathbf{R}_1^T, \tag{A.16}$$

It is observed that the two parameter matrices of the AR filter are determined by the conditional expectation and the conditional covariance with the previous variable $\mathbf{v}_{n-1}$ known.

References

[1] Hansen, M.O.L., Sørensen, J.N., Voutsinas, S., Sørensen, S., and Madsen, H.Aa., State of the art in wind turbine aerodynamics and aeroelasticity, *Progress in Aerospace Sciences*, Vol. 42, 2006, pp. 285–330.

[2] Friedmann, P.P., Rotary-wing aeroelasticity: Current status and future trends, *AIAA Journal*, Vol. 42, 2004, pp. 1953–1972.

[3] Thomsen, K., Petersen, J.T., Nim, E., Øye, S., and Petersen, B., A method for determination of damping for edgewise blade vibrations, *Wind Energy*, Vol. 3, 2000, pp. 233–246.

[4] Hansen, M.H., Improved modal dynamics of wind turbines to avoid stall-induced vibrations, *Wind Energy*, Vol. 6, 2003, pp. 179–195.

[5] Riziotis, V.A., Voutsinas, S.G., Politis, E.S., and Chaviaropoulos, P.K., Aeroelastic stability of wind turbines: the problem, the methods and the issues, *Wind Energy*, Vol. 7, 2004, pp. 373–392.

[6] Hansen, M.H., Thomsen, K., Fuglsang, P., and Knudsen, T., Two methods for estimating aeroelastic damping of operational wind turbine modes from experiments, *Wind Energy*, Vol. 9, 2006, pp. 179–191.

[7] Meirovitch, L., *Dynamics and Control of Structures*, Wiley, New York, 1990.

[8] Khulief, Y.A., Vibration suppression in rotating beams using active modal control, *Journal of Sound and Vibration*, Vol. 242, 2001, pp. 681–699.

[9] Chandiramani, N.K., Librescu, Saxena V., L.I., and Kumar, A., Optimal vibration control of a rotating composite beam with distributed piezoelectric sensing and actuation, *Smart Materials and Structures*, Vol. 13, 2004, pp. 433–442.

[10] Shete, C.D., Chandiramani, N.K., and Librescu, L.I., Optimal control of a pretwisted shearable smart composite rotating beam, *Acta Mechanica*, Vol. 191, 2007, pp. 37–58.

[11] Rice, J.K., and Verhaegen, M., Robust and distributed control of a smart blade, *Wind Energy*, Vol. 13, 2010, pp. 103–116.

[12] Barlas, T.K., and van Kuik, G.A.M., Review of state of the art in smart rotor control research for wind turbines, *Progress in Aerospace Sciences*, Vol. 46, 2010, pp. 1–27.

[13] Buhl, T., Gaunaa, M., and Bak, C., Potential load reduction using airfoils with variable trailing edge geometry, *Journal of Solar Energy Engineering*, Vol. 127, 2005, pp. 503–516.

[14] Andersen, P.B., Henriksen, L., Gaunaa, M., Bak, C., and Buhl, T., Deformable trailing edge flaps for modern megawatt wind turbine controllers using strain gauge sensors, *Wind Energy*, Vol. 13, 2010, pp. 193–206.

[15] Krenk, S., and Høgsberg, J., Optimal resonant control of flexible structures, *Journal of Sound and Vibration*, Vol. 323, 2009, pp. 530–554.

[16] Krenk, S., and Høgsberg, J., Resonant damping of flexible structures under random excitation, in *Computational Methods in Stochastic Dynamics*, eds. Papadrakakis, M., et al., Computational Methods in Applied Sciences, vol. 22, Springer, Dordrecht, 2011, pp., 25–46. (DOI 10.1007/978-90-481-9987-7_2)

[17] Coleman, R.P., Theory of self-excited mechanical oscillations of hinged rotor blades, *Technical Report NACA-WR-L-308*, Langley Research Center, 1943. (http://ntrs.nasa.gov).

[18] Thomas, D.L., Dynamics of rotationally periodic structures, *International Journal for Numerical Methods in Engineering*, Vol. 14, 1979, pp. 81–102.

[19] Kosmatka, J.B. and Friedmann, P.P., Vibration analysis of composite turbopropellers using a non-liear beam-type finite-element approach, *AIAA Journal*, Vol. 27, 1989, pp. 1606–1614.

[20] Géradin, and M., Rixen, D., *Mechanical Vibrations*, second ed., Wiley, Chichester, 1997.

[21] Svendsen, M.N., Krenk, K., and Høgsberg, J., Resonant vibration control of rotating beams, *Journal of Sound and Vibration*, 2010. (doi:10.1016/j.jsv.2010.11.008)

[22] Meirovitch, L., A new method of solution of the eigenvalue problem for gyroscopic systems, *AIAA Journal*, Vol. 12, 1974, pp. 1337–1342.

[23] Meirovitch, L., *Principles and Techniques of Vibrations*, Prentice-Hall, Upper Saddle River, New Jersey, 1997.

[24] Krenk, S., and Nielsen, M.B., Hybrid state-space time integration in a rotating frame of reference. Department of Mechanical Engineering, Technical University of Denmark, 2010. (to be published)

[25] Hansteen, O.E., and Bell, K., Accuracy of mode superposition analysis in structural dynamics, *Earthquake Engineering and Structural Dynamics*, Vol. 7, 1979, pp. 405–411.

[26] Den Hartog, J.P., *Mechanical Vibrations*, 4th ed. McGraw-Hill, New York, 1956. (Reprinted by Dover, New York, 1985.)

[27] Krenk, S., Frequency analysis of the tuned mass damper, *Journal of Applied Mechanics*, Vol. 72, 2005, pp. 936–942.

[28] Preumont, A., *Vibration Control of Active Structures, An Introduction*, 2nd edition, Kluwer, Dordrecht, 2002.

[29] Svendsen, M.N., Krenk, S., and Høgsberg, J., Resonant vibration control of wind turbine blades, *Torque 2010: The Science of Making Torque from Wind*, June 28-30, Crete, Greece, 2010, pp. 543–553.

[30] Krenk, S., and Høgsberg, J., Tuned mass absorbers on damped structures under random load, *Probabilistic Engineering Mechanics*, Vol. 23, 2008, pp. 408–415.

[31] Batchelor, G.K., *The Theory of Homogeneous Turbulence*, Cambridge University Press, Cambridge, UK, 1953.

[32] von Kàrmàn, T., Progres in the statistical theory of turbulence, *Proceedings of the National Academy of Science*, Vol. 34, 1948, pp. 530–539.

[33] Kristensen, L., and Frandsen, S., Model for power spectra of the blade of a wind turbine measured from the moving frame of reference, *Journal of Wind Engineering and Industrial Aerodynamics*, Vol. 10, 1982, pp. 249–262.

[34] Olver, F.W.J., Lozier, D.W., Boisvert, R.F., and Clark, C.W., *NIST Handbook of Mathematical Functions*, Cambridge University Press, Cambridge, UK, 2010.

DTU Mechanical Engineering
Section of Coastal, Maritime and Structural Engineering
Technical University of Denmark

Nils Koppels Allé, Bld. 403
DK- 2800 Kgs. Lyngby
Denmark
Phone (+45) 45 25 13 60
Fax (+45) 45 88 43 25
www.mek.dtu.dk
ISBN: 978-87-90416-42-3

DCAMM
Danish Center for Applied Mathematics and Mechanics

Nils Koppels Allé, Bld. 404
DK-2800 Kgs. Lyngby
Denmark
Phone (+45) 4525 4250
Fax (+45) 4593 1475
www.dcamm.dk
ISSN: 0903-1685